MEAN-FIELD INVESTIGATION OF STRENGTH FUNCTIONS OF GIANT RESONANCES COMPARED WITH THE UNEXPECTED EXPERIMENTAL CHARACTERISTICS

A Dissertation

by

GIACOMO BONASERA

Submitted to the Office of Graduate and Professional Studies of
Texas A&M University
in partial fulfillment of the requirements for the degree of

DOCTOR OF PHILOSOPHY

Chair of Committee,	Shalom Shlomo
Committee Members,	Che-Ming Ko
	Grigory Rogachev
	Sherry J. Yennello
Head of Department,	Grigory Rogachev

August 2019

Major Subject: Physics

ABSTRACT

We calculate properties of nuclear giant resonances using Hartree-Fock based Random Phase Approximation theory adopting a Skyrme-type effective interaction. Centroid energies for isoscalar and isovector giant resonances of multipolarities L = 0-3 in ^{40,48}Ca, ^{68}Ni, ^{90}Zr, ^{116}Sn, ^{144}Sm and ^{208}Pb are obtained for 33 interactions found in the literature. We compare our theoretical results with experimental data and determine the correlation between theoretical centroid energies and each nuclear matter property related to each Skyrme interaction. We obtained strong correlations and agreement with experimental data for the isoscalar giant monopole and quadrupole resonances and the isovector giant dipole resonance (IVGDR). We determined the best range for the incompressibility coefficient (K_{NM} = 210-240MeV), the effective mass (m*/m = 0.7-0.9) and the enhancement coefficient of the energy weighted sum rule of the IVGDR (κ = 0.25-0.70). These constraints, valid across a wide range of masses, may be used in a fit to develop a new energy density functional with improved predictive power.

We also performed a similar analysis for two mass regions: A = 90-100 and A = 44-68. Interest recently arose in these regions when we found significant disagreements between experiment and theory for certain isotopes. Therefore, we extended our investigation to determine if other interactions agreed with the experimental results. However, we found that none of the interactions considered reproduced the unexpected experimental characteristics.

ACKNOWLEDGEMENTS

I would like to thank my advisor, Dr. Shalom Shlomo, and my committee members, Dr. C. M. Ko, Dr. G. Rogachev and Dr. S. J. Yennello for their continued help and guidance. I would also like to thank all of the faculty and staff at the Cyclotron Institute for the many years together and countless opportunities.

Special thanks to all the students at the Cyclotron for making the day to day better. Lastly, I thank my family who has sacrificed and cared for me for so many years.

NOMENCLATURE

A, Z, N	Number of nucleons, protons, and neutrons
I	Isospin: (N-Z)/A
NM	Nuclear matter
CM	Center of mass
E/A	Energy per nucleon at saturation density
E_{CEN}	Centroid energy
EDF	Energy density functional
EOS	Equation of state
EWSR	Energy weighted sum rule
GR	Giant resonance
HF	Hartree-Fock
RPA	Random Phase Approximation
ISGMR (E0) ($T0L0$)	Isoscalar giant monopole resonance
ISGDR (E1) ($T0L1$)	Isoscalar giant dipole resonance
ISGQR (E2) ($T0L2$)	Isoscalar giant quadrupole resonance
ISGOR (E3) ($T0L3$)	Isoscalar giant octupole resonance
IVGMR ($T1L0$)	Isovector giant monopole resonance
IVGDR ($T1L1$)	Isovector giant dipole resonance
IVGQR ($T1L2$)	Isovector giant quadrupole resonance

IVGOR ($T1L3$)	Isovector giant octupole resonance
ρ_0	Saturation density of nuclear matter
J	Symmetry energy coefficient at ρ_0
L	Related to first derivative of symmetry energy at ρ_0
K_{sym}	Related to second derivative of symmetry energy at ρ_0
κ	Enhancement coefficient of the EWSR of the IVGDR
K_{NM}	Incompressibility coefficient of nuclear matter
m*/m	Nucleon effective mass

TABLE OF CONTENTS

LIST OF FIGURES

LIST OF TABLES

CHAPTER I

INTRODUCTION

The collective motion of nucleons (protons and neutrons) in the nucleus have remained the subject of experimental and theoretical studies since at least 1960 [1–3] yet present still unresolved problems. These studies play a key role in the determination of bulk nuclear matter properties which are used to describe for example nuclei, the structure and evolution of stars, and heavy-ion collisions [4,5]. In particular, we focus on the isoscalar (isospin T = 0) and isovector (isospin T = 1) giant resonances up to multipolarity L = 3. For the isoscalar giant resonances protons and neutrons move in phase with each other, while for the isovector giant resonances they move in opposite phase. The energy position and widths of the giant resonance follow a smooth relation with the nucleon number, confirming this motion is indeed due to a coherent participation of many nucleons (collective motion). The first observation of giant resonances is attributed to Baldwin and Klaiber [6] who obtained a large peak in the photo-fission cross-section of U and Th by bombarding targets with gamma rays from a 100-MeV betatron. This was later recognized as the isovector giant dipole resonance (IVGDR). A few decades later, the isoscalar giant quadrupole resonance (ISGQR) was found from proton [7] and electron scattering experiments [8]. Subsequently, Youngblood et al. developed a technique to detect products of inelastic α-scattering up

to 0° leading to the discovery of the isoscalar giant monopole resonance (ISGMR) in ^{144}Sm and ^{208}Pb [9].

From a theoretical point of view, the nucleus can be described as a system of bound nucleons held together by two-body interactions between each pair of nucleons. In such an ab initio model the effective interaction is given by the nucleon-nucleon potential extracted from nucleon-nucleon scattering experimental data. However, the numerical solution of this many-body problem requires advanced computational techniques and is currently limited to small systems. At the other end of the scale, nuclear properties can be described by macroscopic models (like the liquid drop model). However, while these models are good for describing average trends of nuclear binding energies, they are often augmented with ad hoc corrections which makes them not reliable for extrapolating properties of exotic nuclei. Therefore, in this work we concern ourselves with the mean field approach which lies between these two extremes. Within this model, the nucleon is viewed as being held inside a potential-well created by the effective interaction of all the other nucleons. However, an exact expression of the energy density functional (EDF) associated with two-body interaction is generally not known. Therefore, one must determine the parameters of the EDF with fits to experimental data. Today mean-field calculations are usually carried out using either Skyrme's interaction [10], the Gogny force [11] or with the relativistic mean-field model [12].

In chapter II we present the Hartree-Fock (HF) equations using a Skyrme-type effective interaction in order to obtain the ground state properties of the nucleus of

interest, followed by the random phase approximation (RPA) to determine the strength functions and centroid energies. We note that since the original formulation of the effective two-body Skyrme interaction in 1956 by Skyrme [10] and the improvements made by Vautherin and Brink [13], who carried out the first fully self-consistent mean field HF calculations with a Skyrme-type interaction, hundreds of Skyrme parametrizations have been published by fitting different sets of data geared to reproduce particular physical phenomena. Efforts have been made to sift through this myriad of interactions in order to determine the best interactions at describing a variety of physical effects [14]. These interaction, and their associated nuclear matter properties, can be used as constraints for the development of even better interactions. For the spherical HF-RPA calculations performed in this work we employ 33 commonly adopted Skyrme type interactions of the standard form associated with a broad range of Nuclear Matter (NM) properties. We then determined the Pearson linear correlation coefficient between each NM properties. We also employ the Pearson linear correlation coefficient to investigate the sensitivity of the calculated centroid energy of giant resonances to the NM properties of the interactions used in the calculations in order to determine constraints on NM properties. This is a well-established method in the literature and attempts have been made to constrain properties such as the incompressibility coefficient of NM and the symmetry energy as a function of the density [4,15–17].

In chapter III we study the isoscalar and isovector L = 0 - 3 centroid energies across a wide range of spherical nuclei including ^{40,48}Ca, ^{68}Ni, ^{90}Zr, ^{116}Sn, ^{144}Sm and ^{208}Pb, by carrying out spherical HF based RPA calculations. We compare our results

with the existing experimental data. We determined the sensitivity of nuclear matter properties to the calculated centroid energy, E_{CEN}, by calculating the Pearson linear correlation coefficient between them. For the E_{CEN} of the isoscalar giant monopole resonance (ISGMR) we find strong correlation with the incompressibility coefficient, K_{NM}, as well as good agreement with experimental data. Similarly, for the E_{CEN} of the isoscalar giant quadrupole resonance (ISGQR) and the nucleon effective mass, m*/m, and for the E_{CEN} of the isovector giant dipole resonance (IVGDR) and the energy weighted sum rule (EWSR) enhancement coefficient for the IVGDR, κ, we obtain strong correlation and good agreement with experiment. This allows us to determine constraints on the values of K_{NM}, m*/m and κ that can be included in a fit to obtain the parameters of a modern energy density functional (EDF) with improved predicting power. We note that the constraints obtained for K_{NM} and κ may depend on the specific form of the interactions adopted. However, investigations adopting different models of the nucleon-nucleon interaction confirmed the correlation between the ISGMR E_{CEN} and K_{NM} [18]. The relation between the E_{CEN} of the ISGQR and the effective mass arises because m*/m influences the distance between nuclear shells and therefore the response function.

Recently, the isoscalar giant resonance region of ^{92,94,96,98,100}Mo [19,20] and ^{90,92,94}Zr [21] was investigated using inelastic scattering of 240-MeV α particles from the K-500 superconducting cyclotron at Texas A&M University (TAMU). The obtained strength distributions and centroid energies were compared to results of Hartree-Fock based random phase approximation calculations (HF-RPA) using the KDE0v1 [22] Skyrme-type interaction. For some nuclei large discrepancies were found between the

measured and the calculated centroid energy as well as with the shape and magnitude of the strength distributions. In chapter IV we extend our theoretical investigation to include an additional 32 interactions to further study these discrepancies as well as the isovector resonances L = 0 - 3. Additionally we compare our calculated centroid energies of the ISGMR with the experimental data from the Research Center for Nuclear Physics (RCNP) at Osaka University (Osaka, Japan) [23]. Like in chapter III, we investigate the sensitivity of the calculated values of E_{CEN} to NM values by determining the corresponding Pearson linear correlation coefficients and obtain very similar results.

Following the template of chapter III and IV, we study in chapter V the isoscalar and isovector giant resonances L = 0 - 3 for ^{44}Ca, ^{54}Fe, ^{64,68}Zn and ^{56,58,60,68}Ni by comparing results of HF-RPA calculations using 33 Skyrme interactions to experimental data. The motivation for this study arose following our investigations [24,25] in which we found significant discrepancies between the experimental data of the isoscalar resonances obtained at TAMU and the results of the calculations using the KDE0v1 interaction for ^{44}Ca, ^{54}Fe, ^{64,68}Zn. We also investigate the sensitivity of the centroid energy to nuclear matter properties by determining the Pearson linear correlation coefficients and we found slightly lower correlations for these light nuclei. We present our conclusions in chapter VI.

CHAPTER II

SPHERICAL HARTREE-FOCK BASED RANDOM PHASE APPROXIMATION FORMALISM OF GIANT RESONANCES USING SKYRME-TYPE INTERACTIONS

Introduction

In this study we carry out numerical calculations of properties of nuclear giant resonances using Hartree-Fock based random phase approximation theory. In order to solve the HF equations, we adopt a Skyrme-type interaction of the standard form (10-parameters) for the effective nucleon-nucleon interaction. The parameters of the Skyrme interaction are commonly obtained by fitting results of HF calculations of nuclear ground state properties of several nuclei, including binding energies and radii, to experimental results. The HF equations are solved through iteration leading to the ground state wave-functions. The random phase approximation is then carried out with the particle-hole interaction obtained from the Skyrme interaction leading to the determination of the strength functions and centroid energies of the giant resonances. Details of the numerical method employed to solve the RPA can be found in [26–28]. In our calculations we include all the terms of the effective interactions in both the HF and the RPA calculations to ensure self-consistency. We ensured that in our calculations the energy of the spurious state of the isoscalar dipole, which arises from the centre of mass motion, results close to 0 MeV and that the energy weighted sum rule is satisfied.

Hartree-Fock Method

The origins of the Hartree-Fock method date back to the 1920s. Shortly after the formulation of Schrodinger's equations, Hartree approximated the many-body wave-function as a product of single-particle wave-functions and calculated the wave-functions and energies of atoms within the "self-consistent field" method he developed [29]. Subsequently**,** Slater showed that the Hartree method could also be obtained by applying a variational principle to a trial wave function obtained from the product of single-particle wave-functions [30]. Further developments came in 1930 when both Slater and Fock realized that the Hartree method, which used the Pauli exclusion principle to forbid two electrons from occupying the same quantum state [31,32], didn't respect quantum statistics (i.e. particles are indistinguishable from one another). The solution was found by adopting a Slater determinant, composed of one-particle orbits, which ensures that the total wave function is anti-symmetrized. Consequently, with the advent of the first electronic computers in the 1950s, the HF method has been applied to many fields of physics. Simply put, within the HF approximation, the ground state wave-function of the A-nucleon system of interacting particles is given by non-interacting particles inside a mean-field. In order to determine the wave-function one must then minimize the expectation value of the total Hamiltonian.

In this work we approximate the A-nucleon wave function Φ with the product of the single-particle wave-functions $\phi_i(\vec{r}_i, \sigma_i, \tau_i)$. Since neutrons or protons are

indistinguishable fermions the total wave function must be anti-symmetric, therefore a Slater determinant is adopted:

$$\Phi = \frac{1}{\sqrt{A!}} \det \begin{bmatrix} \phi_1(\vec{r}_1, \sigma_1, \tau_1) & \cdots & \phi_i(\vec{r}_1, \sigma_1, \tau_1) \\ \vdots & \ddots & \vdots \\ \phi_1(\vec{r}_i, \sigma_i, \tau_i) & \cdots & \phi_i(\vec{r}_i, \sigma_i, \tau_i) \end{bmatrix}. \tag{2.1}$$

In Eq. (2.1) the coordinates of the *i*-th nucleon $\vec{r}_i$ and σ_i represent the spacial and spin components, while the isospin is given by $\tau_i = \frac{1}{2}$ for protons and $\tau_i = -\frac{1}{2}$ for neutrons. The total Hamiltonian for the nucleus is given by the sum of kinetic plus potential energies:

$$H = T + \sum_{i<j}^{A} V_{ij} + V_{Coul}, \tag{2.2}$$

where

$$T = -\frac{\hbar^2}{2} \sum_{i=1}^{A} \frac{\nabla_i^2}{m_{\tau_i}} \qquad \text{and} \qquad V_{Coul} = e^2 \sum_{i<j}^{Z} \frac{1}{|r_{ij}|} \tag{2.3}$$

are the kinetic and Coulomb terms, respectively. For the two-body interaction, V_{ij}, we use a standard (10-parameter) Skyrme-type effective nucleon-nucleon potential [33]:

$$\begin{aligned} V_{ij} = {} & t_0\left(1 + x_0 P_{ij}^{\sigma}\right)\delta\left(\vec{r}_i - \vec{r}_j\right) + \frac{1}{2} t_1\left(1 + x_1 P_{ij}^{\sigma}\right)\left[\overleftarrow{k}_{ij}^2 \delta\left(\vec{r}_i - \vec{r}_j\right) + \delta\left(\vec{r}_i - \vec{r}_j\right)\vec{k}_{ij}^2\right] \\ & + t_2\left(1 + x_2 P_{ij}^{\sigma}\right)\overleftarrow{k}_{ij}\delta\left(\vec{r}_i - \vec{r}_j\right)\vec{k}_{ij} + \frac{1}{6} t_3\left(1 + x_3 P_{ij}^{\sigma}\right)\rho^{\alpha}\left(\frac{\vec{r}_i + \vec{r}_j}{2}\right)\delta\left(\vec{r}_i - \vec{r}_j\right) \\ & + i W_0 \overleftarrow{k}_{ij}\delta\left(\vec{r}_i - \vec{r}_j\right)\left(\vec{\sigma}_1 + \vec{\sigma}_2\right) \times \vec{k}_{ij} \, . \end{aligned} \tag{2.4}$$

In Eq. (2.4) P_{ij}^{σ} denotes the spin exchange operator, $\vec{\sigma}_i$ is the Pauli spin operator, and the momentum operators are given by $\vec{k}_{ij} = -i\left(\vec{\nabla}_i - \vec{\nabla}_j\right)/2$ and $\overleftarrow{k}_{ij} = -i\left(\overleftarrow{\nabla}_i - \overleftarrow{\nabla}_j\right)/2$. The direction of the arrow indicates the direction the momentum operator acts on. $t_n,\ x_n, W_0$ and α are the ten Skyrme parameters determined by fits to properties of nuclei. The term

proportional to t_0 represents a δ-force with a spin exchange, the t_1 and t_2 terms are the effective range parts, the t_3 term approximates the three-body force and the last term, multiplying W_0, gives a two-body spin orbit interaction.

The local energy density, H_{Skyrme}, can be obtained from the matrix element of V_{ij} and the wave-function given in Eq. (2.1):

$$\langle \Phi | V_{ij} | \Phi \rangle = \int H_{Skyrme}\, d^3r \tag{2.5}$$

leading to [13]:

$$\begin{aligned} H_{Skyrme} \quad &= \tfrac{1}{4} t_0 \left[(2 + x_0)\rho^2 - (2x_0 + 1)\left(\rho_p^2 + \rho_n^2\right) \right] \\ &+ \tfrac{1}{24} t_3 \rho^{\alpha} \left[(2 + x_3)\rho^2 - (2x_3 + 1)\left(\rho_p^2 + \rho_n^2\right) \right] \\ &+ \tfrac{1}{8} [t_1(2 + x_1) + t_2(2 + x_2)]\tau\rho \\ &+ \tfrac{1}{8} [t_2(2x_2 + 1) - t_1(2x_1 + 1)]\left(\tau_p\rho_p + \tau_n\rho_n\right) \\ &+ \tfrac{1}{32} [3t_1(2 + x_1) - t_2(2 + x_2)]\left(\vec{\nabla}\rho\right)^2 \\ &- \tfrac{1}{32} [3t_1(2x_1 + 1) + t_2(2x_2 + 1)] \left[\left(\vec{\nabla}\rho_p\right)^2 + \left(\vec{\nabla}\rho_n\right)^2 \right] \\ &+ \tfrac{W_0}{2} \left[\vec{J} \cdot \vec{\nabla}\rho + x_w \left(\overrightarrow{J_p} \cdot \vec{\nabla}\rho_p + \overrightarrow{J_n} \cdot \vec{\nabla}\rho_n \right) \right] \\ &- \tfrac{1}{16} (t_1 x_1 + t_2 x_2) J^2 + \tfrac{1}{16} (t_1 - t_2)\left(J_p^2 + J_n^2\right). \end{aligned} \tag{2.6}$$

Eq. (2.6) is given as a function of the Skyrme parameters, the total nucleon density $\rho = \rho_p + \rho_n$, the total kinetic energy density $\tau = \tau_p + \tau_n$ and the total spin current density $\vec{J} = \overrightarrow{J_p} + \overrightarrow{J_n}$.

The total Skyrme energy density functional of the system can now be calculated with [33,34]:

$$E = \int \left(K(\vec{r}) + H_{Skyrme}(\vec{r}) + H_{Coul}(\vec{r}) \right) d^3r. \quad (2.7)$$

The kinetic energy term is given by:

$$K = \frac{\hbar^2}{2m_p}\tau_p(\vec{r}) + \frac{\hbar^2}{2m_n}\tau_n(\vec{r}) \, . \quad (2.8)$$

In Eq. (2.7), the Coulomb contribution is given by the direct plus the exchange components [35]:

$$H_{Coul}(r) = H_{Coul}^{dir}(r) + H_{Coul}^{ex}(r), \quad (2.9)$$

with

$$H_{Coul}^{dir}(r) = \frac{1}{2}e^2\rho_p(r)\int \frac{\rho_p(r')}{|r-r'|}d^3r' \, , \quad (2.10)$$

and

$$H_{Coul}^{ex}(r) = -\frac{3}{4}e^2\rho_p(r)\left[\frac{3\rho_p(r)}{\pi}\right]^{1/3} \, . \quad (2.11)$$

The nucleon density, kinetic energy density and spin current density are obtained from:

$$\rho_\tau(\vec{r}) = \sum_{i=1}^{A}\sum_\sigma \phi_i^*(\vec{r},\sigma,\tau)\phi_i(\vec{r},\sigma,\tau) \qquad \rho(\vec{r}) = \sum_\tau \rho_\tau(\vec{r}) \quad (2.12)$$

$$\tau_\tau(\vec{r}) = \sum_{i=1}^{A}\sum_\sigma \vec{\nabla}\phi_i^*(\vec{r},\sigma,\tau)\vec{\nabla}\phi_i(\vec{r},\sigma,\tau) \qquad \tau(\vec{r}) = \sum_\tau \tau_\tau(\vec{r}) \quad (2.13)$$

$$\vec{J}_\tau(\vec{r}) = -i\sum_{i=1}^{A}\sum_{\sigma\sigma'}\phi_i^*(\vec{r},\sigma,\tau)\left[\vec{\nabla}\phi_i(\vec{r},\sigma',\tau)\times\langle\sigma|\vec{\sigma}|\sigma'\rangle\right] \quad \vec{J}(\vec{r}) = \sum_\tau \vec{J}_\tau(\vec{r}) \quad (2.14)$$

where the subscript $\tau = p$ or n and in the summation A = Z or N, for protons or neutrons, respectively.

We can now apply the variational method

$$\langle\delta\Phi|H|\Phi\rangle = 0, \quad (2.15)$$

with the condition of conservation of nucleon number, $\sum_{\sigma,\tau}\int \rho_{\sigma,\tau}\, d\vec{r} = A$. We denote the variations in the nucleon, kinetic energy and spin current densities by the δ prefix; the Hartree-Fock equations, for a Skyrme interaction, are then obtained from [13]:

$$\frac{\delta}{\delta\rho_{\sigma,\tau}}\left(E - \sum_{\sigma,\tau}\varepsilon_i \int \rho_{\sigma,\tau}\, d\vec{r}\right) = 0\,, \tag{2.16}$$

$$\delta E = \sum_{\sigma,\tau}\int\left(\frac{\hbar^2}{2m_\tau^*(\vec{r})}\delta\tau_{\sigma,\tau}(\vec{r}) + U_\tau(\vec{r})\delta\rho_{\sigma,\tau}(\vec{r}) + W_\tau(\vec{r})\delta\vec{J}_{\sigma,\tau}(\vec{r})\right)d\vec{r}. \tag{2.17}$$

In Eq. (2.17), $m_\tau^*(\vec{r})$ is the nucleon effective mass, $U_\tau(\vec{r})$ is the central potential, and $W_\tau(\vec{r})$ represents the spin-orbit potential. These can be written using equations (2.12) to (2.14) together with the parameters of the Skyrme interaction:

$$\frac{\hbar^2}{2m_\tau^*(\vec{r})} = \frac{\hbar^2}{2m_\tau} + \frac{1}{8}[t_1(2+x_1) + t_2(2+x_2)]\rho(\vec{r}) - \frac{1}{8}[t_1(1+2x_1) - t_2(1+2x_2)]\rho_\tau(\vec{r}), \tag{2.18}$$

$$\begin{aligned} U_\tau(\vec{r}) = {} & t_0\left(1+\frac{x_0}{2}\right)\rho(\vec{r}) - t_0\left(\frac{1}{2}+x_0\right)\rho_\tau(\vec{r}) + \frac{1}{8}[t_1(2+x_1) + t_2(2+x_2)]\tau(\vec{r}) \\ & -\frac{1}{8}[t_1(1+2x_1) + t_2(1+2x_2)]\tau_\tau(\vec{r}) + \frac{\alpha+2}{24}t_3(2+x_3)\rho^{\alpha+1}(\vec{r}) \\ & -\frac{\alpha}{24}t_3(1+2x_3)\rho^{\alpha-1}(\vec{r})\left[\rho_p^2(\vec{r}) + \rho_n^2(\vec{r})\right] - \frac{1}{12}t_3(1+2x_3)\rho^\alpha(\vec{r})\rho_\tau(\vec{r}) \\ & -\frac{1}{16}[3t_1(2+x_1) - t_2(2+x_2)]\vec{\nabla}^2\rho(\vec{r}) + \frac{1}{16}[3t_1(1+2x_1) + t_2(1+2x_2)]\vec{\nabla}^2\rho_\tau(\vec{r}) \\ & -\frac{1}{2}W_0\left(\vec{\nabla}\vec{J}(\vec{r}) + \vec{\nabla}\vec{J}_\tau(\vec{r})\right) + \delta_{\frac{1}{2},\tau}e^2\int\frac{\rho_p(\vec{r})}{|\vec{r}-\vec{r}'|}d\vec{r}' \end{aligned} \tag{2.19}$$

and

$$W_\tau(\vec{r}) = \frac{1}{2}W_0\left(\vec{\nabla}\rho(\vec{r}) + \vec{\nabla}\rho_\tau(\vec{r})\right) + \frac{1}{8}(t_1 - t_2)\vec{J}_\tau(\vec{r}) - \frac{1}{8}(t_1x_1 - t_2x_2)\vec{J}(\vec{r}). \tag{2.20}$$

From the time reversal invariance property we can write [13]:

$$\delta\phi_{\bar{\imath}}(\vec{r},\sigma,\tau) = -2\sigma\delta\phi_i^*(\vec{r},-\sigma,\tau) \tag{2.21}$$

leading to the following simplifications for the variations of the nucleon, kinetic and spin current densities [13]:

$$\delta\tau_{\sigma,\tau}(\vec{r}) = 2\sum_{i,\sigma}\vec{\nabla}\delta\phi_i^*(\vec{r},\sigma,\tau)\cdot\vec{\nabla}\phi_i(\vec{r},\sigma,\tau) \tag{2.22}$$

$$\delta\rho_{\sigma,\tau}(\vec{r}) = 2\sum_{i,\sigma}\delta\phi_i^*(\vec{r},\sigma,\tau)\phi_i(\vec{r},\sigma,\tau) \tag{2.23}$$

$$\delta\vec{J}_{\sigma,\tau}(\vec{r}) = -2i\sum_{i,\sigma_1,\sigma_2}\delta\phi_i^*(\vec{r},\sigma_1,\tau)\vec{\nabla}\phi_i(\vec{r},\sigma_2,\tau)\times\langle\sigma_1|\vec{\sigma}|\sigma_2\rangle. \tag{2.24}$$

Substituting Eqs. (2.22) to (2.24) and by introducing the Lagrange multipliers, ε_i (i = 1, …, A), into Eq. (2.17) along with the constraints discussed above, we have:

$$\sum_{i,\sigma_1}\int\delta\phi_i^*(\vec{r},\sigma_1,\tau)\left[\frac{\hbar^2}{2m_\tau^*(\vec{r})}\vec{\nabla}\phi_i(\vec{r},\sigma_1,\tau)\vec{\nabla}+U_\tau(\vec{r})\,\phi_i(\vec{r},\sigma_1,\tau)\right.$$

$$\left.-iW_\tau(\vec{r})\sum_{\sigma_2}\vec{\nabla}\times\langle\sigma_1|\vec{\sigma}|\sigma_2\rangle\phi_i(\vec{r},\sigma_2,\tau)-\varepsilon_i\phi_i(\vec{r},\sigma_1,\tau)\right]d\vec{r}=0. \tag{2.25}$$

This simplifies further because the variation $\delta\phi_i^*(\vec{r},\sigma_1,\tau)=0$, leading to:

$$\sum_{i,\sigma_1}\int\left[\frac{\hbar^2}{2m_\tau^*(\vec{r})}\vec{\nabla}\phi_i(\vec{r},\sigma_1,\tau)\vec{\nabla}+U_\tau(\vec{r})\,\phi_i(\vec{r},\sigma_1,\tau)\right.$$

$$\left.-iW_\tau(\vec{r})\sum_{\sigma_2}\vec{\nabla}\times\langle\sigma_1|\vec{\sigma}|\sigma_2\rangle\phi_i(\vec{r},\sigma_2,\tau)-\varepsilon_i\phi_i(\vec{r},\sigma_1,\tau)\right]d\vec{r}=0. \tag{2.26}$$

We now integrate by parts to obtain the Hartree-Fock equations [13]:

$$\left[-\vec{\nabla}\frac{\hbar^2}{2m_\tau^*(\vec{r})}\vec{\nabla}+U_\tau(\vec{r})-iW_\tau(\vec{r})\left(\vec{\nabla}\times\vec{\sigma}\right)\right]\phi_i(\vec{r},\sigma,\tau)=\varepsilon_i\phi_i(\vec{r},\sigma,\tau)\,. \tag{2.27}$$

Solving Eq. (2.27) we obtain the single particle wave-functions, $\phi_i(\vec{r},\sigma,\tau)$, and corresponding energy, ε_i, for all the A-nucleons which leads to the determination of the total ground state wave function, Φ. In order to calculate the energy of the ground state of a finite nucleus, we must subtract the contribution of the center of mass motion from the total energy density functional of Eq. (2.7):

$$E_{gs} = E - \left\langle \Phi \left| \frac{P_{CM}^2}{2M} \right| \Phi \right\rangle. \tag{2.28}$$

where $P = -i\hbar \sum_i \nabla_i$ is the total linear momentum operator. Note that in general one should also account for the energy of rotation of the total system, however this contribution vanishes if systems are treated within the spherical approximation (as we do).

The single particle wave function, ϕ_i, for the case of a spherical closed-shell nucleus, using spherical coordinate can be written as:

$$\phi_i(\vec{r}, \sigma, \tau) = \frac{R_\alpha(r)}{r} Y_{jlm}(\hat{r}, \sigma) \chi_{m_\tau}(\tau). \tag{2.29}$$

In Eq. (2.29), $\alpha = n, j, l, m_\tau$, where n represents the principal quantum number, j is the angular momentum number and its z-projection m, l is the orbital momentum number and the z-projection of the isospin is m_τ. The second component of Eq. (2.29) are the spinor spherical harmonics, given by:

$$Y_{jlm}(\hat{r}, \sigma) = \sum_{m_l m_s} \left\langle l \frac{1}{2} m_l m_s \middle| jm \right\rangle Y_{lm_l}(\hat{r}) \mu_{m_s}(\sigma), \tag{2.30}$$

where $\mu_{m_s}(\sigma) = \delta_{\sigma, m_s}$ are the eigenfunctions of the z-projections of the spin operators, respectively. The third component of Eq. (2.29), $\chi_{m_\tau}(\tau) = \delta_{\tau, m_\tau}$, are the eigenfunctions of the isospin wave-functions.

Plugging in the orthogonality condition:

$$\sum_m Y_{jlm}^*(\hat{r}, \sigma) Y_{jlm}(\hat{r}, \sigma) = \frac{2j+1}{4\pi}, \tag{2.31}$$

into equations (2.12) and (2.13) for the nucleon and kinetic energy densities, respectively, we obtain:

$$\rho_\tau(\vec{r}) = \rho_\tau(r) = \frac{1}{4\pi r^2}\sum_{n,j_\alpha,l}(2j_\alpha + 1)\, R_\alpha^2(r), \tag{2.32}$$

$$\tau_\tau(\vec{r}) = \tau_\tau(r) = \frac{1}{4\pi}\sum_{n,j_\alpha,l_\alpha}(2j_\alpha + 1)\left[\left(\frac{dR_\alpha(r)}{dr}\right)^2 + \frac{l_\alpha(l_\alpha+1)}{r^2}R_\alpha^2(r)\right]. \tag{2.33}$$

Using Eq. (2.14), we can rewrite the spin current density $\vec{J}_\tau(\vec{r})$ as:

$$\vec{J}_\tau(\vec{r}) = -i\sum_{i=1}^{A}\phi_i^*(\vec{r},\tau)\frac{\vec{r}}{r}\left(\vec{\nabla}\times\vec{\sigma}\right)\phi_i(\vec{r},\tau)\frac{\vec{r}}{r} \tag{2.34}$$

$$= \left[\frac{1}{r^2}\frac{2}{\hbar^2}\sum_{i=1}^{A}\phi_i^*(\vec{r},\tau)\left(\vec{l}\,\vec{s}\right)\phi_i(\vec{r},\tau)\right]\vec{r} = J_\tau(r)\vec{r}, \tag{2.35}$$

which can be further simplified for the spherical wave-function given in Eq. (2.29):

$$J_\tau(r) = \frac{1}{4\pi r^2}\sum_{n,j_\alpha,l_\alpha}(2j_\alpha + 1)\left[j_\alpha(j_\alpha + 1) - l_\alpha(l_\alpha + 1) - \frac{3}{4}\right]R_\alpha^2(r). \tag{2.36}$$

Substituting the wave-function of Eq. (2.29) into the set of non-linear equations for the spinors $\phi_i(\vec{r},\sigma,\tau)$ of Eq. (2.26), we obtain the Hartree-Fock equations subject to spherical symmetry:

$$\frac{\hbar^2}{2m_\tau^*(\vec{r})}\left[-R_\alpha''(\vec{r}) + \frac{l_\sigma(l_\sigma+1)}{r^2}R_\alpha(\vec{r})\right] - \frac{d}{dr}\left(\frac{\hbar^2}{2m_\tau^*(\vec{r})}\right)R_\alpha'(\vec{r})$$

$$+\left[U_\tau(\vec{r}) + \frac{1}{r}\frac{d}{dr}\left(\frac{\hbar^2}{2m_\tau^*(\vec{r})}\right) + \frac{\left[j_\sigma(j_\sigma+1) - l_\sigma(l_\sigma+1) - \frac{3}{4}\right]}{r}W_\tau(\vec{r})\right]R_\alpha(\vec{r}) = \varepsilon_\alpha R_\alpha(\vec{r}), \tag{2.37}$$

where ε_α represents the single particle energies. The effective mass, the potential and the spin-orbit potential are obtained from Eqs. (2.18) to (2.20) after substituting the spherical equations given in (2.32) to (2.36). The A-coupled HF equations are solved by iteration. One starts from an educated guess of the initial set of single particle orbits $\phi_j(\vec{r})$, for example a Wood-Saxons wave function, and then the HF equations are solved for a new set of $\phi_i(\vec{r})$ until convergence is attained. This iterative process leads to the determination of the ground state wave function which can then be used to study ground

state properties of nuclei and as a basis for further calculation of the excited nucleus using various methods (for example the random phase approximation).

Random Phase Approximation

We first derive the RPA equations using the equation of motion method described in [2,36]. Using the creation and destruction operators, $Q_\nu^\dagger$ and Q_ν, respectively, defined by:

$$|\nu\rangle = Q_\nu^\dagger|0\rangle \text{ and } H|\nu\rangle = E_\nu|\nu\rangle \tag{2.38}$$

such that:

$$Q_\nu^\dagger = |\nu\rangle\langle 0|, \tag{2.39}$$

allows us to write the equation of motion (EOM) from the Schrodinger equation:

$$\left[H, Q_\nu^\dagger\right]|0\rangle = (E_\nu - E_0)Q_\nu^\dagger|0\rangle. \tag{2.40}$$

Next, we multiply Eq. (2.40) from the left by an arbitrary state $\langle 0|\delta Q$:

$$\langle 0|\left[\delta Q, \left[H, Q_\nu^\dagger\right]\right]|0\rangle = (E_\nu - E_0)\langle 0|\left[\delta Q, Q_\nu^\dagger\right]|0\rangle. \tag{2.41}$$

Within the RPA formalism the excited states are limited to 1p-1h excitations. Therefore, the general vibration creation operator has the following form:

$$Q_\nu^\dagger = \sum_{mi} X_{mi}^\nu a_m^\dagger a_i - \sum_{mi} Y_{mi}^\nu a_i^\dagger a_m, \tag{2.42}$$

where the indices m and i are used to label the particle and hole states, respectively, of the (Hartree-Fock) mean field. This operator creates and destroys ph pairs, therefore, when applied to the RPA ground state, $|RPA\rangle$, it satisfies:

$$Q_\nu|RPA\rangle = 0, \tag{2.43}$$

while for an excited state we have:

$$|\upsilon\rangle = Q_\nu^\dagger|RPA\rangle. \tag{2.44}$$

Unlike the simpler Tamm-Dancoff approximation, in which $Y_{mi}^\nu = 0$ in Eq. (2.42), for the case of the RPA method we have two column matrices, X_{mi}^ν and Y_{mi}^ν, for the general vibration creation operator. Therefore, we obtain two sets of equations:

$$\langle RPA|\left[a_i^\dagger a_m, \left[H, Q_\nu^\dagger\right]\right]|RPA\rangle = \hbar\Omega_\upsilon\langle RPA|\left[a_i^\dagger a_m, Q_\nu^\dagger\right]|RPA\rangle,$$

$$\langle RPA|\left[a_m^\dagger a_i, \left[H, Q_\nu^\dagger\right]\right]|RPA\rangle = \hbar\Omega_\upsilon\langle RPA|\left[a_m^\dagger a_i, Q_\nu^\dagger\right]|RPA\rangle. \tag{2.45}$$

In Eq. (2.45) $\hbar\Omega_\upsilon$ is the excitation energy, E_ν, of the state $|\upsilon\rangle$; for the ground state, $|RPA\rangle$, one generally uses the HF ground state in the so-called "quasi-boson" approximation. This approximation is possible because the correlated ground state does not differ very much from the Hartree-Fock ground state yet leads to significant simplifications which allow us to determine the expectation values of Eq. (2.45) as:

$$\langle RPA|\left[a_i^\dagger a_m, a_n^\dagger a_j\right]|RPA\rangle = \delta_{ij}\delta_{mn} - \delta_{mn}\langle RPA|a_j a_i^\dagger|RPA\rangle - \delta_{ij}\langle RPA|a_n^\dagger a_m|RPA\rangle$$

$$\approx \langle HF|\left[a_i^\dagger a_m, a_n^\dagger a_j\right]|HF\rangle = \delta_{ij}\delta_{mn}. \tag{2.46}$$

Note that the RPA-terms on the left-hand side of Eq. (2.46) are clearly different from the HF-terms on the right, however they enter with a "random phase" that cancels out. Using $(X^\nu)_{mi} = X_{mi}^\nu$, $(Y^\nu)_{mi} = Y_{mi}^\nu$, allows us to rewrite Eq. (2.45) in compact form:

$$\begin{pmatrix} A & B \\ B^* & A^* \end{pmatrix}\begin{pmatrix} X^\nu \\ Y^\nu \end{pmatrix} = \hbar\Omega_\upsilon \begin{pmatrix} 1 & 0 \\ 0 & -1 \end{pmatrix}\begin{pmatrix} X^\nu \\ Y^\nu \end{pmatrix}. \tag{2.47}$$

The matrices A and B are given by [37]:

$$A_{mi,nj} = \langle HF|\left[a_i^\dagger a_m, \left[H, a_n^\dagger a_j\right]\right]|HF\rangle = (\epsilon_m - \epsilon_i)\delta_{mn}\delta_{ij} + \langle mj|V_{res}|in\rangle \tag{2.48}$$

$$B_{mi,nj} = -\langle HF|\left[a_i^\dagger a_m, \left[H, a_j^\dagger a_n\right]\right]|HF\rangle = \langle mn|V_{res}|ij\rangle\,, \tag{2.49}$$

where ϵ_m and ϵ_i are single particle energies of the Hartree-Fock ph states. The ph coupled matrix elements of the residual interaction, V_{res}, are obtained from the total Skyrme energy density functional (which includes the kinetic, Skyrme and Coulomb contributions). We note that the RPA equations may also be derived from the self-consistent method based on the coordinate-like Q_n (time-even) and momentum-like P^n (time-odd) ph-operators. Our numerical calculations follow the Q-P representations, further details can be found in Refs. [26–28].

Once the RPA states, $|\nu\rangle$, of energy E_ν have been determined we can proceed to calculate the strength function, S(E), using:

$$S(E) = \sum_\nu |\langle 0|F_L|\nu\rangle|^2 \delta(E_\nu - E_0). \tag{2.50}$$

In Eq. (2.50) the single particle scattering operator F_L is given by:

$$F_L = \sum_i f(r_i) Y_{L0}(i)\,, \tag{2.51}$$

for the isoscalar cases (T = 0) and by:

$$F_L = \frac{Z}{A}\sum_n f(r_n) Y_{L0}(n) - \frac{N}{A}\sum_p f\left(r_p\right) Y_{L0}(p) \tag{2.52}$$

for the isovector cases (T = 1). The different multipolarities determine the operator $f(r)$: for the IVGDR we have $f(r) = r$, while for the ISGDR we use $f(r) = r^3 - (5/3)\langle r^2\rangle r$, where we have subtracted the contribution from the spurious state mixing [38,39]. The operator r^2 is used in the case of the isoscalar and isovector monopoles (L = 0) and quadrupoles (L = 2) excitations, while r^3 is used for the isoscalar

and isovector octopole (L = 3) excitations. From the integration of the strength function, S(E), we can determine the energy moments:

$$m_k = \int_{E_1}^{E_2} E^k S(E)\, dE\ , \tag{2.53}$$

where E_1 and E_2 are the excitation energy limits. The centroid energy of the giant resonance is determined from the following relation:

$$E_{CEN} = \frac{m_1}{m_0}\,. \tag{2.54}$$

We note that for $E_1 = 0$ and $E_2 = \infty$, the first energy moment, m_1, of the isoscalar operator F_L may also be directly obtained from the HF ground state wave function:

$$m_1(L, T=0) = \frac{1}{4\pi}\frac{\hbar^2}{2m}\int_0^\infty g_L(r)\,\rho(r) 4\pi r^2 dr\ , \tag{2.55}$$

thus leading to an energy weighted sum rule (EWSR) [1,40]. In Eq. (2.55) $\rho(r)$ is the ground state density obtained from the HF while $g_L(r)$ depends on the multipolarity, L, and its relative operator $f(r)$:

$$g_L(r) = \left(\frac{df}{dr}\right)^2 + L(L+1)\left(\frac{f}{r}\right)^2\,. \tag{2.56}$$

The isovector EWSR is related to Eq. (2.56) by:

$$m_1(L, T=1) = \frac{NZ}{A^2} m_1(L, T=0)\left[1 + \kappa - \kappa_{np}\right], \tag{2.57}$$

where κ is an enhancement factor due to the momentum dependence of the effective nucleon-nucleon interaction given for the standard Skyrme-type interaction Eq. (2.4) by:

$$\kappa = \frac{(1/2)[t_1(1+x_1/2)+t_2(1+x_2/2)]}{(\hbar^2/2m)(4NZ/A^2)}\ \frac{2\int g_L(r)\rho_p(r)\rho_n(r)4\pi r^2 dr}{\int g_L(r)\rho(r)4\pi r^2 dr}\ , \tag{2.58}$$

while the correction factor κ_{np} arising from the small differences between the neutron and proton densities, or in other words because $\rho_n(r) - \rho_p(r) \neq \frac{N-Z}{A}\rho(r)$, and is obtained from:

$$\kappa_{np} = \frac{(N-Z)}{A}\frac{A}{NZ}\frac{\int g_L(r)[Z\rho_n(r) - N\rho_p(r)]4\pi r^2 dr}{\int g_L(r)\rho(r)4\pi r^2 dr}. \quad (2.59)$$

Skyrme Interactions and Nuclear Matter Properties

The popularity of the Skyrme-type interaction is due in part to the great simplification it brings to the calculations thanks to it being a contact interaction (i.e. a delta function multiplying every term) while still yielding results in agreement with experimental data. However, hundreds of parameterizations of the Skyrme interactions have been developed since its first inception. These parameters are generally obtained from fits to sets of experimental data and are fine tuned to reproduce certain physical phenomena; unfortunately, these parameterizations however lead to different values for properties of nuclear matter.

The equation of state (EOS) of symmetric nuclear matter (i.e. N=Z) can be expanded around saturation density, ρ_0, as:

$$\mathrm{E_0}[\rho] = \mathrm{E_0}[\rho_0] + \frac{1}{18}\mathrm{K_{NM}}\left(\frac{\rho-\rho_0}{\rho_0}\right)^2, \quad (2.60)$$

$$\left.\frac{d\mathrm{E/A}}{d\rho}\right|_{\rho_0} = 0 \quad (2.61)$$

where $E_0[\rho]$ is the binding energy per nucleon and K_{NM} is the incompressibility coefficient of nuclear matter obtained from the second derivative of the EOS, $K_{NM} = 9\rho_0^2 \frac{\partial^2 E_0}{\partial \rho^2}\Big|_{\rho_0}$. A similar expansion can be done for asymmetric nuclear matter (i.e. N≠Z), leading to the EOS of asymmetric NM:

$$E[\rho_p, \rho_n] = E_0[\rho] + E_{sym}[\rho]\left(\frac{\rho_n - \rho_p}{\rho}\right)^2, \tag{2.62}$$

where $E_{sym}[\rho]$ is the symmetry energy at matter density ρ, while proton and neutron density are denoted by ρ_p and ρ_n, respectively. The symmetry energy can in turn be expanded around saturation density ρ_0:

$$E_{sym}[\rho] = J + \frac{1}{3}L\left(\frac{\rho - \rho_0}{\rho_0}\right) + \frac{1}{18}K_{sym}\left(\frac{\rho - \rho_0}{\rho_0}\right)^2, \tag{2.63}$$

where $J = E_{sym}[\rho_0]$ is the symmetry energy at saturation density ρ_0, while $L = 3\rho_0 \frac{\partial E_{sym}}{\partial \rho}\Big|_{\rho_0}$ and $K_{sym} = 9\rho_0 \frac{\partial^2 E_{sym}}{\partial \rho^2}\Big|_{\rho_0}$ are related to the first and second derivatives of the symmetry energy, respectively.

The properties of nuclear matter can be expressed in terms of the parameters of the Skyrme interactions. Details of the derivation can be found in [14]. Denoting $\beta = (3\pi^2/2)^{2/3}$ and $\gamma = 3t_1 + t_2(5 + 4x_2)$, the saturation density is obtained from:

$$\beta \frac{\hbar^2}{5m}\rho_0^{5/3} + \frac{3}{8}t_0\rho_0^2 + \frac{\alpha+1}{16}t_3{\rho_0}^{\alpha+2} + \frac{1}{16}\beta\gamma{\rho_0}^{8/3} = 0 \tag{2.64}$$

while the binding energy per particle and the effective mass are related to the Skyrme parameters by:

$$\frac{E_0(\rho_0)}{A} = \beta \frac{3\hbar^2}{10m}\rho_0^{2/3} + \frac{3}{8}t_0\rho_0 + \frac{1}{16}t_3{\rho_0}^{\alpha+1} + \frac{3}{80}\beta\gamma\rho_0^{5/3} \tag{2.65}$$

$$\left(\frac{m^*}{m}\right)^{-1} = 1 + \gamma \frac{\mathrm{m}}{8\hbar^2}\rho_0. \tag{2.66}$$

We can obtain the Fermi momentum, k_f, at saturation density using:

$$k_f \frac{\partial \frac{\mathrm{E}}{\mathrm{A}}(\rho_0)}{\partial k_f} = 0. \tag{2.67}$$

Therefore, by substituting $\rho_0 = \frac{2}{3\pi^2}k_f^3$ into (2.65), we derive:

$$\frac{3}{5}\frac{\hbar^2}{m} + \frac{3}{4\pi^2}t_0 k_f + \frac{1}{8\pi^2}\gamma k_f^3 + \frac{3\alpha+3}{16}\left(\frac{2}{3\pi^2}\right)^{\alpha+1} t_3 k_f^{3(\alpha+1)} = 0 \tag{2.68}$$

Similarly, the incompressibility coefficient, can be obtained from:

$$K_{NM} = k_f^2 \frac{\partial^2 \left(\frac{E}{A}\right)^{(0)}_{NM}}{\partial k_f^2} \tag{2.69}$$

which, in terms of the Skyrme parameters, becomes:

$$K_{NM} = \frac{3}{5}\frac{\hbar^2}{m}k_f^2 + \frac{3}{2\pi^2}t_0 k_f^3 + \frac{1}{2\pi^2}\gamma k_f^5 + \frac{3(\alpha+1)(3\alpha+2)}{16}\left(\frac{2}{3\pi^2}\right)^{\alpha+1} t_3 k_f^{3(\alpha+1)}. \tag{2.70}$$

The symmetry energy coefficients J, L and $\mathrm{K_{sym}}$, as well as the isovector dipole enhancement factor of the EWSR, κ, are given in terms of the saturation density and the Skyrme parameters by:

$$\mathrm{J} = \beta\frac{\hbar^2}{6\mathrm{m}}\rho_0^{2/3} - \frac{1}{8}t_0(2x_0+1)\rho_0 + \frac{1}{24}\beta[t_2(5+4x_2) - 3t_1x_1]\rho_0^{5/3} - \frac{1}{48}t_3(2x_3+1){\rho_0}^{\alpha+1}, \tag{2.71}$$

$$\mathrm{L} = \beta\frac{\hbar^2}{3\mathrm{m}}\rho_0^{2/3} - \frac{3}{8}t_0(2x_0+1)\rho_0 + \frac{5}{24}\beta[t_2(5+4x_2) - 3t_1x_1]\rho_0^{5/3} - \frac{1}{16}t_3(2x_3+1)(\alpha+1){\rho_0}^{\alpha+1}, \tag{2.72}$$

$$\mathrm{K_{sym}} = -\beta\frac{\hbar^2}{3\mathrm{m}}\rho_0^{2/3} + \frac{5}{12}\beta[t_2(5+4x_2) - 3t_1x_1]\rho_0^{5/3} - \frac{3}{16}t_3(2x_3+1)(\alpha+1)\alpha{\rho_0}^{\alpha+1}, \tag{2.73}$$

$$\kappa = \frac{\mathrm{m}}{4\hbar^2}[t_1(2+x_1) + t_2(2+x_2)]\rho_0. \quad (2.74)$$

The Landau parameter, G_0', is obtained from:

$$G_0' = \frac{3}{8}\frac{(t_2 - t_1)}{\frac{\hbar^2}{m}\left(\frac{m}{m^*}\right)}\rho_0 - \frac{k_f}{\pi^2}\frac{\left[\frac{1}{4}t_0 + \frac{1}{24}t_3{\rho_0}^{\alpha}\right]}{\frac{\hbar^2}{m}\left(\frac{m}{m^*}\right)}. \quad (2.75)$$

Details of the Numerical Calculations

In the following chapters we will show centroid energies, E_{CEN}, for the isoscalar (T = 0) and isovector (T = 1) giant resonances of multipolarity L = 0 to 3 for several nuclei, calculated within the fully self-consistent Hartree-Fock (HF)-based random phase approximation (RPA) theory described above. We use the following parametrizations of Skyrme-type interactions: SGII [41], KDE0 [22], KDE0v1 [22], SKM∗ [42], SK255 [18], SkI3 [43], SkI4 [43], SkI5 [43], SV-bas [44], SV-min [44], SV-sym32 [44], SV-m56-O [45], SV-m64-O [45], SLy4 [46], SLy5 [46], SLy6 [46], SkMP [47], SkO [48], SkO' [48], LNS [49], MSL0 [50], NRAPR [51], SQMC650 [52], SQMC700 [52], SkT1 [53], SkT2 [53], SkT3 [53], SkT8 [53], SkT9 [53], SkT1* [53], SkT3* [53], Skxs20 [54] and Zσ [55]. The parameters of all the Skyrme interactions are shown in Table 1 while the conditions for employing the interactions are given in Table 2. These interactions cover a wide range of nuclear matter properties as can be seen from Table 3 and Figure 1.

We calculate the strength distribution within the HF-RPA employing the Skyrme interactions of Table 1. In all cases we used a grid of 100 points with a spacing of 0.2 fm

between them. We also performed some simulations with different sized boxes to ensure our choice didn't affect our results. For the case of nuclei which aren't closed-shell we used the "occupation-number approximation" for the single-particle orbits to carry out our calculations (i.e. the particles where separated across multiple orbits to minimize the single particle energy and to simulate the effect of pairing).

For the calculation of the centroid energy we determined the integration energy limits from the relative strength function or, where available, we used the same integration range that was used for determining the experimental data. When integrating the strength function to determine the energy moment we choose a value of $\gamma = 0.1$ MeV for the Lorentzian smearing parameter.

In order to study the sensitivity of the centroid energy to the values of NM properties associated with each interaction we determined the Pearson linear correlation coefficient, C, which is defined as:

$$\mathrm{C} = \frac{\sum_{i=1}^{n}(x_i-\bar{x})(y_i-\bar{y})}{\sqrt{\sum_{i=1}^{n}(x_i-\bar{x})^2}\sqrt{\sum_{i=1}^{n}(y_i-\bar{y})^2}} \tag{2.76}$$

where $\bar{x}$ and $\bar{y}$ are the averages of the two quantities x and y and n=33 is the number of interactions. Based on our sample size we classify the correlations as [56]: strong ($|\mathrm{C}| > 0.80$), medium ($|\mathrm{C}| = 0.61 - 0.80$), weak ($|\mathrm{C}| = 0.35 - 0.61$) and no correlation ($|\mathrm{C}| < 0.35$).

In Table 4 the calculated Pearson linear correlation coefficient between different sets of NM properties is shown. We point out the weak correlation between K_{NM} and m*/m, the medium correlation between m*/m and the enhancement coefficient for the energy

weighted sum rule (EWSR) of the IVGDR, κ, and the varying degrees of correlation between the symmetry energy coefficients J, L and K_{sym}.

Table 1 Parameters of the Skyrme interactions. Units are: t_0 (MeV fm^3), t_1 (MeV fm^5), t_3 (MeV fm$^{3(\alpha+1)}$), W_0 (MeV), and the remaining parameters are dimensionless.

Force	t_0	t_1	t_2	t_3	W_0	x_0	x_1	x_2	x_3	X_w	α
SGII	-2645.00	340.00	-41.90	15595.00	105.00	0.0900	-0.0588	1.4250	0.0604	1.0000	1/6
KDE0	-2526.51	430.94	-398.38	14235.52	128.96	0.7583	-0.3087	-0.9495	1.1445	1.0000	0.1676
KDE0v1	-2553.08	411.70	-419.87	14603.61	124.41	0.6483	-0.3472	-0.9268	0.9475	1.0000	0.1673
SKM*	-2645.00	410.00	-135.00	15595.00	130.00	0.0900	0.0000	0.0000	0.0000	1.0000	1/6
SK255	-1689.35	389.30	-126.07	10989.60	95.39	-0.1461	0.1660	0.0012	-0.7449	1.0000	0.3563
SkI3	-1762.88	561.61	-227.09	8106.20	188.51	0.3083	-1.1722	-1.0907	1.2926	0.0000	1/4
SkI4	-1885.83	473.83	1006.86	9703.61	366.19	0.4051	-2.8891	-1.3252	1.1452	-0.9850	1/4
SkI5	-1772.91	550.84	-126.69	8206.25	123.63	-0.1171	-1.3088	-1.0487	0.3410	1.0000	1/4
SV-bas	-1879.64	313.75	112.68	12527.38	124.63	0.2585	-0.3817	-2.8236	0.1232	0.5474	0.3000
SV-min	-2112.25	295.78	142.27	13988.57	111.29	0.2439	-1.4349	-2.6259	0.2581	0.8255	0.2554
SV-sym32	-1883.28	319.18	197.33	12559.47	132.75	0.0077	-0.5943	-2.1692	-0.3095	0.4019	0.3
SV-m56-O	-1905.40	571.19	1594.80	8439.04	133.27	0.6440	-2.9737	-1.2553	1.7966	0.7949	0.2000
SV-m64-O	-2083.86	484.60	1134.35	10720.67	113.97	0.6198	-2.3327	-1.3059	1.2101	1.1042	0.2000
SLy4	-2488.91	486.82	-546.39	13777.00	123.00	0.8340	-0.3440	-1.0000	1.3540	1.0000	1/6
SLy5	-2484.88	483.13	-549.40	13763.00	126.00	0.7780	-0.3280	-1.0000	1.2670	1.0000	1/6
SLy6	-2479.50	462.18	-448.61	13673.00	122.00	0.8250	-0.4650	-1.0000	1.3550	1.0000	1/6
SkMP	-2372.24	503.62	57.28	12585.30	160.00	-0.1576	-0.4029	-2.9557	-0.2679	1.0000	1/6
SkO	-2103.65	303.35	791.67	13553.25	353.16	-0.2107	-2.8108	-1.4616	-0.4299	-1.1256	1/4
SkO'	-2099.42	301.53	154.78	13526.46	287.79	-0.0295	-1.3257	-2.3234	-0.1474	-0.5760	1/4
LNS	-2484.97	266.74	-337.14	14588.20	96.00	0.0628	0.6585	-0.9538	-0.0341	1.0000	0.1667
MSL0	-2118.06	395.20	-63.95	12857.70	133.30	-0.0709	-0.3323	1.3583	-0.2282	1.0000	0.2359
NRAPR	-2719.70	417.64	-66.69	15042.00	41.96	0.1615	-0.0480	0.0272	0.1361	1.0000	0.1442
SQMC650	-2462.70	436.10	-151.90	14154.50	110.50	0.1300	0.0000	0.0000	0.0000	1.3899	0.1667
SQMC700	-2429.10	371.00	-96.70	13773.60	104.60	0.1000	0.0000	0.0000	0.0000	1.3910	0.1667
SkT1	-1794.00	298.00	-298.00	12812.00	110.00	0.1540	-0.5000	-0.5000	0.0890	1.0000	1/3
SkT2	-1791.60	300.00	-300.00	12792.00	120.00	0.1540	-0.5000	-0.5000	0.0890	1.0000	1/3
SkT3	-1791.80	298.50	-99.50	12794.00	126.00	0.1380	-1.0000	1.0000	0.0750	1.0000	1/3
SkT8	-1892.50	367.00	-228.76	11983.00	109.00	0.4480	-0.5000	-0.5000	0.6950	1.0000	0.2850
SkT9	-1891.40	377.40	-239.16	11982.00	130.00	0.4410	-0.5000	-0.5000	0.6860	1.0000	0.2850
SkT1*	-1800.50	296.00	-296.00	12884.00	95.00	0.1570	-0.5000	-0.5000	0.0920	1.0000	1/3
SkT3*	-1800.50	296.00	-98.67	12884.00	95.00	0.1420	-1.0000	1.0000	0.0760	1.0000	1/3
Skxs20	-2885.24	302.73	-323.42	18237.49	162.73	0.1375	-0.2555	-0.6074	0.0543	0.0000	1/6
Z_σ	-1983.76	362.25	-104.27	11861.40	123.69	1.1717	0.0000	0.0000	1.7620	1.0000	1/4

Table 2 Conditions for using the interactions of Table 1 as they were designed. Here HBTM = 0, 1 and 2, for $\frac{\hbar^2}{2m}$= 20.7525 MeVfm^2 for neutron and proton, $\frac{\hbar^2}{2m}$ = 20.7213 MeVfm^2 for proton and $\frac{\hbar^2}{2m}$ = 20.7498 MeVfm^2 for neutron, and $\frac{\hbar^2}{2m}$= 20.7355 MeVfm^2 for neutron and proton, respectively; JTM, contribution to the spin-orbit potential from $\mathbf{t_1}$ and $\mathbf{t_2}$ is taken for 1 and not for 0; CEX, Coulomb exchange on for 1 and off for 0; RHOC, proton density is used for Coulomb potential for 0 and charge density is used for Coulomb potential for 1; ZPE, the center-of-mass correction is given by (1− 1/A) factor on the mass for 0 and is calculated after from $\mathbf{E_{c.m.}} = \frac{1}{2mA}\langle \hat{\mathbf{P}}^2 \rangle$ for 1.

Force	Ref.	HBTM	JTM	CEX	RHOC	ZPE
SGII	[41]	0	0	1	0	0
KDE0	[22]	2	1	0	0	1
KDE0v1	[22]	2	1	0	0	1
SKM*	[42]	0	0	1	0	0
SK255	[18]	2	1	0	0	1
SkI3	[43]	0	0	1	0	1
SkI4	[43]	0	0	1	0	1
SkI5	[43]	0	0	1	0	1
SV-bas	[44]	1	0	1	0	1
SV-min	[44]	1	0	1	0	1
SV-sym32	[44]	1	0	1	0	1
SV-m56-O	[45]	1	0	1	0	1
SV-m64-O	[45]	1	0	1	0	1
SLy4	[46]	2	0	1	0	0
SLy5	[46]	2	1	1	0	0
SLy6	[46]	2	0	1	0	1
SkMP	[47]	0	0	1	0	0
SkO	[48]	2	0	1	0	1
SkO'	[48]	2	1	1	0	1
LNS	[49]	2	0	1	0	0
MSL0	[50]	2	1	0	0	1
NRAPR	[51]	2	1	1	0	1
SQMC650	[52]	2	0	1	0	0
SQMC700	[52]	2	0	1	0	0
SkT1	[53]	1	1	1	1	0
SkT2	[53]	1	1	1	1	0
SkT3	[53]	1	1	1	1	0
SkT8	[53]	1	1	1	1	0
SkT9	[53]	1	1	1	1	0
SkT1*	[53]	1	1	1	1	0
SkT3*	[53]	1	1	1	1	0
Skxs20	[54]	0	1	0	0	1
Z_σ	[55]	0	1	1	0	1

Table 3 Nuclear Matter properties associated with each Skyrme interaction of Table 1. We have the saturation density ρ_0 [fm^{-3}], the total binding energy per nucleon E/A [MeV], the incompressibility coefficient K_{NM} [MeV] of NM, the coefficients related to the symmetry energy density J [MeV], L [MeV] and K_{sym} [MeV], the isoscalar effective mass m*/m, the enhancement factor of the EWSR of the IVGDR κ, the Landau parameter G_0' and the strength of the spin-orbit interaction W_0 (MeV).

Force	ρ_0	E/A	K_{NM}	J	L	K_{sym}	m*/m	κ	W_0	G_0'
SGII	0.159	15.59	215.0	26.80	37.63	-145.90	0.79	0.49	105.00	0.5052
KDE0	0.161	16.11	228.8	33.00	45.22	-144.78	0.72	0.30	128.96	0.0474
KDE0v1	0.165	16.23	227.5	34.58	54.70	-127.12	0.74	0.23	124.41	0.0006
SKM*	0.160	15.78	216.7	30.03	45.78	-155.94	0.79	0.53	130.00	0.3142
SK255	0.157	16.33	255.0	37.40	95.00	-58.33	0.80	0.54	95.39	0.3733
SkI3	0.158	15.96	258.1	34.80	100.52	73.04	0.58	0.25	188.51	0.2035
SkI4	0.160	15.92	247.9	29.50	60.39	-40.56	0.65	0.25	366.19	1.3813
SkI5	0.156	15.83	255.7	36.70	129.33	159.57	0.58	0.25	123.63	0.3013
SV-bas	0.160	15.90	234.0	30.00	45.21	-221.75	0.90	0.40	124.63	0.7279
SV-min	0.161	15.91	222.0	30.01	44.76	-156.57	0.95	0.08	111.29	0.7963
SV-sym32	0.159	15.94	233.81	32.00	57.07	-148.79	0.90	0.40	132.745	0.8319
SV-m56-O	0.157	15.81	254.6	27.00	49.96	-45.04	0.56	0.60	133.27	1.6523
SV-m64-O	0.159	15.82	241.4	27.01	30.63	-144.76	0.64	0.60	113.97	1.4667
SLy4	0.160	15.97	229.9	32.00	45.96	-119.73	0.70	0.25	123.00	-0.1337
SLy5	0.160	15.98	229.9	32.03	48.27	-112.76	0.70	0.25	126.00	-0.1414
SLy6	0.159	15.92	229.8	31.96	47.44	-112.71	0.69	0.25	122.00	-0.0038
SkMP	0.157	15.56	230.9	29.88	70.31	-49.82	0.65	0.71	160.00	0.4653
SkO	0.160	15.84	223.34	31.97	79.14	-43.17	0.90	0.17	353.16	1.6191
SkO'	0.160	15.75	222.3	31.95	68.93	-78.82	0.90	0.15	287.79	0.7923
LNS	0.175	15.32	210.78	33.43	61.45	-127.36	0.83	0.38	96.00	0.1367
MSL0	0.160	16.00	230.00	30.00	60.00	-99.33	0.80	0.43	133.30	0.4160
NRAPR	0.161	15.85	225.65	32.78	59.63	-123.32	0.69	0.66	41.96	0.4100
SQMC650	0.172	15.57	218.11	33.65	52.92	-173.15	0.78	0.59	110.5	0.2018
SQMC700	0.171	15.49	222.20	33.47	59.06	-140.84	0.76	0.56	104.60	0.3600
SkT1	0.161	15.98	236.16	32.02	56.18	-134.83	1.00	0.00	110.00	0.1642
SkT2	0.161	15.94	235.73	32.00	56.16	-134.67	1.00	0.00	120.00	0.1573
SkT3	0.161	15.95	235.74	31.50	55.31	-132.05	1.00	0.00	126.00	0.4516
SkT8	0.161	15.94	235.70	29.92	33.72	-187.52	0.83	0.20	109.00	0.2386
SkT9	0.160	15.88	234.91	29.76	33.74	-185.62	0.83	0.20	130.00	0.2142
SkT1*	0.162	16.20	238.95	32.31	56.58	-136.66	1.00	0.00	95.00	0.1757
SkT3*	0.162	16.20	238.95	31.97	56.32	-133.65	1.00	0.00	95.00	0.4616
Skxs20	0.162	15.79	201.76	35.49	67.07	-122.25	0.96	0.08	162.73	0.1286
Z_σ	0.163	15.88	233.33	26.69	-29.38	-401.43	0.78	0.51	123.69	0.3951

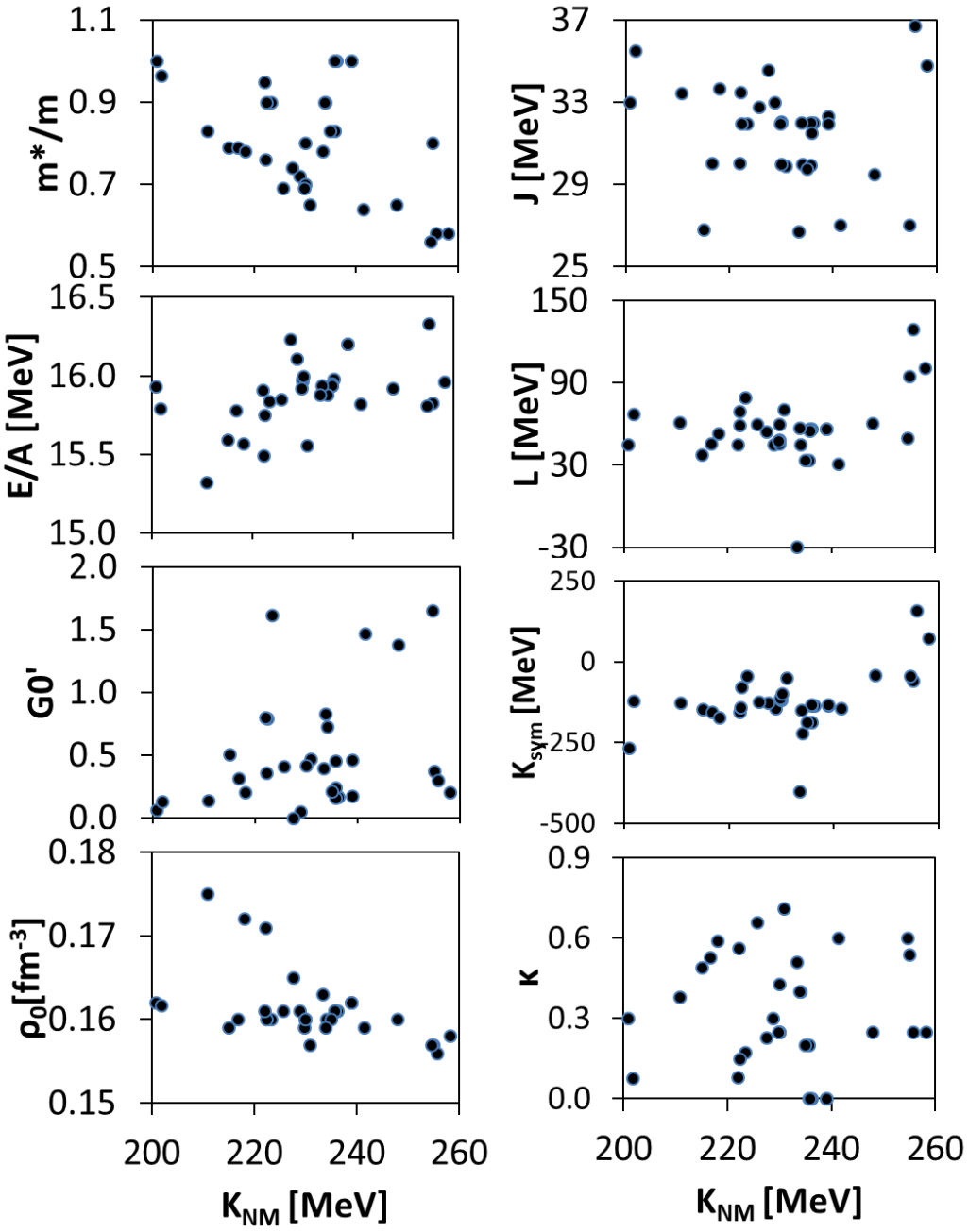

Figure 1 NM properties associated with each Skyrme interaction as a function of the incompressibility coefficient, K_{NM}. We show from top left to bottom, the effective mass m^*/m, the total binding energy per nucleon E/A, the Landau parameter G_0', the saturation density ρ_0, the symmetry energy at saturation density *J*, the first derivative of the symmetry energy L, the second derivative of the symmetry energy K_{sym} and the enhancement coefficient κ of the IVGDR EWSR.

Table 4 Calculated Pearson linear correlation coefficients, C, for NM properties. The parameters of all 33 Skyrme effective nucleon-nucleon interactions shown in Table 1 were used to calculate C.

	K_{NM}	J	L	K_{sym}	m^*/m	κ	$W_0(X_W=1)$
K_{NM}	1.00	0.03	0.30	0.43	-0.37	-0.02	0.03
J	0.03	1.00	0.72	0.49	0.07	-0.24	-0.25
L	0.30	0.72	1.00	0.91	-0.15	-0.13	-0.08
K_{sym}	0.43	0.49	0.91	1.00	-0.41	-0.08	0.05
m^*/m	-0.37	0.07	-0.15	-0.41	1.00	-0.63	-0.19
κ	-0.02	-0.24	-0.13	-0.08	-0.63	1.00	-0.03
$W_0(X_W=1)$	0.03	-0.25	-0.08	0.05	-0.19	-0.03	1.00

CHAPTER III

GIANT RESONANCES IN ^{40,44}Ca, ^{68}Ni, ^{90}Zr, ^{116}Sn, ^{144}Sm AND ^{208}Pb[*1]

We show results of centroid energies, E_{CEN}, of the isoscalar (T = 0) and isovector (T = 1) giant resonances of multipolarities L = 0 to 3 in ^{40,48}Ca, ^{68}Ni, ^{90}Zr, ^{116}Sn, ^{144}Sm and ^{208}Pb, calculated within the fully self-consistent Hartree-Fock (HF)-based random phase approximation (RPA) theory described in Chapter II, using the 33 Skyrme-type effective nucleon-nucleon interactions of the standard form shown in Table 1 and Table 2. All the nuclei considered here are closed-shell except for ^{144}Sm for which we used the occupation-number approximation for the single particle orbits to carry out our calculations. For the calculation of the centroid energy we used Eqs. (2.53) and (2.54) with the energy ranges shown in Table 5 which were determined from the experimental data (when available) and from the shape of the relative strength function.

We compared our calculated centroid energies to the experimental data of Table 6, in order to extract limit the range of values of NM properties. Except for the ^{68}Ni measurement, which was carried out at GANIL using inelastic scattering at 50A MeV [57], the isoscalar data were obtained at Texas A&M University using inelastic scattering of 240 MeV α-particles [58–61]. A complete explanation of the experimental method used for the TAMU experiments can be found in [62–64]. The isovector centroid

[*1] Parts of the chapter are reproduced with permission from G. Bonasera, M. R. Anders, and S. Shlomo, "Giant Resonances in ^{40,48}Ca, ^{68}Ni, ^{90}Zr, ^{116}Sn, ^{144}Sm and ^{208}Pb", Phys. Rev. C **98**, 054316 (2018), Copyright American Physical Society 2018.

energies were obtained from various sources in the literature which used monochromatic photon beams to obtain the photonuclear cross-sections [40,65–72], except for the ^{208}Pb IVGDR which was obtained from polarized proton inelastic scattering [73]. We also evaluate the Pearson linear correlation coefficient between the E_{CEN} of every multipolarity and each NM property, shown in Table 7. We obtain strong correlation between E_{CEN} of the ISGMR and the incompressibility coefficient of nuclear matter, K_{NM}, between E_{CEN} of the ISGDR, ISGQR, ISGOR, IVGOR and the effective mass, m*/m, and between E_{CEN} of the isovector resonances and the EWSR enhancement coefficient, κ, of the IVGDR.

In what follows we cover each giant resonance individually and show the calculated centroid energy plotted with several of the NM properties related to the interaction used for the calculation. Experimental data is shown as dashed lines where available.

Table 5 Integration energy ranges for ^{40,48}Ca, ^{68}Ni, ^{90}Zr, ^{116}Sn, ^{144}Sm and ^{208}Pb. Excitation energy range $\boldsymbol{E_1 - E_2}$ (in MeV) used in the integration of the strength function to determine the energy moments.

	^{40}Ca	^{48}Ca	^{68}Ni	^{90}Zr	^{116}Sn	^{144}Sm	^{208}Pb
L0T0	7 - 60	7 - 60	7 - 60	7 - 60	7 - 60	7 - 60	7 - 60
L1T0	20 - 60	20 - 60	20 - 60	20 - 60	16 - 60	16 - 60	16 - 60
L2T0	7 - 60	7 - 60	7 - 60	7 - 60	7 - 60	7 - 60	7 - 60
L3T0	20 - 60	20 - 60	20 - 60	15 - 60	15 - 60	15 - 60	15 - 60
L0T1	7 - 60	7 - 60	7 - 60	7 - 60	7 - 60	7 - 60	7 - 60
L1T1	0 - 60	0 - 60	0 - 60	0 - 60	0 - 60	0 - 60	0 - 60
L2T1	7 - 60	7 - 60	7 - 60	7 - 60	7 - 60	7 - 60	7 - 60
L3T1	25 - 60	25 - 60	25 - 60	25 - 60	25 - 60	25 - 60	25 - 60

Table 6 E_{CEN} experimental data in MeV for ^{40,48}Ca, ^{68}Ni, ^{90}Zr, ^{116}Sn, ^{144}Sm and ^{208}Pb. Values and references for centroid energy experimental data: [58] for a, [74] for b, [57] for c, [60] for d, [61] for e, [40] for f, [65] for g, [66] for h, [67] for i, [68] for j, [69] for k, [70] for m, [71] for n and [73] for p.

	^{40}Ca	^{48}Ca	^{68}Ni	^{90}Zr	^{116}Sn	^{144}Sm	^{208}Pb
L0T0	19.18 (37)[a]	19.88 (16)[b]	21.9 (19)[c]	17.88 (12)[d]	15.85 (20)[e]	15.40 (30)[e]	13.96 (20)[e]
L1T0	23.36 (70)[a]	27.30 (15)[b]		27.40 (50)[d]	25.50 (60)[e]	24.51 (40)[e]	22.20 (30)[e]
L2T0	17.84 (43)[a]	18.61 (24)[b]		14.56 (20)[d]	13.50 (35)[e]	12.78 (30)[e]	10.89 (30)[e]
L3T0				23.10 (30)[d]	23.30 (80)[e]	19.80 (50)[e]	19.60 (50)[e]
L0T1	31.0 (20)[f]						26.00 (200)[f]
L1T1	19.80 (50)[g]	19.50 (50)[i]	17.10 (20)[j]	16.83 (04)[k]	15.67 (04)[m]	15.30 (10)[n]	13.40 (50)[p]
L2T1	31.0 (15)[h]						22.80 (50)[f]

Table 7 Pearson linear correlation for ^{40,48}Ca, ^{68}Ni, ^{90}Zr, ^{116}Sn, ^{144}Sm and ^{208}Pb. Calculated Pearson linear correlation coefficient between centroid energies and each nuclear matter property.

	K_{NM}	J	L	K_{sym}	m*/m	κ	$W_0(X_W=1)$
ISGMR	0.87	-0.10	0.25	0.45	-0.51	0.13	0.11
ISGDR	0.52	-0.10	0.13	0.36	-0.88	0.55	0.04
ISGQR	0.41	-0.09	0.15	0.41	-0.93	0.54	0.22
ISGOR	0.42	-0.10	0.15	0.43	-0.96	0.56	0.16
IVGMR	0.23	-0.26	-0.12	0.00	-0.70	0.86	-0.09
IVGDR	0.05	-0.37	-0.42	-0.30	-0.60	0.84	-0.06
IVGQR	0.18	-0.35	-0.29	-0.13	-0.74	0.80	0.00
IVGOR	0.25	-0.32	-0.19	0.02	-0.83	0.81	0.04

Isoscalar Giant Monopole Resonance

The centroid energy, E_{CEN}, of the ISGMR is plotted in Figure 2 as a function of the nuclear matter incompressibility coefficient, K_{NM}. One nucleus is shown per panel and the experimental result is demarcated by the dashed lines. We find the anticipated strong correlation between the E_{CEN} of this compression mode and K_{NM} [1,17,75] with a calculated Pearson linear correlation coefficient C ~ 0.87. The figure shows for ^{40}Ca that the values of the calculated centroid energies are above the experimental result. For the isotope of ^{48}Ca we found that interactions with K_{NM} = 200 – 240 MeV agree with data. For the isotope of ^{68}Ni we obtain a lower E_{CEN} than the experiment except for a few Skyrme parametrizations associated with a large value (~260 MeV) of K_{NM}. For the isotopes of ^{90}Zr, ^{144}Sm and ^{208}Pb we found good agreement between the experimental

result and the calculations when using interactions associated with K_{NM} = 210–240 MeV. For the isotope of ^{116}Sn, the calculated values for E_{CEN} are about 1 MeV larger than the experimental data for interactions with K_{NM} = 200–240 MeV, which remains an open problem [76]. In Figure 3 we show the calculated centroid energies plotted with the effective mass, m*/m for which we obtained a weak correlation with C ~ -0.51. We also study the relation between the E_{CEN} of the ISGMR and the symmetry energy coefficients J and L but don't obtain any correlation. On the other hand, a weak correlation (C ~ 0.45) is found between the calculated values of E_{CEN} and the second derivative of the symmetry energy, see Figure 4. As shown in Table 7 we do not obtain any correlations with the remaining NM properties or with W_0. The complete list of the calculated values of centroid energies is given in Table 14 of the Appendix for the ISGMR.

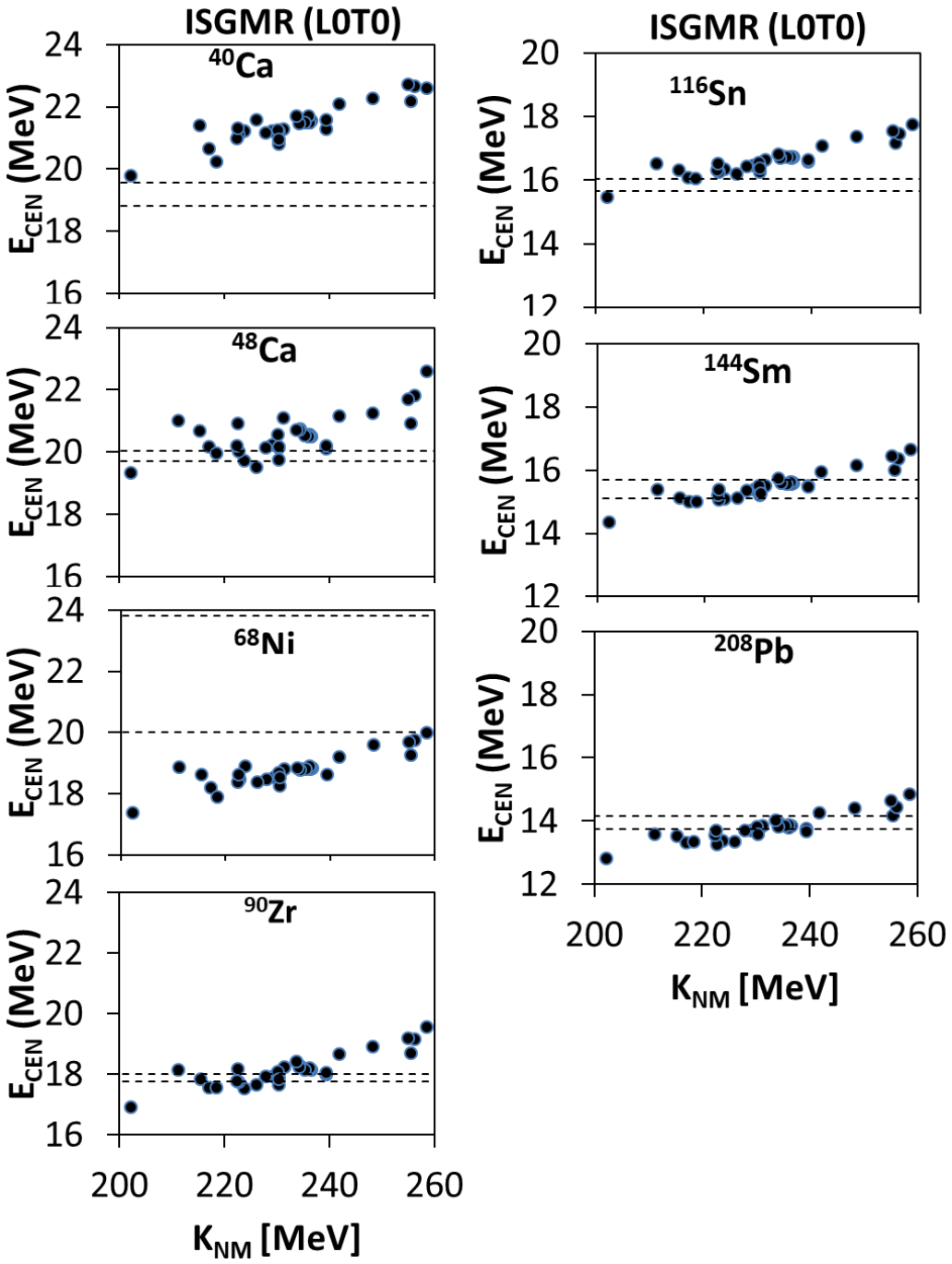

Figure 2 ISGMR E_{CEN} with K_{NM} in ^{40,48}Ca, ^{68}Ni, ^{90}Zr, ^{116}Sn, ^{144}Sm and ^{208}Pb. The calculated centroid energies of the ISGMR (full circle) are plotted as a function of the incompressibility coefficient. One nucleus is shown per panel while the experimental data is delimited by the dashed line. Strong correlation is obtained between the calculated E_{CEN} and K_{NM} (C ~ 0.87).

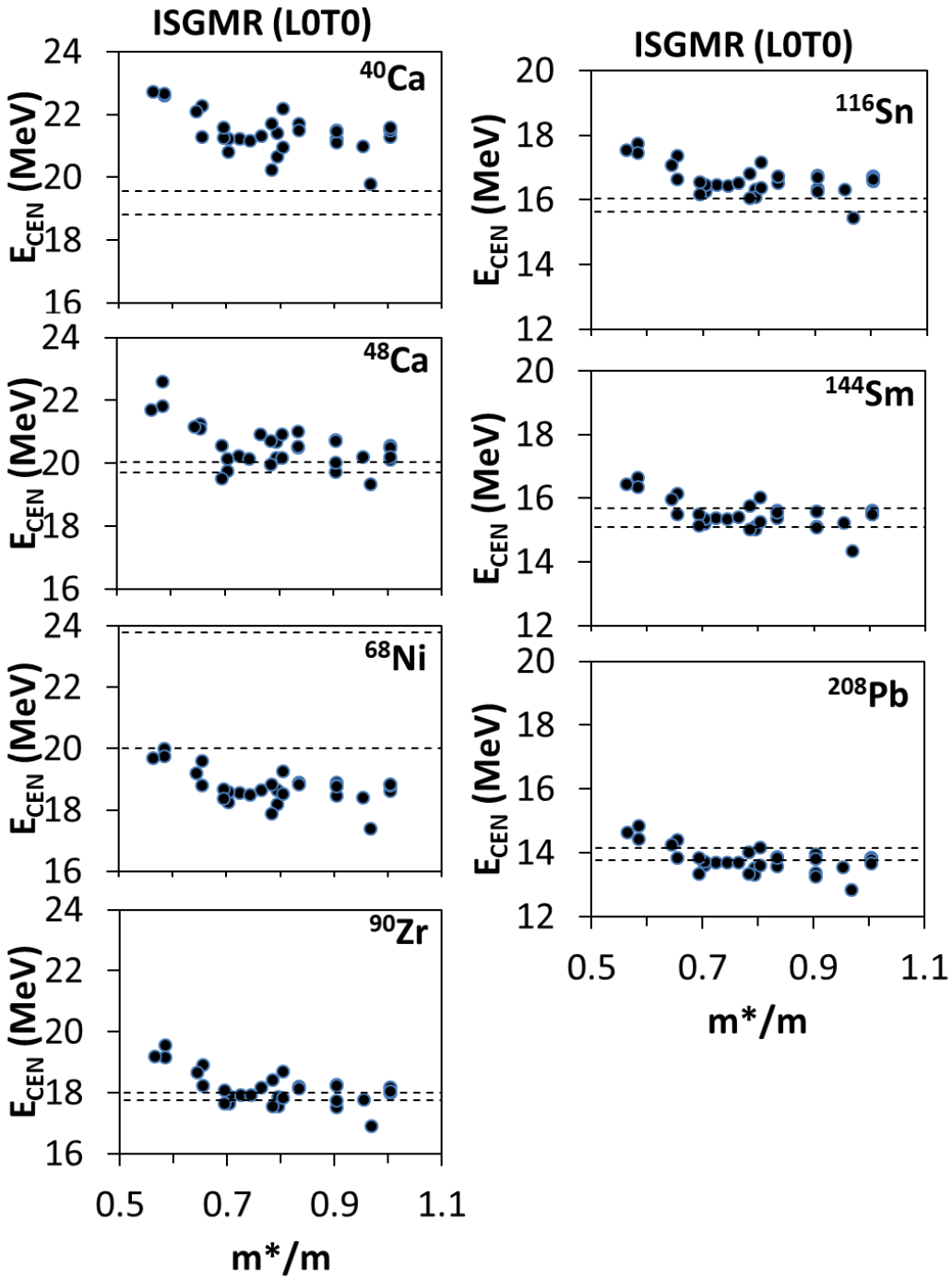

Figure 3 ISGMR E_{CEN} with m*/m in ^{40,48}Ca, ^{68}Ni, ^{90}Zr, ^{116}Sn, ^{144}Sm and ^{208}Pb. Like Figure 2 but for the effective mass, m*/m. Weak correlation is obtained between the calculated E_{CEN} and m*/m, with a Pearson linear correlation coefficient C ~ -0.51.

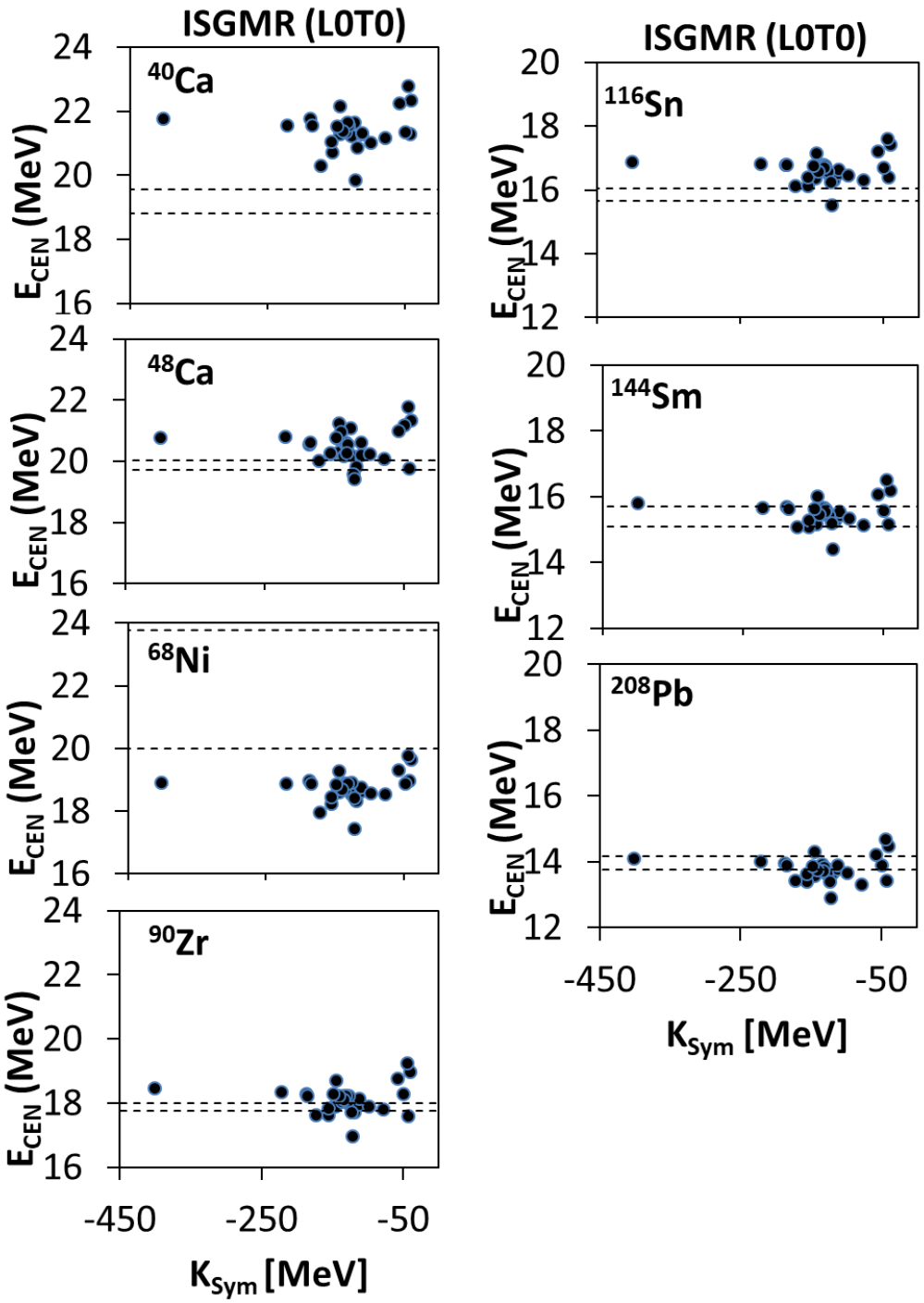

Figure 4 ISGMR E_{CEN} with K_{sym} in ^{40,48}Ca, ^{68}Ni, ^{90}Zr, ^{116}Sn, ^{144}Sm and ^{208}Pb. Like Figure 2 but for the second derivative of the symmetry energy coefficient. Weak correlation is obtained between the calculated values of E_{CEN} and K_{sym}, with a Pearson linear correlation coefficient C ~ -0.45.

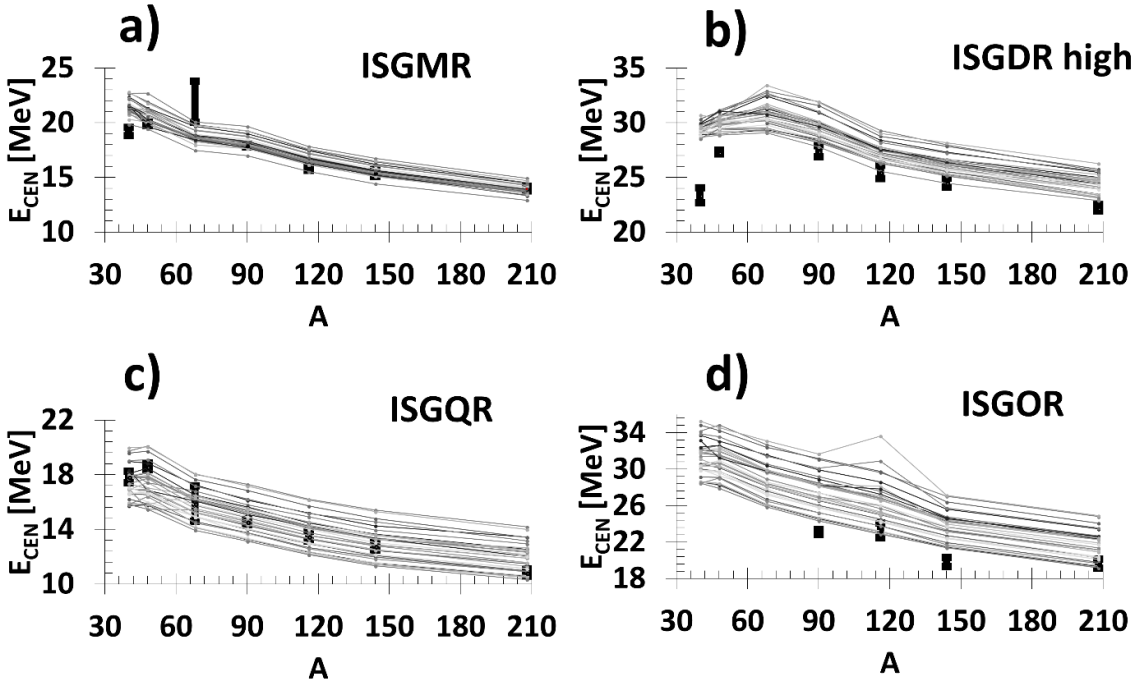

Figure 5 Isoscalar E_{CEN} overview in ^{40,48}Ca, ^{68}Ni, ^{90}Zr, ^{116}Sn, ^{144}Sm and ^{208}Pb. The centroid energies [MeV] are plotted as a function of the nucleon mass. The different multipolarities L = 0-3 are shown in panels a to d. Available experimental errors are marked with the solid vertical lines while the calculated centroid energies are plotted by dots with lines connecting the same interactions to help guide the eye.

We plotted the centroid energies for all 7 nuclei considered here as a function of their mass in Figure 5a. The theoretical centroid energies are plotted by dots with lines connecting the results of the different interactions to help guide the eye, while the experimental range is shown by the solid vertical line. We see from this overview plot that the experimental result for E_{CEN} increases with the mass for the isotopes of ^{40,48}Ca and ^{68}Ni but then steadily decreases for the higher masses. The calculated results do not show this behavior for the low mass region and instead we find that the value of E_{CEN} steadily decreases as A increases.

Isoscalar Giant Dipole Resonance

The centroid energy, E_{CEN}, of the high-energy component of the ISGDR ($3\hbar\omega$, excitations) is plotted against the incompressibility coefficient, K_{NM}, in Figure 6. The correlation we obtained between the calculated values of E_{CEN} and K_{NM} is weak with a calculated Pearson linear correlation coefficient C ~ 0.52. A similar plot, but as a function of the nucleon effective mass, m*/m, is shown in Figure 7. We find a strong correlation between the calculated values of E_{CEN} and m*/m for the ISGDR (C ~ -0.88). As the figure shows, most of our calculations are above the experimental result. For ^{40,48}Ca we find that the interactions considered predict the centroid energy up to 6 MeV above the experimental data. In the case of the isotope of ^{90}Zr our calculations are within 3 MeV of the experimental centroid energy with the interactions with high value of effective mass (m*/m > 0.9) agreeing with the experimental result. A very similar result is found for ^{208}Pb, while slightly better agreement is found between the data and the theory for the isotopes of ^{116}Sn and ^{144}Sm. We note however, that for the ISGDR comparing the calculated and the measured centroid energies may not lead to the correct conclusions because the fractions of the EWSR are around 70% in the case of the Ca isotopes [58,77] while they are close to 100% for ^{116}Sn, ^{144}Sm and ^{208}Pb [61]. As shown in Table 7, no correlations are found between the calculated values of E_{CEN} and the symmetry energy coefficients *J* and *L* (C ~ -0.10 and 0.13, respectively), while weak correlation is obtained with K_{sym} (C ~ 0.36). In Figure 8 we plot the centroid energy as a function of the enhancement coefficient, κ, of the EWSR for the IVGDR showing the weak correlation (C ~ 0.55) between the two quantities. This correlation is due to the

medium correlation between κ and m*/m which are both influenced by the momentum dependent term of the Skyrme-interaction, see Table 4 for the complete list of correlations between NM properties. In Table 15 of the Appendix we show the calculated values of the ISGDR E_{CEN}.

In Figure 5b we plot the centroid energies against the mass, A, for all the nuclei considered here. The experimental data, available for all but the Ni isotope, is demarked by solid vertical lines. The calculated centroid energies are marked by dots with a line connecting the results of each interactions to help guide the eye. We find a similar trend in both theory and experimental cases: an increasing value of E_{CEN} for the lighter nuclei, from ^{40}Ca to ^{48}Ca to (at least for the calculation) ^{68}Ni, and then a steady decrease beginning with ^{90}Zr all the way down to ^{208}Pb. We emphasize however that the theory is consistently above the data, therefore the interactions with a higher value of effective mass, and thus a lower centroid energy, are closer to the experimental result.

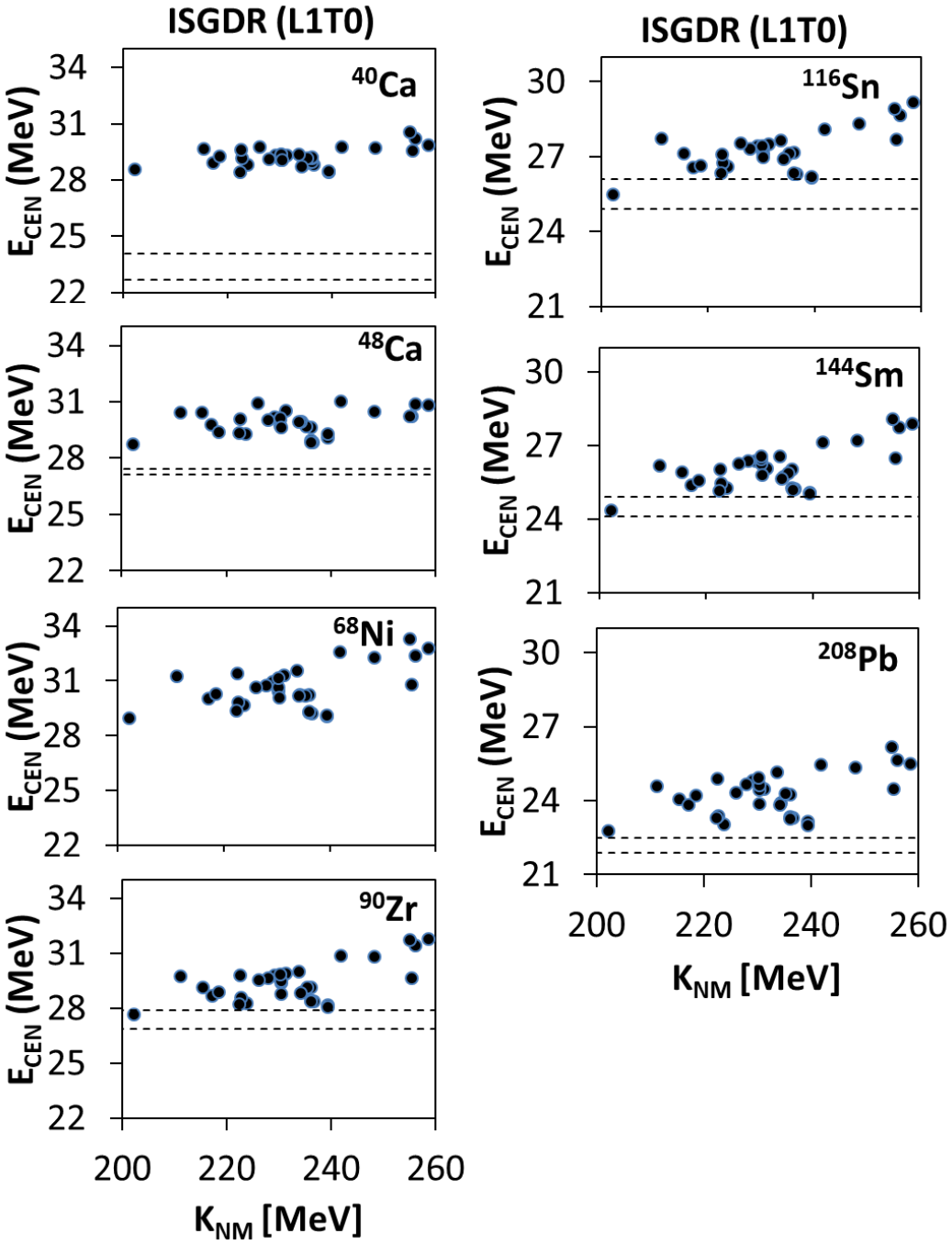

Figure 6 ISGDR E_{CEN} with K_{NM} in ^{40,48}Ca, ^{68}Ni, ^{90}Zr, ^{116}Sn, ^{144}Sm and ^{208}Pb. Like Figure 2 but for the ISGDR centroid energy plotted with the incompressibility coefficient. Weak correlation is obtained between the calculated values of E_{CEN} and K_{NM}, with a Pearson linear correlation coefficient C ~ 0.52.

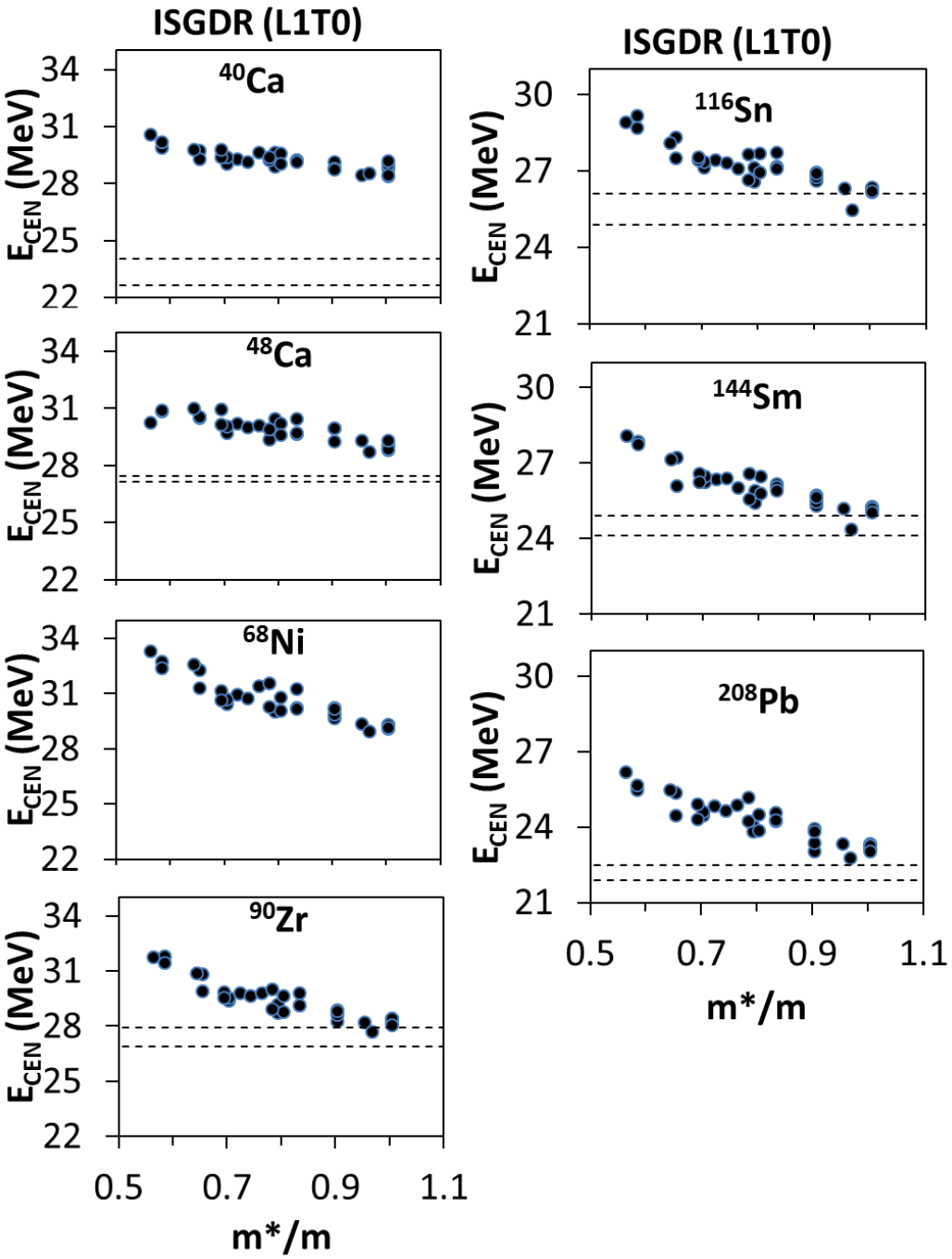

Figure 7 ISGDR E_{CEN} with m*/m in ^{40,48}Ca, ^{68}Ni, ^{90}Zr, ^{116}Sn, ^{144}Sm and ^{208}Pb. Like Figure 2 but for the ISGDR centroid energy as a function of the effective mass. A strong correlation is obtained between the calculated values of E_{CEN} and m*/m, with a Pearson linear correlation coefficient C ~ -0.88.

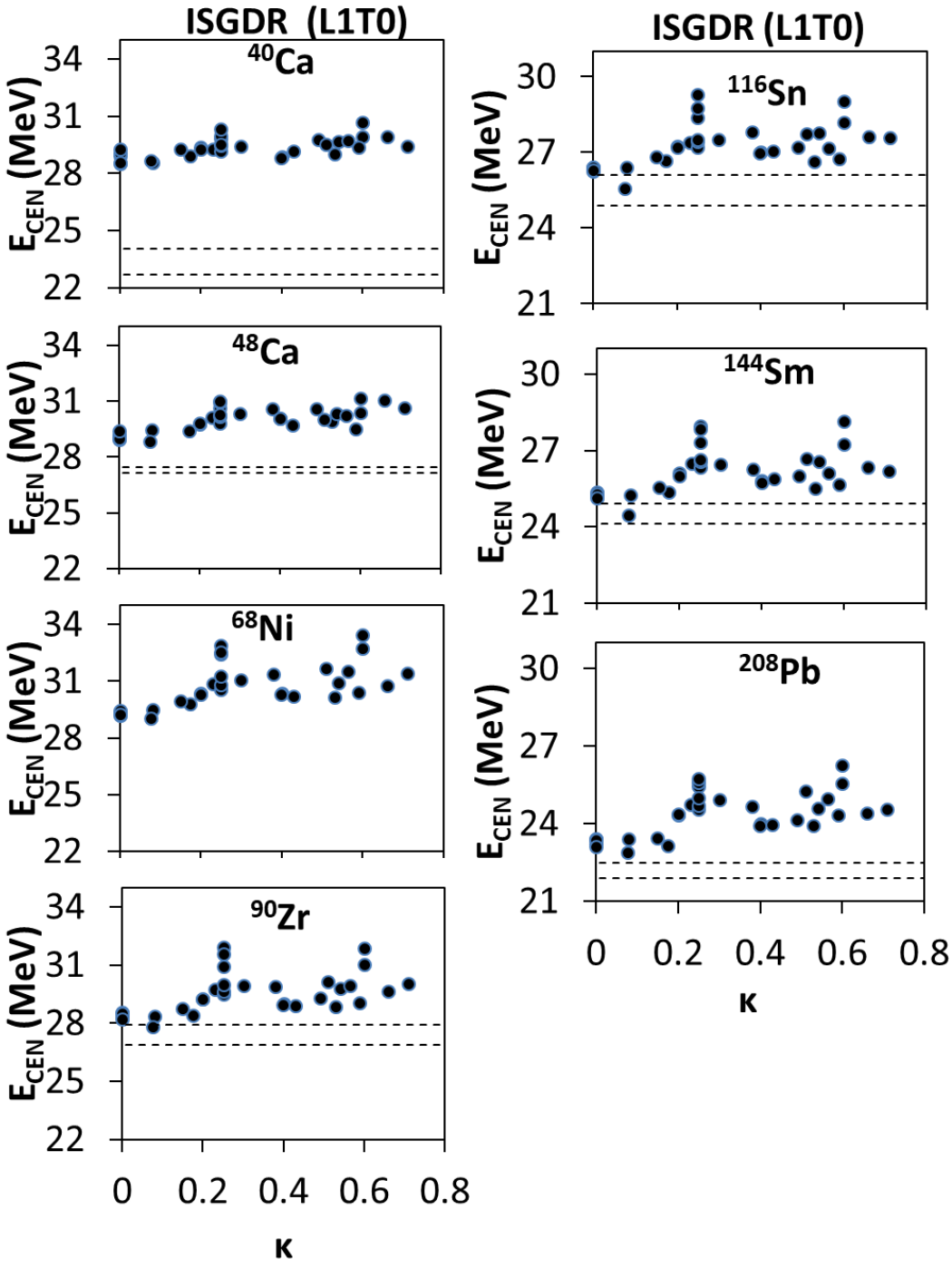

Figure 8 ISGDR E_{CEN} with κ in ^{40,48}Ca, ^{68}Ni, ^{90}Zr, ^{116}Sn, ^{144}Sm and ^{208}Pb. Like Figure 2 but for the ISGDR centroid energy as a function of the enhancement coefficient of the EWSR for the IVGDR. A weak correlation is obtained between the calculated values of E_{CEN} and κ, with a Pearson linear correlation coefficient C ~ 0.55.

Isoscalar Giant Quadrupole Resonance

In Figure 9 the centroid energy, E_{CEN}, (full circles) is plotted with the effective mass, m*/m, of the relative interaction used in its calculations for the ISGQR. One nucleus is shown per panel and the experimental range, available for all nuclei, is shown as dashed lines. As can be seen from the figure, we found a strong correlation between the calculated values of E_{CEN} and m*/m with the centroid energy decreasing as the effective mass is increasing. The calculated Pearson linear correlation coefficient between the values of E_{CEN} and m*/m is C ~ -0.93. We find that the centroid energy for the Ca isotopes is reproduced by interactions within the m*/m = 0.6 - 0.8 region. For ^{68}Ni, ^{90}Zr, ^{116}Sn and ^{144}Sm the interactions in the region of m*/m = 0.7 - 0.9 yielded the best results while for ^{208}Pb a slightly higher region of m*/m = 0.8 - 1.0 is the closest to the data. Overall however, the region contained by m*/m = 0.7 - 0.9 reproduces the most data. In Figure 10 the centroid energy is plotted with the incompressibility coefficient, K_{NM}, and a weak correlation is obtained for the two calculated quantities with C ~ 0.41. We didn't obtain any correlation between the calculated values of E_{CEN} and the symmetry energy coefficients J and L (C ~ -0.09 and 0.15, respectively), while a weak correlation is found with K_{sym} and κ (C ~ 0.41 and 0.54, respectively). In Table 16 of the Appendix we show the values of the calculated centroid energies for the ISGQR.

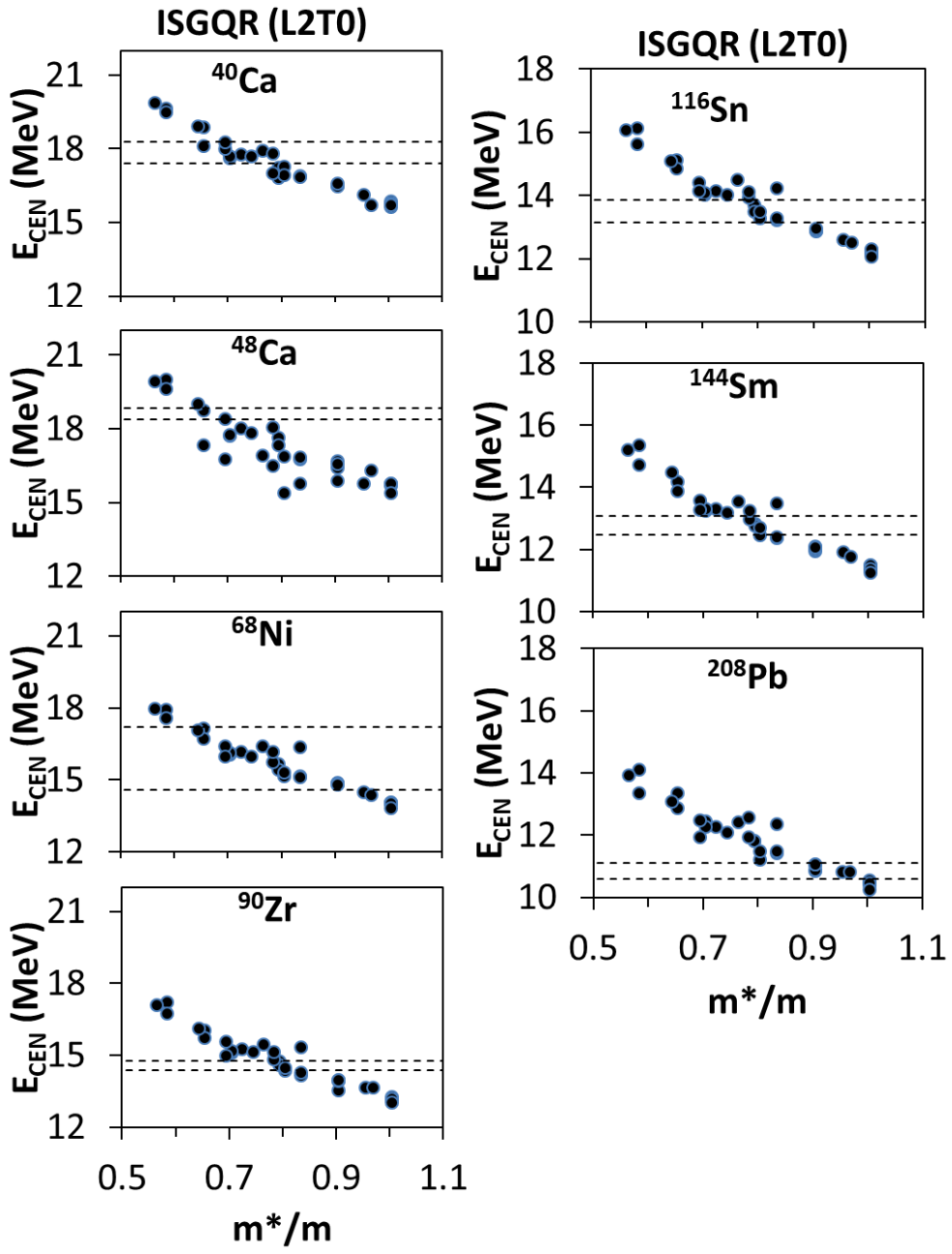

Figure 9 ISGQR E_{CEN} with m*/m in ^{40,48}Ca, ^{68}Ni, ^{90}Zr, ^{116}Sn, ^{144}Sm and ^{208}Pb. Like Figure 2 but for the ISGQR centroid energy plotted with the effective mass. A strong correlation is obtained between the calculated values of E_{CEN} and m*/m, with a Pearson linear correlation coefficient C ~ -0.93.

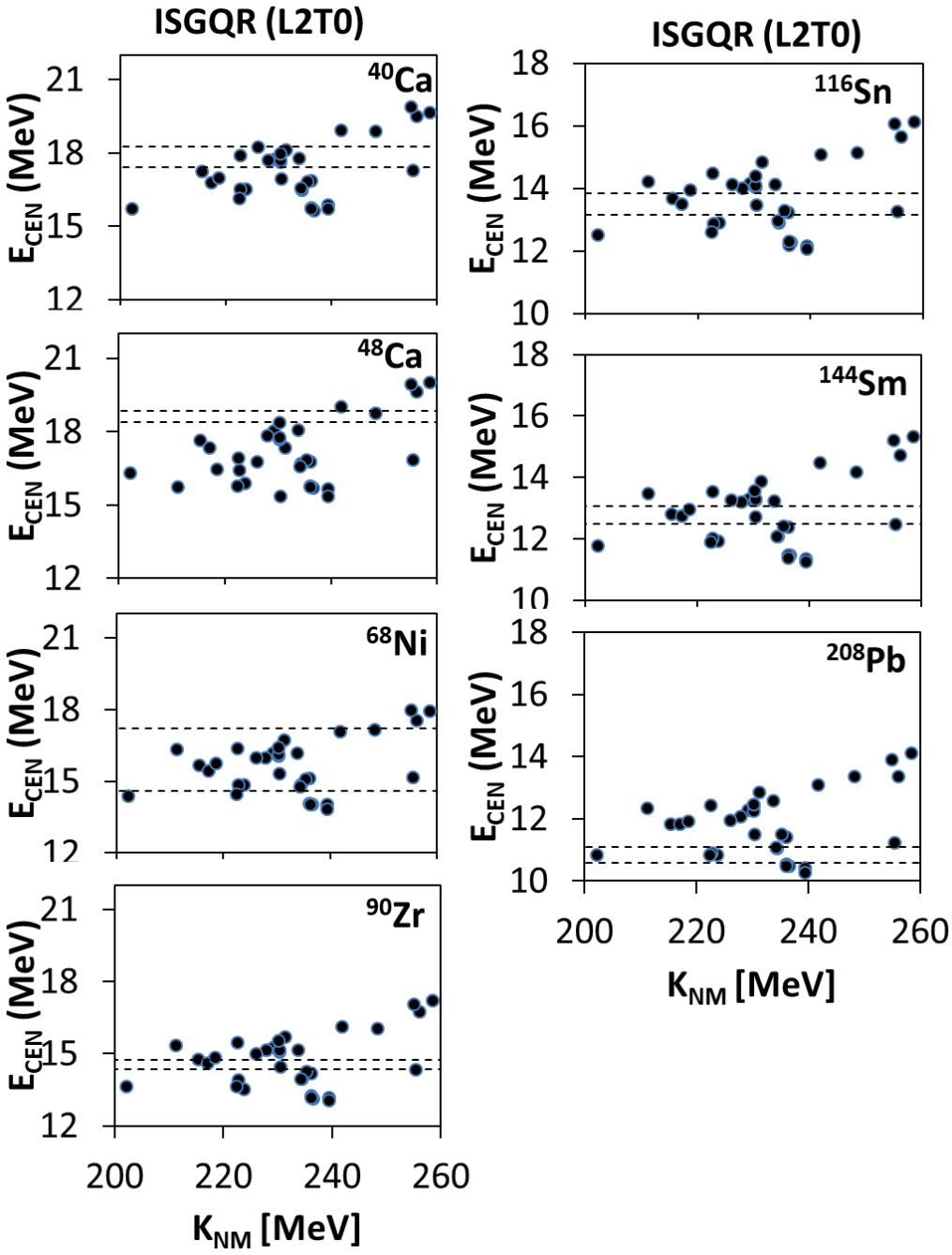

Figure 10 ISGQR E_{CEN} with K_{NM} in ^{40,48}Ca, ^{68}Ni, ^{90}Zr, ^{116}Sn, ^{144}Sm and ^{208}Pb. Like Figure 2 but for the ISGQR centroid energy plotted with the incompressibility coefficient. A weak correlation is obtained between the calculated values of E_{CEN} and K_{NM}, with a Pearson linear correlation coefficient C ~ 0.41.

In Figure 5c the centroid energies of the nuclei studied in this chapter are plotted with their mass, A. The data is shown for all cases by the solid vertical line while the calculated E_{CEN} are marked by dots connected by a line for each interaction. We find a general decreasing trend for the value of E_{CEN} as the mass increases, except for ^{48}Ca whose centroid energy was measured about 1 MeV above that of ^{40}Ca, an effect reproduced by 17 of the 33 interactions considered here but only up to 0.58 MeV. Although the data falls inside the theory "band", we can see from Figure 5c that the experimental result slowly drifts towards the bottom of the band i.e. towards the higher effective mass interactions (which give a lower E_{CEN}) for the larger nuclei.

Isoscalar Giant Octupole Resonance

The centroid energy, E_{CEN}, of the ISGOR is plotted in Figure 11 as with the effective mass, m*/m. The data for the four heaviest nuclei ^{90}Zr, ^{116}Sn, ^{144}Sm and ^{208}Pb is delimited by dashed lines. We found a strong correlation between the theoretical calculations of E_{CEN} and m*/m with a Pearson linear correlation coefficient C ~ -0.96. We obtain similar centroid energy values between theory and experiment for ^{116}Sn and ^{208}Pb for interactions with a high value of effective mass (m*/m > 0.8), while for ^{90}Zr and ^{144}Sm all of the interactions considered are above the experimental result. In Figure 12 we plot the centroid energy with the incompressibility coefficient. In this case we found a weak correlation (C ~ 0.42) between these two quantities. A similar result is obtained for the second derivative of the symmetry energy K_{sym} with a calculated value

of C ~ 0.43. The other symmetry energy coefficients, J and L, are not correlated with E_{CEN} (C ~ -0.10 and 0.15, respectively). For the enhancement coefficient, κ, of the EWSR for the IVGDR we determined a weak correlation with E_{CEN}, a reflection of the connection between m*/m and κ, see Table 7 for details. In Table 17 of the Appendix we show the values of the calculated centroid energies for the ISGOR.

Figure 5d shows an overview of the ISGOR centroid energies for the nuclei of this chapter plotted against their mass. The data is delimited by the solid vertical lines, is shown for ^{90}Zr, ^{116}Sn, ^{144}Sm and ^{208}Pb. Overall, we obtain the predicted decreasing trend for the value of E_{CEN} as the mass increases for both theory and experiment. However, 9 of the 33 interactions adopted predict the highest values of E_{CEN} in the heavier Ca isotope, while only 2 interactions resulted in a higher centroid energy for ^{116}Sn than ^{90}Zr, in agreement with data.

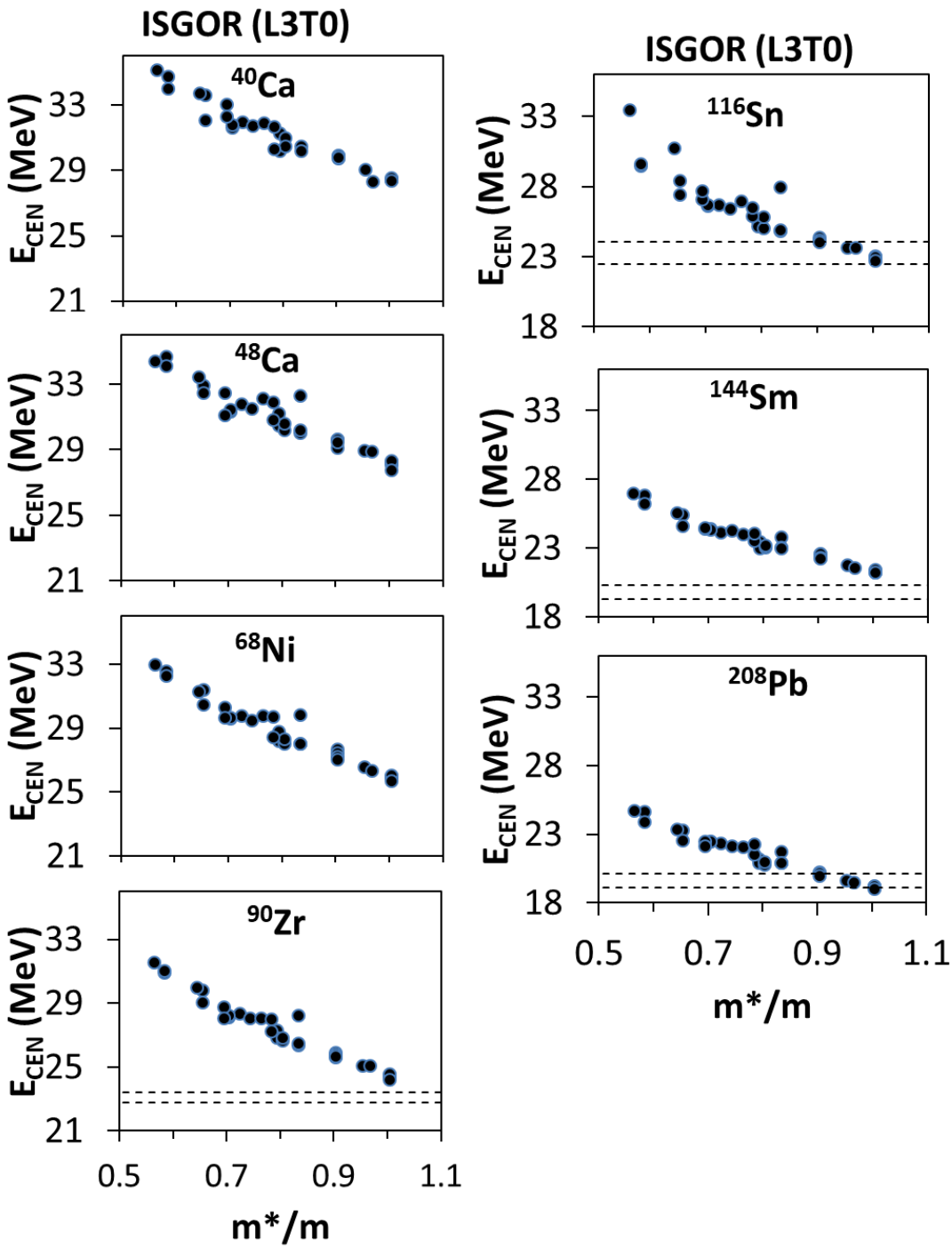

Figure 11 ISGOR E_{CEN} with m*/m in ^{40,48}Ca, ^{68}Ni, ^{90}Zr, ^{116}Sn, ^{144}Sm and ^{208}Pb. Like Figure 2 but for the ISGOR centroid energy plotted with the effective mass. A strong correlation is obtained between the theoretical values of E_{CEN} and m*/m, with a Pearson linear correlation coefficient C ~ -0.96.

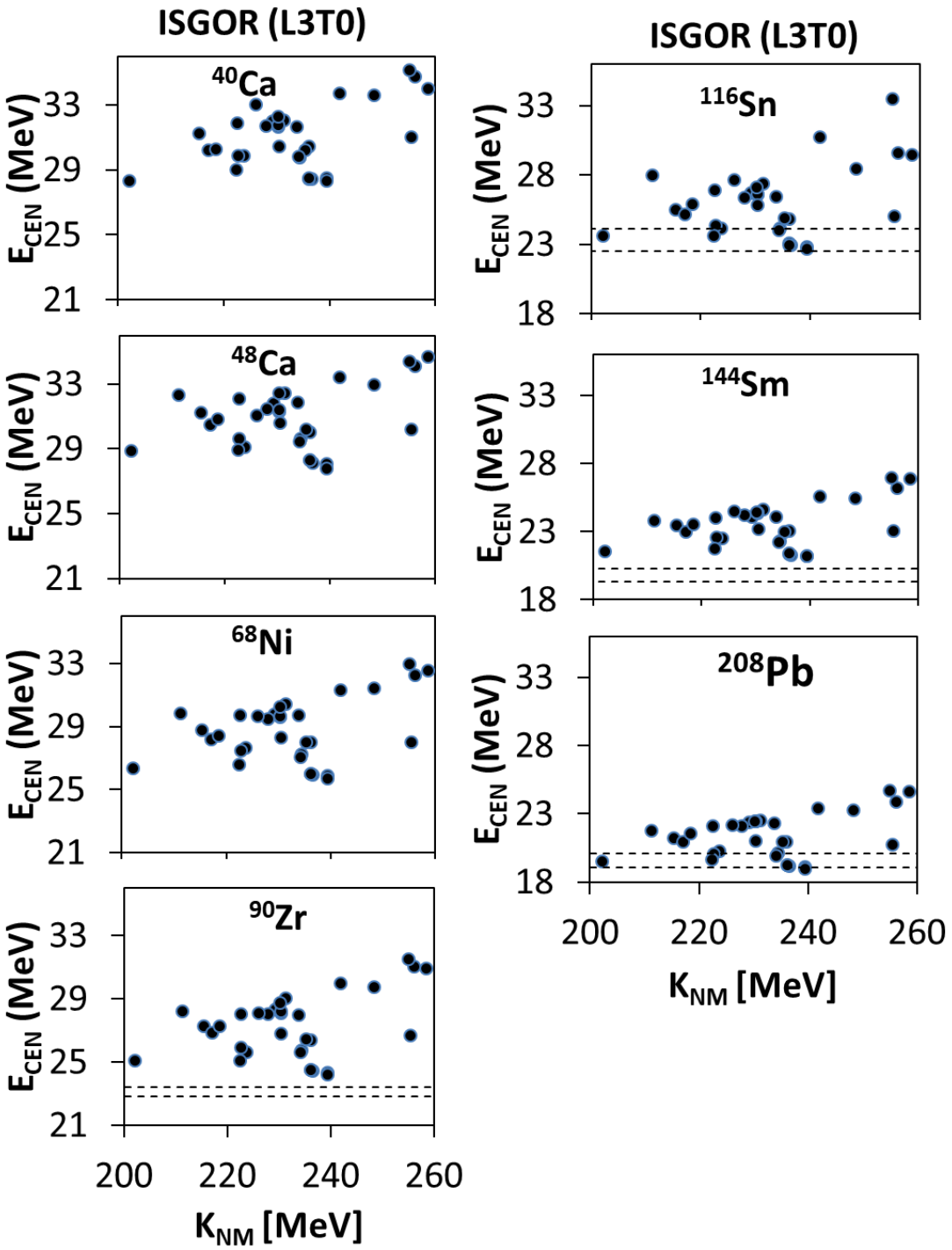

Figure 12 ISGOR E_{CEN} with K_{NM} in ^{40,48}Ca, ^{68}Ni, ^{90}Zr, ^{116}Sn, ^{144}Sm and ^{208}Pb. Like Figure 2 but for the ISGOR centroid energy plotted with the incompressibility coefficient. A weak correlation is obtained between the theoretical values of E_{CEN} and K_{NM}, with a Pearson linear correlation coefficient C ~ 0.42.

Isovector Giant Monopole Resonance

The centroid energy, E_{CEN}, of the isovector giant monopole resonance (IVGMR), is plotted as a function of the incompressibility coefficient in Figure 13. The HF-RPA calculations are shown as full circles and the data, available for ^{40}Ca and ^{208}Pb, is marked with dashed lines. Despite this being an isovector compression mode no correlations are found between the theoretical values of E_{CEN} and K_{NM} with a Pearson linear correlation coefficient C ~ 0.23. In Figure 14 we plot the E_{CEN} as a function of the effective mass, m*/m. We found a medium correlation between E_{CEN} and m*/m with a value of C ~ -0.70 but we cannot determine constraints on the effective mass, or any other NM properties, because of the large error bars on the experimental data. Moving onto the isovector properties, we find an even larger correlation between E_{CEN} and κ with a value of C ~ 0.86 as can be seen in Figure 15. For the other isovector properties, including J, L and K_{sym} no correlation is found for the calculated E_{CEN} (C ~ -0.26, -0.12 and 0.00, respectively). Similar to the work done for the Ca isotopes [78], we studied the centroid energy difference of ^{48}Ca - ^{40}Ca using more Skyrme interactions and reaffirm a strong correlation (Pearson correlation coefficient C = 0.83) with the value of W_0 for the interactions with x_w = 1. In Table 18 we show for completeness the values E_{CEN} for the IVGMR.

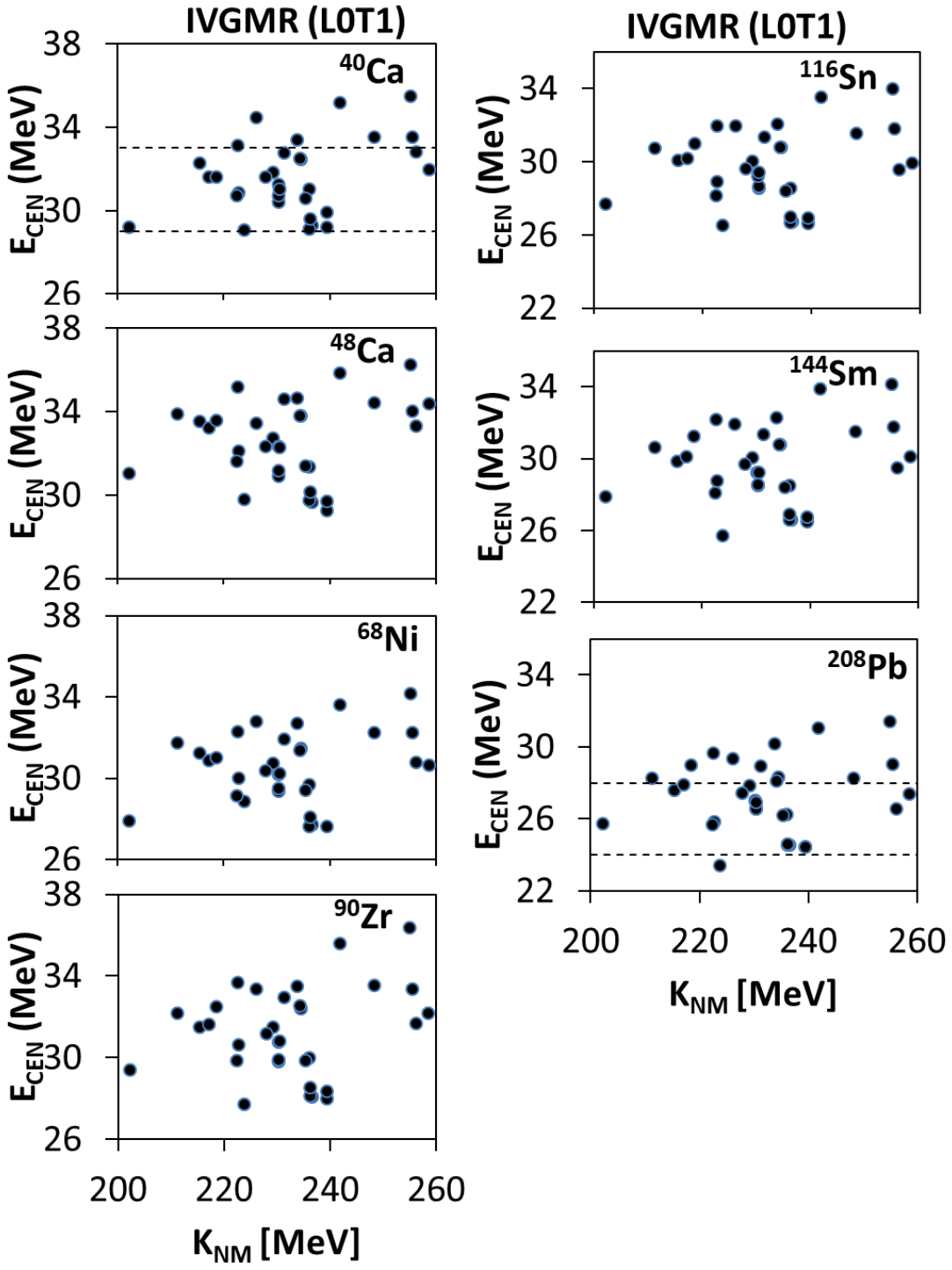

Figure 13 IVGMR E_{CEN} with K_{NM} in ^{40,48}Ca, ^{68}Ni, ^{90}Zr, ^{116}Sn, ^{144}Sm and ^{208}Pb. Like Figure 2 but for the IVGMR centroid energy plotted with the incompressibility coefficient. No correlation is obtained between the calculated values of E_{CEN} and K_{NM}, with a Pearson linear correlation coefficient C ~ 0.23.

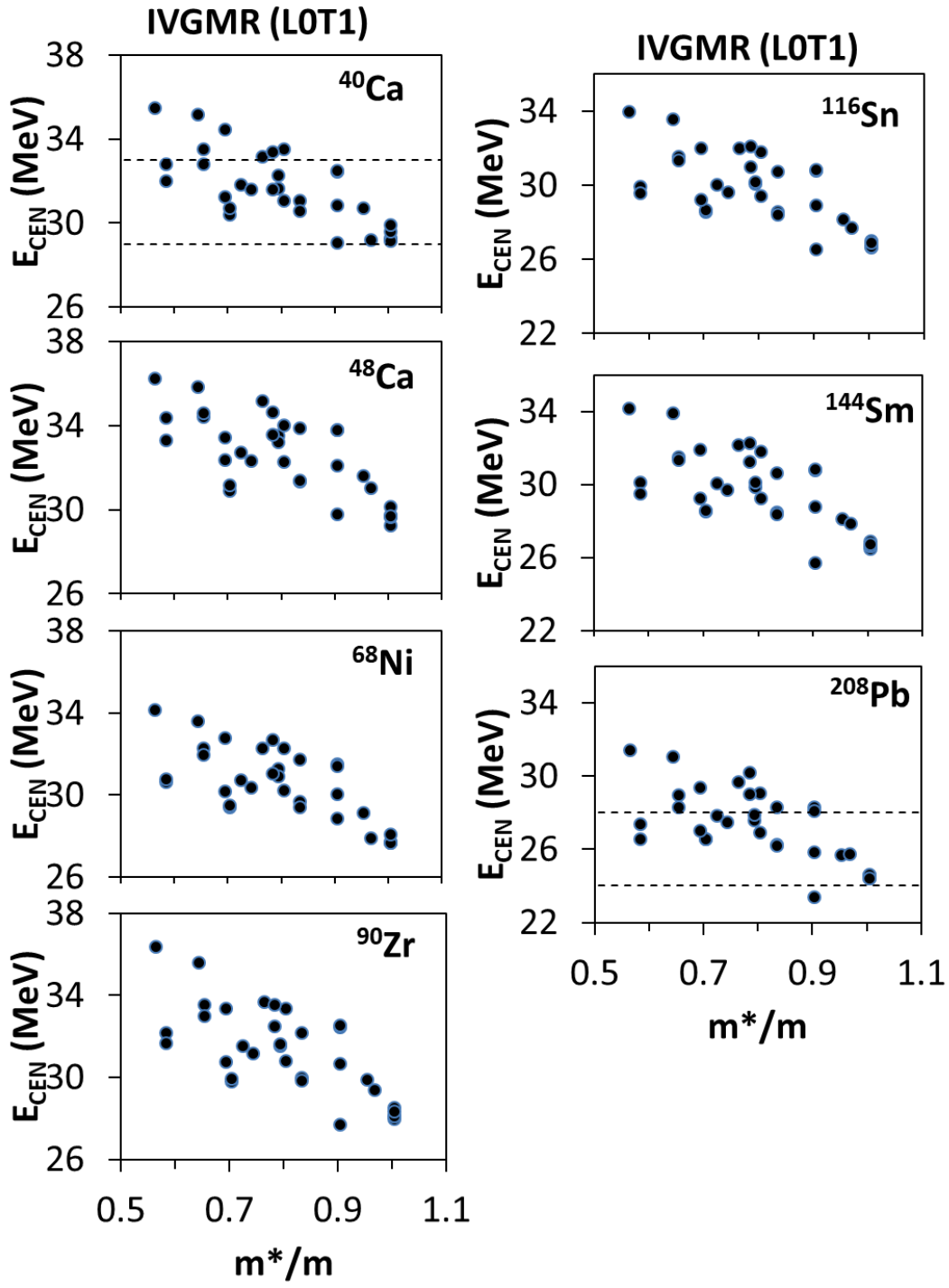

Figure 14 IVGMR E_{CEN} with m*/m in ^{40,48}Ca, ^{68}Ni, ^{90}Zr, ^{116}Sn, ^{144}Sm and ^{208}Pb. Like Figure 2 but for the IVGMR centroid energy plotted with the effective mass. A medium correlation is obtained between the calculated values of E_{CEN} and m*/m, with a Pearson linear correlation coefficient C ~ -0.70.

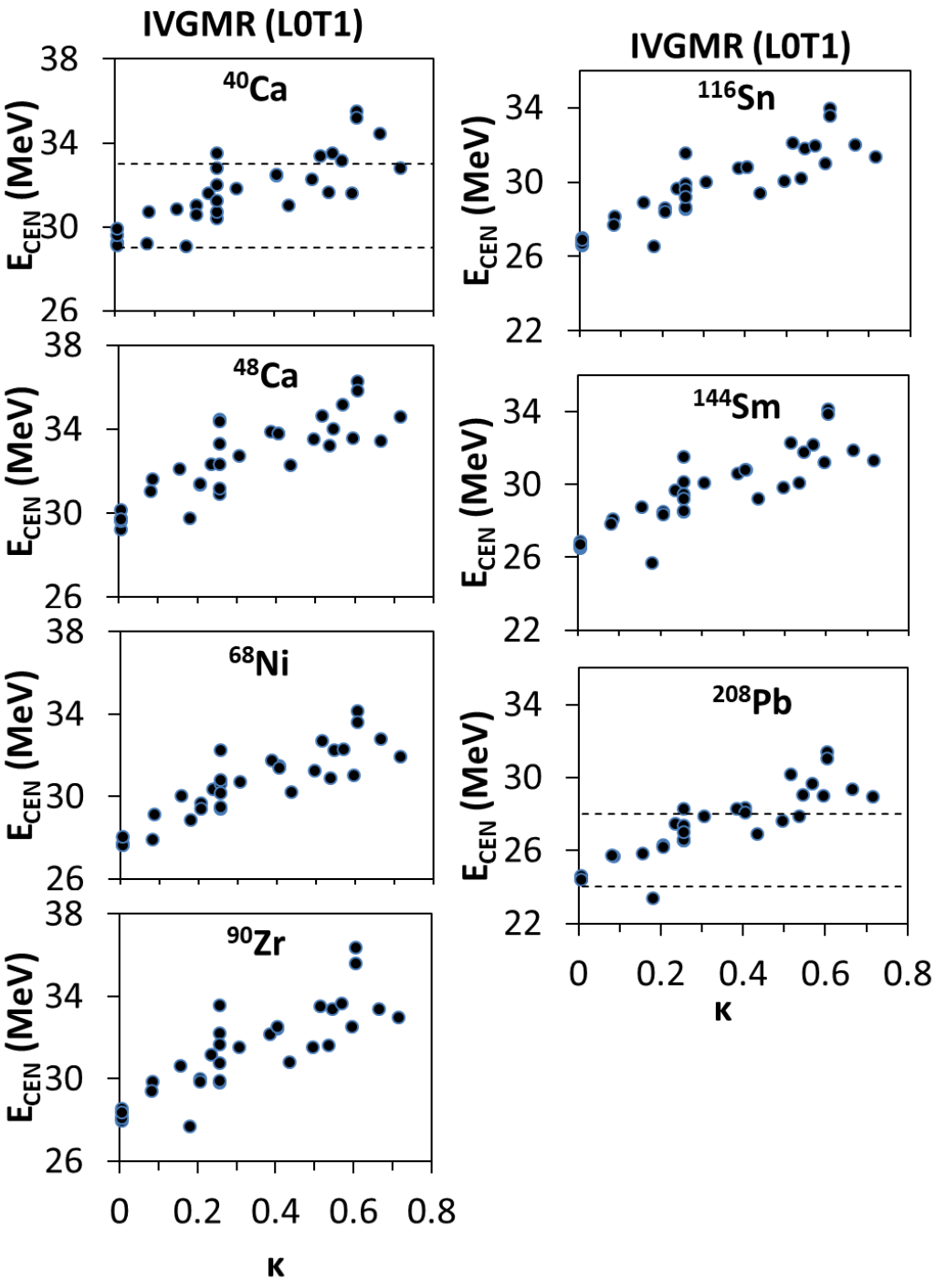

Figure 15 IVGMR E_{CEN} with κ in ^{40,48}Ca, ^{68}Ni, ^{90}Zr, ^{116}Sn, ^{144}Sm and ^{208}Pb. Like Figure 2 but for the IVGMR centroid energy as plotted with the enhancement coefficient of the EWSR for the IVGDR. A strong correlation is obtained between the calculated values of E_{CEN} and κ, with a Pearson linear correlation coefficient C ~ 0.86.

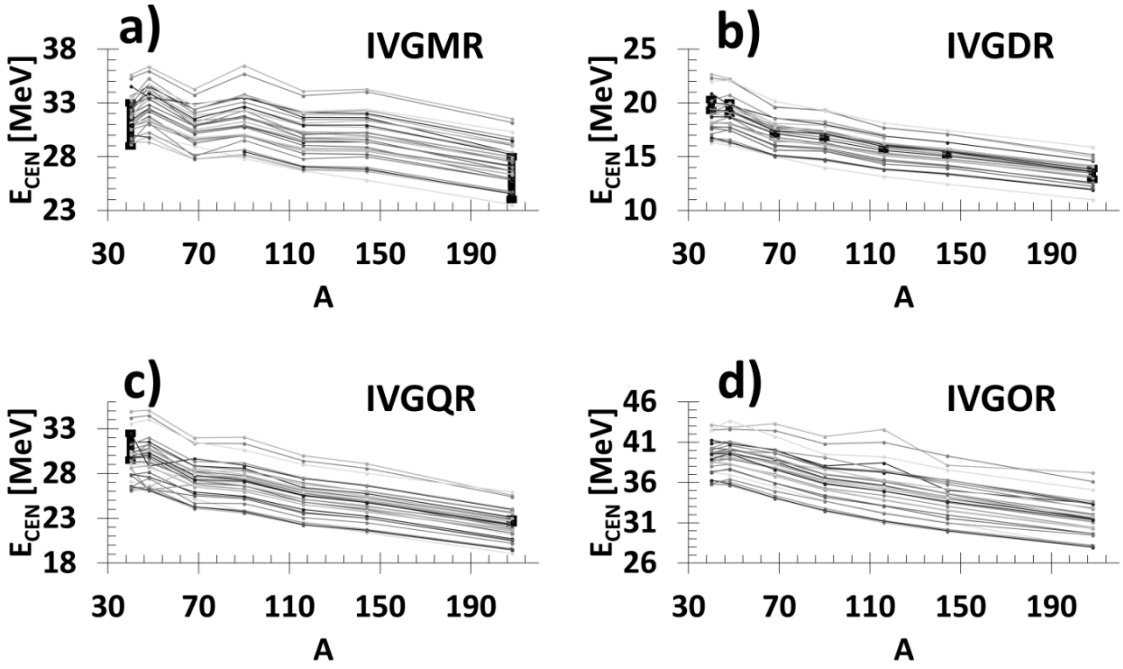

Figure 16 Isovector E_{CEN} overview in ^{40,48}Ca, ^{68}Ni, ^{90}Zr, ^{116}Sn, ^{144}Sm and ^{208}Pb. Similar to Figure 5 but for the isovector resonances. Experimental data is available for the IVGDR but only available for ^{40}Ca and ^{208}Pb for the IVGMR and IVGQR.

In Figure 16a we plot the E_{CEN} of the IVGMR against the nucleon mass. A majority of the calculations, shown by dots with a line connecting the same interaction to guide the eye, predict a decreasing see-saw trend for the value of the centroid energy as the mass is increasing. We see from the figure that the calculated values of the centroid energy for the heavier Ca isotopes are above the lighter one except for NRAPR and SkT3*. Likewise, all but one interaction (SKO), predicted the values of E_{CEN} for ^{90}Zr above those of ^{68}Ni, while the centroid energy of ^{144}Sm was determined to be within 0.2 MeV (for most interactions) of the centroid energy of ^{116}Sn.

Isovector Giant Dipole Resonance

The centroid energy, E_{CEN}, resulting from the HF-RPA (full circles) calculation for the isovector giant dipole resonance (IVGDR) is plotted against the symmetry energy coefficient, J, in Figure 17. Data is available for all nuclei with very small error bars in some cases. We found weak correlation between the theoretical values of E_{CEN} and J (C ~ -0.37). Similarly, for the 1st and 2nd derivatives of the symmetry energy, L and K_{sym}, we obtained weak and no correlations with the theoretical values of the centroid energy with C ~ -0.42 and C ~ -0.30, respectively. The lack of a correlation for these quantities goes against the common expectation that the value of the centroid energy for the isovector dipole is sensitive to the density dependence of $E_{sym}(\rho)$ [40,79]. We note that for an improved determination of the density dependence of $E_{sym}(\rho)$ one should also study the relation between the centroid energy and the neutron-proton asymmetry, (N-Z)/A, or other quantities for example the IVGDR polarizability. In Figure 18 the centroid energy is plotted with the EWSR enhancement coefficient, κ, of the IVGDR. We obtained a strong correlation between the theoretical values of E_{CEN} and κ, with a Pearson linear correlation coefficient C ~ 0.84. It can be seen from the figure that the centroid energies resulting from interactions associated with κ = 0.25 - 0.70 are the best at reproducing the data. In Figure 19 the centroid energy is plotted against the effective mass. In this case we obtained weak correlation between E_{CEN} and m*/m with C ~ -0.60. The correlations between other NM properties and the E_{CEN} of the IVGDR are presented in Table 7. For completeness the calculated E_{CEN} of the IVGDR are shown in Table 19 of the Appendix.

In Figure 16b the IVGDR centroid energy is plotted as a function of mass for the 7 nuclei studied in this section. The results of the 33 interactions are plotted by dots connected with a line for each interaction to guide the eye while the experimental data is shown as vertical black lines. A clear decrease in the value of E_{CEN} as the nucleon mass is increased is seen in the figure for both the experimental and theoretical results. Some deviations to this trend are found for the Ca isotopes for which 12 of the interactions considered predict the heavier isotope to have a centroid energy up to 0.60 MeV larger than that of ^{40}Ca. We also see from this figure that the data is always in the middle of the theoretical "band" i.e. the same interactions, with $\kappa = 0.25 - 0.70$, reproduce all the data.

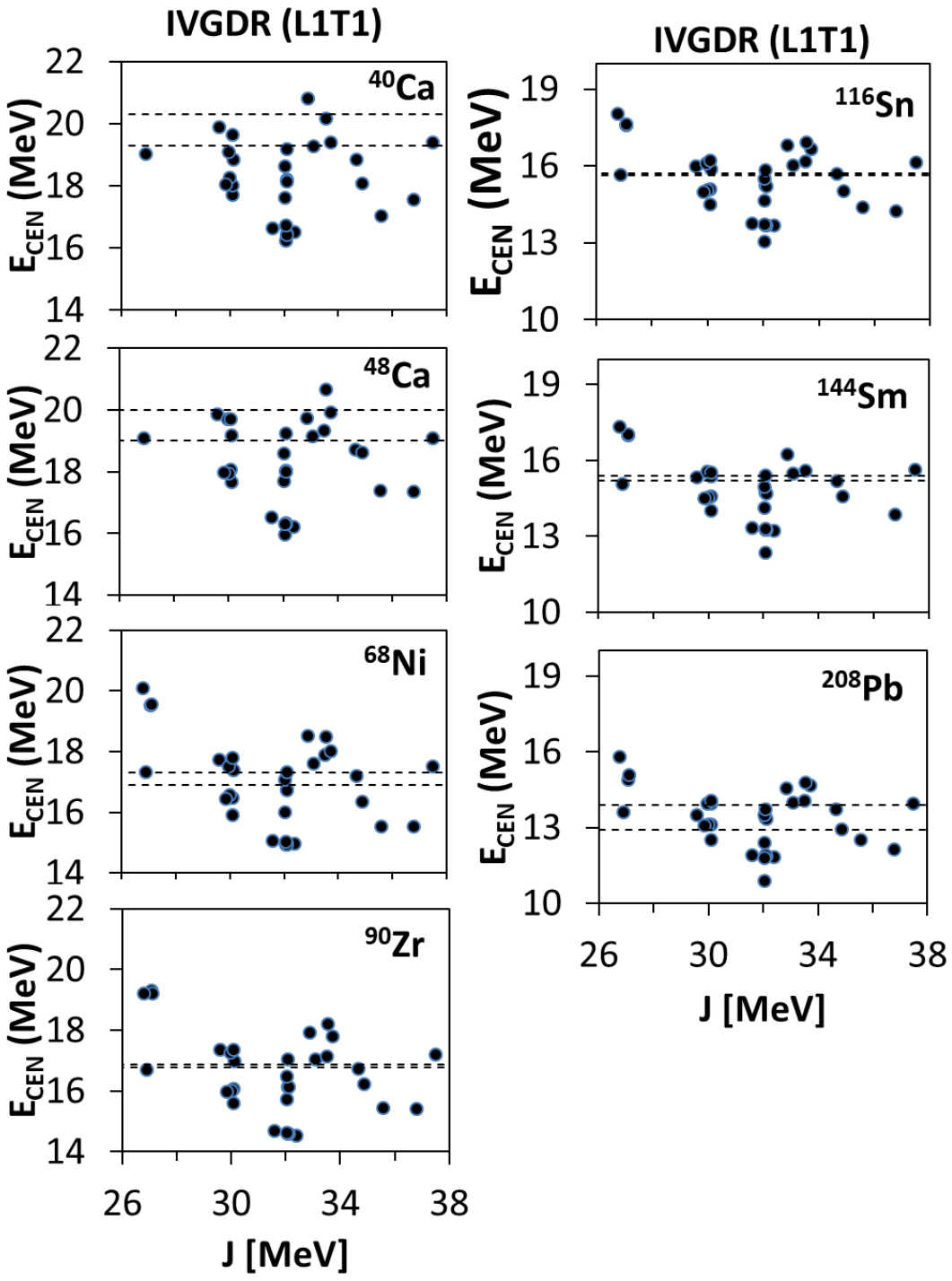

Figure 17 IVGDR E_{CEN} with J in ^{40,48}Ca, ^{68}Ni, ^{90}Zr, ^{116}Sn, ^{144}Sm and ^{208}Pb. Like Figure 2 but for the IVGDR centroid energy plotted with the symmetry energy at saturation density. No correlation is obtained between the calculated values of E_{CEN} and J, with a Pearson linear correlation coefficient C ~ -0.37.

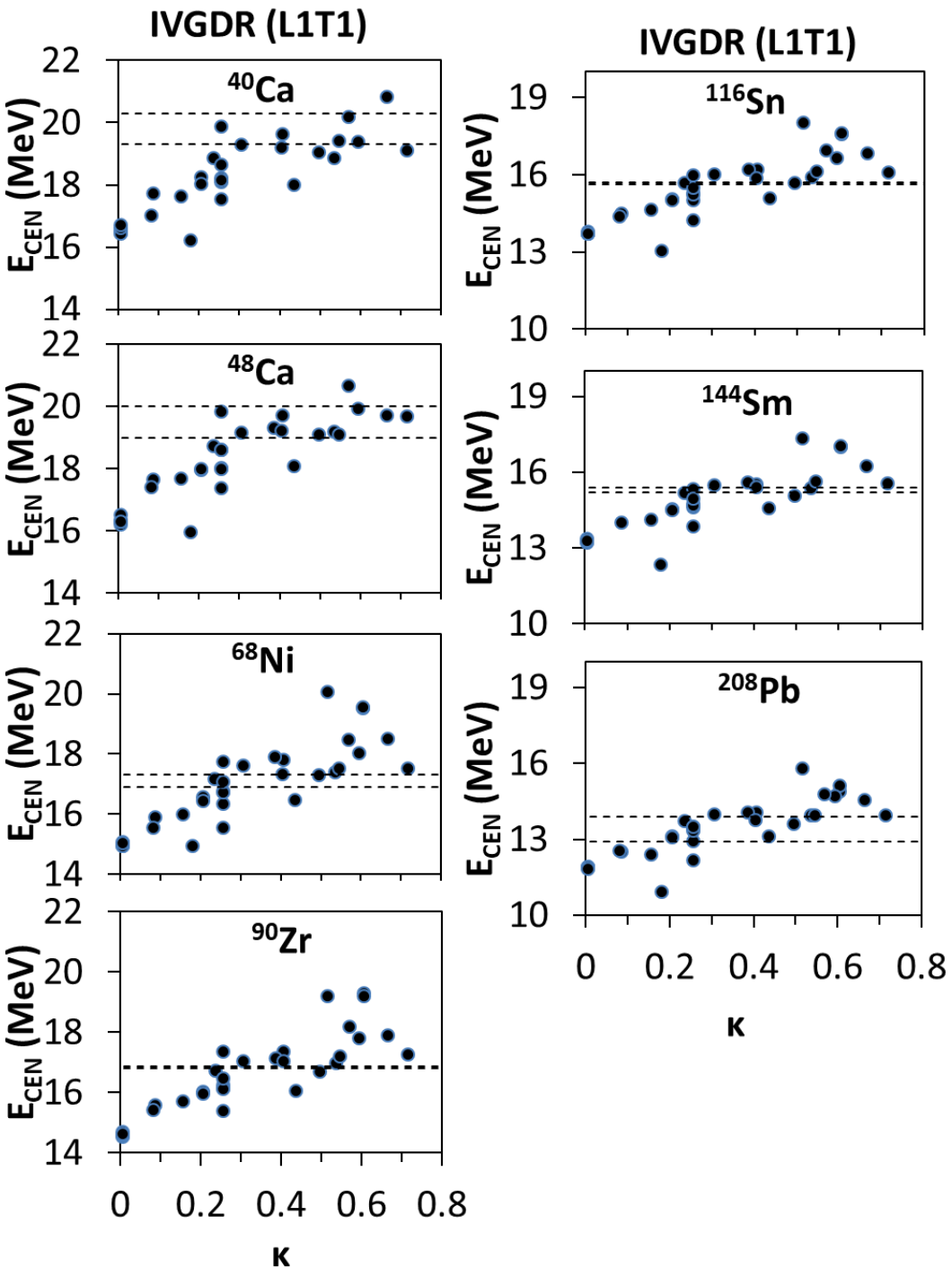

Figure 18 IVGDR E_{CEN} with κ in ^{40,48}Ca, ^{68}Ni, ^{90}Zr, ^{116}Sn, ^{144}Sm and ^{208}Pb. Like Figure 2 but for the IVGDR centroid energy plotted with the enhancement coefficient of the EWSR for the IVGDR. A strong correlation is obtained between the calculated values of E_{CEN} and κ, with a Pearson linear correlation coefficient C ~ 0.84.

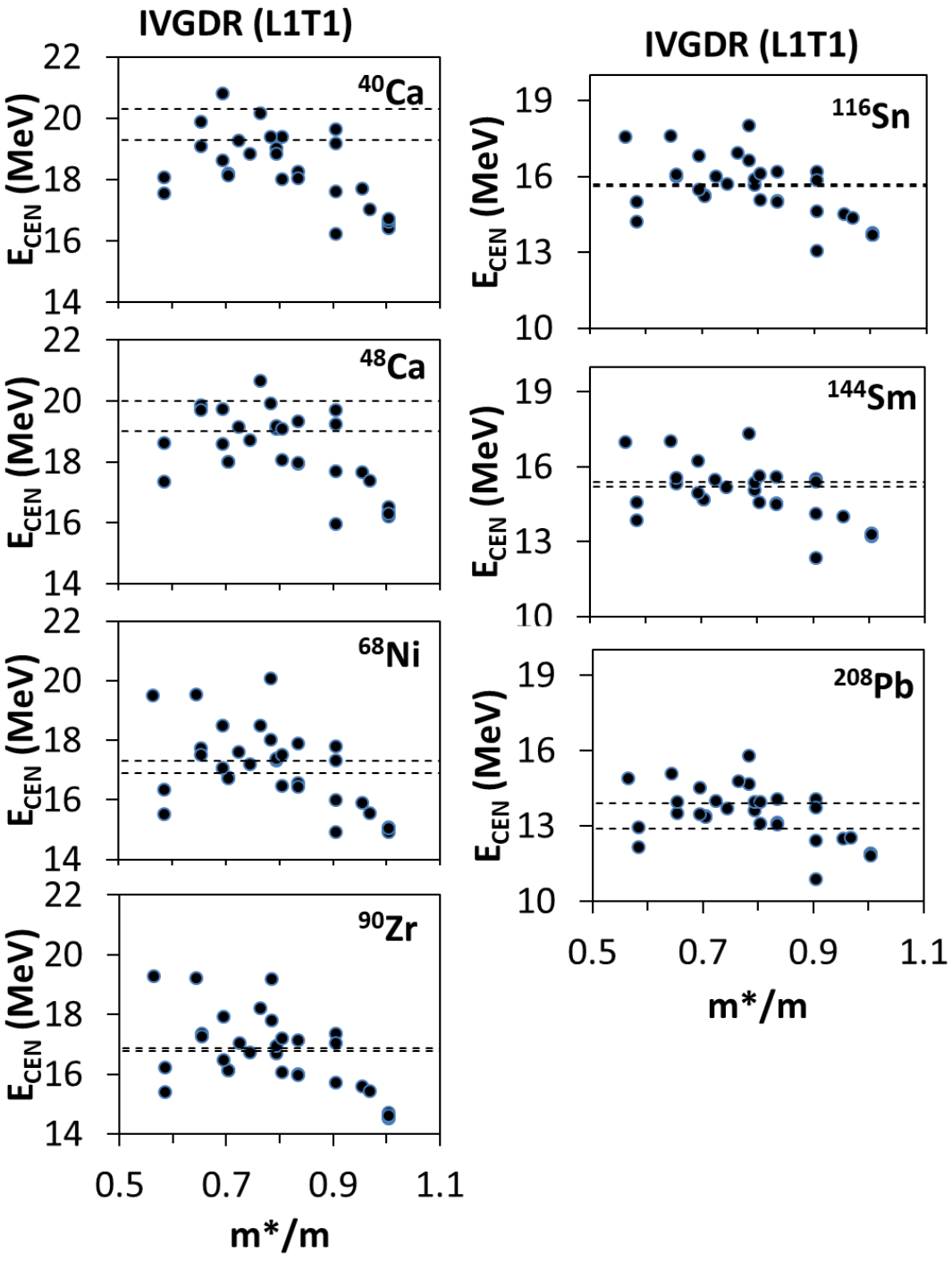

Figure 19 IVGDR E_{CEN} with m*/m in ^{40,48}Ca, ^{68}Ni, ^{90}Zr, ^{116}Sn, ^{144}Sm and ^{208}Pb. Like Figure 2 but for the IVGDR centroid energy plotted with the effective mass. A weak correlation is obtained between the calculated values of E_{CEN} and m*/m, with a Pearson linear correlation coefficient C ~ -0.60.

Isovector Giant Quadrupole Resonance

The centroid energy, E_{CEN}, of the isovector giant quadrupole resonance (IVGQR) is plotted with the symmetry energy, J, in Figure 20. Measurements are available for ^{40}Ca and ^{208}Pb and are delimited with dashed lines. We only obtain a weak correlation between the calculated values of E_{CEN} and J with C ~ -0.35. Similarly, no correlation was found between the calculated values of E_{CEN} and both the first and second derivatives of J with C ~ -0.29 and C ~ 0.13, respectively. In Figure 21 the centroid energy is plotted as a function of the energy weighted sum rule (EWSR) enhancement coefficient, κ, of the IVGDR. We obtain a medium correlation between the calculated values of E_{CEN} and κ with a Pearson linear correlation coefficient C ~ 0.80. In agreement with our constraints derived from the IVGDR on κ, we find that the same interactions also reproduce the centroid energy of the IVGQR for ^{40}Ca and ^{208}Pb. In Figure 22 we plot E_{CEN} with the effective mass. In this case we obtain a medium correlation (C ~ -0.74) between the calculated values of E_{CEN} and m*/m and obtain good agreement with the available experimental data for interactions with m*/m = 0.6 - 0.9. We do not obtain any correlation between the calculated values of E_{CEN} and K_{NM} (C ~ 0.18) or any other NM properties, see Table 7. The theoretical centroid energies of the IVGQR are shown in Table 20 of the Appendix.

In Figure 16c the centroid energy of the IVGQR is plotted as a function of mass for the nuclei studied in this section. We see from the figure that the value of E_{CEN} decreases with A, however, for the Ca isotopes we found that 9 Skyrme interactions yielded a larger E_{CEN} for the heavier isotope.

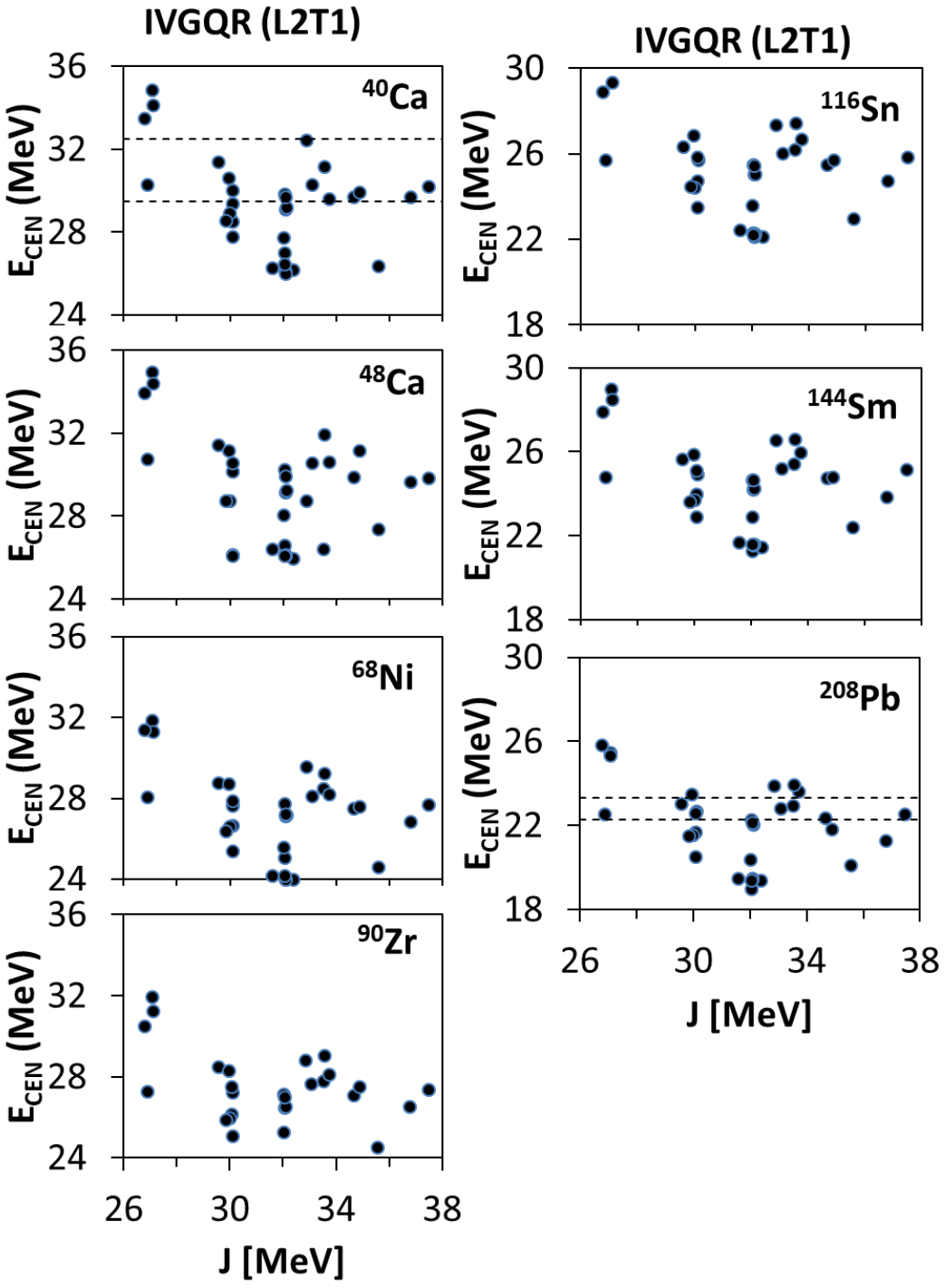

Figure 20 IVGQR E_{CEN} with J in ^{40,48}Ca, ^{68}Ni, ^{90}Zr, ^{116}Sn, ^{144}Sm and ^{208}Pb. Like Figure 2 but for the IVGQR centroid energy plotted with the symmetry energy at saturation density. No correlation is obtained between the calculated values of E_{CEN} and J, with a Pearson linear correlation coefficient C ~ -0.35.

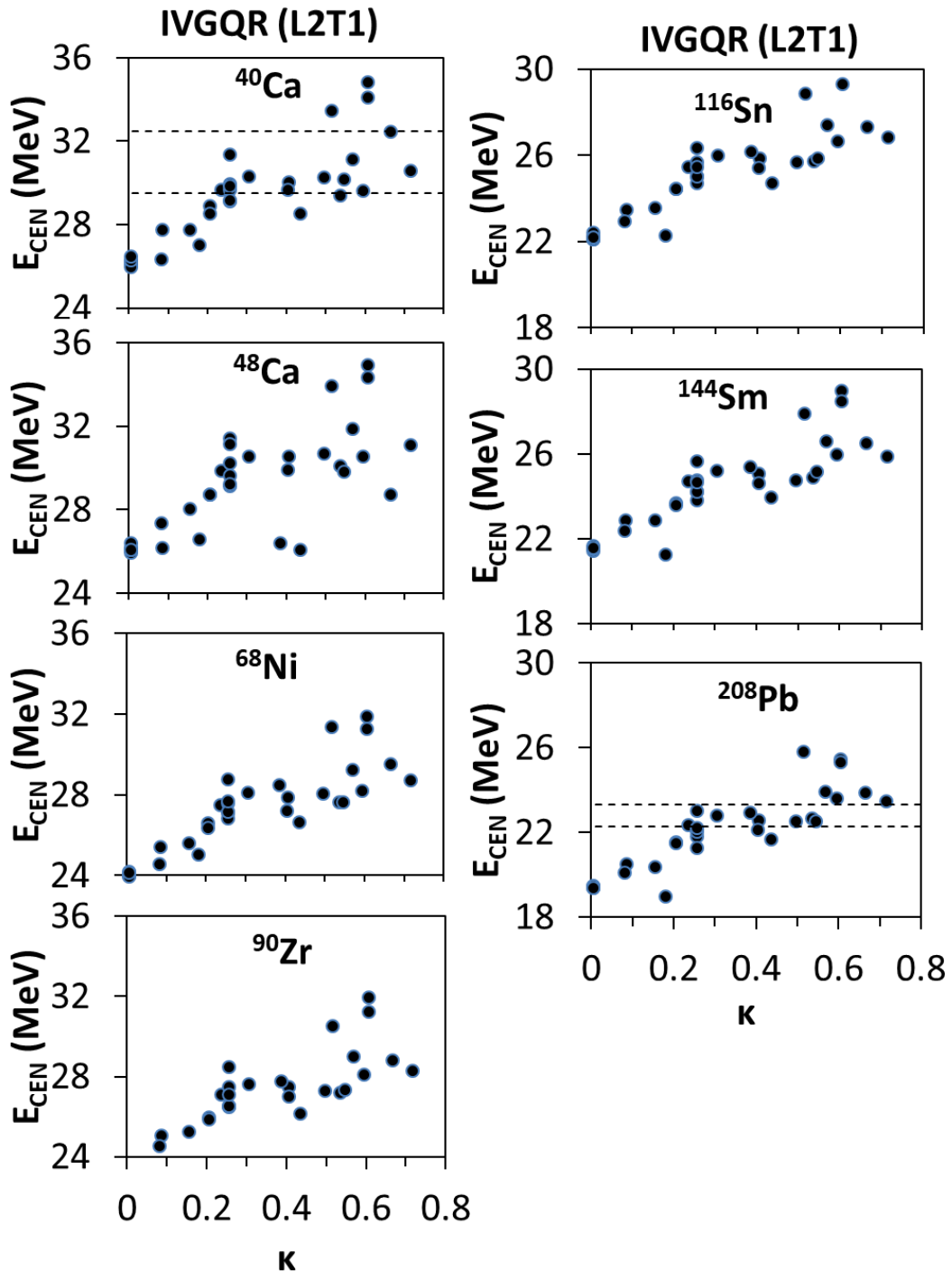

Figure 21 IVGQR E_{CEN} with κ in ^{40,48}Ca, ^{68}Ni, ^{90}Zr, ^{116}Sn, ^{144}Sm and ^{208}Pb. Like Figure 2 but for the IVGQR centroid energy plotted with the enhancement coefficient of the EWSR for the IVGDR. A medium correlation is obtained between the calculated values of E_{CEN} and κ, with a Pearson linear correlation coefficient C ~ 0.80.

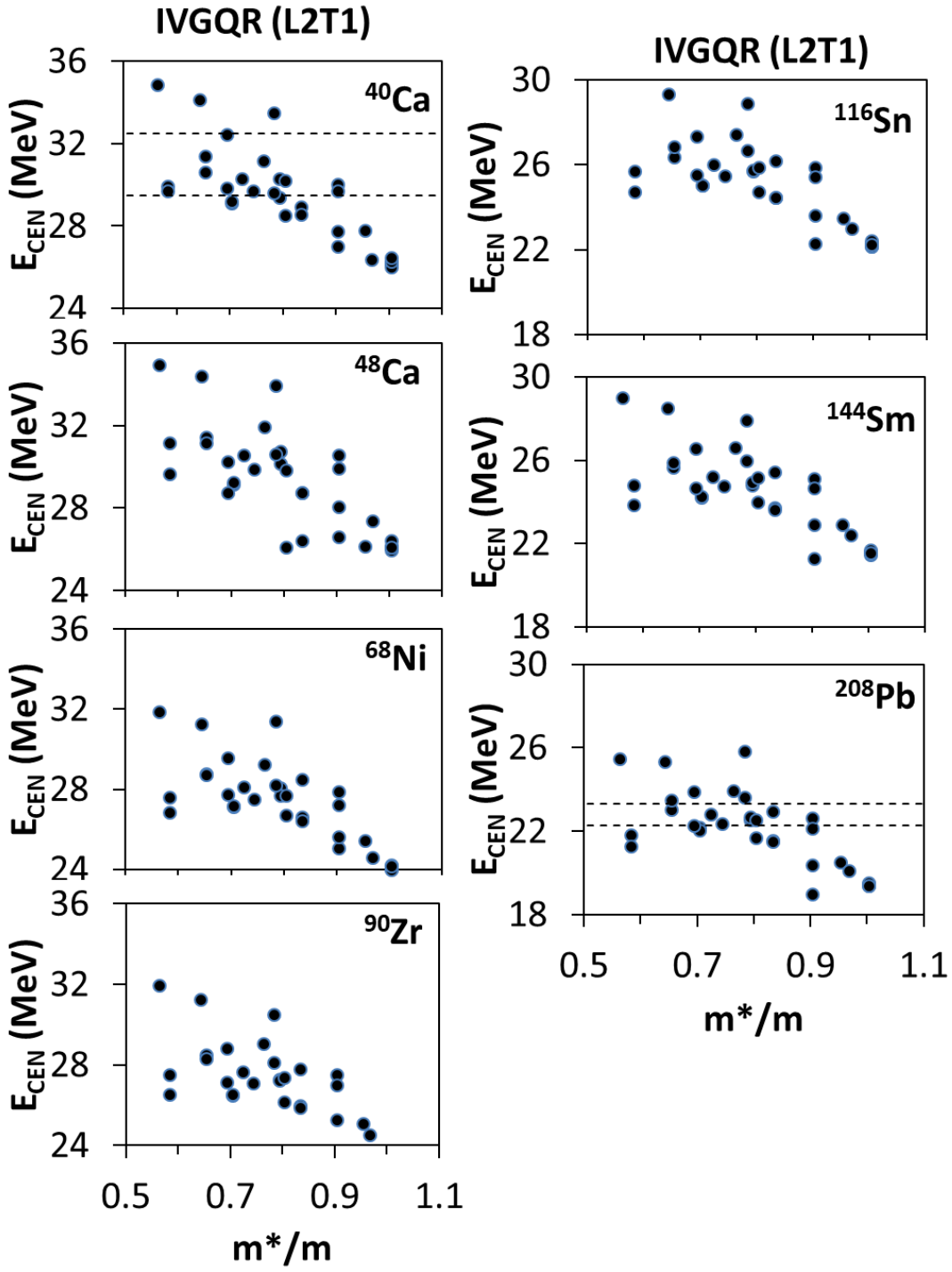

Figure 22 IVGQR E_{CEN} with m*/m in ^{40,48}Ca, ^{68}Ni, ^{90}Zr, ^{116}Sn, ^{144}Sm and ^{208}Pb. Like Figure 2 but for the IVGQR centroid energy plotted with the effective mass. A medium correlation is obtained between the calculated values of E_{CEN} and m*/m, with a Pearson linear correlation coefficient C ~ -0.74.

Isovector Giant Octupole Resonance

No experimental data is available for the centroid energy, E_{CEN}, of the isovector giant octupole resonance (IVGOR) for the nuclei studied here. In Figure 23 the centroid energy, E_{CEN}, is plotted as a function of the symmetry energy coefficient J. No correlation is found between the calculated values of E_{CEN} and J (C ~ -0.32). Similarly, for the 1st and 2nd derivatives of J no correlation is found with E_{CEN} (C ~ -0.19 and 0.02, respectively). Conversely, we obtained a strong correlation between the calculated values of E_{CEN} and the EWSR enhancement coefficient, κ, for the IVGDR (Pearson linear correlation coefficient C ~ 0.81) as can be seen from Figure 24. Similarly, we obtained a strong correlation between m*/m and E_{CEN} (C ~ -0.83) as shown in Figure 25. No other correlation is found between E_{CEN} and NM properties, see Table 7 for values of C. The calculated centroid energies of the IVGOR are shown in Table 21 of the Appendix.

We plot the IVGOR centroid energies as a function of nucleon mass in Figure 16d. We find a smooth decrease in the value of E_{CEN} as A increases, with some exceptions for the Ca isotopes where 22 of the 33 interactions predict the centroid energy of ^{48}Ca slightly above that of ^{40}Ca.

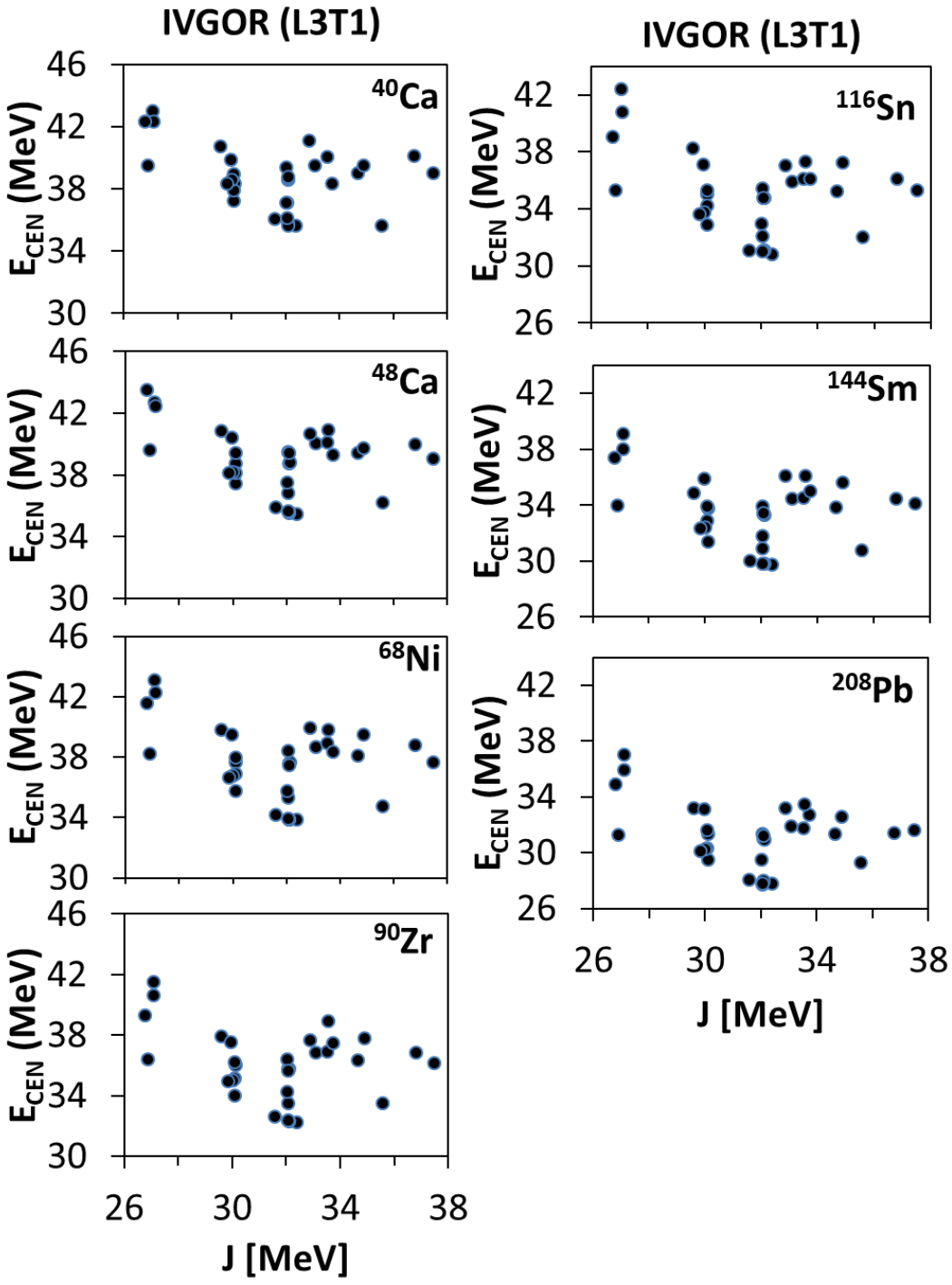

Figure 23 IVGOR E_{CEN} with J in ^{40,48}Ca, ^{68}Ni, ^{90}Zr, ^{116}Sn, ^{144}Sm and ^{208}Pb. Like Figure 2 but for the IVGOR centroid energy plotted with the symmetry energy at saturation density. No correlation is obtained between the calculated values of E_{CEN} and J, with a Pearson linear correlation coefficient C ~ -0.32.

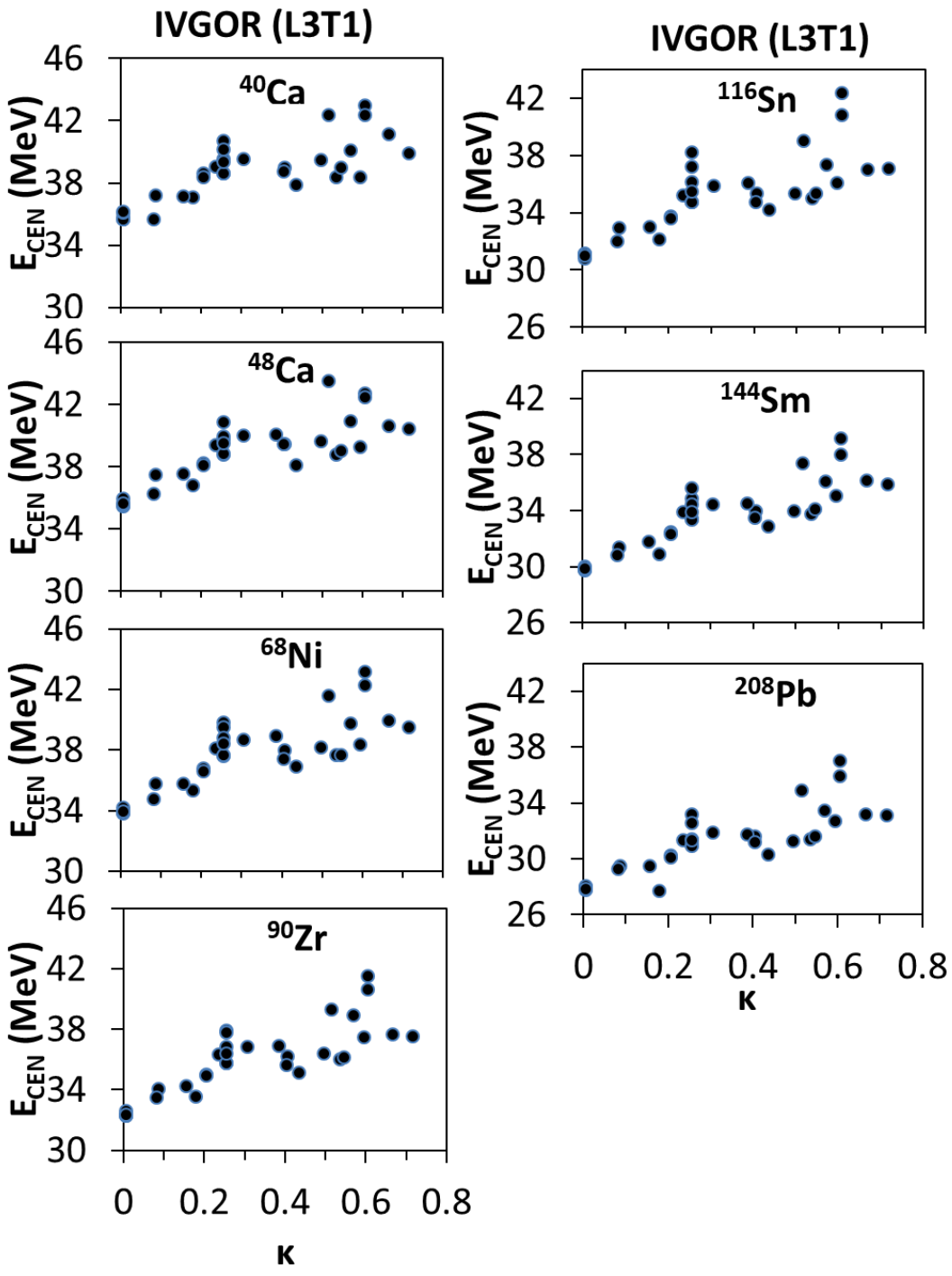

Figure 24 IVGOR E_{CEN} with κ in ^{40,48}Ca, ^{68}Ni, ^{90}Zr, ^{116}Sn, ^{144}Sm and ^{208}Pb. Like Figure 2 but for the IVGOR centroid energy plotted with the enhancement coefficient of the EWSR for the IVGDR. A strong correlation is obtained between the calculated values of E_{CEN} and κ, with a Pearson linear correlation coefficient C ~ 0.81.

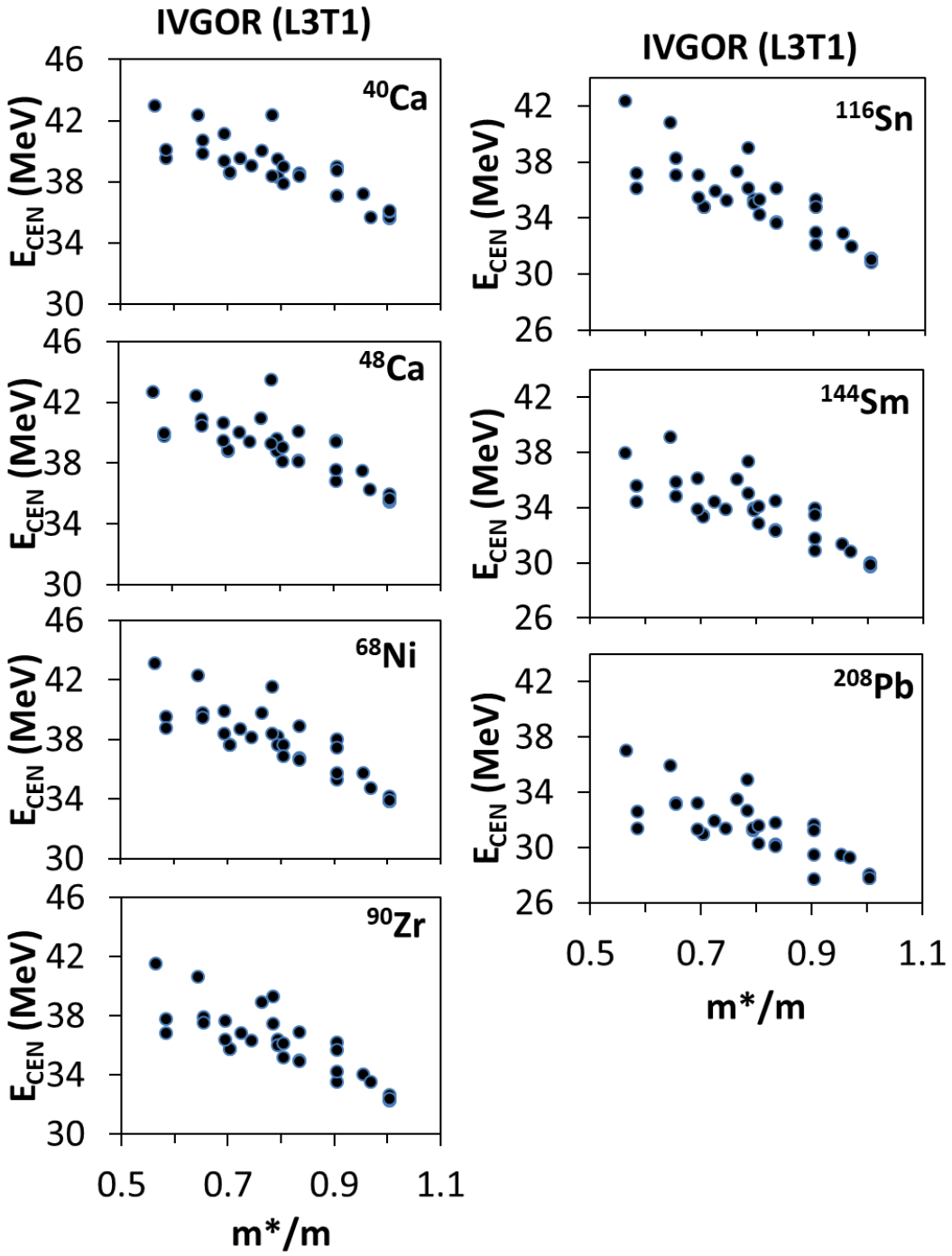

Figure 25 IVGOR E_{CEN} with m*/m in ^{40,48}Ca, ^{68}Ni, ^{90}Zr, ^{116}Sn, ^{144}Sm and ^{208}Pb. Like Figure 2 but for the IVGOR centroid energy plotted with the effective mass. A strong correlation is obtained between the calculated values of E_{CEN} and m*/m, with a Pearson linear correlation coefficient C ~ -0.83.

Conclusions

We have discussed results of fully self-consistent spherical HF based RPA calculations, employing 33 Skyrme type effective nucleon-nucleon interactions of the standard form shown in Table 1, for the centroid energies, E_{CEN}, of the isoscalar and isovector giant resonances of multipolarities L = 0 - 3 in ^{40,48}Ca, ^{68}Ni, ^{90}Zr, ^{116}Sn, ^{144}Sm and ^{208}Pb and compared with available experimental data. The sensitivity of the theoretical E_{CEN} of each giant resonance to the properties of nuclear matter at saturation density associated with the adopted interactions was investigated by determining the Pearson linear correlation coefficients, C, between E_{CEN} and the various NM properties.

We reproduced the data for the centroid energy of the ISGMR, ISGQR and IVGDR for most of the nuclei considered. For the ISGDR and ISGOR we found that most of the interactions are consistently higher than the experimental values for the centroid energy. Strong correlation was found between the calculated values of the centroid energy of the ISGMR and the incompressibility coefficient of nuclear matter, K_{NM}. We obtained medium to strong correlations for the calculated values of centroid energy and nucleon effective mass, m*/m, for all the resonances considered. We also obtained strong correlations between the isovector centroid energies and the enhancement coefficient, κ, of the EWSR of the IVGDR. We report that no correlation was found for the isovector centroid energies and the symmetry energy coefficients J, L and K_{sym}.

Using the available experimental data and the strong correlations of the ISGMR, ISGQR and IVGDR with K_{NM}, m*/m and κ, respectively, we obtained the best

description of the experimental data for interactions associated with the following ranges of NM properties: K_{NM} = 210 – 240 MeV, m*/m = 0.7 - 0.9 and κ = 0.25 - 0.70. We note that when deciding on a best range for the effective mass more weight was given to the results of heavier nuclei.

CHAPTER IV

GIANT RESONANCES IN ^{92,94,96,98,100}Mo AND ^{90,92,94}Zr[*2]

In this chapter we present the centroid energies, E_{CEN}, of isoscalar and isovector giant resonances of multipolarity L = 0 - 3 for the isotopes of ^{92,94,96,98,100}Mo and ^{90,92,94}Zr obtained from the HF based RPA, described previously in chapter II, employing 33 Skyrme type effective nucleon-nucleon interactions of the standard form given in Table 1. Except for ^{90}Zr, the nuclei considered here are open-shell nuclei. We used the occupation number approximation for the single-particle orbits to carry out our calculations.

For the calculation of the E_{CEN} we adopted the energy range shown in Table 8 which were obtained from the study of the structure of the corresponding strength functions. We compare our theoretical centroid energies to the experimental results of Table 9. The isoscalar giant resonances have been measured at Texas A&M University using inelastic scattering of 240 MeV α-particles [58–61]. A detailed explanation of the experimental method used for the TAMU experiments can be found in [62–64]. We also compare our calculations for the ISGMR centroid energy with the experimental result from the Research Center for Nuclear Physics (RCNP) at Osaka University (Osaka, Japan) [23]. The isovector centroid energies were obtained from various sources in the

[*2] Parts of the chapter are reproduced with permission from G. Bonasera, S. Shlomo, D. H. Youngblood, Y.-W. Lui, Krishichayan, and J. Button, "Isoscalar and isovector giant resonances in ^{92,94,96,98,100}Mo and ^{90,92,94}Zr", Nucl. Phys. A (2019, accepted for publication), Copyright Elsevier 2019.

literature, see Table 9 for details. We also calculate the Pearson linear correlation coefficient between the centroid energy of each multipolarity and each NM property, shown in Table 10. We obtain strong correlation between E_{CEN} of the ISGMR and the incompressibility coefficient of nuclear matter, K_{NM}, between E_{CEN} of the ISGDR, ISGQR, ISGOR, IVGOR and the effective mass, m*/m, and between E_{CEN} of the isovector resonances and the EWSR enhancement coefficient, κ, of the IVGDR.

In what follows we cover each giant resonance separately and show plots of the calculated E_{CEN} as a function of various NM properties associated with the interaction used in the calculation. Experimental data is shown as dashed lines where available. We also investigate the effect of isospin asymmetry, $I = \frac{N-Z}{A}$, on the centroid energy by studying these isotopes and isotones.

Table 8 Integration energy ranges for ^{92,94,96,98,100}Mo and ^{90,92,94}Zr. Energy ranges $E_1 - E_2$ (in MeV) used in the integration of the strength function to determine the centroid energies of the isoscalar and isovector giant resonances.

	^{92}Mo	^{94}Mo	^{96}Mo	^{98}Mo	^{100}Mo	^{90}Zr	^{92}Zr	^{94}Zr
L0T0	9 - 36	9 - 36	9 - 36	9 - 36	9 - 36	9 - 36	9 - 36	9 - 36
L1T0	20 - 36	20 - 36	20 - 36	20 - 36	20 - 36	20 - 36	20 - 36	20 - 36
L2T0	9 - 36	9 - 36	9 - 36	9 - 36	9 - 36	9 - 36	9 - 36	9 - 36
L3T0	15 - 36	15 - 36	15 - 36	15 - 36	15 - 36	15 - 36	15 - 36	15 - 36
L0T1	15 - 60	15 - 60	15 - 60	15 - 60	15 - 60	15 - 60	15 - 60	15 - 60
L1T1	0 - 60	0 - 60	0 - 60	0 - 60	0 - 60	0 - 60	0 - 60	0 - 60
L2T1	15 - 60	15 - 60	15 - 60	15 - 60	15 - 60	15 - 60	15 - 60	15 - 60
L3T1	22 - 60	22 - 60	22 - 60	22 - 60	22 - 60	22 - 60	22 - 60	22 - 60

Table 9 E_{CEN} experimental data in MeV for ^{92,94,96,98,100}Mo and ^{90,92,94}Zr. The data for the isoscalar giant resonances in ^{92,96,98,100}Mo isotopes is taken from Ref. [19], in ^{94}Mo from Ref. [20], in ^{90,92,94}Zr from Ref. [21]. The ISGMR data for ^{92}Mo and ^{90,92}Zr, from the Osaka group (marked with *), is from Ref. [23]. The data for the isovector giant dipole resonances in ^{92,94,96,98,100}Mo is taken from Ref. [81] and in ^{90,92,94}Zr from Ref. [69].

	L0T0	L1T0	L2T0	L3T0	L1T1
^{92}Mo	19.62 (28) 18.20 (13)*	27.60 (50)	14.51 (25)	21.80 (30)	16.90 (.10)
^{94}Mo	17.99 (72)	26.49 (43)	14.55 (13)	24.60 (46)	16.40 (10)
^{96}Mo	16.95 (12)	30.00 (70)	13.85 (20)	21.40 (30)	16.20 (10)
^{98}Mo	16.01 (19)	27.40 (70)	13.85 (20)	21.5 (30)	15.80 (10)
^{100}Mo	16.13 (11)	30.10 (70)	13.60 (15)	21.51 (30)	15.70 (10)
^{90}Zr	17.88 (12) 18.13 (09)*	27.40 (50)	14.56 (20)	23.10 (30)	16.83 (04)
^{92}Zr	18.23 (14) 18.05 (05)*	30.00 (70)	14.35 (15)	23.90 (30)	16.27 (04)
^{94}Zr	16.16 (11)	27.00 (50)	14.49 (15)	23.60 (30)	16.20 (04)

Table 10 Pearson linear correlation for ^{92,94,96,98,100}Mo and ^{90,92,94}Zr. Calculated Pearson linear correlation coefficient between centroid energies and each nuclear matter property.

	K_{NM}	J	L	K_{sym}	m*/m	κ	$W_0(X_W=1)$
ISGMR	0.87	-0.05	0.25	0.42	-0.51	0.15	0.07
ISGDR	0.53	-0.07	0.12	0.37	-0.91	0.53	0.03
ISGQR	0.37	-0.07	0.15	0.41	-0.96	0.57	0.06
ISGOR	0.38	-0.08	0.13	0.39	-0.98	0.61	0.07
IVGMR	0.25	-0.24	-0.09	0.04	-0.71	0.85	-0.08
IVGDR	0.04	-0.35	-0.39	-0.29	-0.61	0.85	-0.22
IVGQR	0.16	-0.34	-0.27	-0.11	-0.77	0.85	-0.13
IVGOR	0.21	-0.28	-0.18	0.02	-0.86	0.83	-0.07

Isoscalar Giant Monopole Resonance

The centroid energy, E_{CEN}, of the isoscalar giant monopole resonance (ISGMR), calculated within the spherical HF-based RPA, is plotted in Figure 26 as a function of the incompressibility coefficient of nuclear matter, K_{NM}, of the corresponding interaction used in the calculation. One isotope is shown for each panel and the relative experimental region is marked with dashed lines (for the TAMU data). For ^{92}Mo we also included solid lines to show the Osaka data [23], however we did not include the Osaka data for ^{90,92}Zr because it agrees closely with the TAMU data. We obtained a strong correlation between the calculated values of E_{CEN} and K_{NM} with a Pearson linear correlation coefficient C ~ 0.87, in agreement with our results of Chapter III. However, in this case, we can't make constraints on the value of K_{NM} due to the disagreement between the theoretical and experimental results. For the data from the TAMU experiment of ^{92}Mo we obtained agreement with interactions with a value of $K_{NM} > 260$ MeV. On the opposite end we find that interactions with $K_{NM} < 200$ MeV reproduced the experimental data for ^{94}Zr, while interactions with $K_{NM} = 210 – 240$ MeV reproduced the data of ^{96}Mo and ^{90,92}Zr. For the remaining neutron rich isotopes of ^{98,100}Mo and ^{94}Zr we find that none of the interactions reproduced the experimental result, with the theoretical calculations consistently above the experimental value by 2 MeV. In Figure 27 we plotted E_{CEN} of the ISGMR as a function of the effective mass, m*/m, for which we found a weak correlation (C ~ -0.51). In Figure 28 we plot the centroid energy against the symmetry energy coefficient, J. We do not obtain any correlation between the theoretical values of E_{CEN} and J (C ~ -0.05). Similarly, no correlation is found with the

first derivative of J while a weak correlation is found with its second derivative (C ~ 0.42). We do not obtain any correlation with any of the other NM properties or with W_0, see Table 10. The complete list of calculated values of the isoscalar monopole centroid energies is given in Table 22.

In Figure 29 we plot the change in the centroid energy $\Delta E_{CEN} = E_{CEN}(I_0) - E_{CEN}(I)$ against the isospin asymmetry coefficient I = (N-Z)/A. The ISGMR E_{CEN} are plotted in Figure 29a for the Mo isotopes and Figure 29b for the Zr isotopes. The theoretical results are plotted by dots a with line connecting the results of the same interaction to guide the eye, while the experimental data is shown by the solid vertical lines. We find a general decreasing trend in the value of E_{CEN} as the value of I increases (and thus A increases), in both values of the theory and the experiment. However, the magnitude of the decrease in the value of the centroid energy from one isotope to the next found in the experimental data is not reproduced by the calculations [77]. For ^{92}Zr and ^{92}Mo the centroid energies obtained by the experiment at TAMU were greater than that of ^{90}Zr by 0.35 and 1.74 MeV, respectively. In the case of our calculations we only obtained the centroid energy larger in ^{92}Mo than ^{90}Zr for the SKO interaction while the calculations for the Zr isotopes result in mostly the same value of E_{CEN} for all the interactions considered.

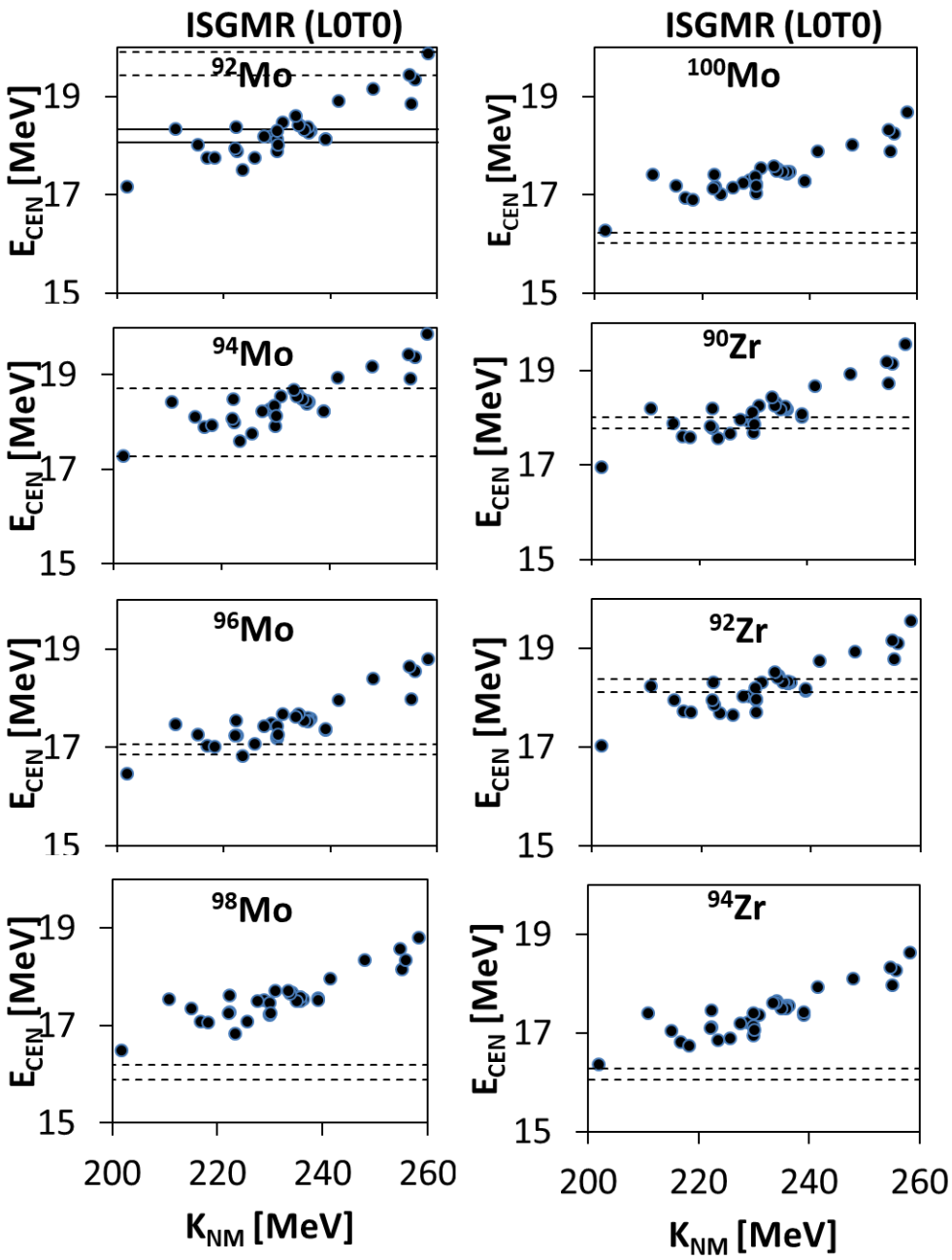

Figure 26 ISGMR E_{CEN} with K_{NM} in ^{92,94,96,98,100}Mo and ^{90,92,94}Zr. Theoretical centroid energies [MeV] (full circle) of the ISGMR plotted with the incompressibility coefficient K_{NM}. One isotope is shown per panel, the experimental data is delimited by dashed lines (Texas A&M) and solid lines (Osaka). A strong correlation is obtained between the calculated values of E_{CEN} and K_{NM}, with a Pearson linear correlation coefficient C ~ 0.87.

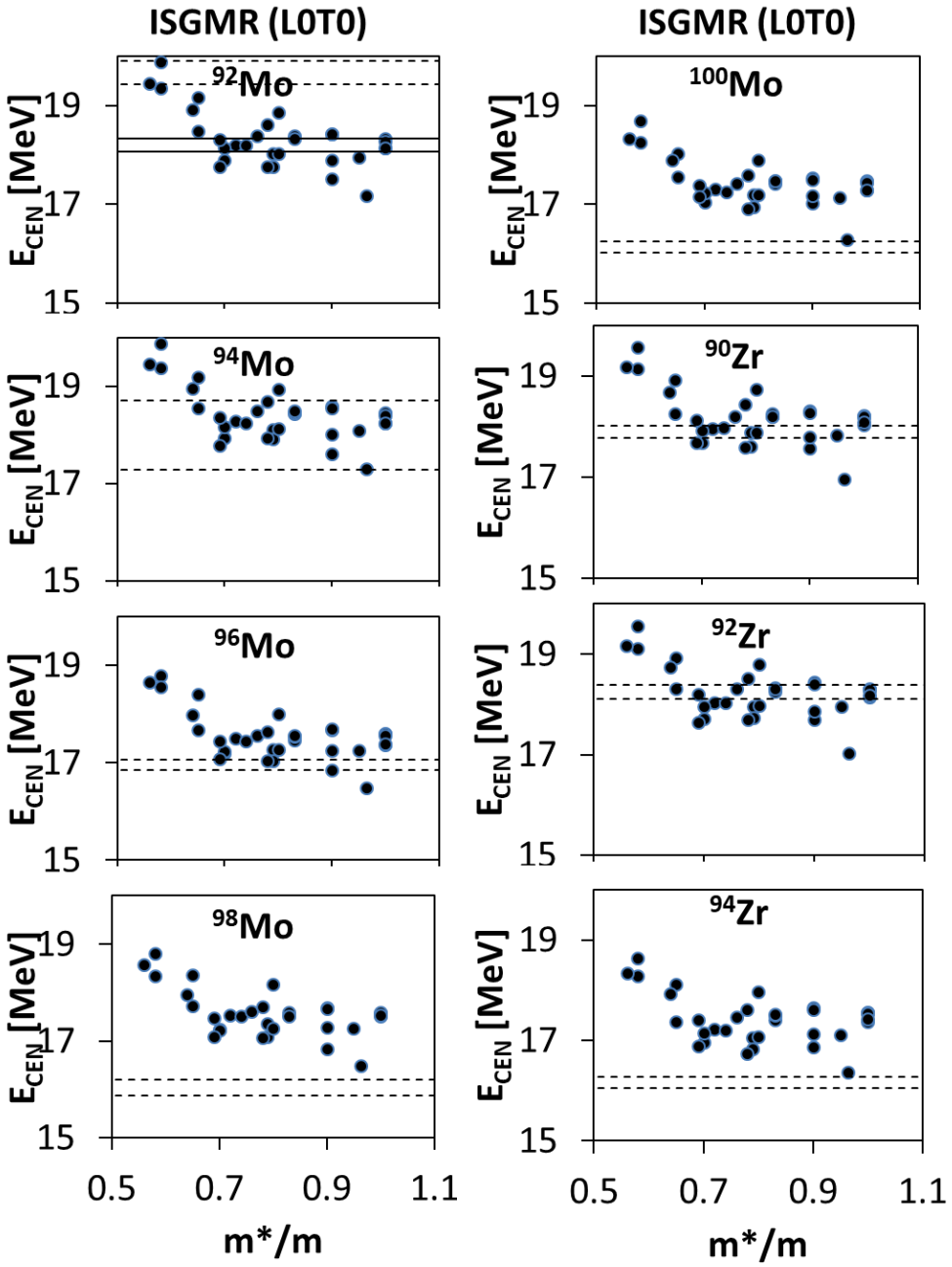

Figure 27 ISGMR E_{CEN} with m*/m in ^{92,94,96,98,100}Mo and ^{90,92,94}Zr. Like Figure 26 but for the ISGMR centroid energy plotted with the effective mass. A weak correlation is obtained between the calculated values of E_{CEN} and m*/m, with a Pearson linear correlation coefficient C ~ -0.51.

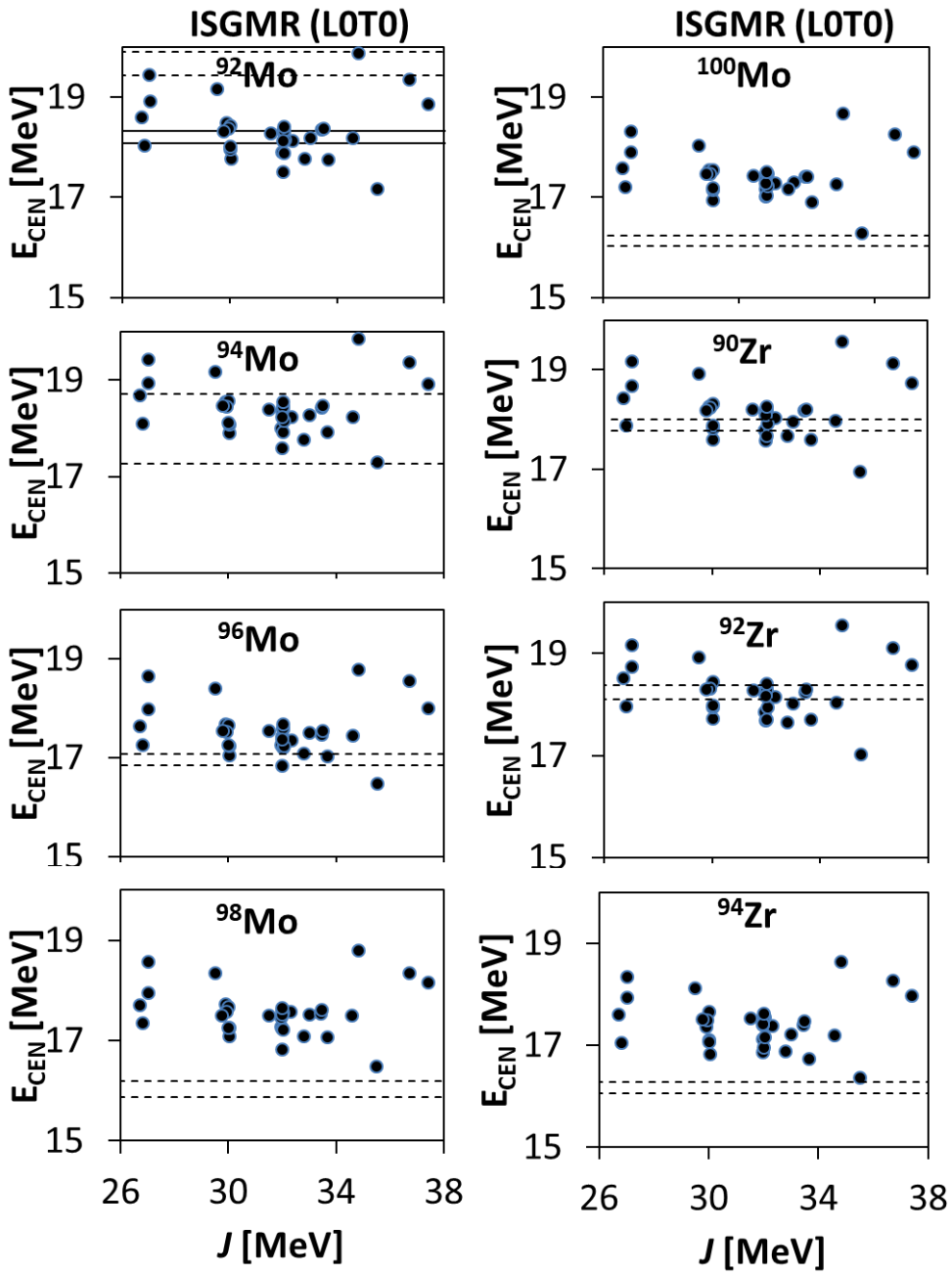

Figure 28 ISGMR E_{CEN} with J in ^{92,94,96,98,100}Mo and ^{90,92,94}Zr. Like Figure 26 but for the ISGMR centroid energy plotted with the symmetry energy at saturation density. No correlation is obtained between the calculated values of E_{CEN} and J, with a Pearson linear correlation coefficient C ~ -0.05.

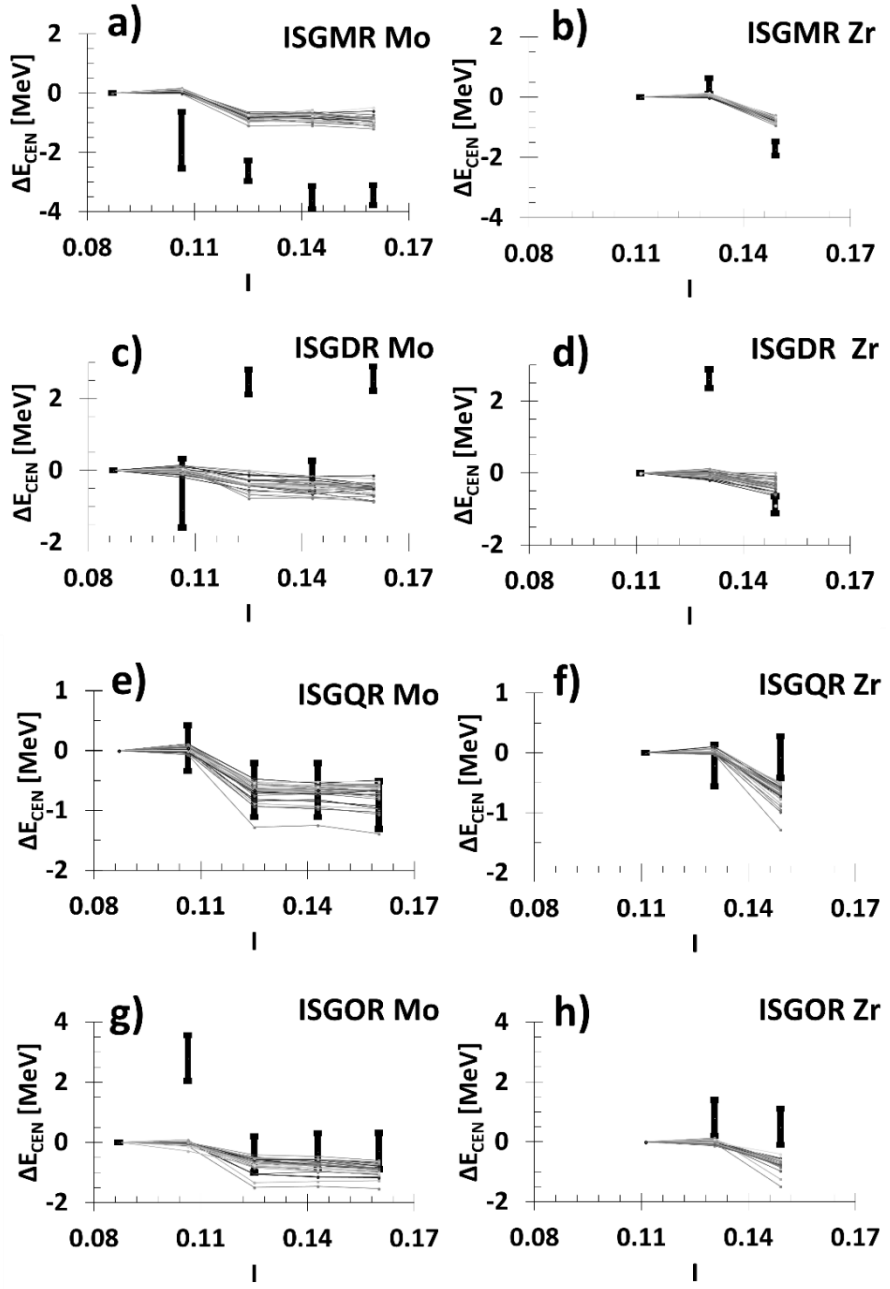

Figure 29 Isoscalar E_{CEN} overview in ^{92,94,96,98,100}Mo and ^{90,92,94}Zr. The difference between the centroid energy [MeV] (calculated as $E_{CEN}(^{92}Mo)$ - $E_{CEN}(^{92,94,96,98,100}Mo)$ and $E_{CEN}(^{90}Zr)$ – $E_{CEN}(^{90,92,94}Zr)$ in the left and right figures, respectively) is plotted against the asymmetry coefficient I = (N-Z)/A of each isotope, for the isoscalar giant resonances of multipolarity L = 0-3. The experimental error bar is shown by the solid vertical line, while the theoretical calculations are shown as dots connected by lines to guide the eye.

Isoscalar Giant Dipole Resonance

The centroid energy, E_{CEN}, of the ISGDR is plotted in Figure 30 as a function of the incompressibility coefficient, K_{NM}. One isotope is shown per panel with the appropriate experimental region marked by the dashed lines while the calculations are shown as solid circles. We obtained a weak correlation between the calculated values of E_{CEN} and K_{NM} (C ~ 0.53). We found a strong correlation between the calculated values of the centroid energy and the effective mass (C ~ -0.91) shown in Figure 31. However, different interactions reproduce different isotopes such that we can't decide on a best range of values for m*/m. In particular, the experimental centroid energy of ^{96,100}Mo and ^{92}Zr agrees with the centroid energies resulting from the interactions with the lowest value of m*/m ~ 0.6, while the E_{CEN} for the rest of the nuclei agrees with the result obtained from interactions with a value of m*/m = 0.8 - 1.0. Next, we plot the centroid energy as a function of the symmetry energy coefficient J in Figure 32. No correlation is found between the calculated values of E_{CEN} and J (C ~ -0.07). Similarly, no correlation is found with the first derivative of J, while a weak correlation is obtained between the calculated values of E_{CEN} and K_{sym} (C ~ 0.37). No correlation is found with other NM properties, see Table 10 for details. For completeness the calculated centroid energies of the ISGDR are shown in Table 23 of the Appendix.

In the case of the Mo isotopes, the value of E_{CEN} as a function of the asymmetry coefficient, I = (N-Z)/A, follows a seesaw in the experimental data while for the theoretical calculations we find that all the interactions considered predict a slow decrease as the neutron number is increased, as seen in Figure 29c. Similarly, for the

case of the Zr isotopes in Figure 29d, the experimental data shows an increase in the value of the centroid energy from ^{90}Zr to ^{92}Zr but a decrease from ^{90}Zr to ^{94}Zr. Conversely, the 33 interactions resulted in a slow decrease in the value of E_{CEN} as neutrons are added to ^{90}Zr, as was the case for Mo isotopes. These experimental fluctuations where not seen for the wide range of spherical nuclei considered in Chapter III.

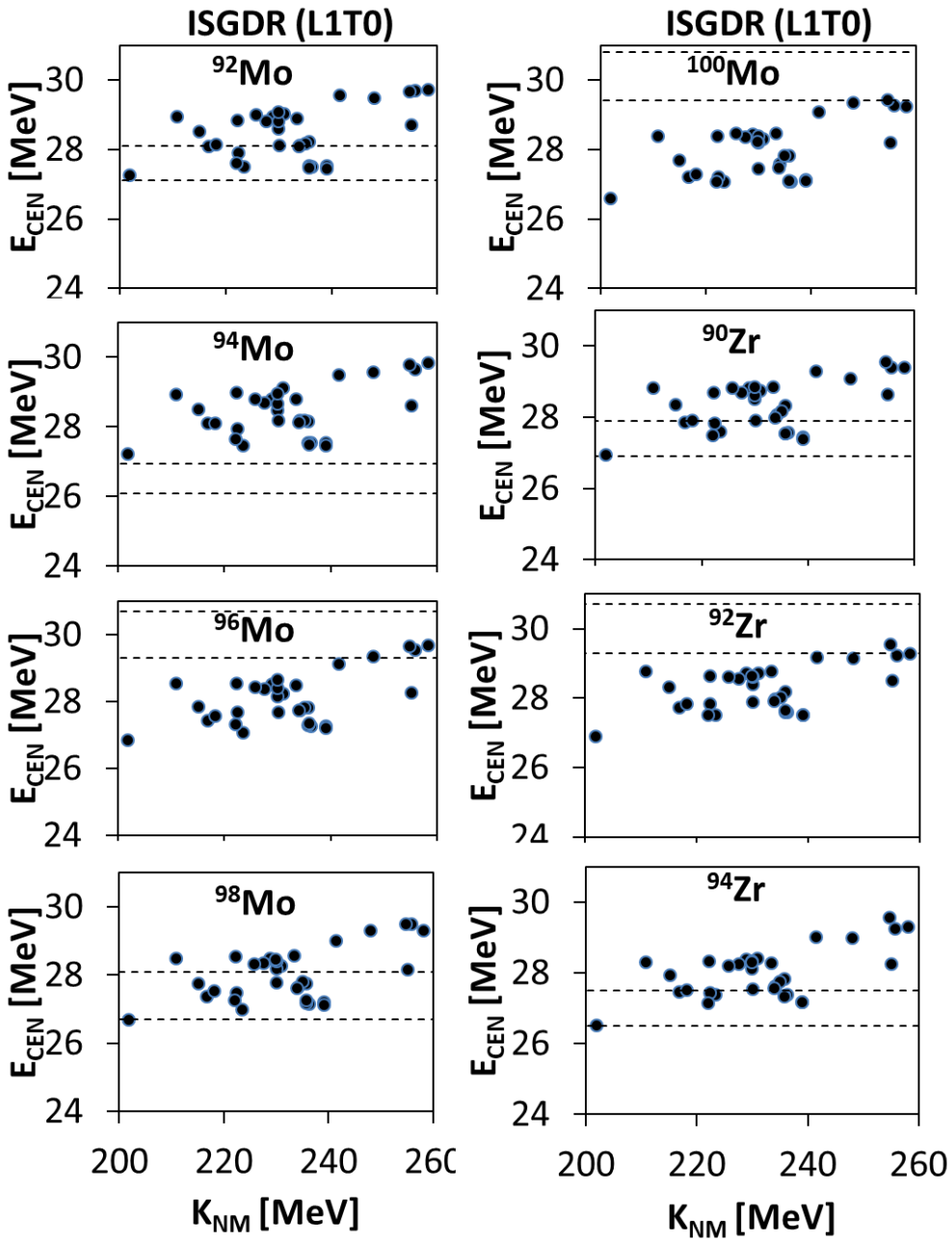

Figure 30 ISGDR E_{CEN} with K_{NM} in ^{92,94,96,98,100}Mo and ^{90,92,94}Zr. Similar to Figure 26 but for the ISGDR centroid energy plotted with the incompressibility coefficient. A weak correlation is obtained between the calculated values of E_{CEN} and K_{NM}, with a Pearson linear correlation coefficient C ~ 0.53.

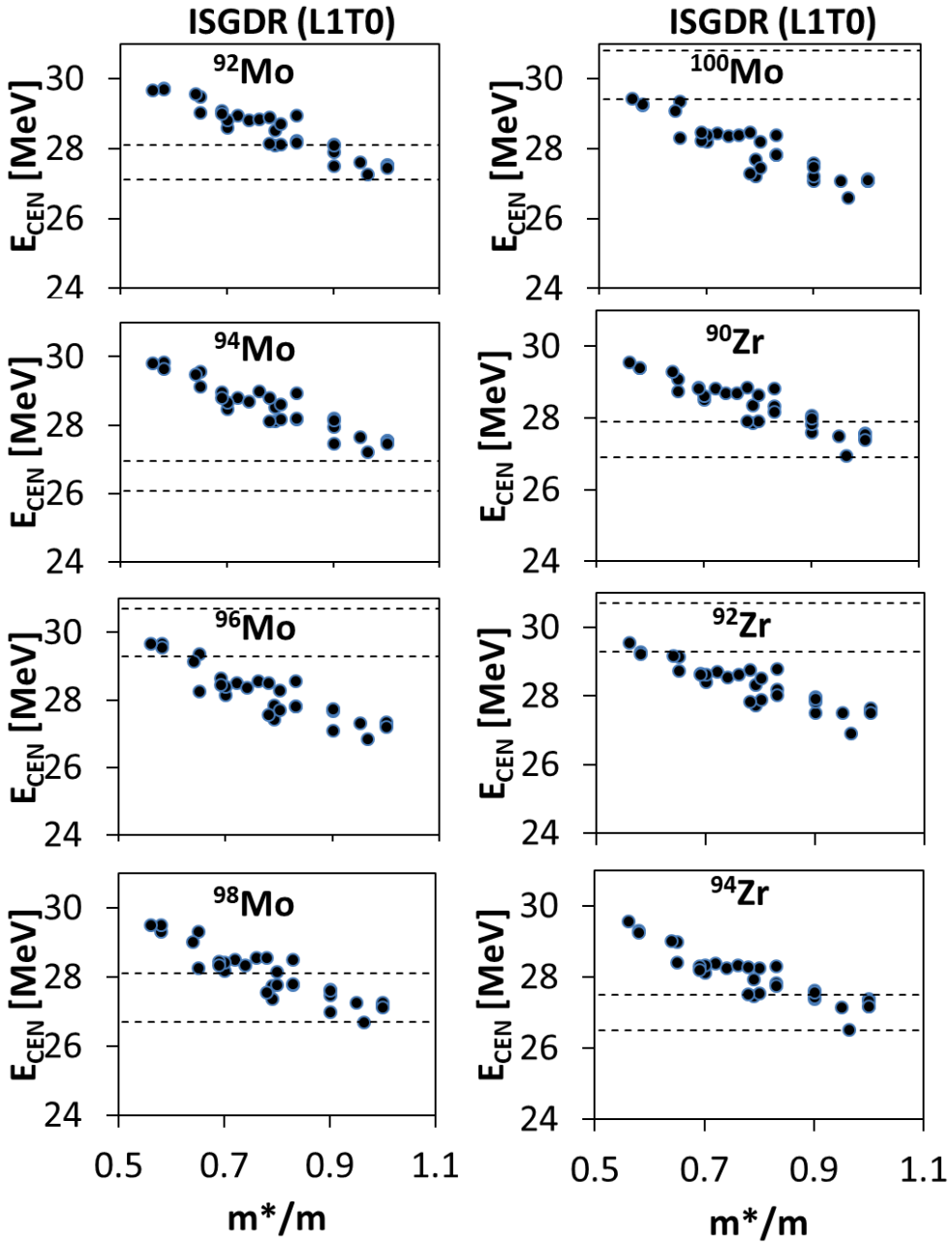

Figure 31 ISGDR E_{CEN} with m*/m in ^{92,94,96,98,100}Mo and ^{90,92,94}Zr. Like Figure 26 but for the ISGDR centroid energy plotted with the effective mass. A strong correlation is obtained between the calculated values of E_{CEN} and m*/m, with a Pearson linear correlation coefficient C ~ -0.91.

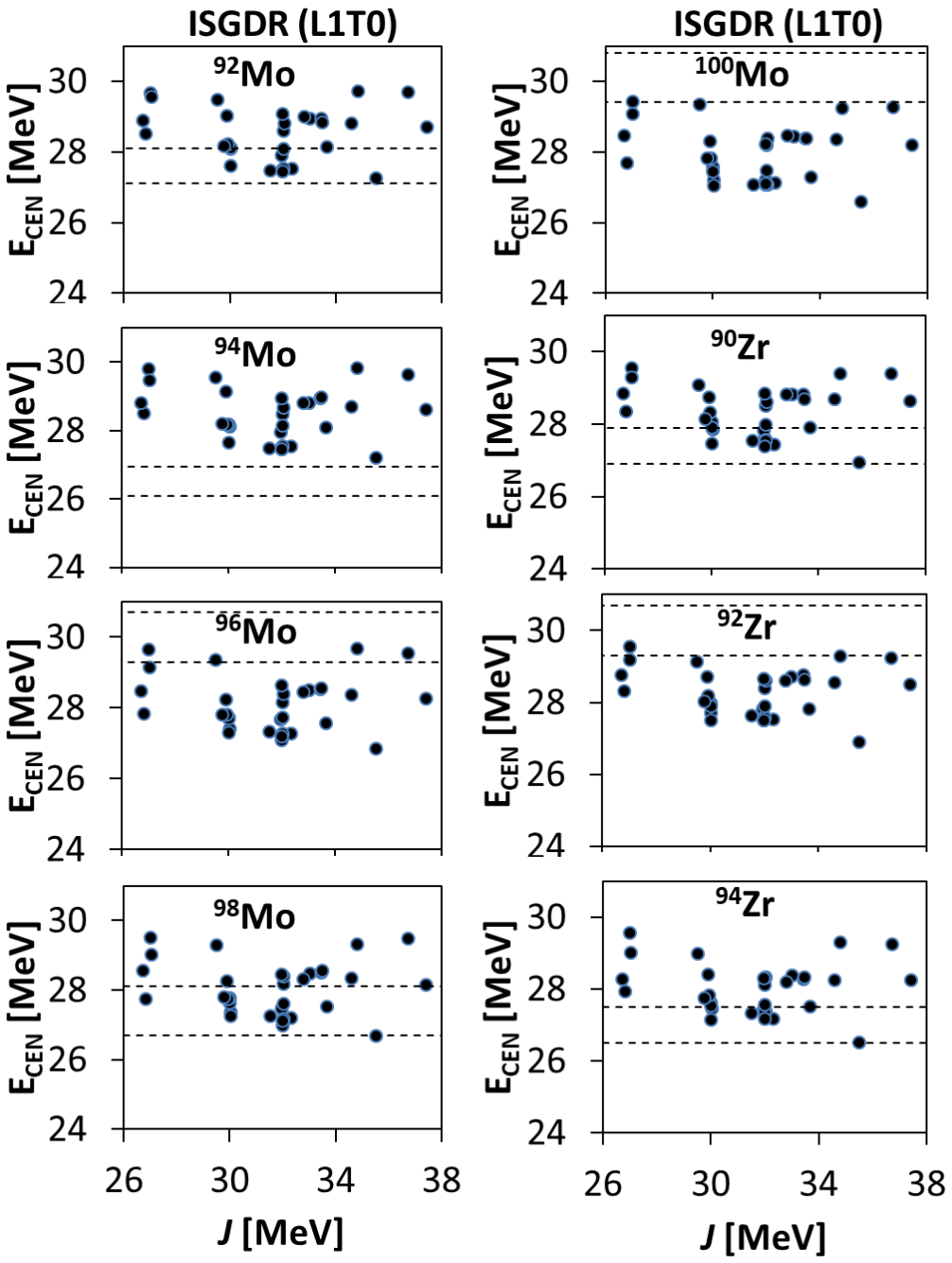

Figure 32 ISGDR E_{CEN} with J in ^{92,94,96,98,100}Mo and ^{90,92,94}Zr. Like Figure 26 but for the ISGDR centroid energy plotted with the symmetry energy at saturation density. No correlation is obtained between the calculated values of E_{CEN} and J, with a Pearson linear correlation coefficient C ~ -0.07.

Isoscalar Giant Quadrupole Resonance

The centroid energy, E_{CEN}, of the ISGQR is shown in Figure 33 as function of the nucleon effective mass, m*/m. We obtained strong correlation (C ~ -0.96) between the calculated values of E_{CEN} and m*/m, in agreement with our findings in Chapter III. We found good agreement with the data for interactions associated with an effective mass in the range 0.8 - 0.9, in agreement with Chapter III. In particular, we found that the Mo isotopes with more neutrons prefer a slightly higher effective mass while for the Zr isotopes we found the opposite trend. In the case of the incompressibility coefficient, K_{NM}, we show in Figure 34 a weak correlation with the calculated E_{CEN} (C ~ 0.37). For the symmetry energy coefficients of J and L we obtained no correlation with the E_{CEN}, while a weak correlation was found with K_{sym} (C ~ 0.41). Details of correlations with other NM properties are shown in Table 10. The calculated values of the centroid energies of the ISGQR are shown in Table 24 of the Appendix.

The difference in the centroid energy $\Delta E_{CEN} = E_{CEN}(I_0)-E_{CEN}(I)$ is plotted as a function of isospin in Figure 29 e and f for the Mo and Zr isotopes, respectively. For both sets of isotopes we obtained a clear decrease in the value of the centroid energy as the neutron number increases for both theoretical and experimental results. We note that the centroid energy of the isotope of ^{94}Zr breaks this trend in the experimental case where it is obtained above that of its neighboring nuclei, an effect not reproduced by any of the interactions.

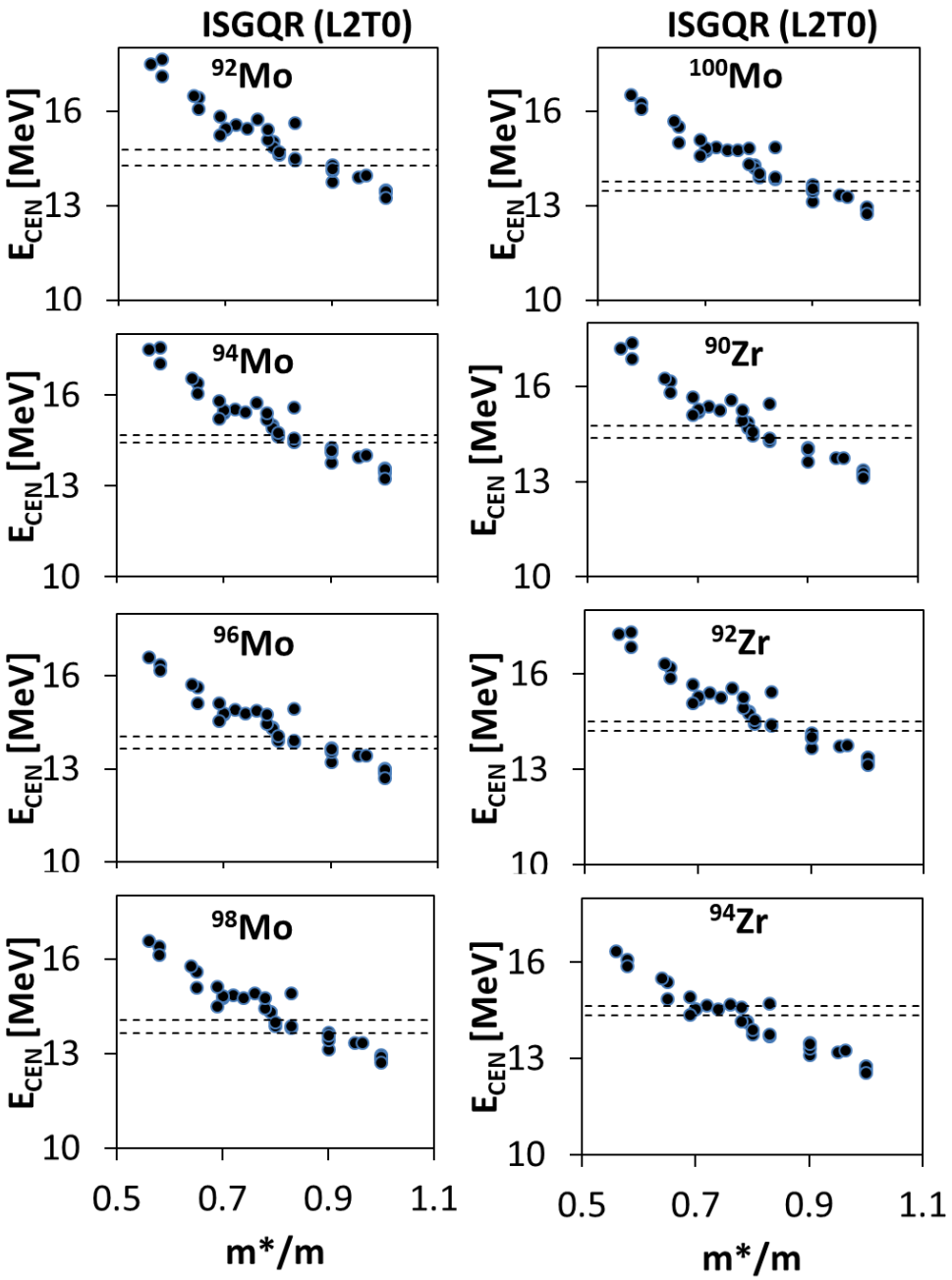

Figure 33 ISGQR E_{CEN} with m*/m in ^{92,94,96,98,100}Mo and ^{90,92,94}Zr. Similar to Figure 26 but for the ISGQR centroid energy plotted with the effective mass. A strong correlation is obtained between the calculated values of E_{CEN} and m*/m, with a Pearson linear correlation coefficient C ~ -0.96.

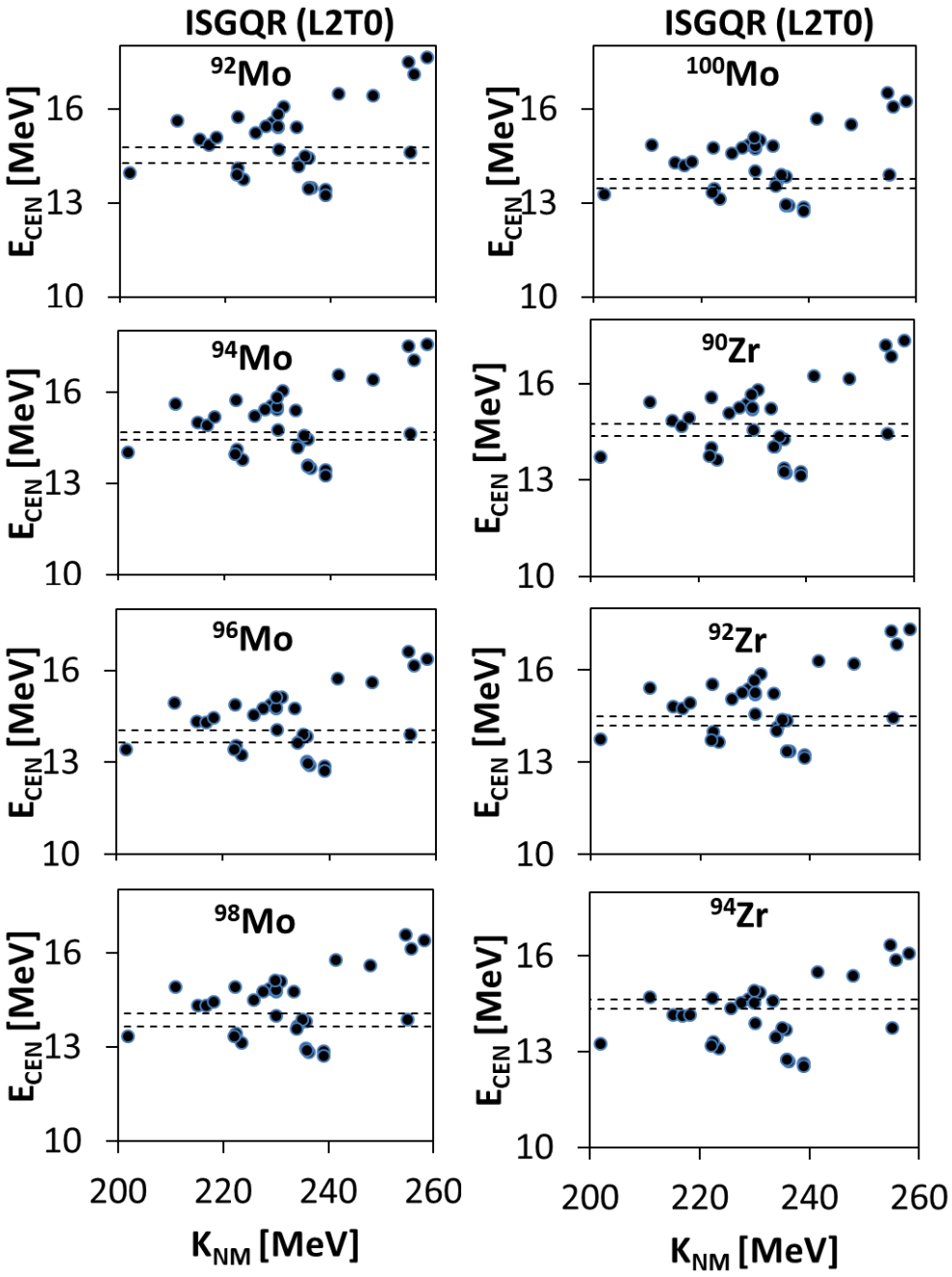

Figure 34 ISGQR E_{CEN} with K_{NM} in ^{92,94,96,98,100}Mo and ^{90,92,94}Zr. Like Figure 26 but for the ISGQR centroid energy plotted with the incompressibility coefficient. A weak correlation is obtained between the calculated values of E_{CEN} and K_{NM}, with a Pearson linear correlation coefficient C ~ 0.37.

Isoscalar Giant Octupole Resonance

In Figure 35 we show the centroid energy, E_{CEN}, of the ISGOR plotted with the effective mass, m*/m. We obtained a strong correlation (C ~ -0.98) between the calculated values of E_{CEN} and m*/m. As shown in the figure, the calculated values are consistently above the experimental values, similar to what we obtained in Chapter III. We note that in the case of ^{92,94}Zr we found agreement with the experimental data for interactions associated with a large m*/m ~ 1 (mostly from the SkT series). In Figure 36 we plot the centroid energy as a function of the NM incompressibility coefficient, K_{NM}. We obtained a weak correlation (C ~ 0.39) between E_{CEN} and K_{NM}. For the symmetry energy coefficients J and L we found no correlation with the calculated centroid energy, and weak correlation with K_{sym} (C ~ 0.38). A complete list of the Pearson linear correlation coefficients between E_{CEN} and NM properties is shown in Table 10. The calculated values of the centroid energies of the ISGOR are shown in Table 25 of the Appendix.

The difference in the centroid energy $\Delta E_{CEN} = E_{CEN}(I_0)-E_{CEN}(I)$ is plotted as a function of isospin in Figure 29g and h for the Mo and Zr isotopes, respectively. In both cases we obtained a slow decreasing trend for the values of E_{CEN} as the neutron numbers increases for the theoretical results. For the experiment instead, ^{94}Mo breaks this pattern and was measured 3 MeV above the other isotopes. Conversely to the calculated values of the centroid energy for the Zr isotopes, the experimental result seems to trend upward as neutron number is increased.

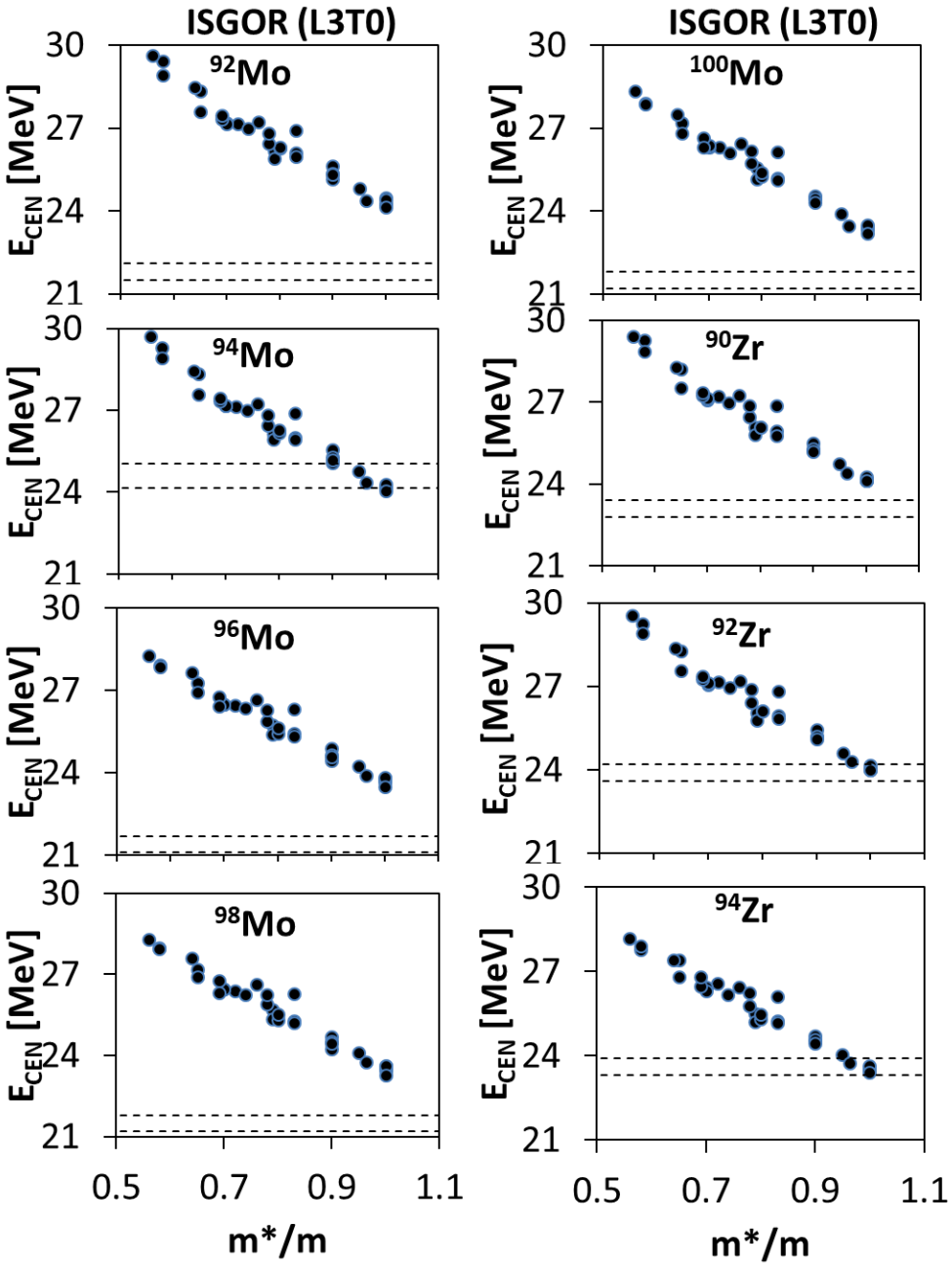

Figure 35 ISGOR E_{CEN} with m*/m in ^{92,94,96,98,100}Mo and ^{90,92,94}Zr. Similar to Figure 26 but for the ISGOR centroid energy as a function of the effective mass. A strong correlation is obtained between the calculated values of E_{CEN} and m*/m, with a Pearson linear correlation coefficient C ~ -0.98.

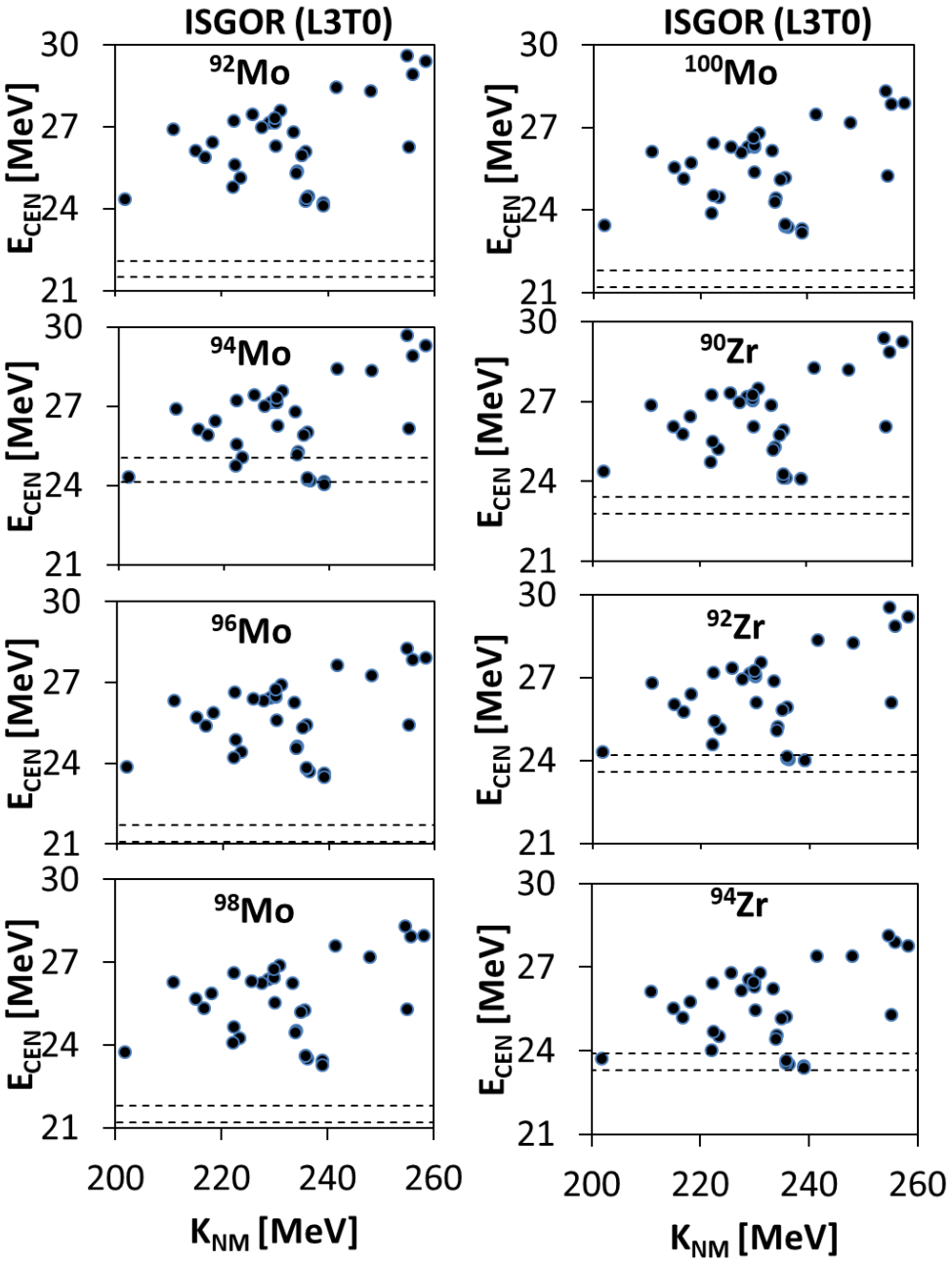

Figure 36 ISGOR E_{CEN} with K_{NM} in ^{92,94,96,98,100}Mo and ^{90,92,94}Zr. Similar to Figure 26 but for the ISGOR centroid energy plotted with the incompressibility coefficient. A weak correlation is obtained between the calculated values of E_{CEN} and K_{NM}, with a Pearson linear correlation coefficient C ~ 0.38.

Isovector Giant Monopole Resonance

We plot the centroid energy, E_{CEN}, of the IVGMR, a compression mode, as a function of the incompressibility coefficient of nuclear matter, K_{NM}, in Figure 37. The calculations are shown by the solid circles, but no experimental data is available. No correlation is found between the calculated values of E_{CEN} and K_{NM} with a value of C ~ 0.25. In Figure 38 we plot the centroid energy as a function of the effective mass, m*/m. We obtained a medium correlation between E_{CEN} and m*/m (C ~ -0.71). Next, we show the centroid energy as a function of the symmetry energy coefficient, J, in Figure 39. No correlation is found between the calculated values of E_{CEN} and J (C ~ -0.24). Similarly, no correlation is found between the centroid energy and the first or the second derivative of the symmetry energy (C < 0.10 in both cases). We show the IVGMR centroid energy as a function of the IVGDR energy weighted sum rule enhancement coefficient, κ, in Figure 40. We obtained a strong correlation between the values of E_{CEN} and κ (C ~ 0.85). In Figure 41a and 41b we plot the centroid energies as a function of the asymmetry coefficient, I, for the two sets of isotopes. As can be seen in the figures, the theory predicts a decreasing value of E_{CEN} as the systems become heavier and more neutron rich. For completeness we present the calculated values of E_{CEN} for the isovector giant monopole resonance in Table 26 of the Appendix.

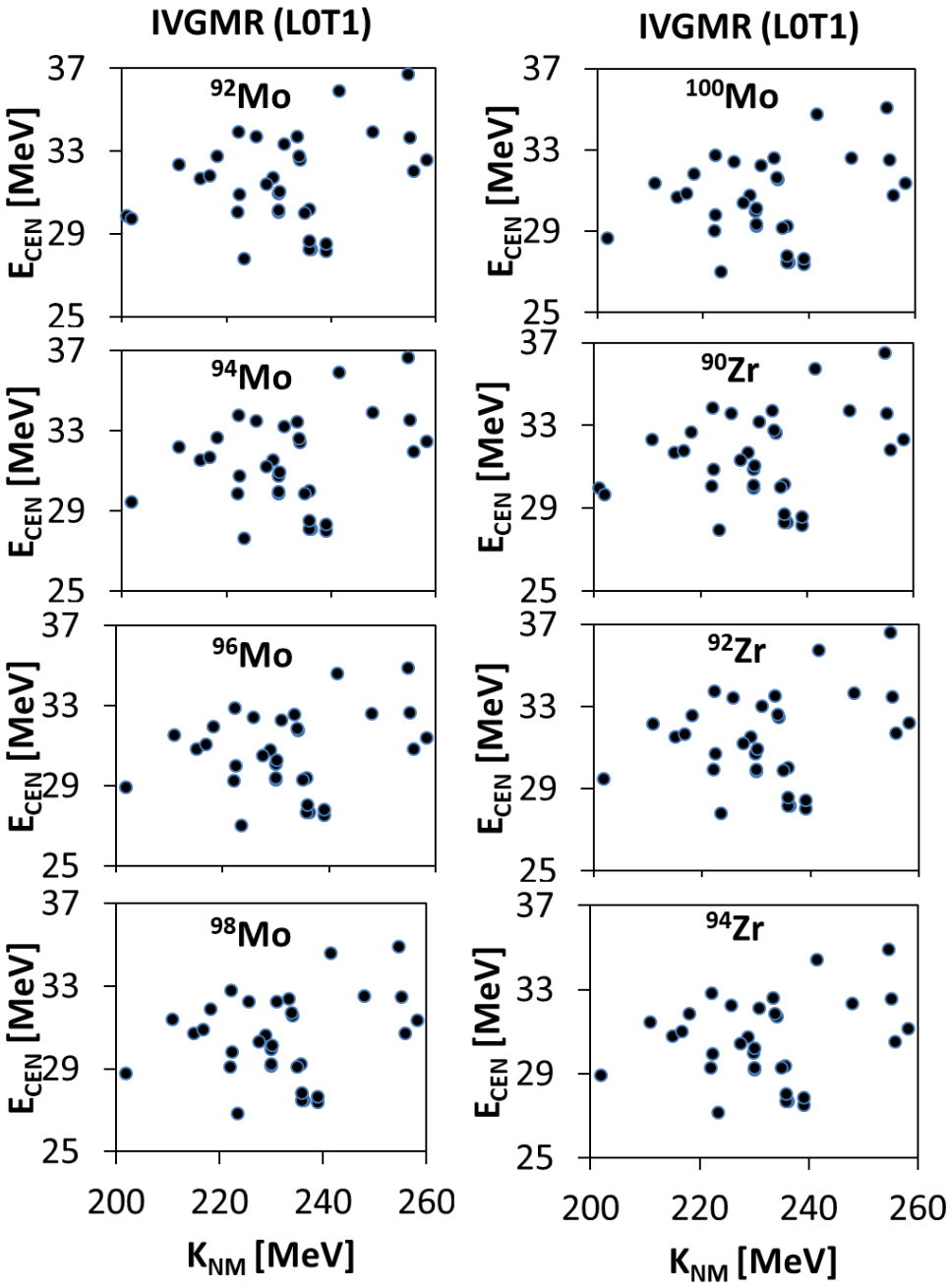

Figure 37 IVGMR E_{CEN} with K_{NM} in ^{92,94,96,98,100}Mo and ^{90,92,94}Zr. Similar to Figure 26 but for the IVGMR centroid energy as a function of the incompressibility coefficient. No correlation is obtained between the calculated values of E_{CEN} and K_{NM}, with a Pearson linear correlation coefficient C ~ 0.25.

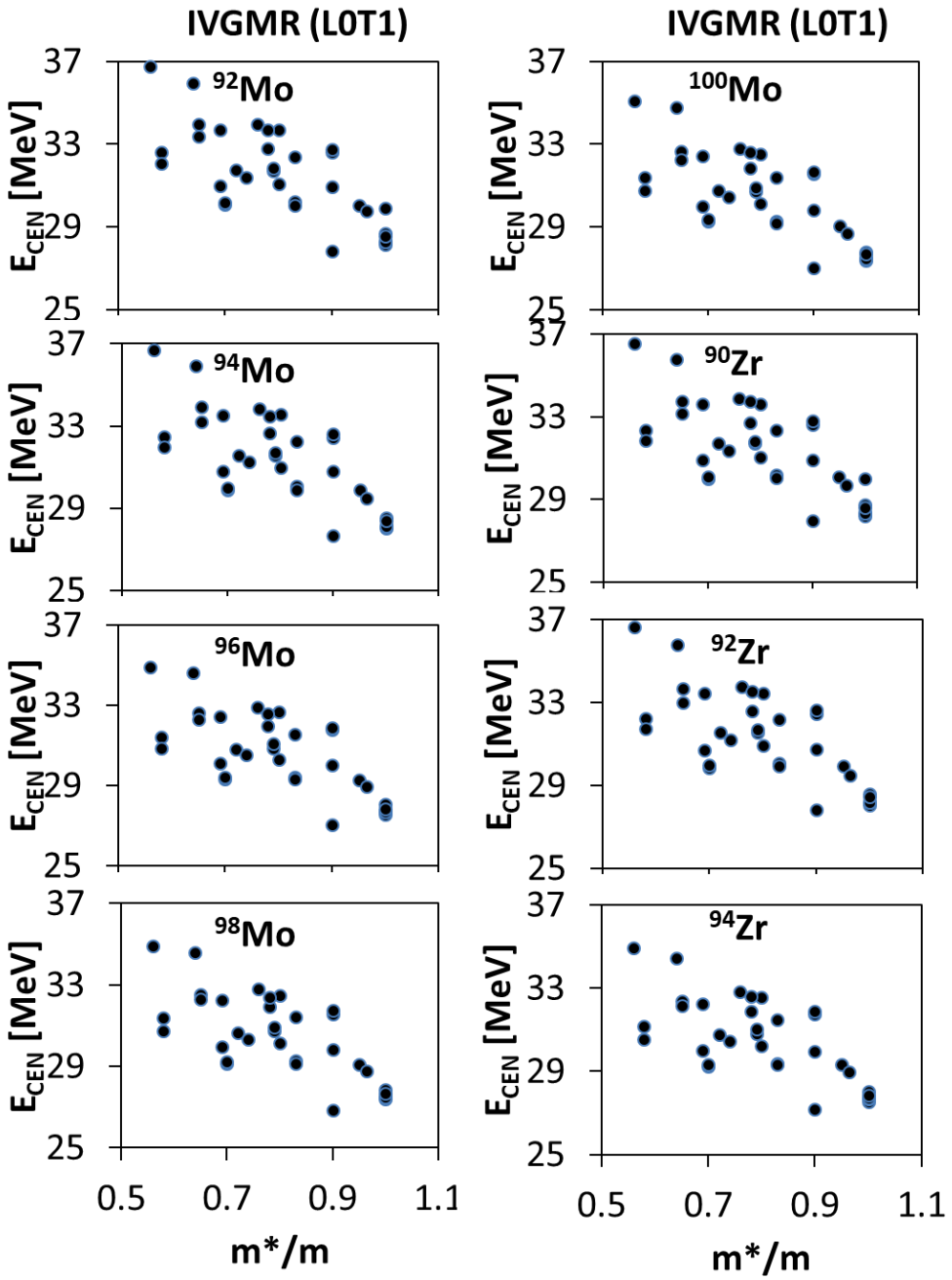

Figure 38 IVGMR E_{CEN} with m*/m in ^{92,94,96,98,100}Mo and ^{90,92,94}Zr. Similar to Figure 26 but for the IVGMR centroid energy as a function of the effective mass. A medium correlation is obtained between the calculated values of E_{CEN} and m*/m, with a Pearson linear correlation coefficient C ~ -0.71.

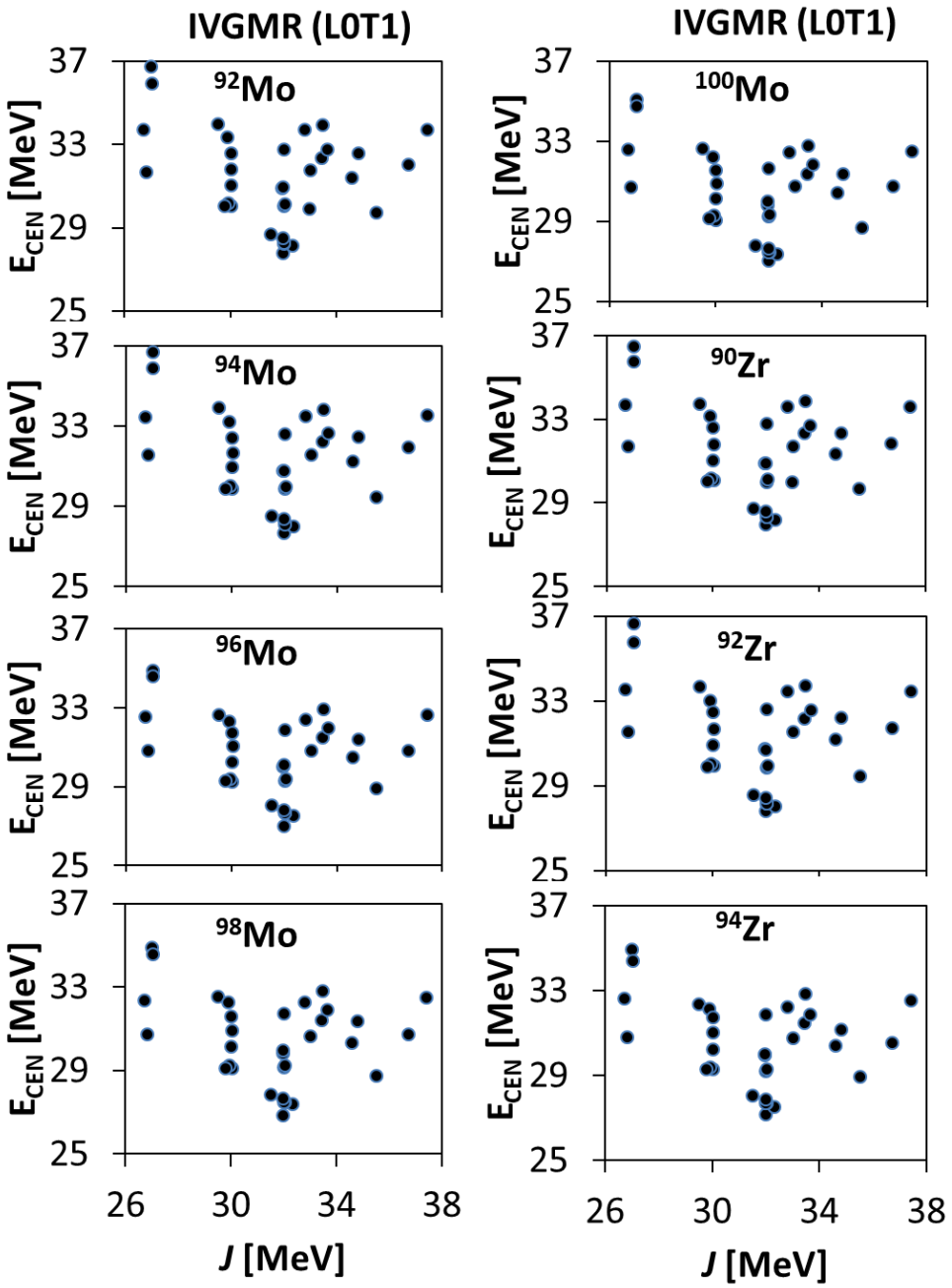

Figure 39 IVGMR E_{CEN} with J in ^{92,94,96,98,100}Mo and ^{90,92,94}Zr. Similar to Figure 26 but for the IVGMR centroid energy as a function of the symmetry energy at saturation density. No correlation is obtained between the calculated values of E_{CEN} and J, with a Pearson linear correlation coefficient C ~ -0.24.

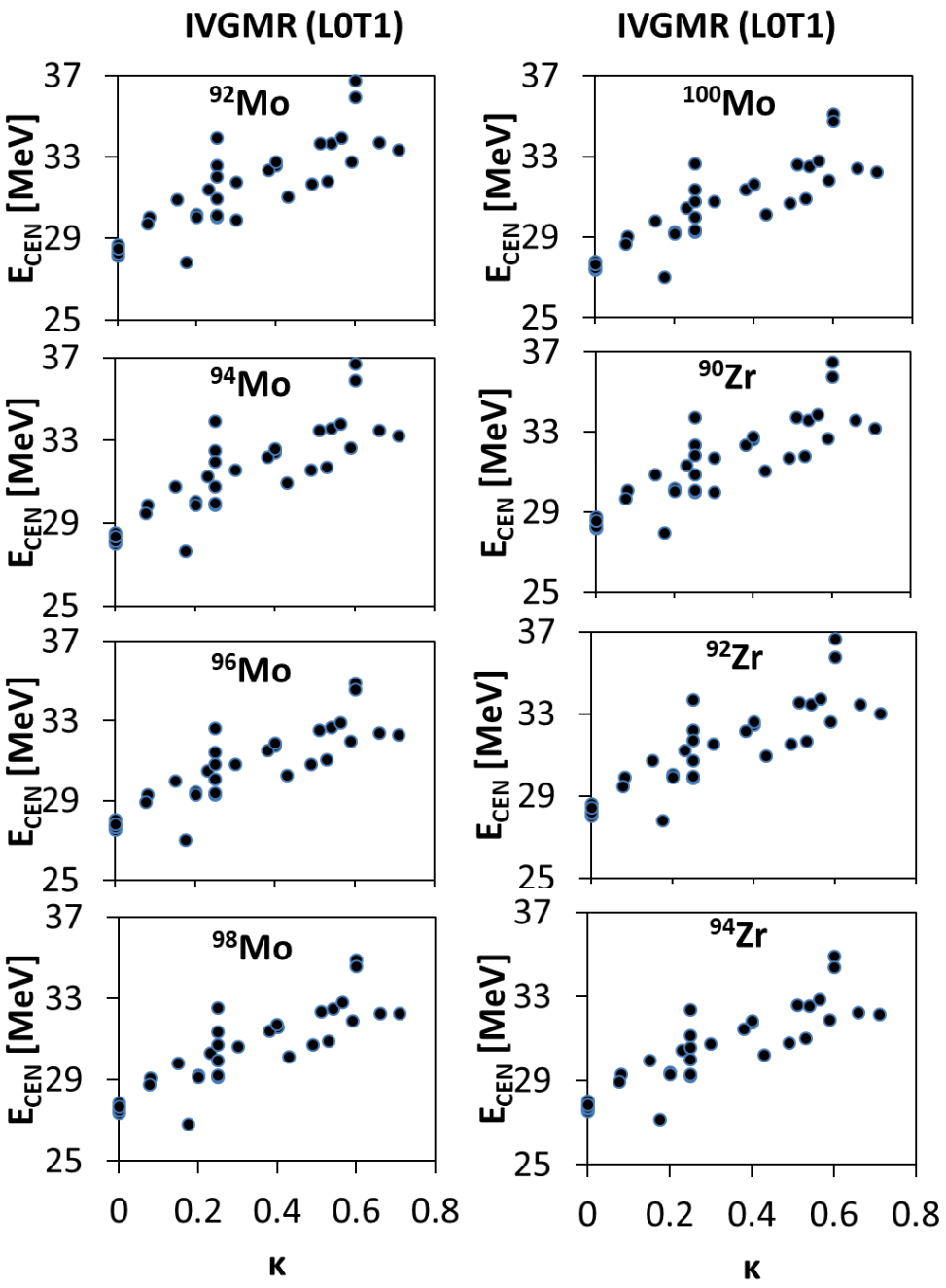

Figure 40 IVGMR E_{CEN} with κ in ^{92,94,96,98,100}Mo and ^{90,92,94}Zr. Similar to Figure 26 but for the IVGMR centroid energy as a function of the enhancement coefficient of the EWSR for the IVGDR. A strong correlation is obtained between the calculated values of E_{CEN} and κ, with a Pearson linear correlation coefficient C ~ 0.85.

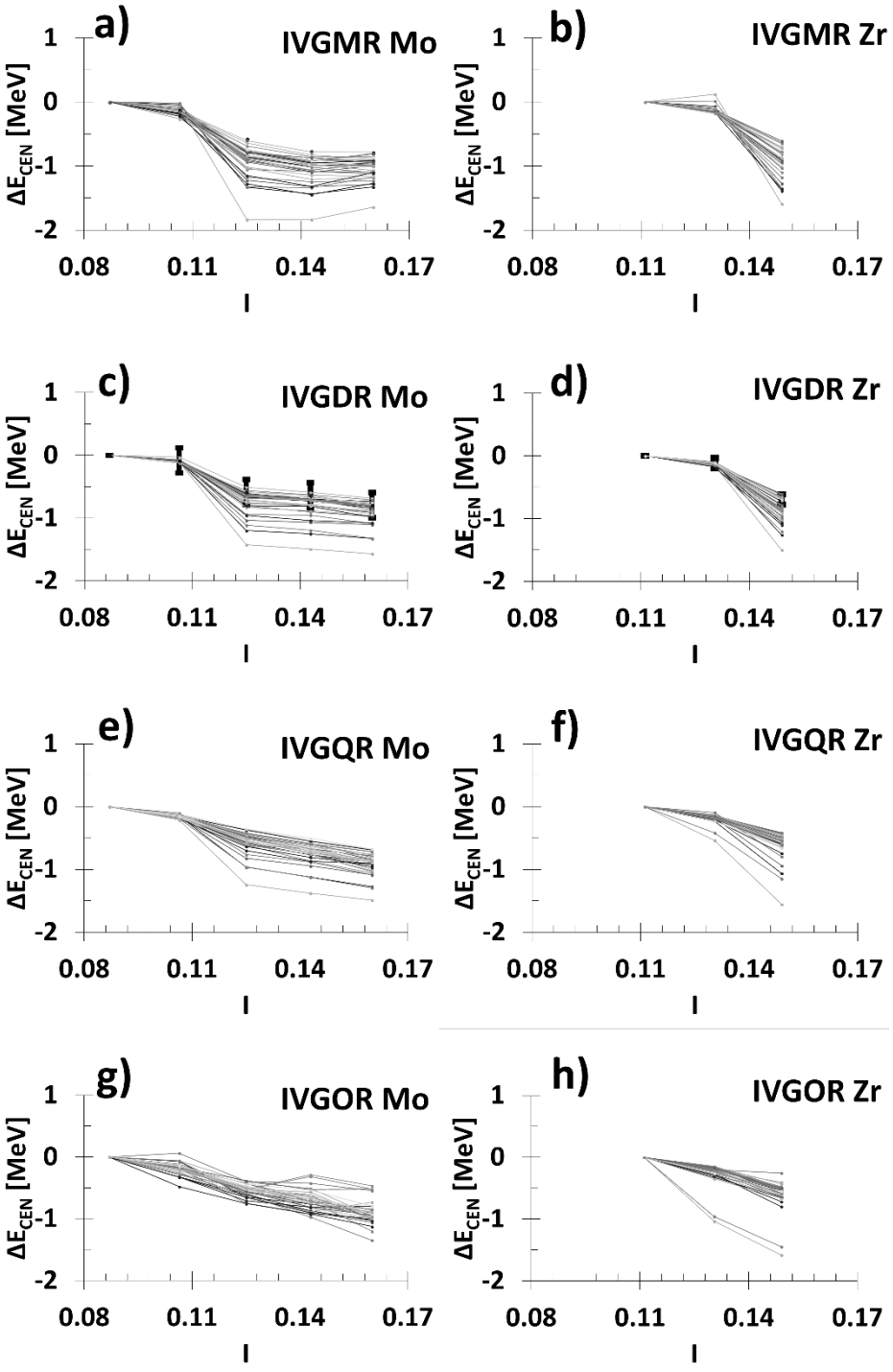

Figure 41 Isovector E_{CEN} overview in ^{92,94,96,98,100}Mo and ^{90,92,94}Zr. Similar to Figure 29 but for the isovector resonances. Experimental data is available for the IVGDR only.

Isovector Giant Dipole Resonance

The centroid energy, E_{CEN}, of the IVGDR is plotted as a function of the symmetry energy coefficient, J, in Figure 42. The experimental uncertainties are delimited by dashed lines and were obtained from Ref. [81] for Mo and Ref. [69] for Zr. We find that for all the nuclei the interactions considered agree with the experimental result and are at most within a few MeV. We note that although this is an isovector resonance we find only weak correlation between the calculated values of E_{CEN} and J (C ~ -0.35), as well as for its first derivative *L* (C ~ -0.39) while no correlation is found for the second derivative K_{sym} (C ~ -0.29). This agrees with our findings from Chapter III. We plot in Figure 43 the centroid energy as a function of the enhancement coefficient, κ, of the energy weighted sum rule for the IVGDR. A strong correlation is obtained between the calculated values of E_{CEN} and κ (C ~ 0.85). We see from the figure that interactions with κ = 0.25 - 0.7 best reproduce most of the experimental data, also in good agreement with Chapter III. Next, we show in Figure 44 the centroid energy plotted as a function of the effective mass, m*/m, for which we obtain a medium correlation (C ~ -0.61) due mostly to the correlation between κ and m*/m, discussed previously. Lastly, we plot in Figure 41c and Figure 41d the centroid energies as a function of the asymmetry coefficient, I. We find that in both the theoretical and the experimental cases the centroid energy decreases as the asymmetry (and the mass) increases. For completeness we give the calculated values of the centroid energies of the IVGDR in Table 27 of the Appendix.

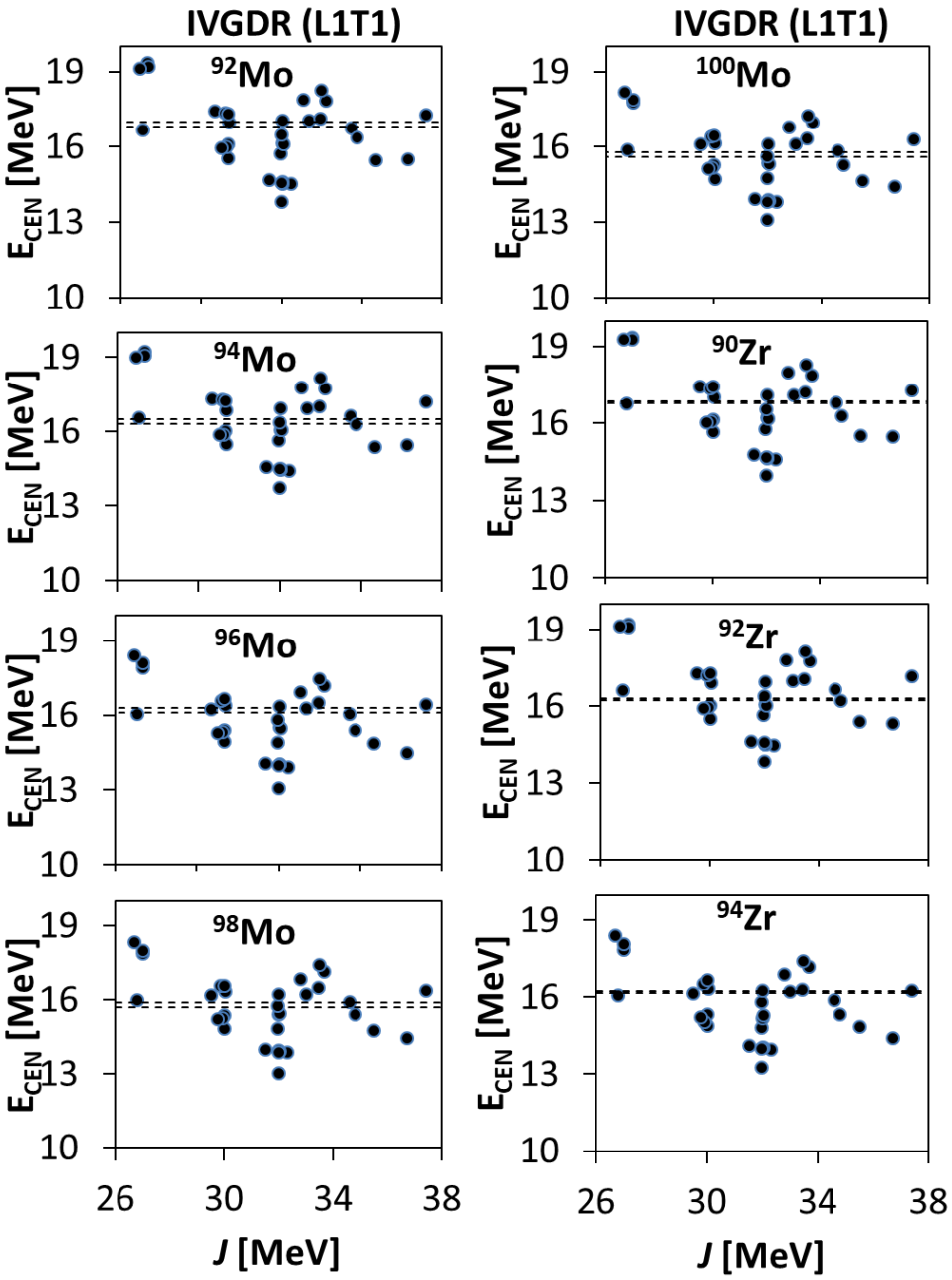

Figure 42 IVGDR E_{CEN} with J in ^{92,94,96,98,100}Mo and ^{90,92,94}Zr. Similar to Figure 26 but for the IVGDR centroid energy as a function of the symmetry energy at saturation density. No correlation is obtained between the calculated values of E_{CEN} and J, with a Pearson linear correlation coefficient C ~ -0.35.

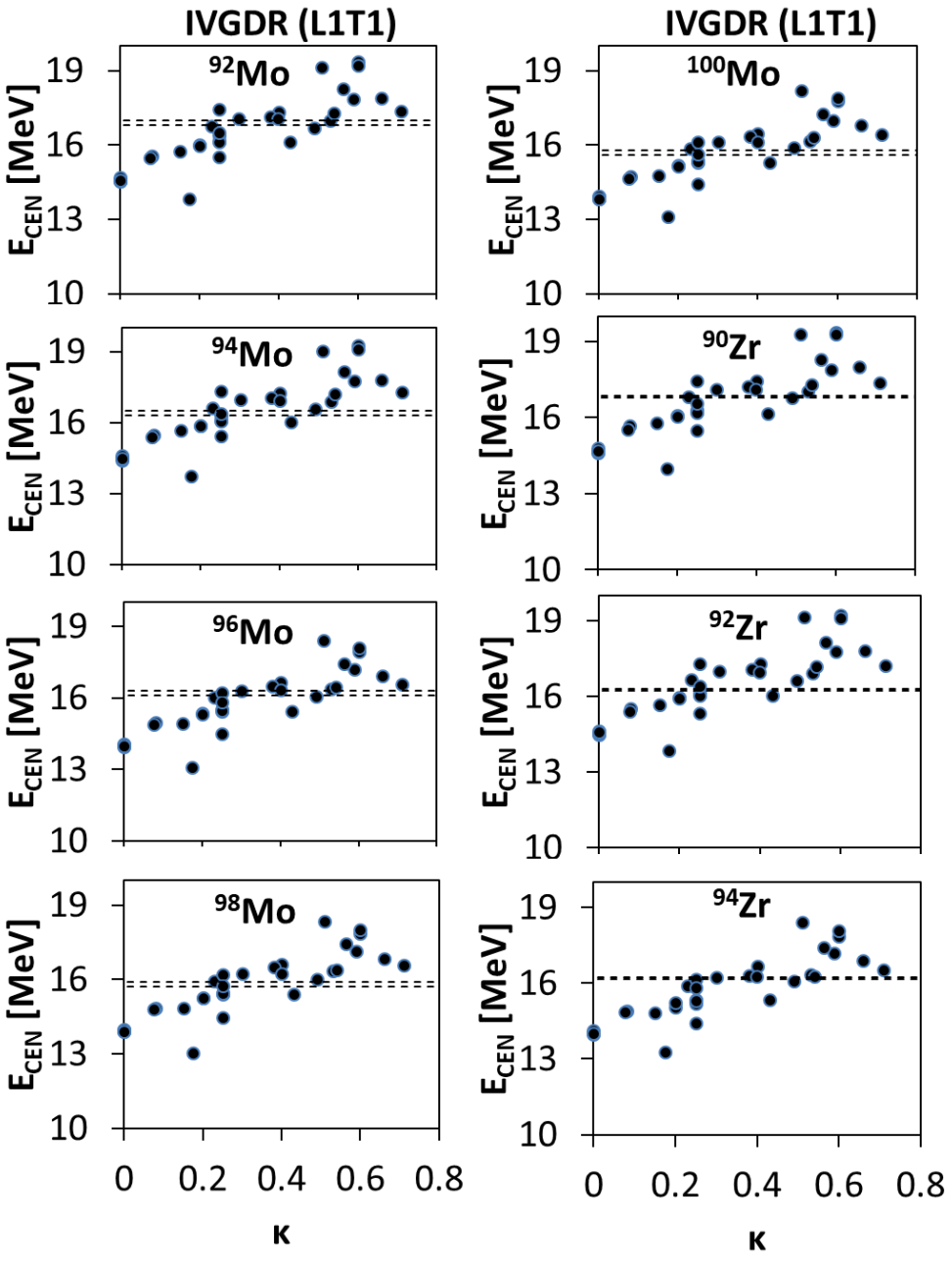

Figure 43 IVGDR E_{CEN} with κ in ^{92,94,96,98,100}Mo and ^{90,92,94}Zr. Similar to Figure 26 but for the IVGDR centroid energy as a function of the enhancement coefficient of the EWSR for the IVGDR. A strong correlation is obtained between the calculated values of E_{CEN} and κ, with a Pearson linear correlation coefficient C ~ 0.85.

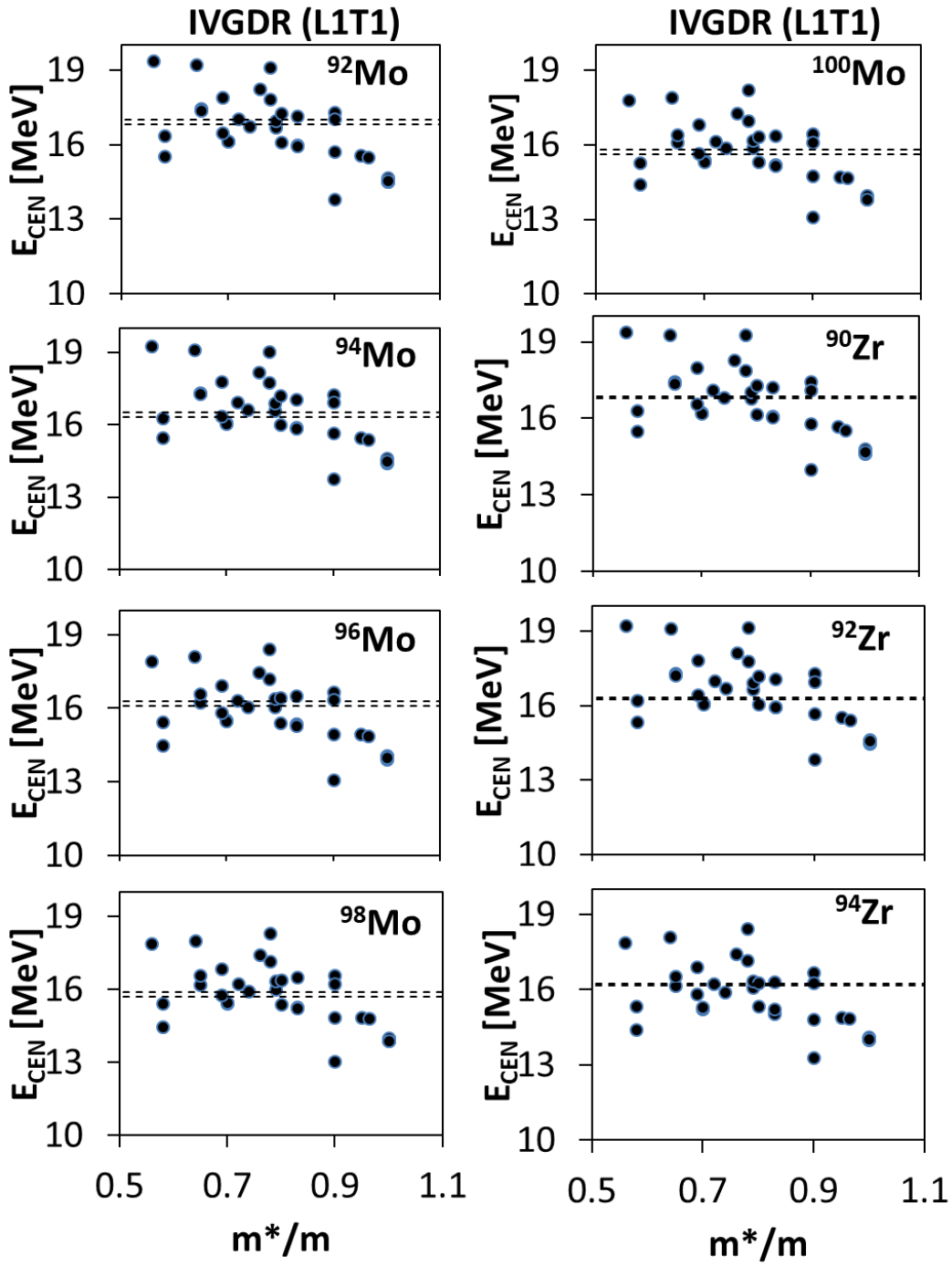

Figure 44 IVGDR E_{CEN} with m*/m in ^{92,94,96,98,100}Mo and ^{90,92,94}Zr. Similar to Figure 26 but for the IVGDR centroid energy as a function of the effective mass. A medium correlation is obtained between the calculated values of E_{CEN} and m*/m, with a Pearson linear correlation coefficient C ~ -0.61.

Isovector Giant Quadrupole Resonance

The centroid energy, E_{CEN}, of the IVGQR is plotted in Figure 45 as a function of the symmetry energy coefficient, J. No experimental data is available for this resonance. There is no correlation between the calculated values of E_{CEN} and J (C ~ -0.34). Similarly, no correlation is obtained with the first or the second derivative of the symmetry energy (C ~ -0.27 and -0.11, respectively). Next, we show in Figure 46 the centroid energy as a function of the enhancement coefficient for the EWSR of the IVGDR, κ, for which we obtained a strong correlation (C ~ 0.85). We also find a medium correlation between the calculated values of the centroid energy and the effective mass, see Figure 47 (C ~ -0.77). We study the centroid energy as a function of the asymmetry coefficient in Figure 41e and Figure 41f. As expected, we obtain a decreasing value of the centroid energy as the asymmetry (and the mass) increases. The calculated values of the centroid energies of the IVGQR are given in Table 28 of the Appendix.

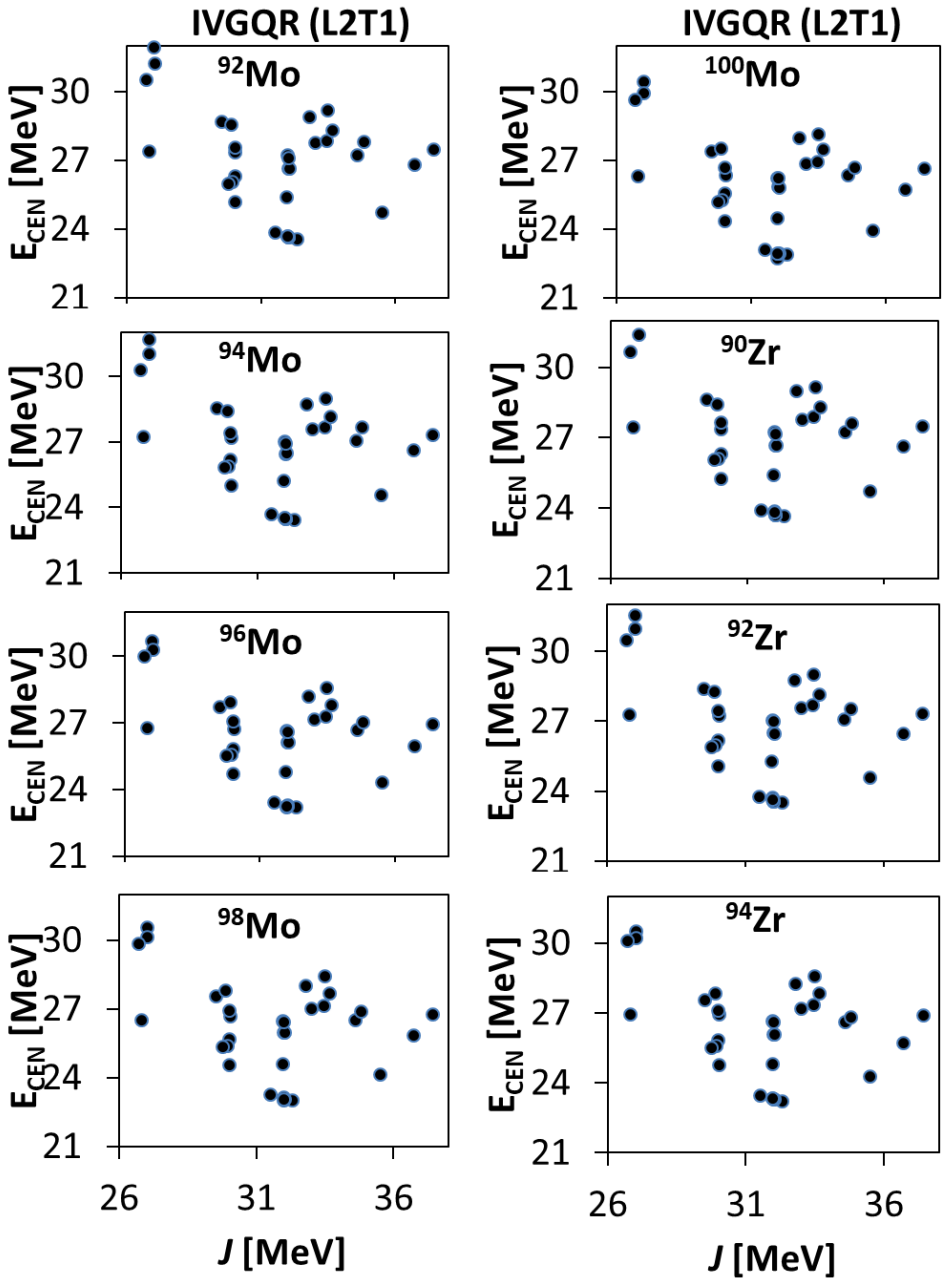

Figure 45 IVGQR E_{CEN} with J in ^{92,94,96,98,100}Mo and ^{90,92,94}Zr. Similar to Figure 26 but for the IVGQR centroid energy as a function of the symmetry energy at saturation density. No correlation is obtained between the calculated values of E_{CEN} and J, with a Pearson linear correlation coefficient C ~ -0.34.

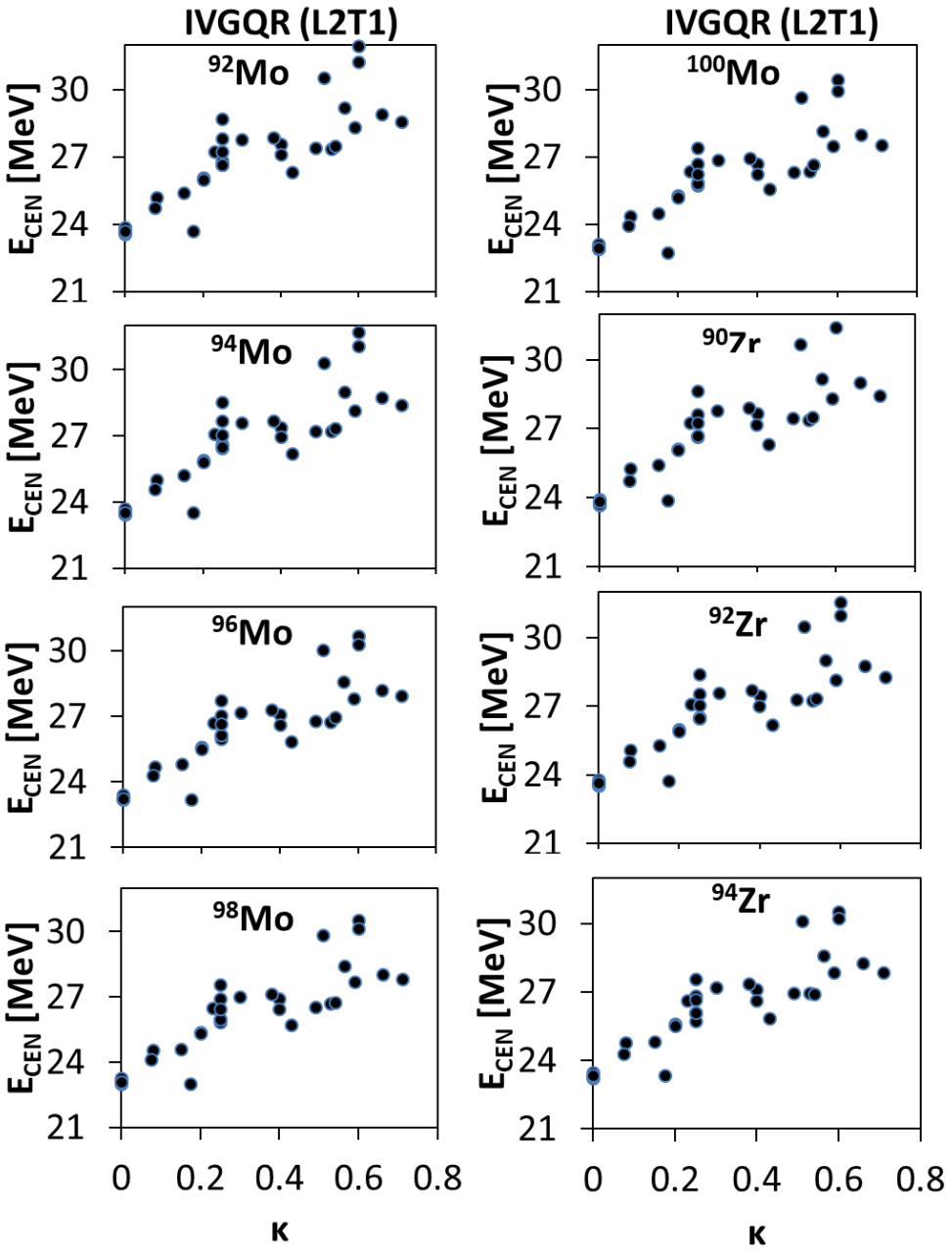

Figure 46 IVGQR E_{CEN} with κ in ^{92,94,96,98,100}Mo and ^{90,92,94}Zr. Similar to Figure 26 but for the IVGQR centroid energy as a function of the enhancement coefficient of the EWSR for the IVGDR. A strong correlation is obtained between the calculated values of E_{CEN} and κ, with a Pearson linear correlation coefficient C ~ 0.85.

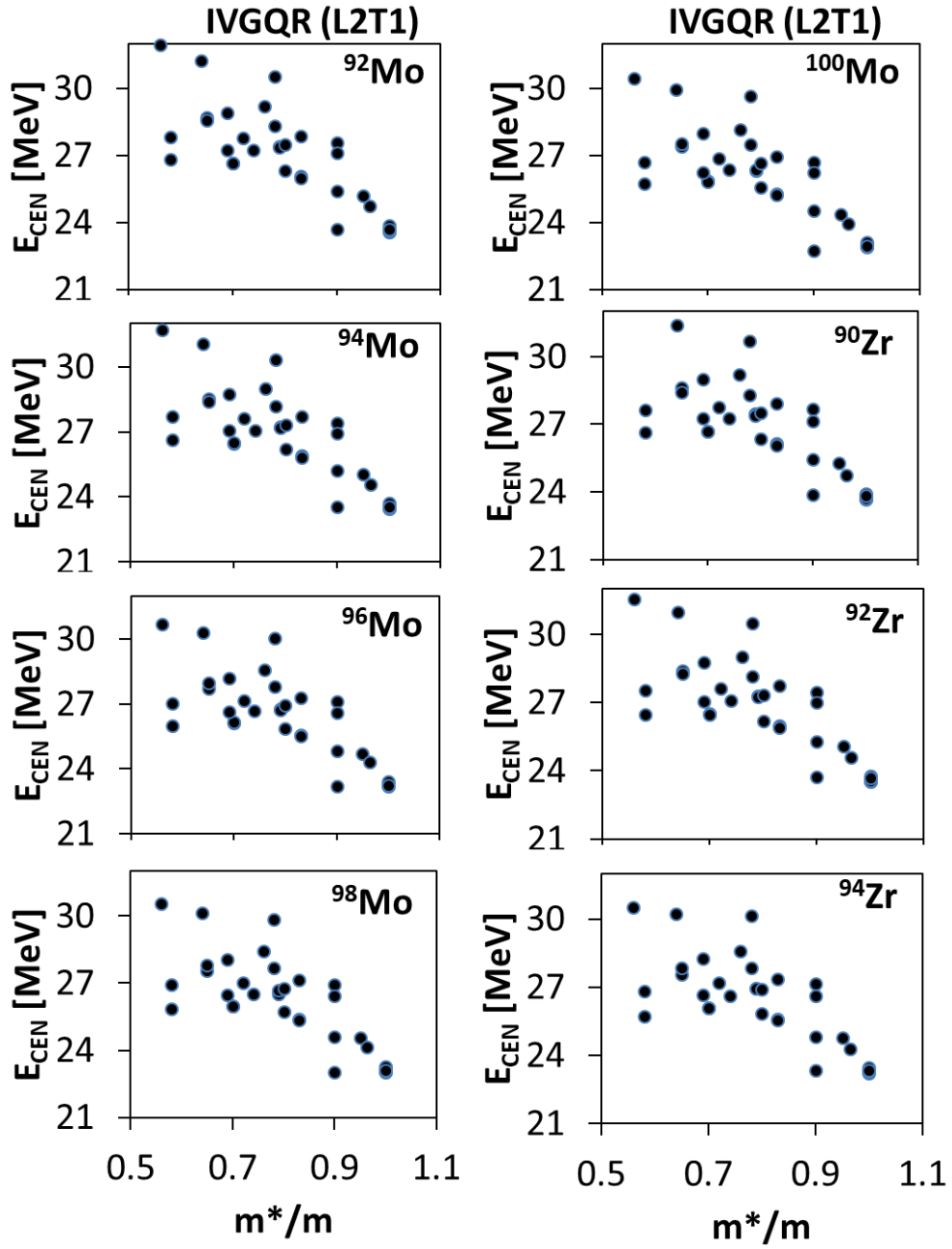

Figure 47 IVGQR E_{CEN} with m*/m in ^{92,94,96,98,100}Mo and ^{90,92,94}Zr. Similar to Figure 26 but for the IVGQR centroid energy as a function of the effective mass. A medium correlation is obtained between the calculated values of E_{CEN} and m*/m, with a Pearson linear correlation coefficient C ~ -0.77.

Isovector Giant Octupole Resonance

The centroid energy, E_{CEN}, of the IVGOR is plotted as a function of the symmetry energy coefficient, J, in Figure 48. No experimental data is available for this resonance. We obtained no correlation between the calculated values of E_{CEN} and J (C ~ -0.28). Similarly, no correlation was found between the centroid energy and either the first or the second derivative of the symmetry energy (C ~ -0.18 and ~ 0.02). In Figure 49 we demonstrate the strong correlation between the IVGOR centroid energy and IVGDR energy weighted sum rule enhancement coefficient, κ, (C ~ 0.83). We obtained a strong correlation between the calculated values of the centroid energy and the effective mass (C ~ -0.86), shown in Figure 50. The overview of all the calculated Pearson linear correlation coefficients is shown in Table 10. In Figure 41g and Figure 41h we plot the centroid energies as a function of the asymmetry coefficient, I, for Mo and Zr, respectively. In both cases we find the expected decreasing trend of the centroid energy as the neutrons are added to the system. However, for ^{98}Mo and ^{100}Mo we obtain some deviation for the interactions Sly4 and Sly5. The calculated values of the centroid energies of the IVGOR are shown in Table 29 of the Appendix.

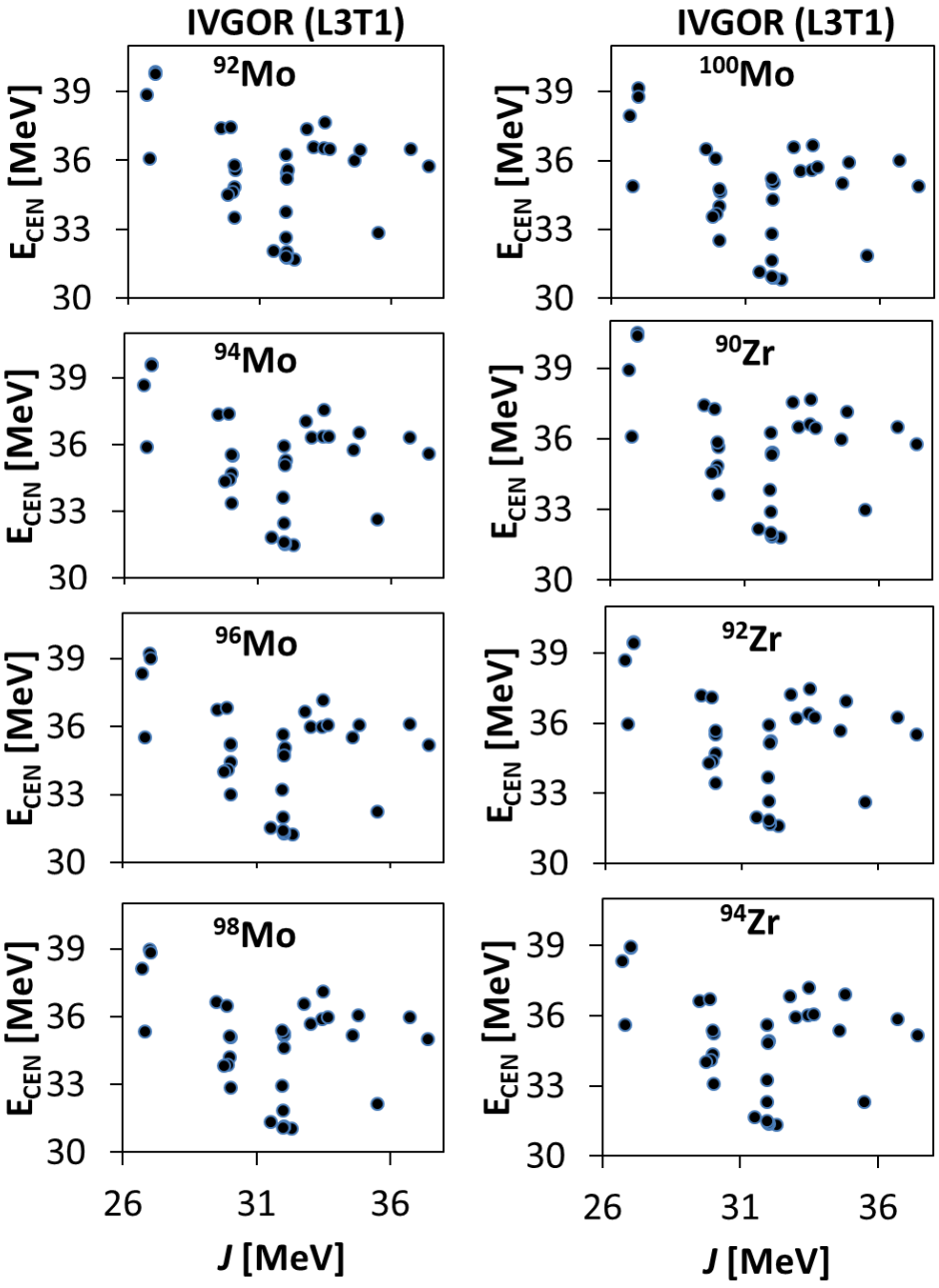

Figure 48 IVGOR E_{CEN} with J in ^{92,94,96,98,100}Mo and ^{90,92,94}Zr. Similar to Figure 26 but for the IVGOR centroid energy as a function of the symmetry energy at saturation density. No correlation is obtained between the calculated values of E_{CEN} and J, with a Pearson linear correlation coefficient C ~ -0.28.

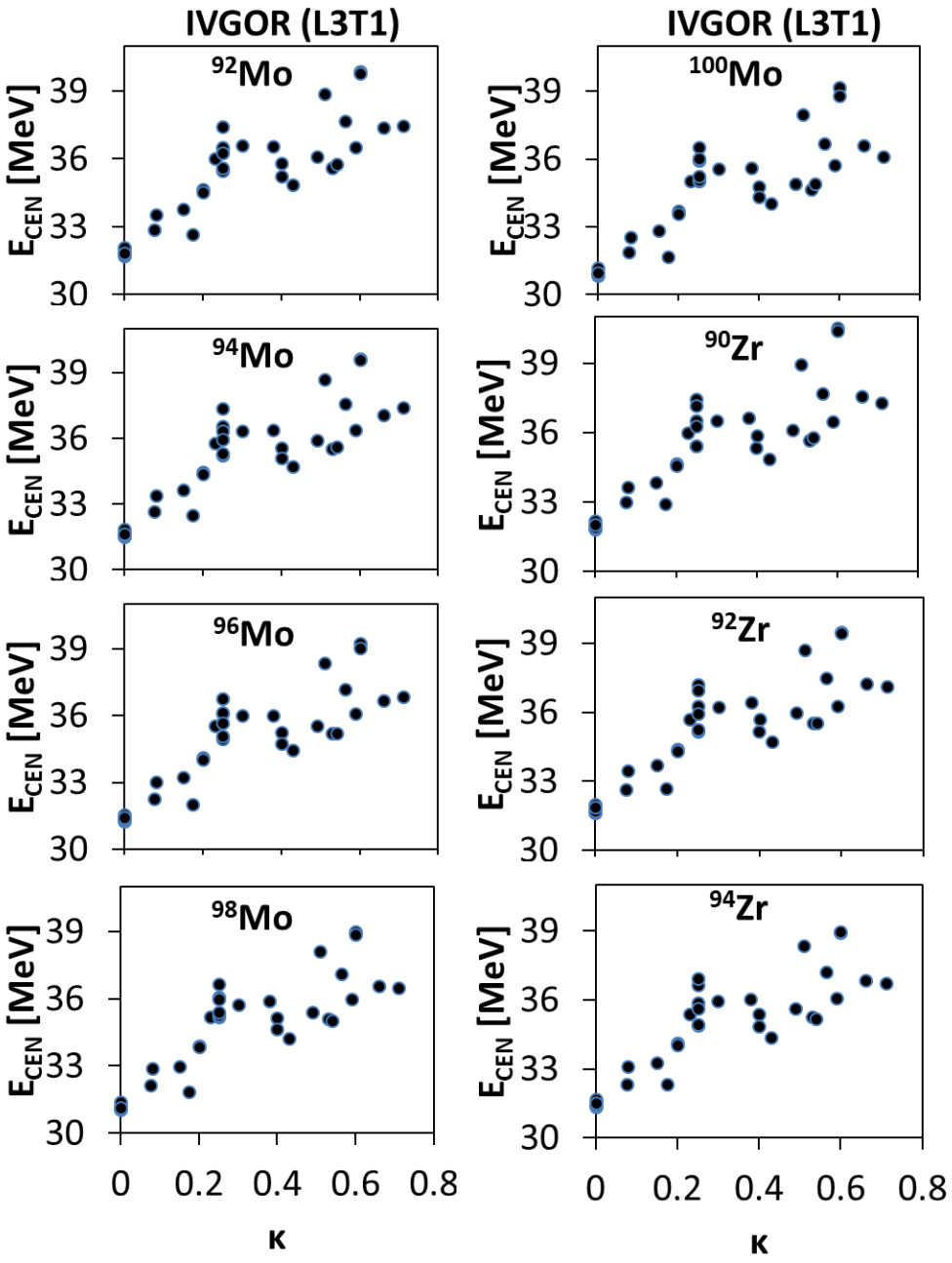

Figure 49 IVGOR E_{CEN} with κ in ^{92,94,96,98,100}Mo and ^{90,92,94}Zr. Similar to Figure 26 but for the IVGOR centroid energy as a function of the enhancement coefficient of the EWSR for the IVGDR. A strong correlation is obtained between the calculated values of E_{CEN} and κ, with a Pearson linear correlation coefficient C ~ 0.83.

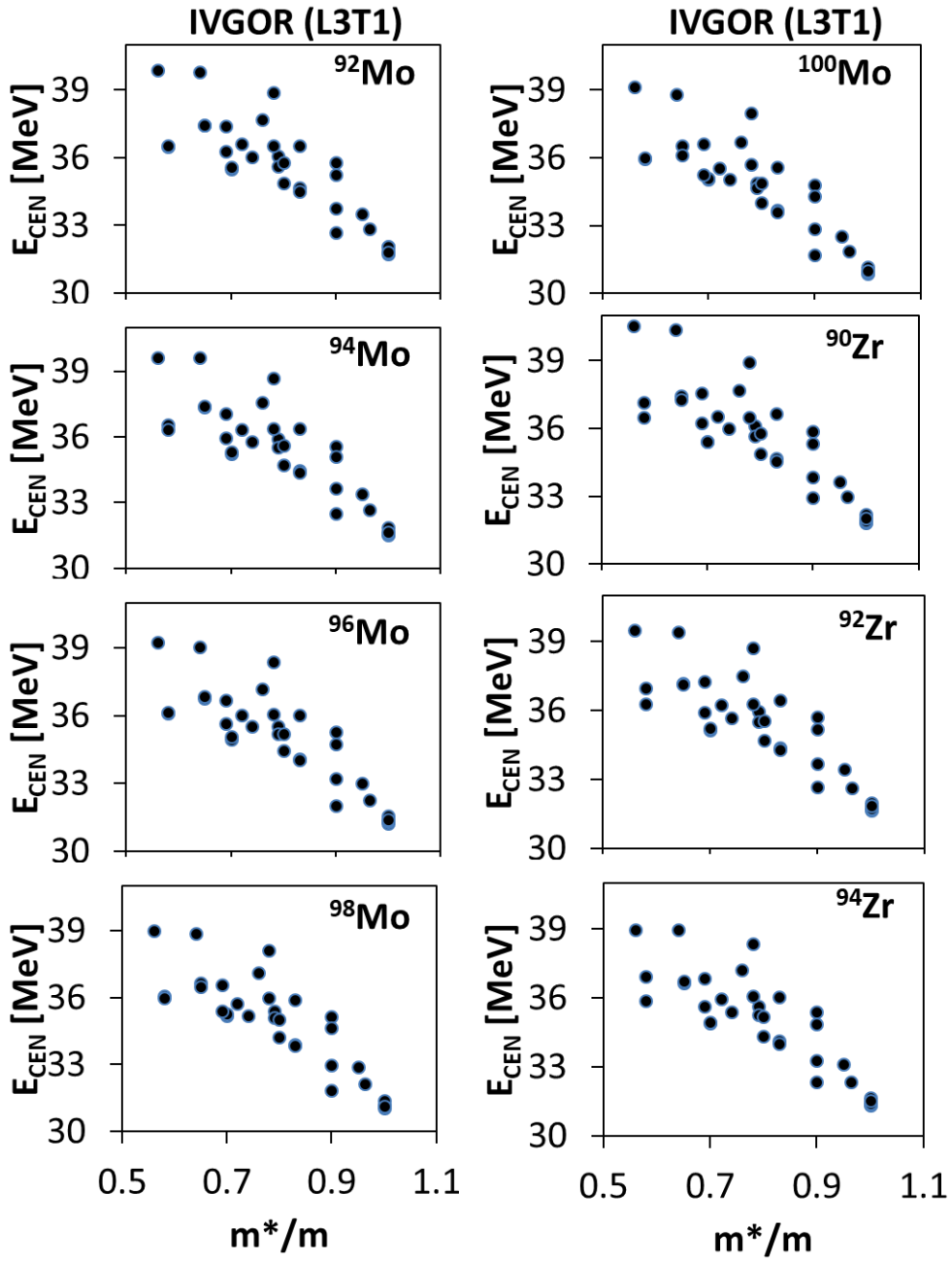

Figure 50 IVGOR E_{CEN} with m*/m in ^{92,94,96,98,100}Mo and ^{90,92,94}Zr. Similar to Figure 26 but for the IVGOR centroid energy as a function of the effective mass. A medium correlation is obtained between the calculated values of E_{CEN} and m*/m, with a Pearson linear correlation coefficient C ~ -0.86.

Conclusions

We have presented results of spherical Hartree-Fock based random phase approximation (HF-RPA) calculations for centroid energies, E_{CEN}, of isoscalar and isovector resonances of multipolarity L = 0 - 3. In our calculations we adopted 33 different Skyrme-type effective nucleon-nucleon interactions which cover a wide range of values of the properties of nuclear matter, see Table 1 and Table 3 for details. We focused our attention on the isotopes of ^{92,94,96,98,100}Mo and ^{90,92,94}Zr and compared with the recent experimental data to further investigate the disagreement with theoretical results obtained using only the KDE0v1 interaction [19–21]. We also studied the sensitivity of the calculated values of the centroid energy of each giant resonance with each nuclear matter property, see Table 10.

The disagreement between the theoretical calculations and the experimental data for the isoscalar centroid energies, and in particular for the E_{CEN} of the ISGMR in ^{94}Zr and ^{92,98,100}Mo which were obtained 1 – 3 MeV from the experimental data, remains an unresolved problem. Further investigations are required into the issue. One possible solution may be found by using the calculated HF-based RPA microscopic transition densities in the analysis of the experimental cross-section data [38,82] instead of the semi-classical transition densities used for the folding-model distorted wave Born approximation. Another possibility is to go beyond the mean-field approximation by including nuclear structure effects [83–86].

CHAPTER V

GIANT RESONANCES IN ^{44}Ca, ^{54}Fe, ^{64,68}Zn AND ^{56,58,60,68}Ni

We present the centroid energies, E_{CEN}, of isoscalar and isovector giant resonances of multipolarity L = 0 - 3 for the isotopes of ^{44}Ca, ^{54}Fe, ^{64,68}Zn and ^{56,58,60,68}Ni calculated within the spherical HF based RPA, described previously in Chapter II, using 33 different Skyrme-type defined in Table 1 and Table 2. Most of the nuclei considered in this chapter are open shell so we used the occupation number approximation for the single particle orbits to carry out our calculations.

For the calculation of the E_{CEN} we integrated the strength function, S(E), using the energy ranges shown in Table 11 which were obtained from the shape of the corresponding S(E) and from the experimental data. We compare our calculated E_{CEN} to the experimental results of Table 12. The isoscalar giant resonances have been measured at Texas A&M University using inelastic scattering of 240 MeV alpha particles [24,25,87] except for the unstable isotopes ^{56,68}Ni which were measured using inverse kinematics [57,88,89]. A detailed explanation of the experimental method used for the TAMU experiments can be found in [62–64]. The experimental data for the isovector giant dipole resonance was taken from the online tabulation maintained by the Centre for Photonuclear Experiments (Moscow State University) [90]. We also determined the Pearson linear correlation coefficient between the centroid energy of each multipolarity and each NM property. As shown in Table 13, we obtain medium

correlation between E_{CEN} of the ISGMR and the incompressibility coefficient of nuclear matter, K_{NM}, strong correlation between E_{CEN} of the ISGDR, ISGQR, ISGOR, IVGOR and the effective mass, m*/m, and between E_{CEN} of the isovector resonances and the EWSR enhancement coefficient, κ, of the IVGDR. We note that the magnitudes of the correlation obtained here were slightly less than those of chapters III and IV.

In what follows we consider each giant resonance separately and present plots of the calculated centroid energy as a function of various NM properties associated with the interaction used in the calculation. Experimental data is shown as dashed lines where available. We also plot the centroid energy as a function of nucleon mass, A.

Table 11 Integration energy ranges for ^{44}Ca, ^{54}Fe, ^{64,68}Zn and ^{56,58,60,68}Ni. Energy ranges E1 – E2 (in MeV) used in the integration of the strength function to determine the centroid energies of the isoscalar and isovector giant resonances.

	^{44}Ca	**^{54}Fe**	**^{56}Ni**	**^{58}Ni**	**^{60}Ni**	**^{64}Zn**	**^{68}Zn**	**^{68}Ni**
L0T0	9 - 40	9 - 40	12 - 35	9 - 40	9 - 40	9 - 40	9 - 40	12 - 30
L1T0	20 - 40	20 - 40	20 - 40	20 - 40	20 - 40	20 - 40	20 - 40	20 - 40
L2T0	9 - 40	9 - 40	12 - 35	9 - 40	9 - 40	9 - 40	9 - 40	12 - 30
L3T0	15 - 40	15 - 40	15 - 40	15 - 40	15 - 40	15 - 40	15 - 40	15 - 40
L0T1	7 - 60	7 - 60	7 - 60	7 - 60	7 - 60	7 - 60	7 - 60	7 - 60
L1T1	0 - 60	0 - 60	0 - 60	0 - 60	0 - 60	0 - 60	0 - 60	0 - 60
L2T1	7 - 60	7 - 60	7 - 60	7 - 60	7 - 60	7 - 60	7 - 60	7 - 60
L3T1	25 - 60	25 - 60	25 - 60	25 - 60	25 - 60	25 - 60	25 - 60	25 - 60

Table 12 E_{CEN} experimental data in MeV for ^{44}Ca, ^{54}Fe, ^{64,68}Zn and ^{56,58,60,68}Ni. The isoscalar data was taken from the following references: [24] for a, [25] for b, [88] for c, [87] for d, [57] for e, [89] for f. The isovector data was taken from the online "Centre for Photonuclear Experimental Data" maintained by Moscow State University [90].

	ISGMR	ISGDR	ISGQR	ISGOR	IVGDR
^{44}Ca	19.49 (34)[a]	35.03 (145)[a]	17.21 (48)[a]	-	21.63 (50)
^{54}Fe	19.66 (37)[b]	29.40 (83)[b]	18.05 (87)[b]	-	18.94 (50)
^{56}Ni	19.30 (50)[c]	-	16.20 (50)[c]	-	20.91 (50)
^{58}Ni	19.32 (32)[d]	34.06 (30)[d]	16.34 (13)[d]	23.20 (30)[d]	20.41 (50)
^{60}Ni	18.10 (29)[d]	36.12 (28)[d]	15.88 (14)[d]	24.40 (26)[d]	20.41 (50)
^{64}Zn	18.88 (79)[b]	25.66 (121)[b]	15.85 (31)[b]	-	19.53 (50)
^{68}Zn	16.60 (17)[b]	27.65 (39)[b]	15.54 (32)[b]	-	17.18 (50)
^{68}Ni	21.1 (19)[e]	-	15.9 (13)[f]	-	17.10 (20)

Table 13 Pearson linear correlation for ^{44}Ca, ^{54}Fe, ^{64,68}Zn and ^{56,58,60,68}Ni. Calculated Pearson linear correlation coefficient between centroid energies and each nuclear matter property.

	K_{NM}	m*/m	$W_0(X_W=1)$	J	L	K_{sym}	κ
ISGMR	0.73	-0.26	-0.07	-0.04	0.16	0.24	0.02
ISGDR	0.39	-0.83	-0.02	-0.17	0.01	0.23	0.58
ISGQR	0.40	-0.93	0.07	-0.05	0.15	0.41	0.53
ISGOR	0.32	-0.89	0.04	-0.15	-0.01	0.24	0.58
IVGMR	0.22	-0.64	-0.12	-0.24	-0.13	-0.03	0.80
IVGDR	0.09	-0.62	-0.12	-0.39	-0.40	-0.27	0.80
IVGQR	0.17	-0.73	-0.13	-0.38	-0.34	-0.17	0.81
IVGOR	0.23	-0.82	-0.04	-0.29	-0.18	0.01	0.79

Isoscalar Giant Monopole Resonance

The centroid energy, E_{CEN}, of the ISGMR is plotted as a function of the incompressibility coefficient of nuclear matter, K_{NM}, in Figure 51. Each nucleus is shown in its own panel and the experimental data is marked by the dashed lines. We obtained a medium correlation between the calculated values of E_{CEN} and K_{NM} with C ~ 0.73. As can be seen from the figures for ^{44}Ca, ^{54}Fe, ^{56,58}Ni and ^{64}Zn interactions associated with a value of K_{NM} = 200 – 240 MeV reproduce the data. This is the same region we extracted in Chapter III for a wide range of nuclear masses. However, for the isotopes of ^{60}Ni and ^{68}Zn we find that most of the interactions are above the experimental results. We note however, that the experimental value of E_{CEN} for ^{68}Zn is much lower than that of other nuclei in the region. On the other hand, most of the interactions are below the result of ^{68}Ni with only interactions with K_{NM} > 240MeV reproducing the data. In Figure 52 we plot the ISGMR centroid energy as a function of the effective mass, m*/m. We don't obtain any correlation between the calculated values of E_{CEN} and m*/m (C ~ -0.26). We also do not obtain any correlation between the calculated values of the centroid energy and the symmetry energy coefficient J, (C ~ -0.04), see Figure 53. Similarly, no correlation is found between the calculated values of centroid energy and the first derivative of the symmetry energy (C ~ 0.16), or the second derivative (C ~ 0.24) shown in Figure 54. As can be seen from Table 13, no correlation is found between E_{CEN} and any of the other NM properties considered. We also point out that the correlations obtained for these light nuclei are smaller in magnitude than those

of Chapter III. For completeness we show in Table 30 of the Appendix the calculated centroid energies for this giant resonance.

In Figure 55a we plot the centroid energies of ^{44}Ca, ^{54}Fe and ^{64,68}Zn as a function of the nucleon mass. The experimental result is marked by a solid vertical line while the theoretical calculations are plotted as dots with lines connecting the same interactions to guide the eye. As the figure shows, a slight increase is predicted by most interactions in the value of the centroid energy going from ^{44}Ca to ^{54}Fe and then a steady decline for the Zn isotopes. The experimental value of the centroid energy instead is relatively constant for the first 3 nuclei and then drops for ^{68}Zn. In Figure 55b we show a similar plot but for the Ni isotopes. Here the calculations result in a steady decrease in the value of the centroid energy as the mass increases, with a kink for the ^{58}Ni isotope. On the other hand, the experimental value for E_{CEN} is similar for ^{56,58}Ni, then decreases slightly for ^{60}Ni but increases again for ^{68}Ni.

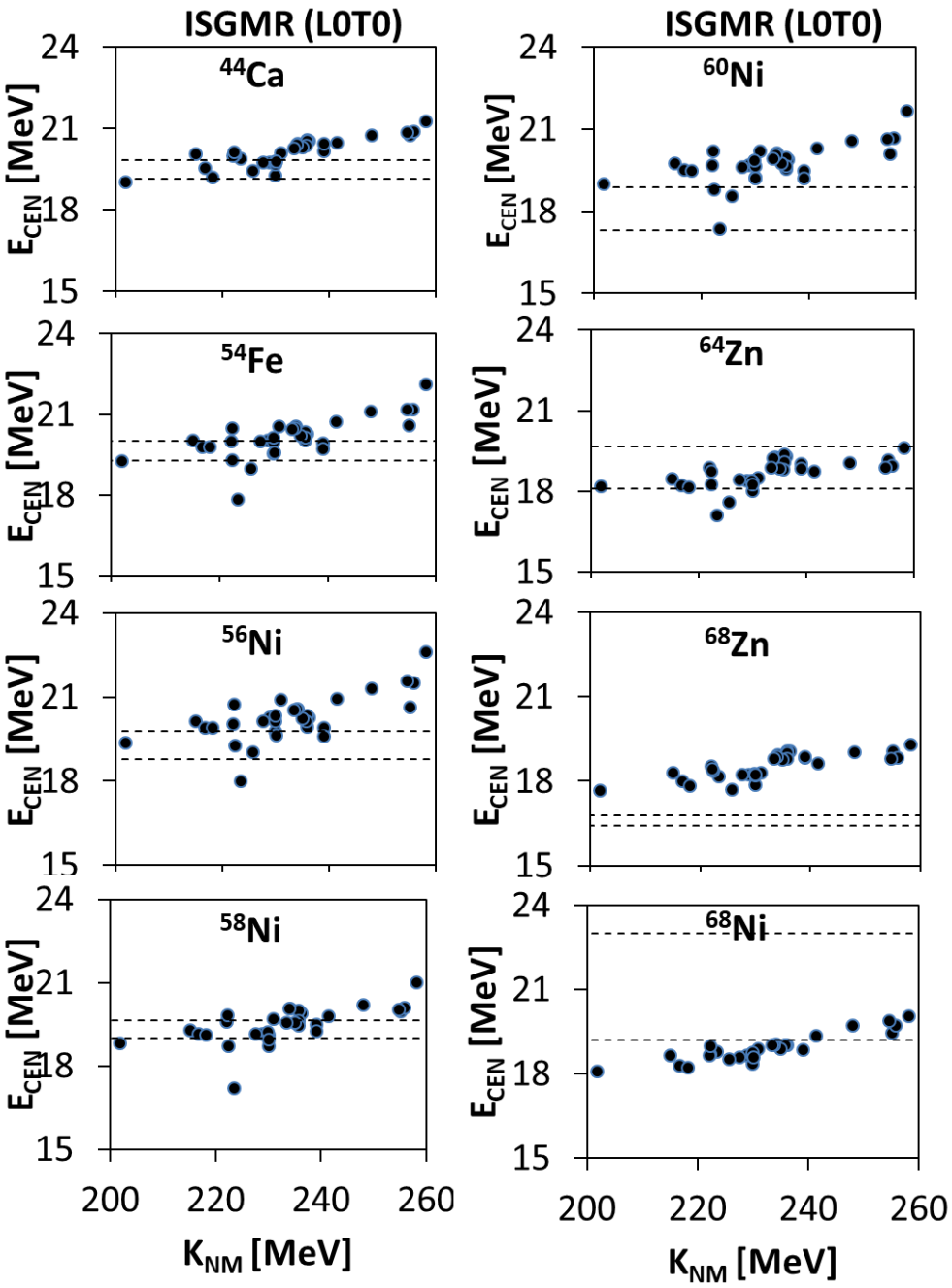

Figure 51 ISGMR E_{CEN} with K_{NM} in ^{44}Ca, ^{54}Fe, ^{64,68}Zn and ^{56,58,60,68}Ni. Calculated centroid energies [MeV] (full circle) of the ISGMR as a function of the incompressibility coefficient, K_{NM}. Each nucleus has its own panel, the experimental uncertainties are contained by the dashed lines. A medium correlation is obtained between the calculated values of E_{CEN} and K_{NM}, with a Pearson linear correlation coefficient C ~ 0.73.

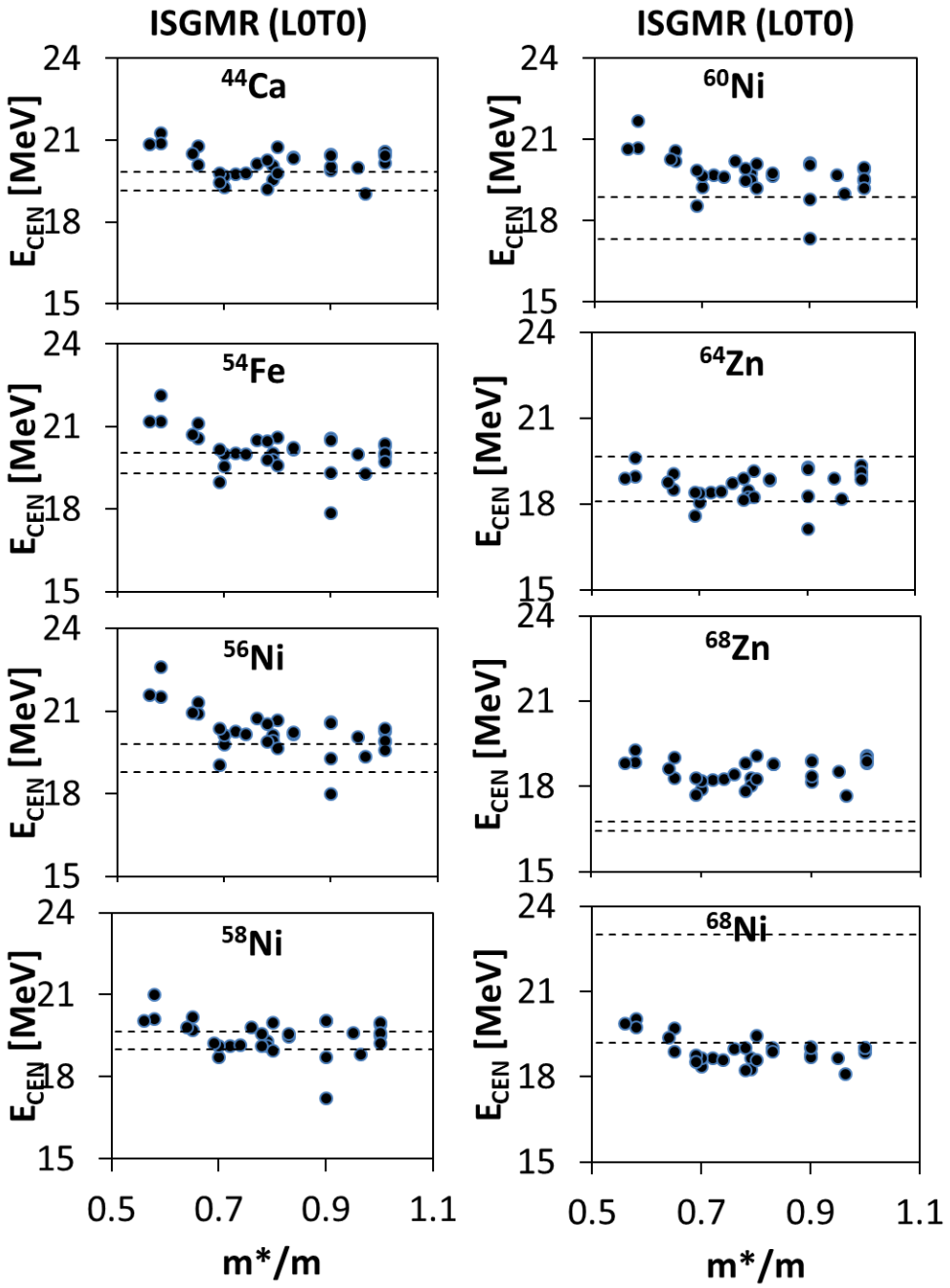

Figure 52 ISGMR E_{CEN} with m*/m in ^{44}Ca, ^{54}Fe, ^{64,68}Zn and ^{56,58,60,68}Ni. Similar to Figure 51 but for the ISGMR centroid energy as a function of the effective mass. No correlation is obtained between the calculated values of E_{CEN} and m*/m, with a Pearson linear correlation coefficient C ~ -0.26.

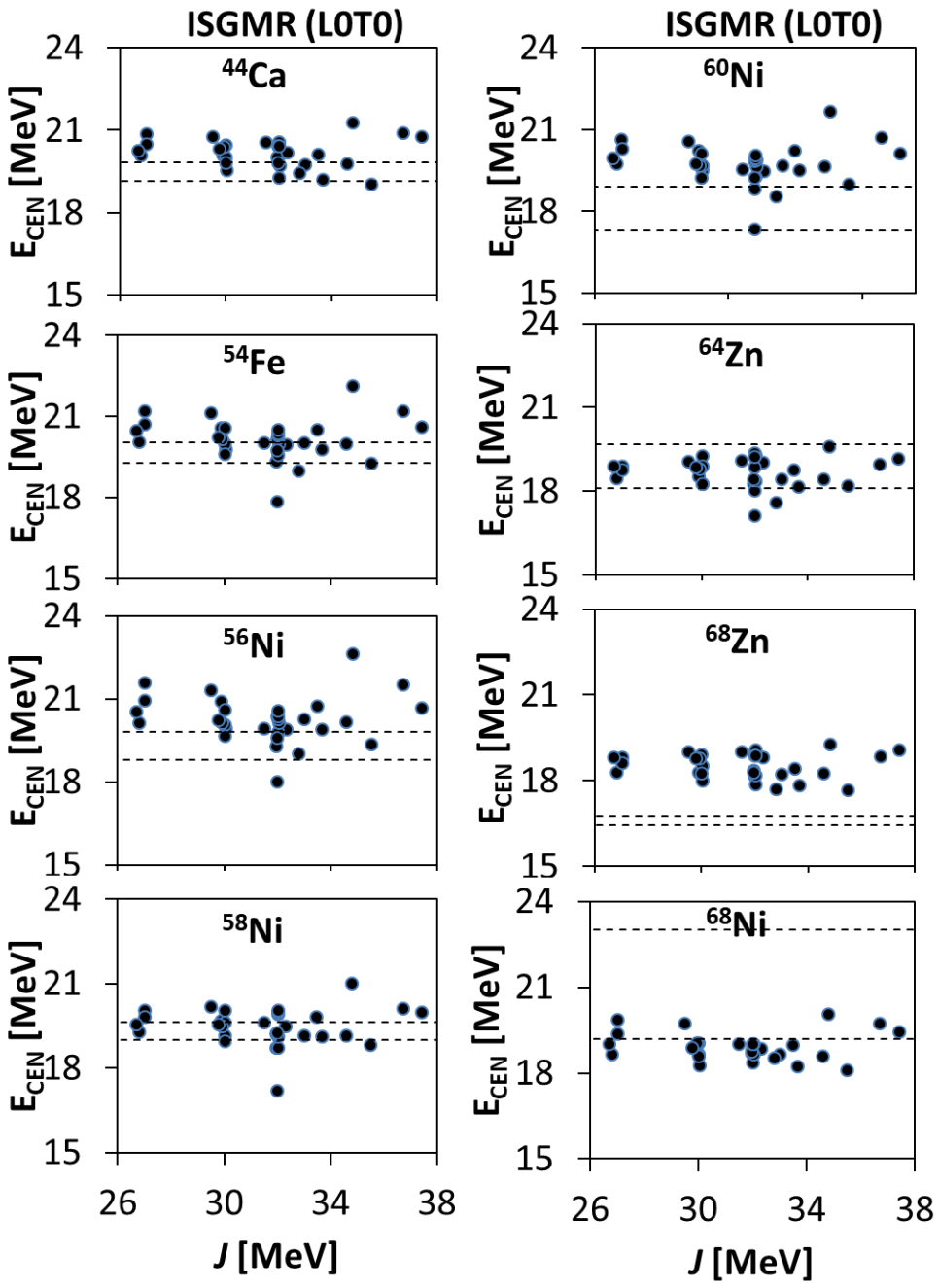

Figure 53 ISGMR E_{CEN} with J in ^{44}Ca, ^{54}Fe, ^{64,68}Zn and ^{56,58,60,68}Ni. Similar to Figure 51 but for the ISGMR centroid energy as a function of the symmetry energy at saturation density. No correlation is obtained between the calculated values of E_{CEN} and J, with a Pearson linear correlation coefficient C ~ -0.04.

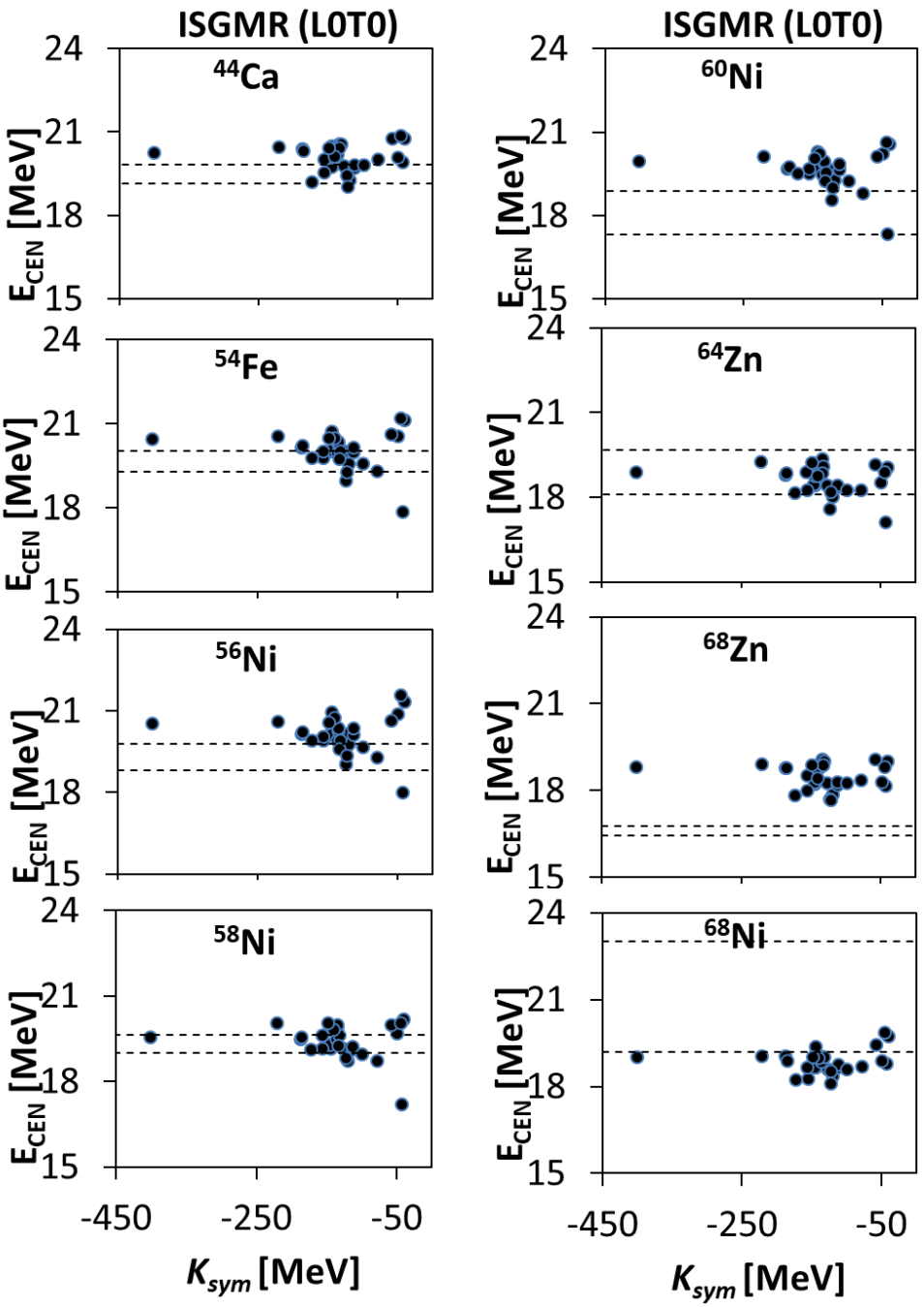

Figure 54 ISGMR E_{CEN} with K_{sym} in ^{44}Ca, ^{54}Fe, ^{64,68}Zn and ^{56,58,60,68}Ni. Similar to Figure 51 but for the ISGMR centroid energy as a function of the second derivative of the symmetry energy at saturation density. No correlation is obtained between the calculated values of E_{CEN} and K_{sym}, with a Pearson linear correlation coefficient C ~ 0.24.

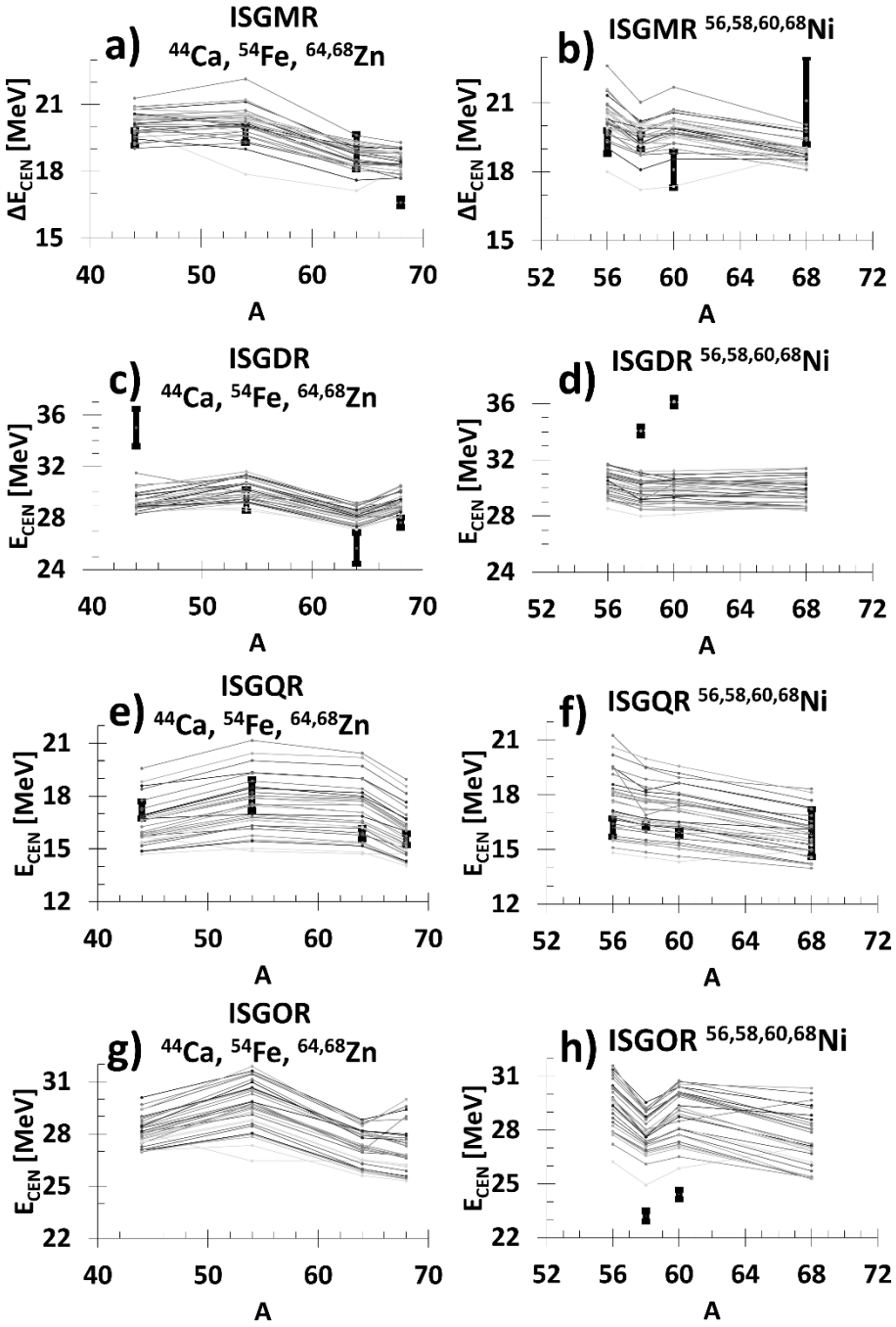

Figure 55 Isoscalar E_{CEN} overview in ^{44}Ca, ^{54}Fe, ^{64,68}Zn and ^{56,58,60,68}Ni. The isoscalar (L = 0 - 3) centroid energies [MeV] are plotted as a function of the nucleon mass. The isotopes of ^{44}Ca, ^{54}Fe and ^{64,68}Zn are shown on the left panels while ^{56,58,60,68}Ni are on the right. Available experimental errors are shown by solid vertical lines while the calculations are shown as dots with lines connecting the same interactions to help guide the eye.

Isoscalar Giant Dipole Resonance

The centroid energy, E_{CEN}, of the ISGDR is plotted in Figure 56 as a function of the incompressibility coefficient, K_{NM}. Each nucleus is shown in its own panel and the experimental data is marked by the dashed lines but is not available for ^{56,68}Ni. We obtained a weak correlation between the calculated values of E_{CEN} and K_{NM} (C ~ 0.39). For the effective mass, m*/m, on the other hand, shown in Figure 57, we find a strong correlation with the centroid energy with C ~ 0.83. We see from the figure that the calculated values of the centroid energy are in agreement with data only for ^{54}Fe. For the isotopes of ^{44}Ca and ^{58,60}Ni the calculations are several MeV below the experimental values, while we find the opposite for the ^{64,68}Zn isotopes for which the calculated values are 1 - 4 MeV above the experimental values. We point out however that the experimental centroid energy for the Zn isotopes is up to 10 MeV below that of the other nuclei considered in this chapter. Next, we show in Figure 58 the centroid energy as a function of the symmetry energy coefficient, J. No correlation is found between the calculated centroid energies and J (C ~ -0.17) or with the first and second derivative of J (C ~ 0.01 and 0.23, respectively). In Table 13 we show the calculated Pearson linear correlation coefficients for the remaining NM properties considered here. For completeness we show in Table 31 of the Appendix the calculated centroid energies for this giant resonance.

In Figure 55c the centroid energies, E_{CEN}, of ^{44}Ca, ^{54}Fe and ^{64,68}Zn are plotted as a function of their mass. Experimental data is marked by the solid vertical lines while the results of the calculations are shown as dots with lines connecting the same interactions

to guide the eye. As shown in the figure, the theoretical calculations predict the value of E_{CEN} between 28 and 30 MeV for most interactions. We find that the increase in the value of the centroid energy from ^{64}Zn to the heavier ^{68}Zn is reproduced by all interactions considered, albeit shifted by a few MeV. The centroid energy of Ni isotopes is plotted as a function of mass in Figure 55d. The calculations result in a relatively constant value across this isotope chain, while for the experimental result we find that the centroid energy for ^{58}Ni is lower than that of ^{60}Ni while no data is available for the unstable isotopes of ^{56,68}Ni.

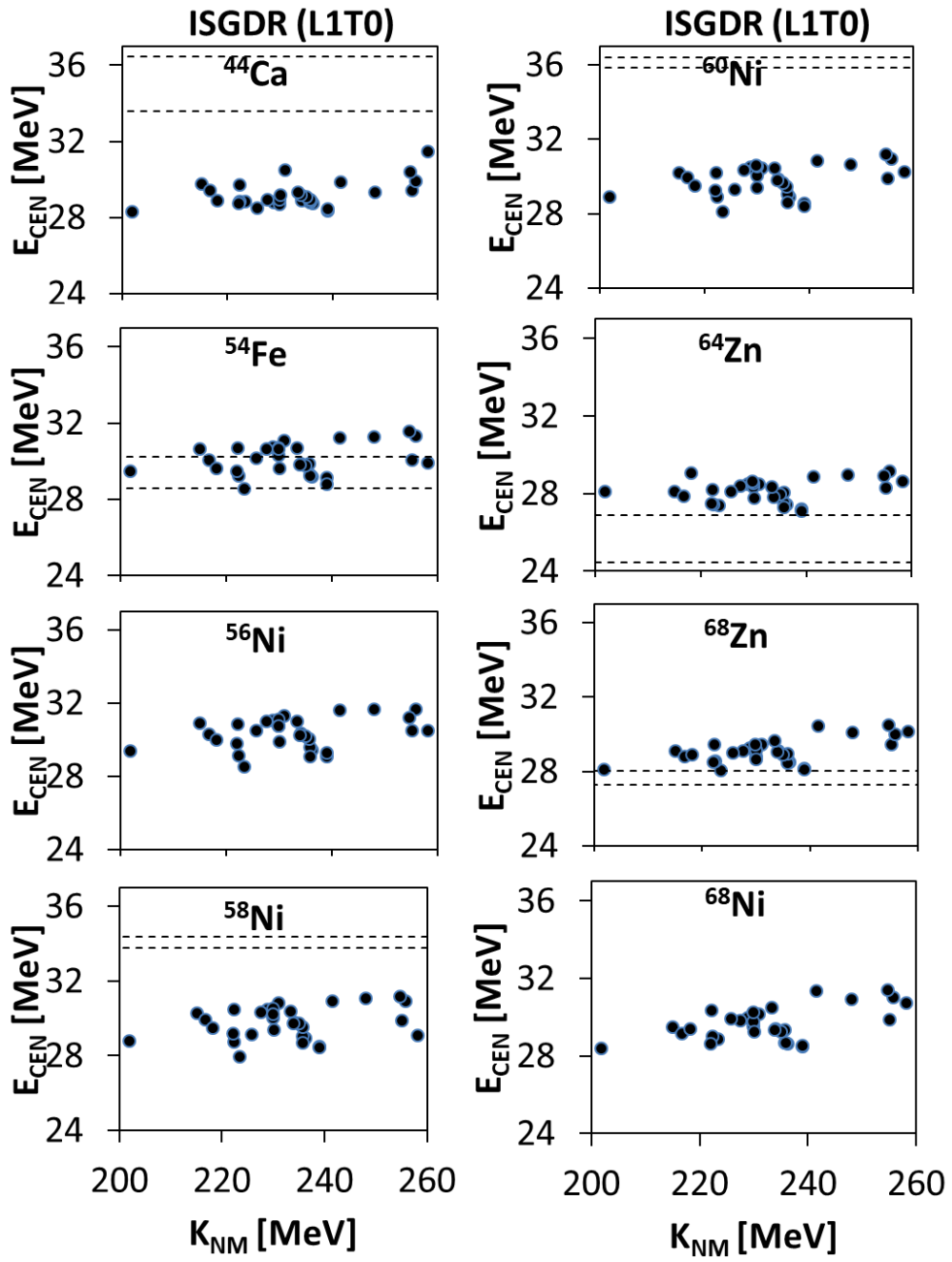

Figure 56 ISGDR E_{CEN} with K_{NM} in ^{44}Ca, ^{54}Fe, ^{64,68}Zn and ^{56,58,60,68}Ni. Similar to Figure 51 but for the ISGDR centroid energy as a function of the incompressibility coefficient. A weak correlation is obtained between the calculated values of E_{CEN} and K_{NM}, with a Pearson linear correlation coefficient C ~ 0.39.

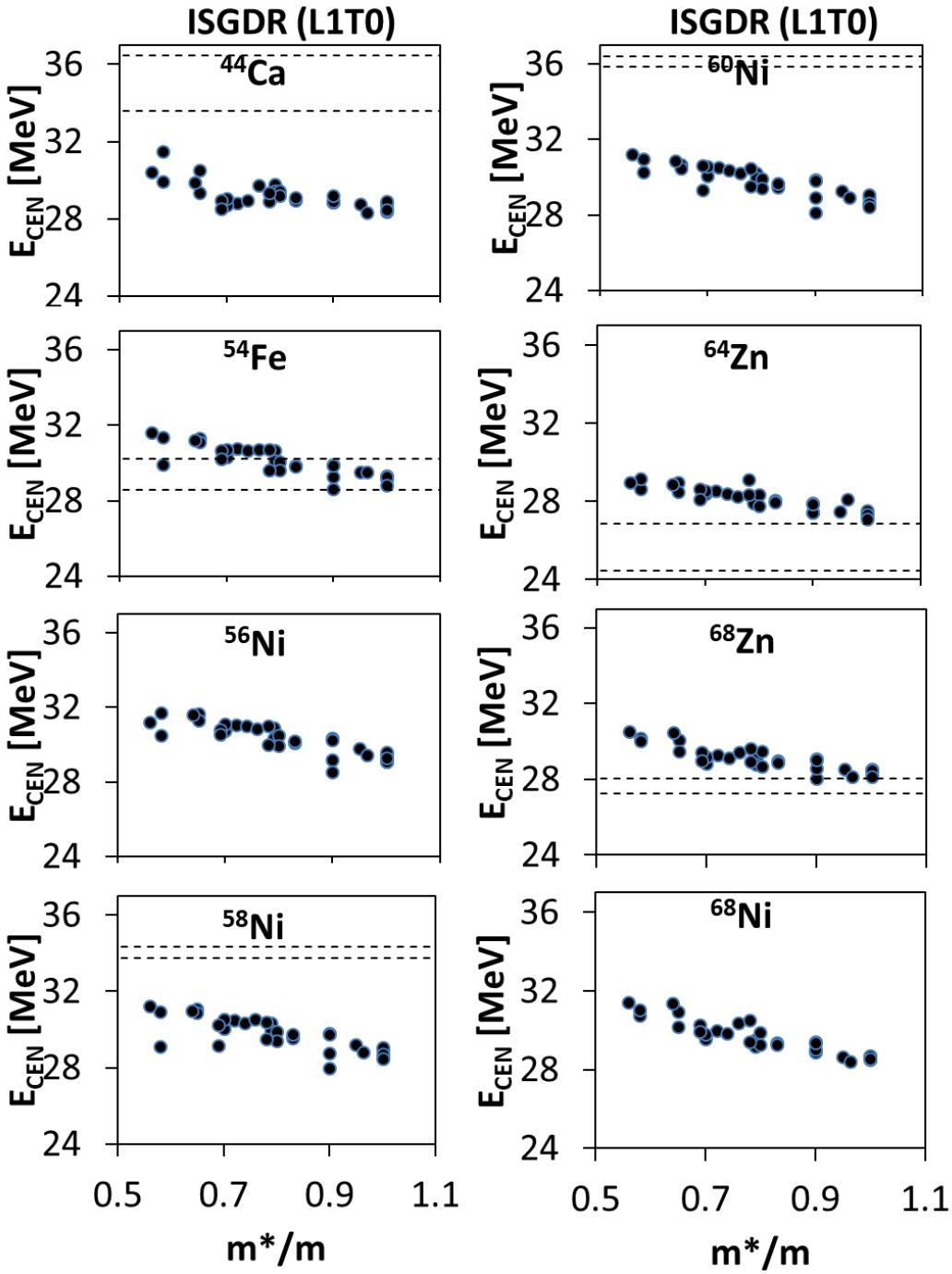

Figure 57 ISGDR E_{CEN} with m*/m in ^{44}Ca, ^{54}Fe, ^{64,68}Zn and ^{56,58,60,68}Ni. Similar to Figure 51 but for the ISGDR centroid energy as a function of the effective mass. A strong correlation is obtained between the calculated values of E_{CEN} and m*/m, with a Pearson linear correlation coefficient C ~ -0.83.

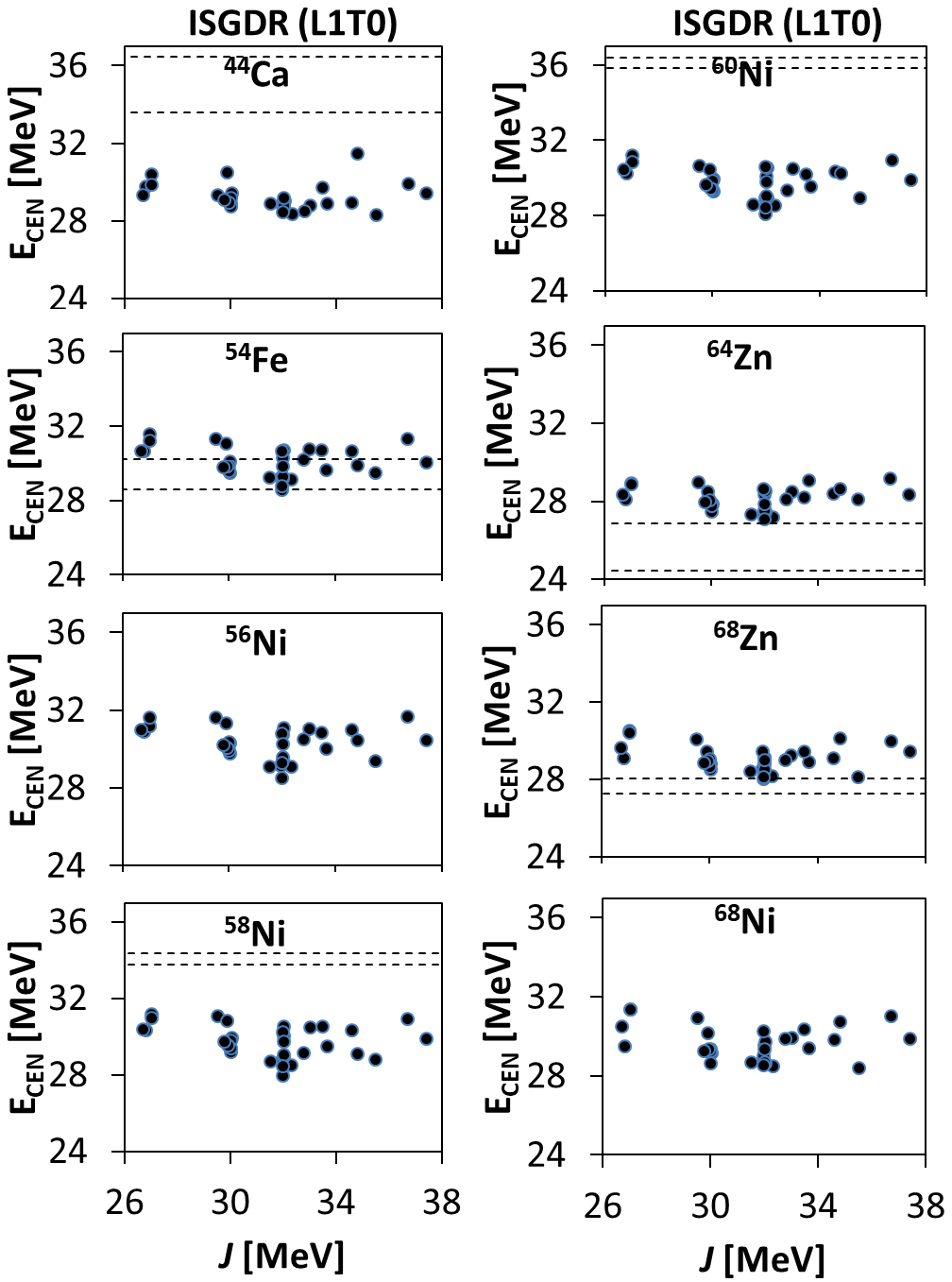

Figure 58 ISGDR E_{CEN} with J in ^{44}Ca, ^{54}Fe, ^{64,68}Zn and ^{56,58,60,68}Ni. Similar to Figure 51 but for the ISGDR centroid energy as a function of the symmetry energy at saturation density. No correlation is obtained between the calculated values of E_{CEN} and J, with a Pearson linear correlation coefficient C ~ -0.17.

Isoscalar Giant Quadrupole Resonance

The centroid energy, E_{CEN}, of the ISGQR is shown in Figure 59 as a function of the effective mass, m*/m. We obtained a strong correlation between the calculated values of E_{CEN} and m*/m (C~ -0.93), in agreement with the results of Chapter III. For the ISGQR we have experimental data for all the isotopes considered. For the lightest nuclei, ^{44}Ca and ^{54}Fe, interactions associated with m*/m = 0.6 - 0.8 reproduce the data the best while for all the other nuclei a slightly higher range for m*/m is in better agreement with the experimental data. For ^{56,58,60}Ni and ^{64}Zn the experimental centroid energy is in some cases even reproduced by interactions with m*/m ~ 1. Next, we show in Figure 60 the centroid energy as a function of the incompressibility coefficient, K_{NM}, for which we obtained a weak correlation (C ~ 0.40). We cannot make conclusions on a good range for K_{NM} using the ISGQR because the correlation is not strong enough and we find that interaction across the entire range can reproduce the experimental data. For the remaining correlations between E_{CEN} and NM properties shown in Table 13, we only find a weak correlation with K_{sym} (C ~ 0.41) and with the isovector enhancement factor, κ, of the IVGDR (C ~ 0.52). For completeness we show in Table 32 of the Appendix the calculated centroid energies for this giant resonance.

In Figure 55e the centroid energies of ^{44}Ca, ^{54}Fe and ^{64,68}Zn are plotted as a function of their mass. Experimental data is marked by the solid vertical lines while the results of the calculations are shown as dots with lines connecting the same interactions to help guide the eye. The resulting trend of the calculated E_{CEN} agrees with the experimental data: an increasing value of the centroid energy from ^{44}Ca to ^{54}Fe and then

a decrease for ^{64,68}Zn. This peculiar behavior was already pointed out in Chapter III, where we covered the centroid energy for a wide range of nuclear masses, but was not found in Chapter IV, where we focused on the region of A = 90 - 100. The calculated centroid energy of the Ni isotopes on the other hand, shown in Figure 55f, seems to steadily decrease as the mass increases while the experimental values are a bit more constant around 16 MeV. From this figure we also reiterate the point above regarding the effective mass. Using the knowledge that a higher effective mass corresponds to a lower centroid energy we can clearly see that the experimental data for the Zn and Ni isotopes falls in the lower part of the "theory band" (higher effective mass) while ^{44}Ca and ^{54}Fe are slightly higher in this band.

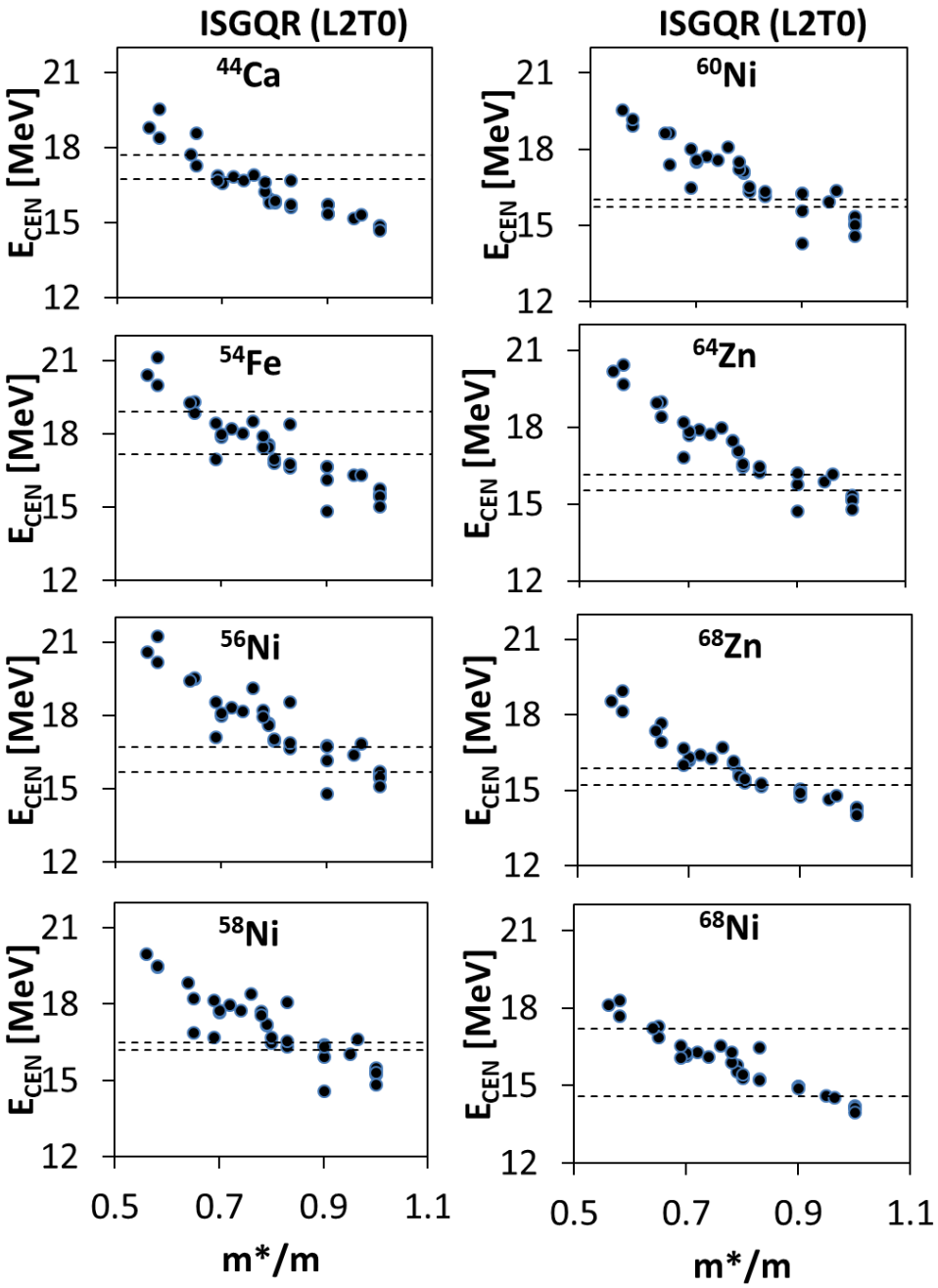

Figure 59 ISGQR E_{CEN} with m*/m in ^{44}Ca, ^{54}Fe, ^{64,68}Zn and ^{56,58,60,68}Ni. Similar to Figure 51 but for the ISGQR centroid energy as a function of the effective mass. A strong correlation is obtained between the calculated values of E_{CEN} and m*/m, with a Pearson linear correlation coefficient C ~ -0.93.

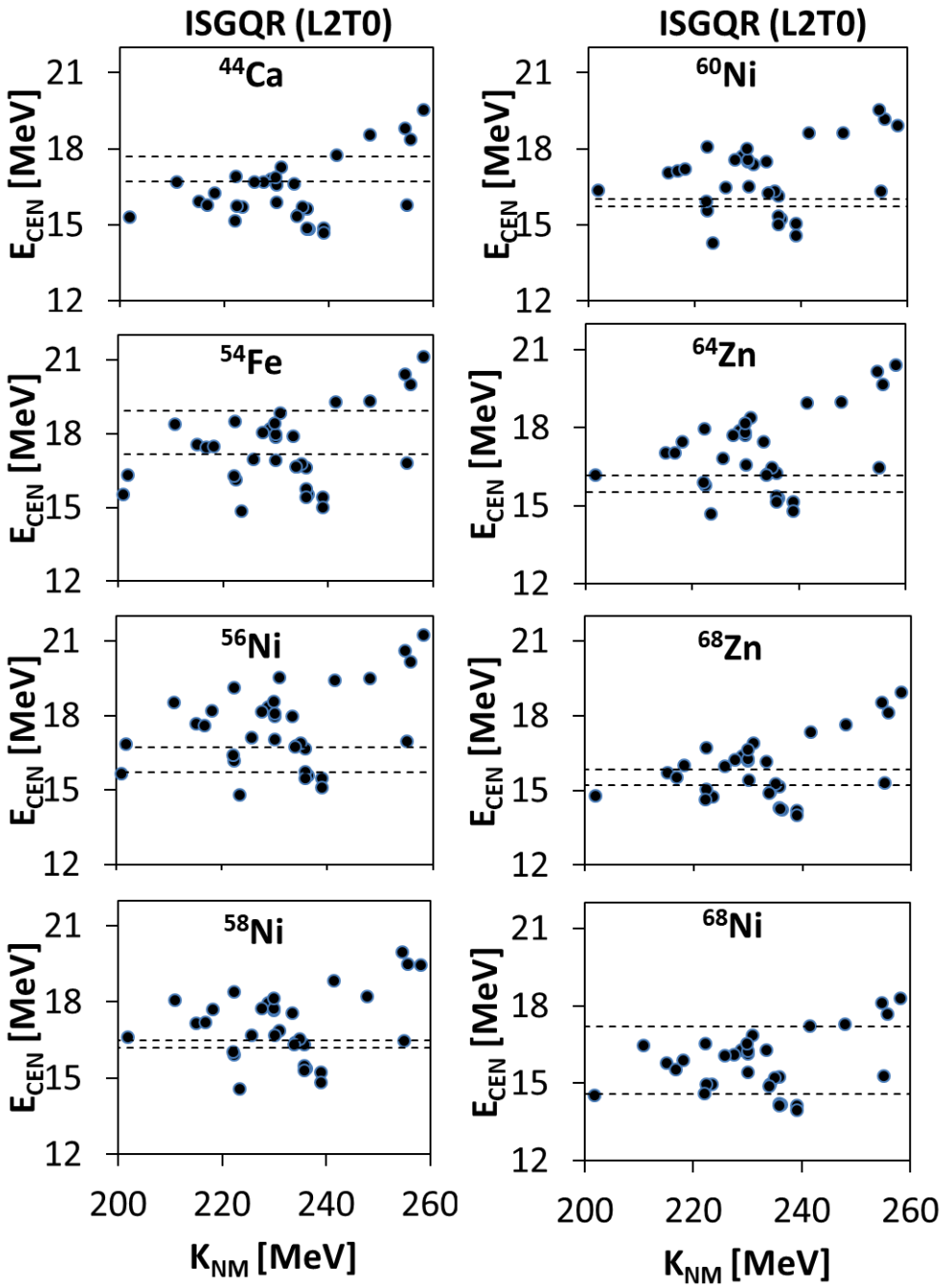

Figure 60 ISGQR E_{CEN} with K_{NM} in ^{44}Ca, ^{54}Fe, ^{64,68}Zn and ^{56,58,60,68}Ni. Similar to Figure 51 but for the ISGQR centroid energy as a function of the incompressibility coefficient. A weak correlation is obtained between the calculated values of E_{CEN} and K_{NM}, with a Pearson linear correlation coefficient C ~ 0.40.

Isoscalar Giant Octupole Resonance

In Figure 61 we plot the centroid energy, E_{CEN}, of the ISGOR as a function of the effective mass, m*/m. We obtained a strong correlation between the calculated values of E_{CEN} and m*/m (C ~ 0.89). The experimental data, available for ^{58,60}Ni and delimited by the dashed lines, is several MeV below the result of all the interactions used. This was also seen in Chapter III and it is possibly that the reason of the discrepancies may lie in the fact that the strength distribution of the ISGOR extends well beyond the experimental sensitivity leaving a large amount of the high energy strength undetected which would shift the centroid energy upward. In Figure 62 the centroid energy is plotted as a function of the incompressibility coefficient, K_{NM}. We find no correlation between the calculated values of E_{CEN} and K_{NM} (C ~ 0.33). Similarly, as can be seen from Table 13, we find no correlation with any of the symmetry energy coefficients while only a weak correlation is found with the isovector enhancement factor (C ~ -0.58). For completeness we show in Table 33 of the Appendix the calculated centroid energies for this giant resonance.

In Figure 55g the centroid energies of ^{44}Ca, ^{54}Fe and ^{64,68}Zn are plotted as a function of their mass. We see from the figure that the value of the centroid energy seems to fluctuate for these nuclei. In Figure 55h we show the centroid energy of the Ni isotopes as a function of their mass. We obtained a decreasing trend for the centroid energy as the mass increases, but we found that the E_{CEN} of ^{58}Ni is predicted below that of ^{60}Ni, in agreement with the data.

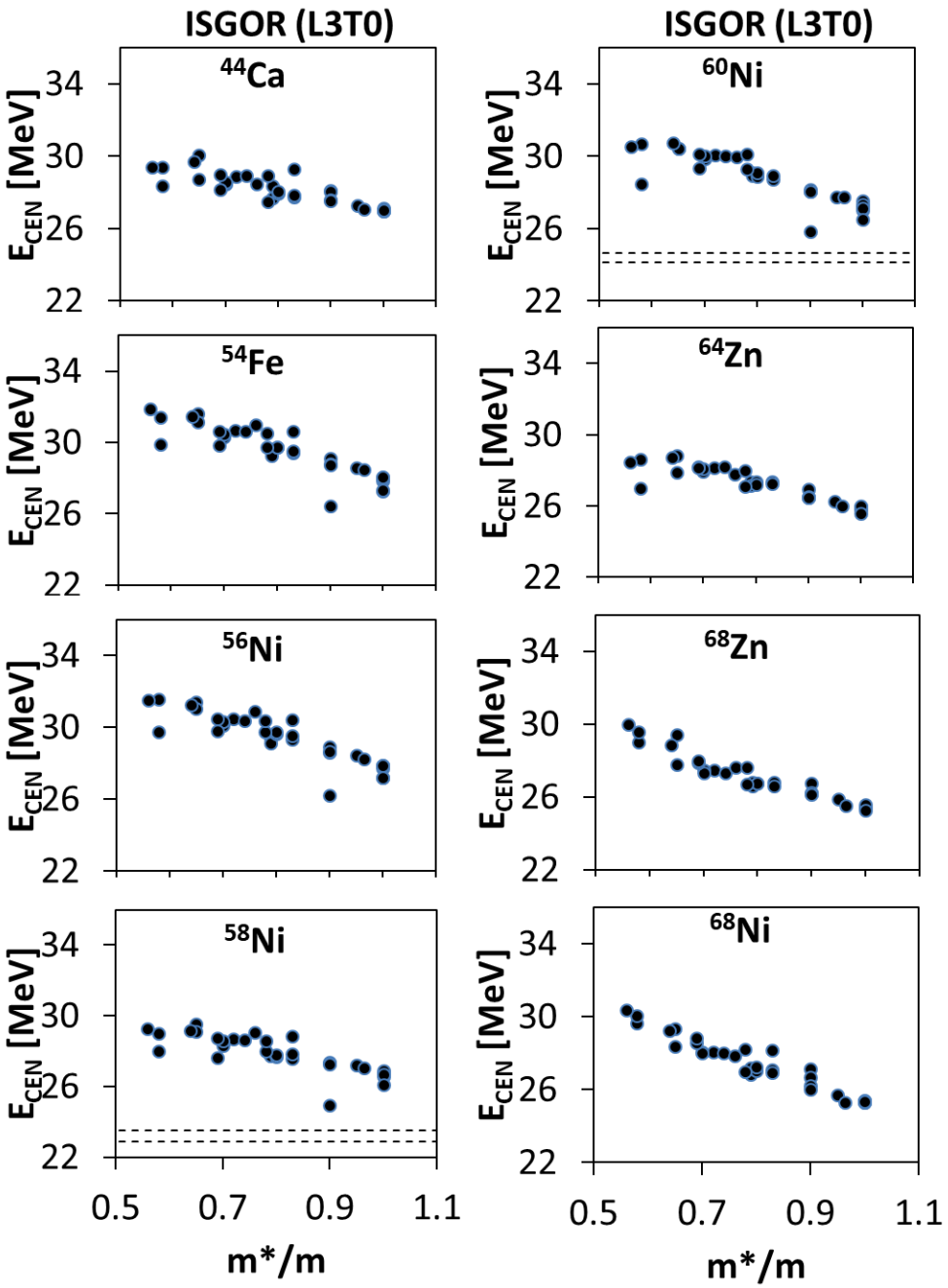

Figure 61 ISGOR E_{CEN} with m*/m in ^{44}Ca, ^{54}Fe, ^{64,68}Zn and ^{56,58,60,68}Ni. Similar to Figure 51 but for the ISGOR centroid energy as a function of the effective mass. A strong correlation is obtained between the calculated values of E_{CEN} and m*/m, with a Pearson linear correlation coefficient C ~ -0.89.

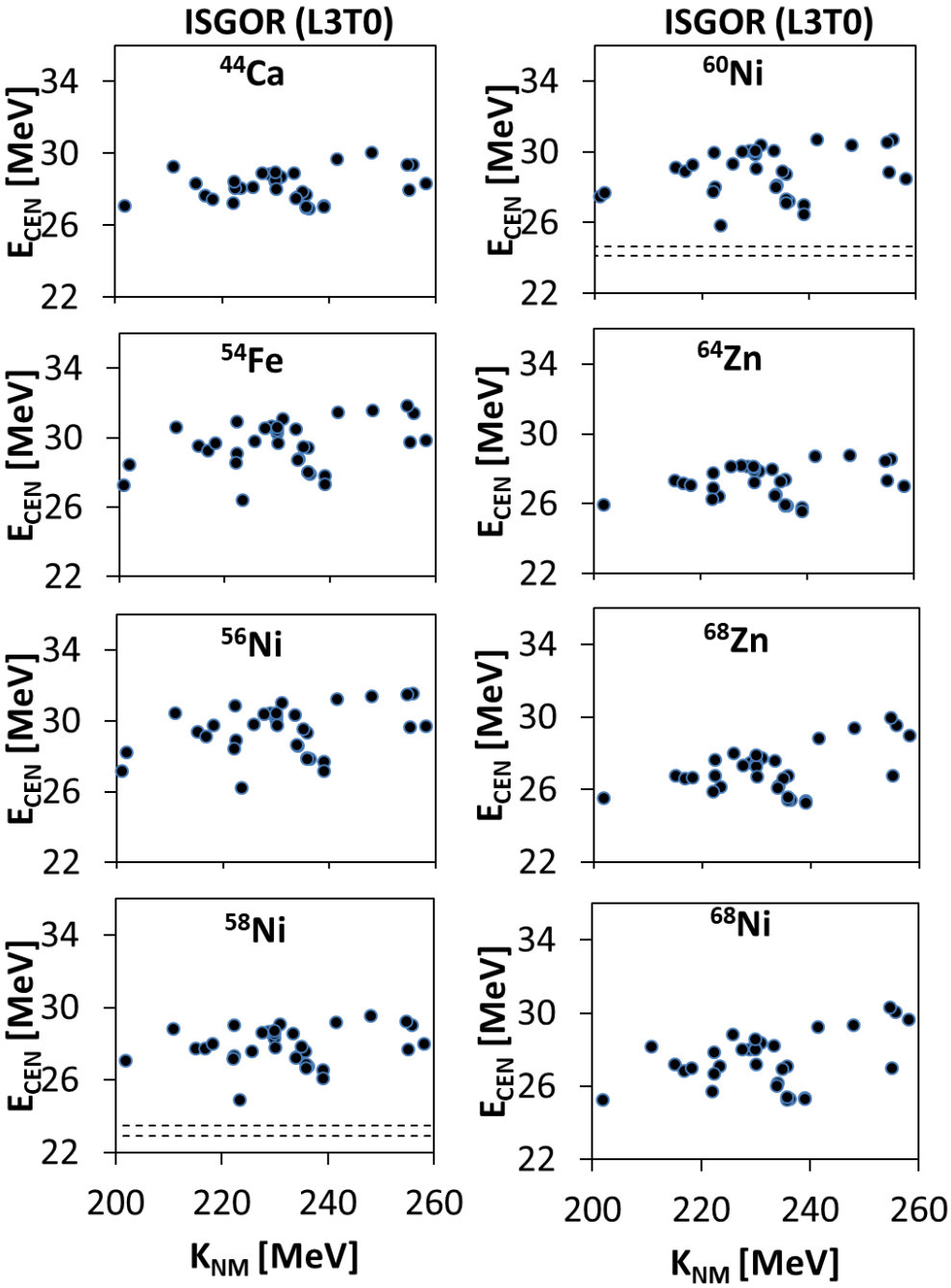

Figure 62 ISGOR E_{CEN} with K_{NM} in ^{44}Ca, ^{54}Fe, ^{64,68}Zn and ^{56,58,60,68}Ni. Similar to Figure 51 but for the ISGOR centroid energy as a function of the incompressibility coefficient. No correlation is obtained between the calculated values of E_{CEN} and K_{NM}, with a Pearson linear correlation coefficient C ~ 0.32.

Isovector Giant Monopole Resonance

We plot the centroid energy, E_{CEN}, of the IVGMR as a function of the incompressibility coefficient of nuclear matter, K_{NM}, in Figure 63. The calculations are shown by the full circles, but no experimental data is available. Despite being a compression mode, we don't find any correlation between the calculated centroid energies and the incompressibility coefficient (C ~ 0.22). As can be seen from the figure, we predict the centroid energy to fall between 28 and 35 MeV except for the isotopes of ^{54}Fe and ^{56}Ni where we see some interactions resulting with values as high as 38.5 MeV. In Figure 64 we plot the centroid energy as a function of the effective mass, m*/m, and obtain a medium correlation between E_{CEN} and m*/m (C ~ -0.64). We find no correlations between the calculated centroid energy and the symmetry energy coefficient J (shown in Figure 65) or its first and second derivative, see Table 13 for details. In Figure 66 we plot the centroid energy as a function of the enhancement coefficient, κ, of the energy weighted sum rule (EWSR) for the isovector giant dipole resonance (IVGDR). We obtained a strong correlation between the calculated values of E_{CEN} and κ (C ~ 0.80), in agreement with Chapter III. For completeness we show in Table 34 of the Appendix the calculated centroid energies for this giant resonance.

In Figure 67a the centroid energies of ^{44}Ca, ^{54}Fe and ^{64,68}Zn are plotted as a function of their mass for the IVGMR. We obtain an increasing value for centroid energy going from ^{44}Ca to ^{54}Fe and going from ^{64}Zn to ^{68}Zn, but the values of the centroid energy of the Zn isotopes are predicted below that of ^{54}Fe. In Figure 67b we plot the centroid energy of the Ni isotopes as a function of mass. We obtain a decreasing

trend for the value of the centroid energy as the mass increases, with a particularly steep decrease from the unstable isotopes of ^{56}Ni to ^{58}Ni for interactions with a higher value of the enhancement coefficient, κ.

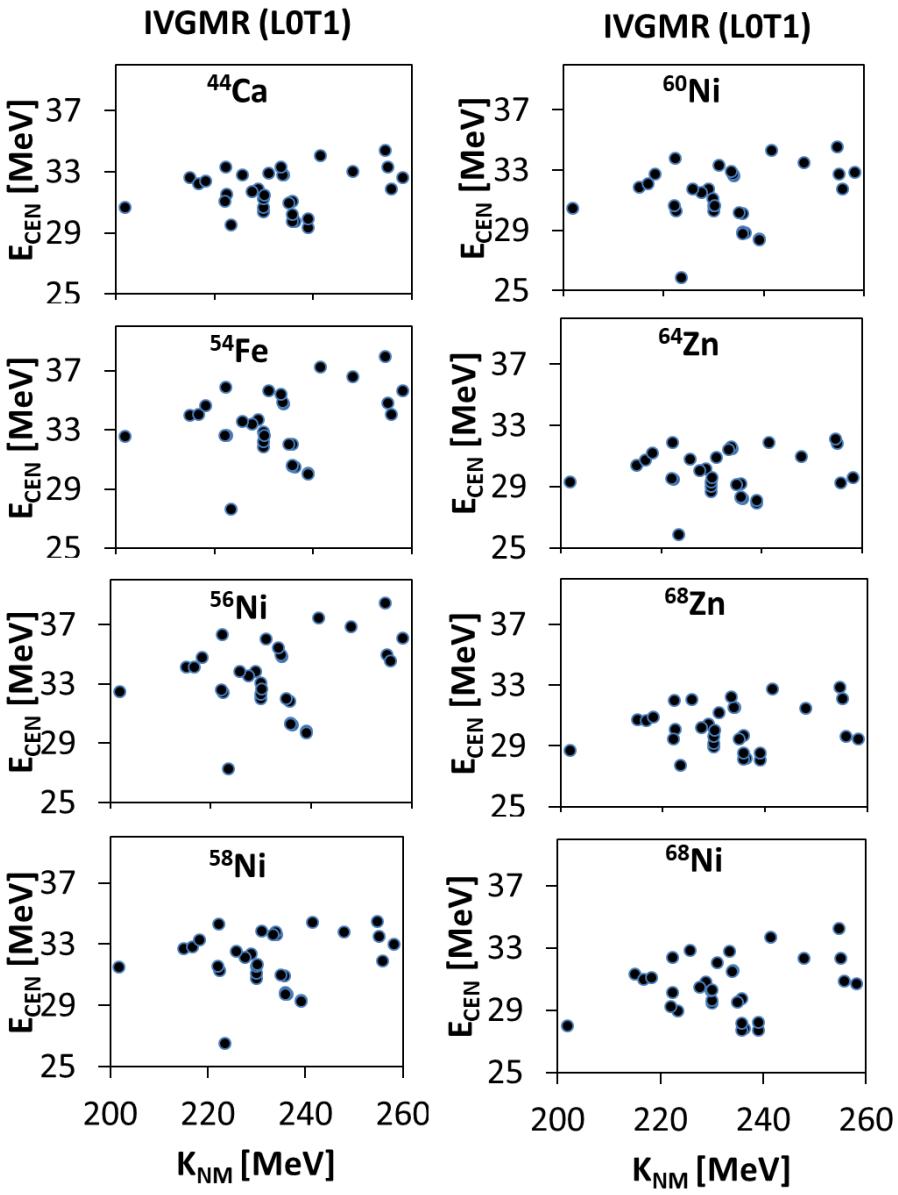

Figure 63 IVGMR E_{CEN} with K_{NM} in ^{44}Ca, ^{54}Fe, ^{64,68}Zn and ^{56,58,60,68}Ni. Similar to Figure 51 but for the IVGMR centroid energy as a function of the incompressibility coefficient. No correlation is obtained between the calculated values of E_{CEN} and K_{NM}, with a Pearson linear correlation coefficient C ~ 0.22.

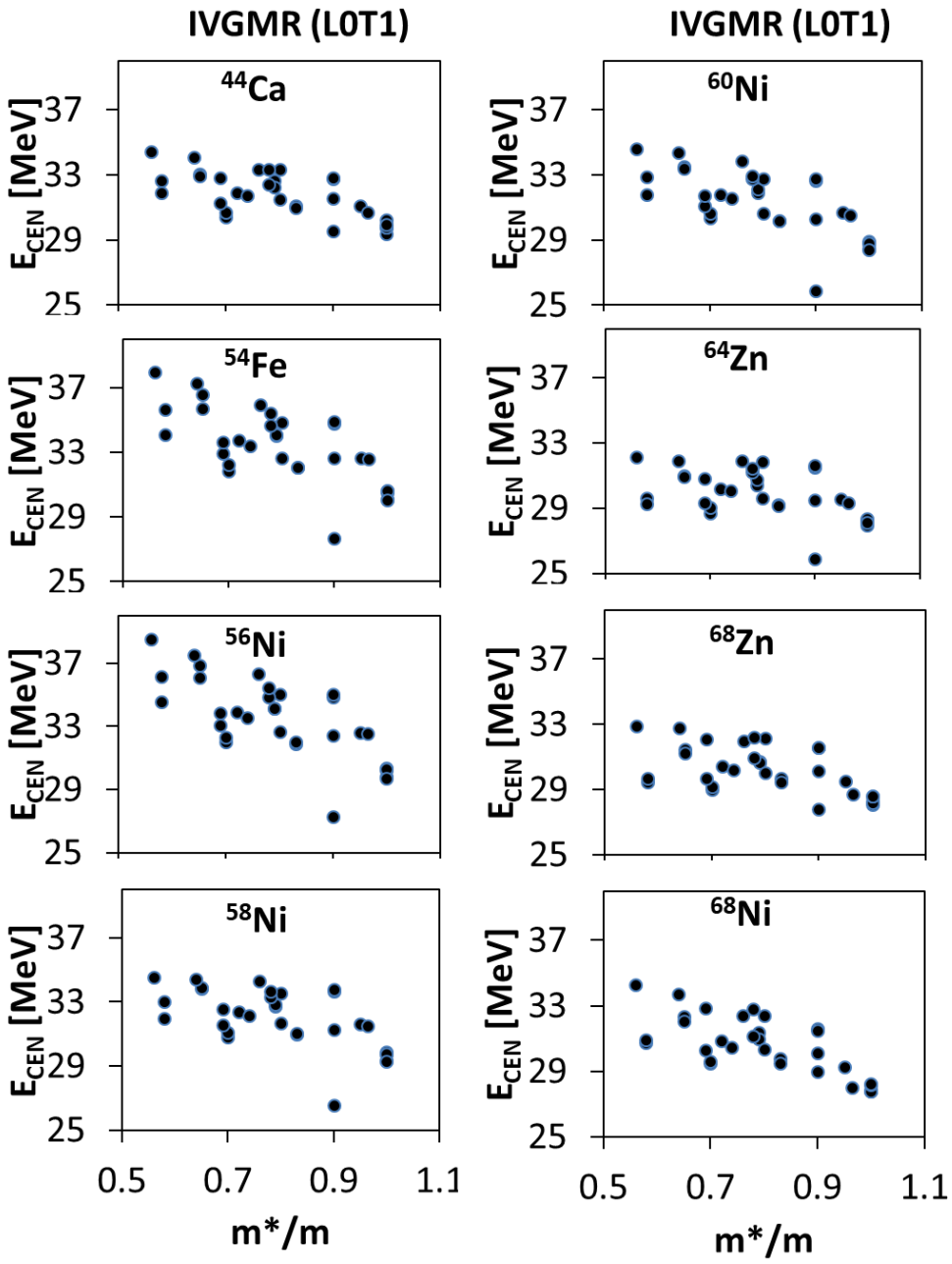

Figure 64 IVGMR E_{CEN} with m*/m in ^{44}Ca, ^{54}Fe, ^{64,68}Zn and ^{56,58,60,68}Ni. Similar to Figure 51 but for the IVGMR centroid energy as a function of the effective mass. A medium correlation is obtained between the calculated values of E_{CEN} and m*/m, with a Pearson linear correlation coefficient C ~ -0.64.

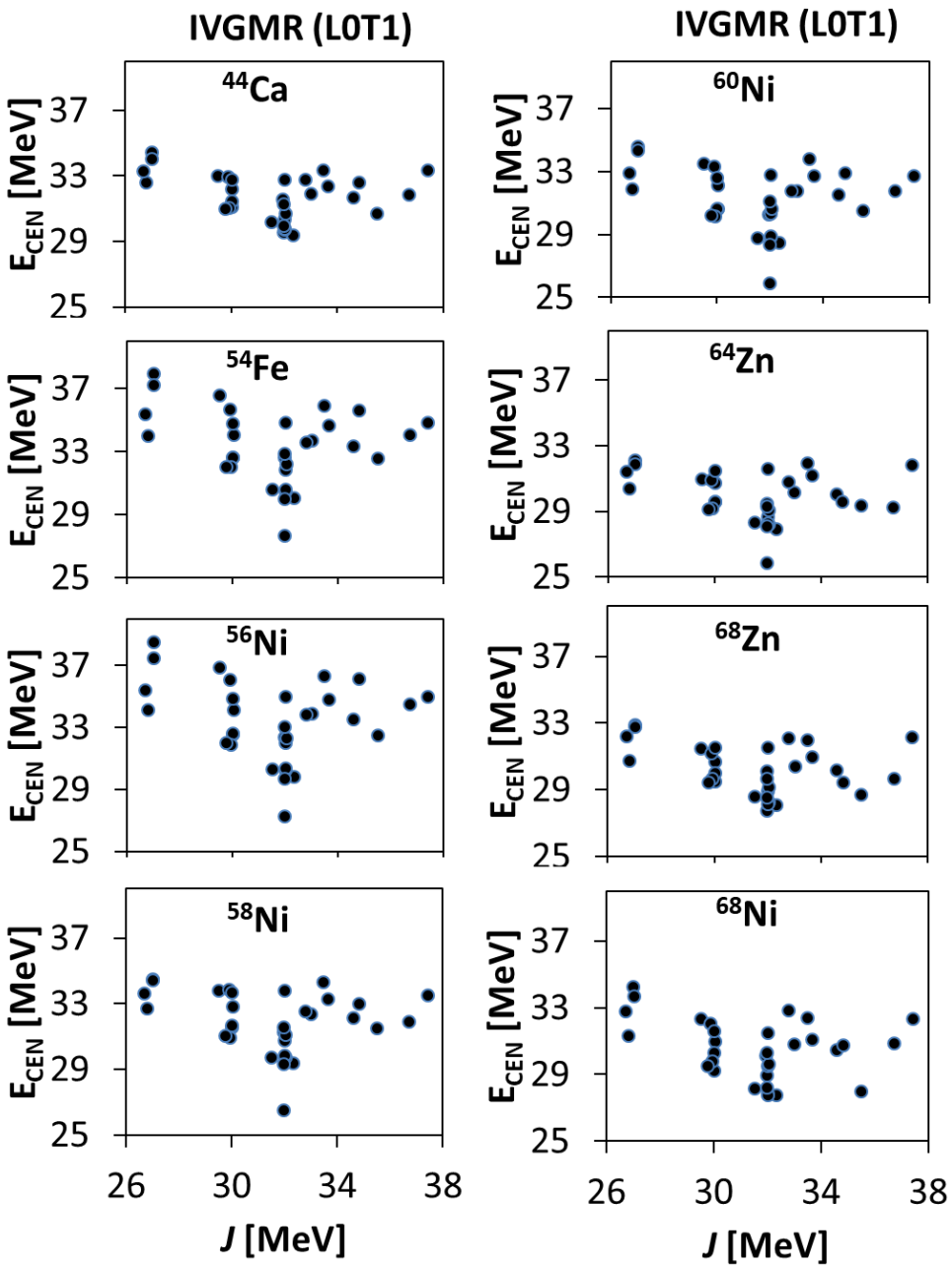

Figure 65 IVGMR E_{CEN} with J in ^{44}Ca, ^{54}Fe, ^{64,68}Zn and ^{56,58,60,68}Ni. Similar to Figure 51 but for the IVGMR centroid energy as a function of the symmetry energy at saturation density. No correlation is obtained between the calculated values of E_{CEN} and J, with a Pearson linear correlation coefficient C ~ -0.24.

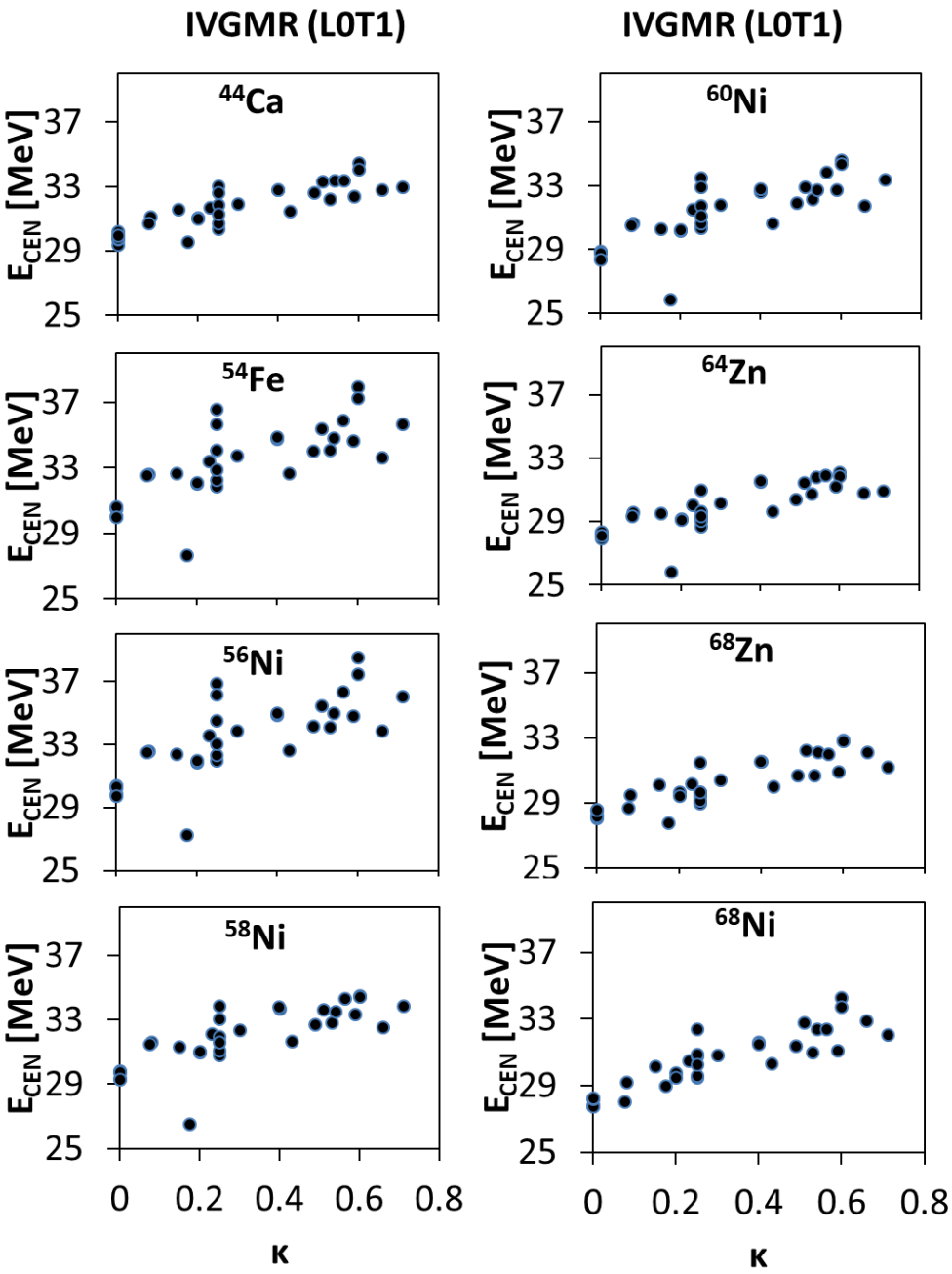

Figure 66 IVGMR E_{CEN} with κ in ^{44}Ca, ^{54}Fe, ^{64,68}Zn and ^{56,58,60,68}Ni. Similar to Figure 51 but for the IVGMR centroid energy as a function of the enhancement coefficient of the EWSR for the IVGDR. A strong correlation is obtained between the calculated values of E_{CEN} and κ, with a Pearson linear correlation coefficient C ~ 0.80.

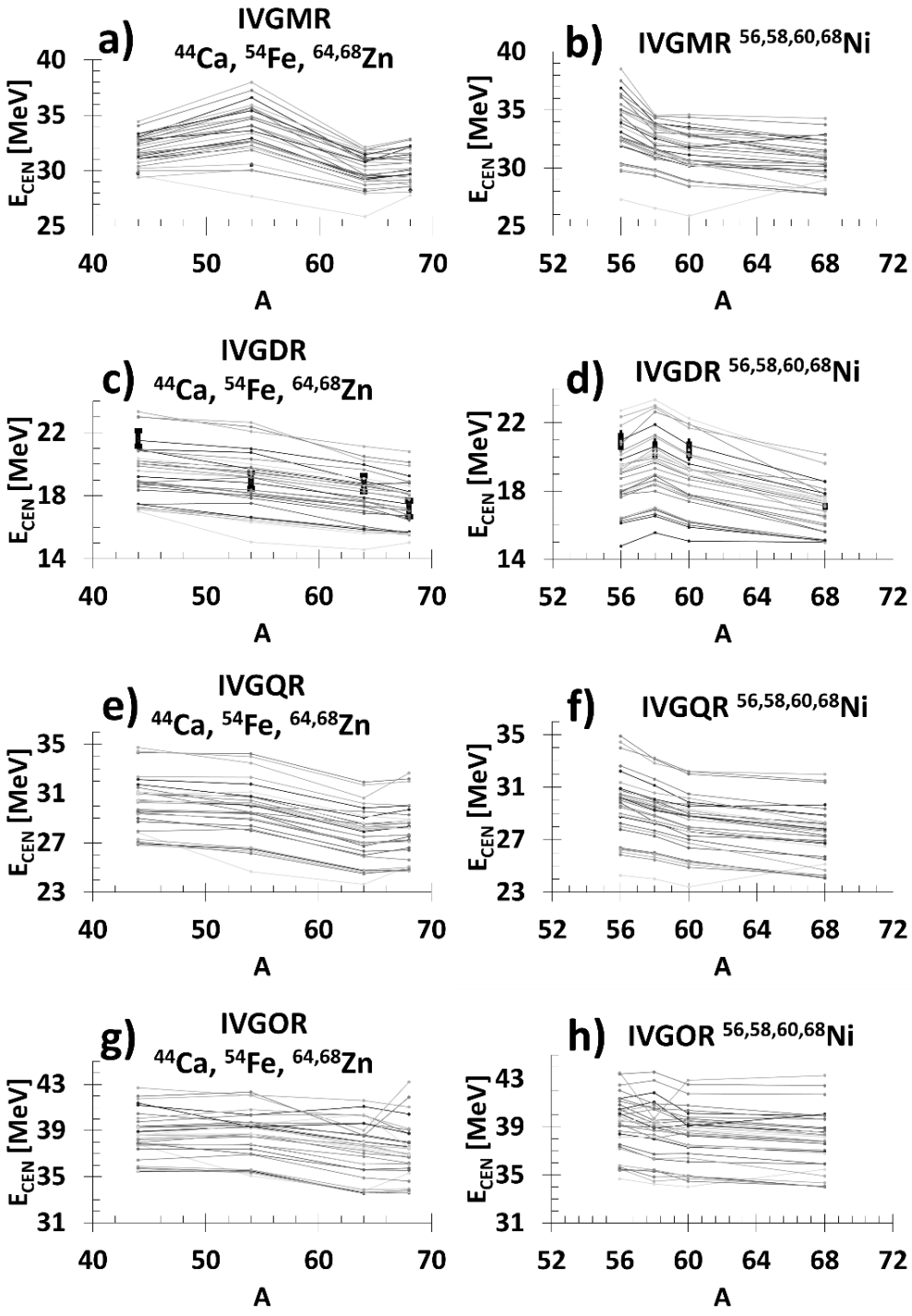

Figure 67 Isovector E_{CEN} overview in ^{44}Ca, ^{54}Fe, ^{64,68}Zn and ^{56,58,60,68}Ni. Similar to Figure 55 but for the isovector resonances L = 0 - 3. Experimental data is only available for the IVGDR.

Isovector Giant Dipole Resonance

The centroid energy, E_{CEN}, of the IVGDR is plotted in Figure 68 as a function of the symmetry energy coefficient, J. We obtained a weak correlation between the calculated values of E_{CEN} and J with C ~ -0.39. Next, we plot in Figure 69 the centroid energy as a function of the enhancement coefficient of the EWSR for the IVGDR, κ. We find a strong correlation between the calculated values of E_{CEN} and κ (Pearson linear correlation coefficient C ~ 0.80). As can be seen from the figure, most of the calculated results are below the experimental data for ^{44}Ca, ^{56,60}Ni and ^{64}Zn. Conversely, for ^{54}Fe and ^{68}Zn, good agreement is found between theory and experiment for interactions associated with κ as low as 0.1 while for ^{58,68}Ni interactions with κ = 0.25 - 0.7 give the closest results to the experimental values. Overall, we conclude that a range of κ = 0.25 - 0.7 is the best at reproducing most of the data, in agreement with Chapter III. In Figure 70 we plot the centroid energy as a function of the effective mass, m*/m. A medium correlation is obtained between the calculated values of E_{CEN} and m*/m (C ~ -0.62). Table 13 shows all the calculated Pearson linear correlation coefficients between the centroid energy of the IVGDR and NM properties. For completeness we show in Table 35 of the Appendix the calculated centroid energies for this giant resonance.

In Figure 67c the IVGDR centroid energies of ^{44}Ca, ^{54}Fe and ^{64,68}Zn are plotted as a function of their mass. We find a decreasing value for the centroid energy as the mass increases, with the experimental value for ^{64}Zn slightly higher than that of ^{54}Fe. In Figure 67d the centroid energies of the Ni isotopes are plotted as a function of mass. The calculated values of the centroid energy were obtained the highest for ^{58}Ni and a steady

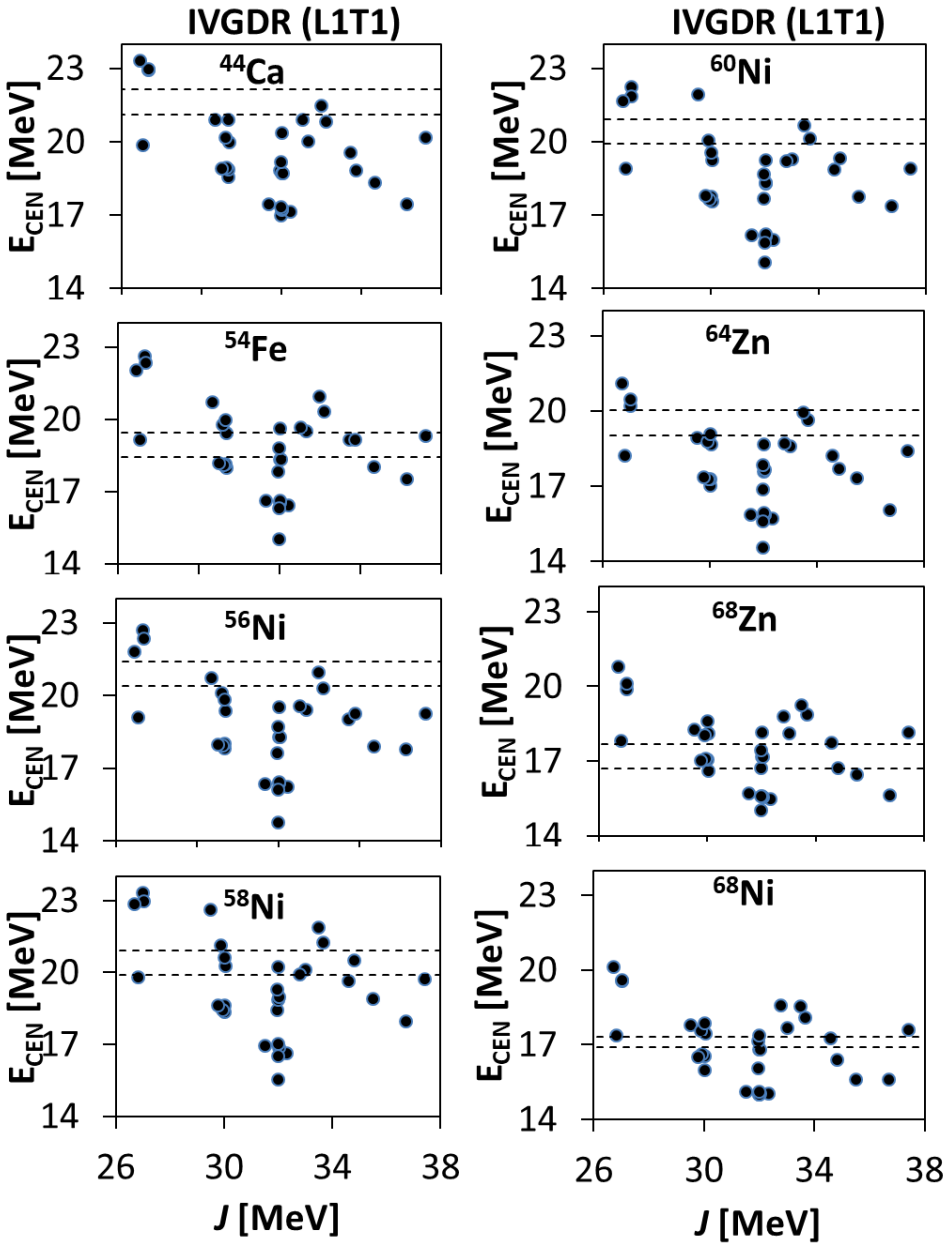

Figure 68 IVGDR E_{CEN} with J in ^{44}Ca, ^{54}Fe, ^{64,68}Zn and ^{56,58,60,68}Ni. Similar to Figure 51 but for the IVGDR centroid energy as a function of the symmetry energy at saturation density. Weak correlation is obtained between the calculated values of E_{CEN} and J, with a Pearson linear correlation coefficient C ~ -0.39.

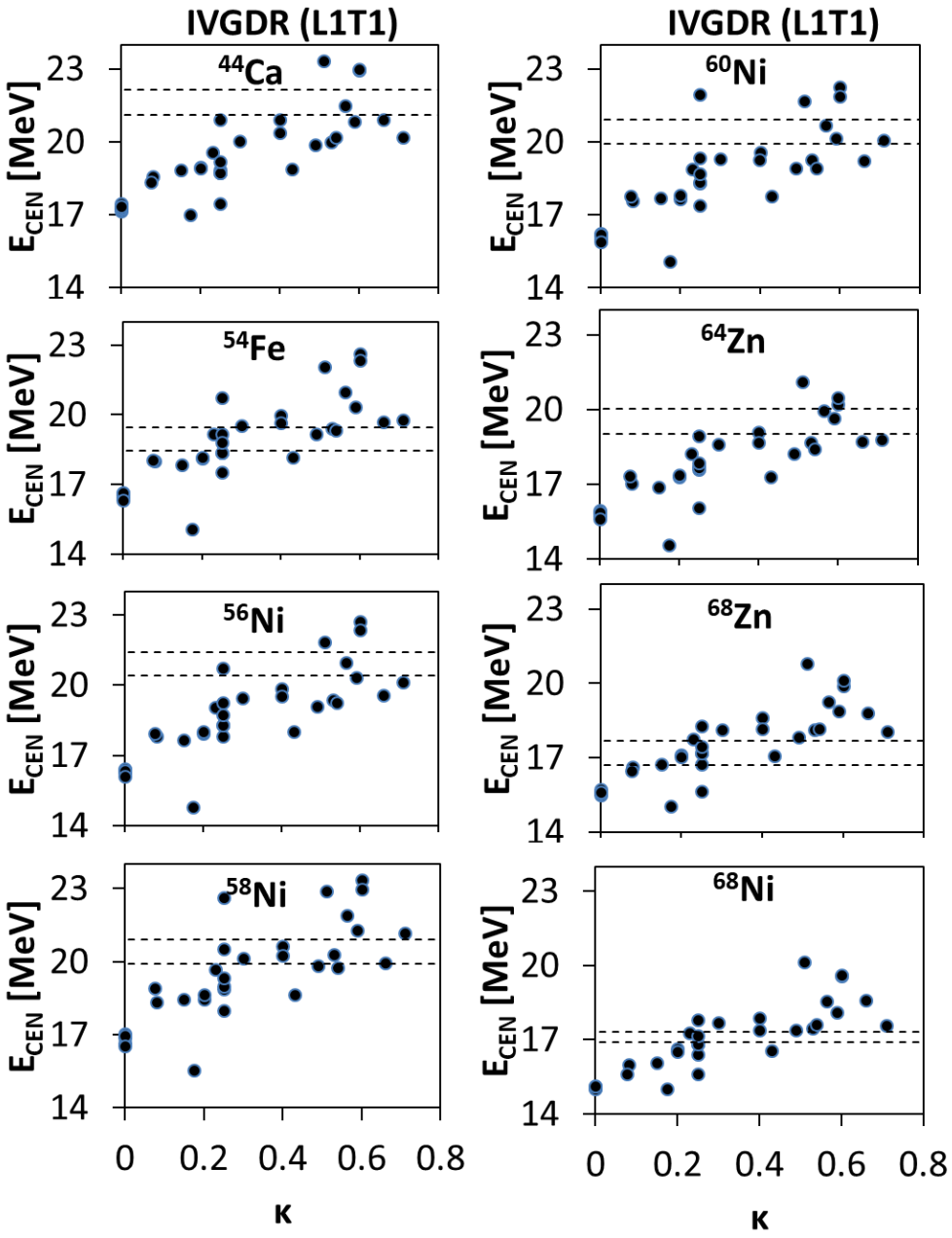

Figure 69 IVGDR E_{CEN} with κ in ^{44}Ca, ^{54}Fe, ^{64,68}Zn and ^{56,58,60,68}Ni. Similar to Figure 51 but for the IVGDR centroid energy as a function of the enhancement coefficient of the EWSR for the IVGDR. A strong correlation is obtained between the calculated values of E_{CEN} and κ, with a Pearson linear correlation coefficient C ~ 0.80.

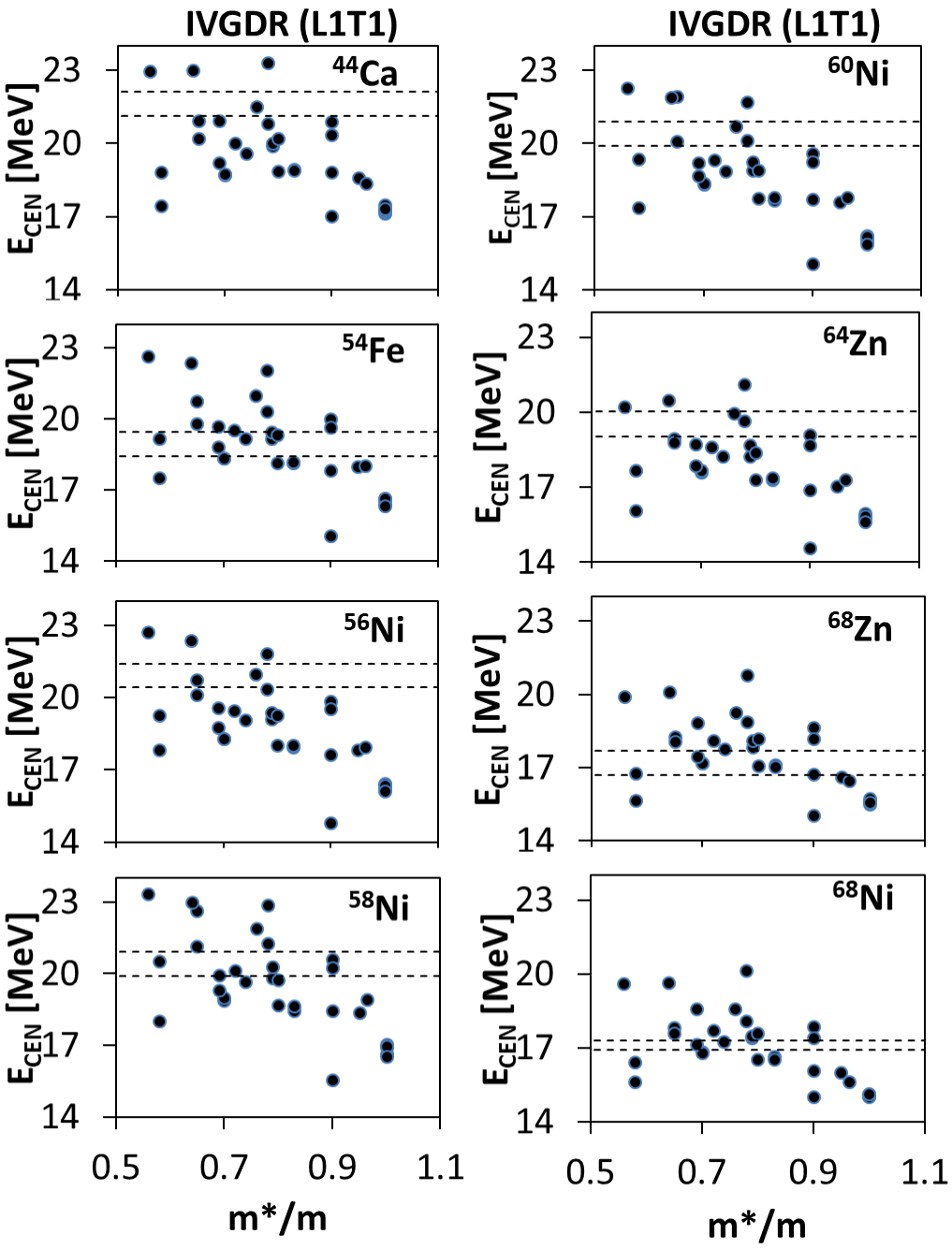

Figure 70 IVGDR E_{CEN} with m*/m in ^{44}Ca, ^{54}Fe, ^{64,68}Zn and ^{56,58,60,68}Ni. Similar to Figure 51 but for the IVGDR centroid energy as a function of the effective mass. A medium correlation is obtained between the calculated values of E_{CEN} and m*/m, with a Pearson linear correlation coefficient C ~ -0.62.

decrease from there. Experimentally on the other hand, the centroid energies of ^{56,58,60}Ni are all around 20.5 MeV while ^{68}Ni is substantially lower.

Isovector Giant Quadrupole Resonance

The centroid energy, E_{CEN}, of the IVGQR is plotted in Figure 71 as a function of the symmetry energy coefficient, J. No experimental data is available. The interactions predict the centroid energy to fall between 25 - 35 MeV. Weak correlation is found between the calculated values of E_{CEN} and J with a calculated Pearson linear correlation coefficient C ~ -0.38. We do not find any correlation between the centroid energies and the first or the second derivative of J (C ~ -0.34 and C ~ -0.17, respectively). We show, in Figure 72, the centroid energy as a function of the enhancement coefficient, κ, of the EWSR for the IVGDR. We obtained a strong correlation between the calculated values of E_{CEN} and κ (Pearson linear correlation coefficient C ~ 0.81). In Figure 73 we plotted E_{CEN} as a function of the effective mass, m*/m, we determined a medium correlation (C ~ -0.73) between the calculated values of E_{CEN} and m*/m. As can be seen from Table 13, no correlation is found between the calculated values of E_{CEN} and the remaining NM properties we considered. For completeness we show in Table 36 of the Appendix the calculated centroid energies for this giant resonance.

In Figure 67e the centroid energies of ^{44}Ca, ^{54}Fe and ^{64,68}Zn are plotted as a function of their mass for the IVGQR. We obtain a slow decrease in the value of the

centroid energy as the mass increases for most interactions. A similar result is obtained for the Ni isotopes shown in Figure 67f.

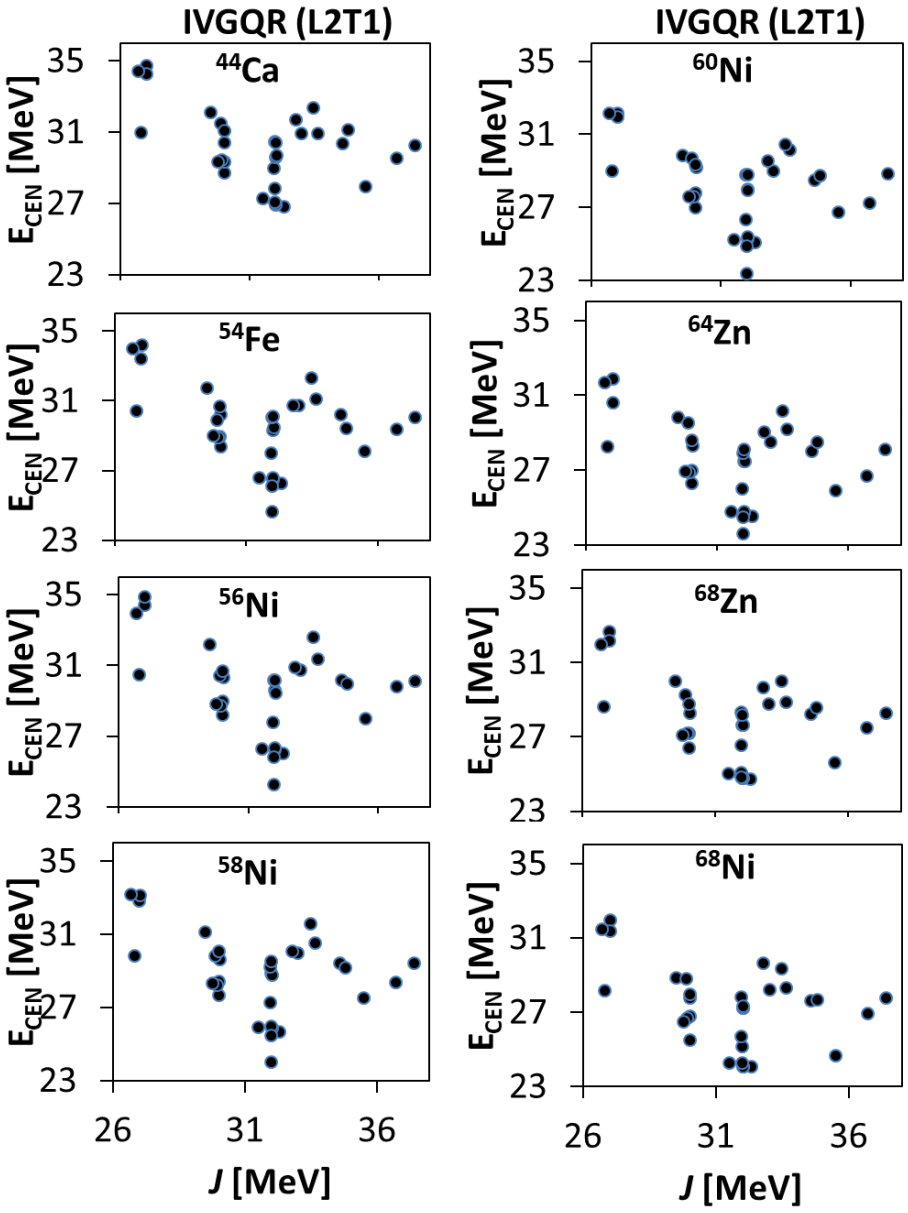

Figure 71 IVGQR E_{CEN} with J in ^{44}Ca, ^{54}Fe, ^{64,68}Zn and ^{56,58,60,68}Ni. Similar to Figure 51 but for the IVGQR centroid energy as a function of the symmetry energy at saturation density. Weak correlation is obtained between the calculated values of E_{CEN} and J, with a Pearson linear correlation coefficient C ~ -0.38.

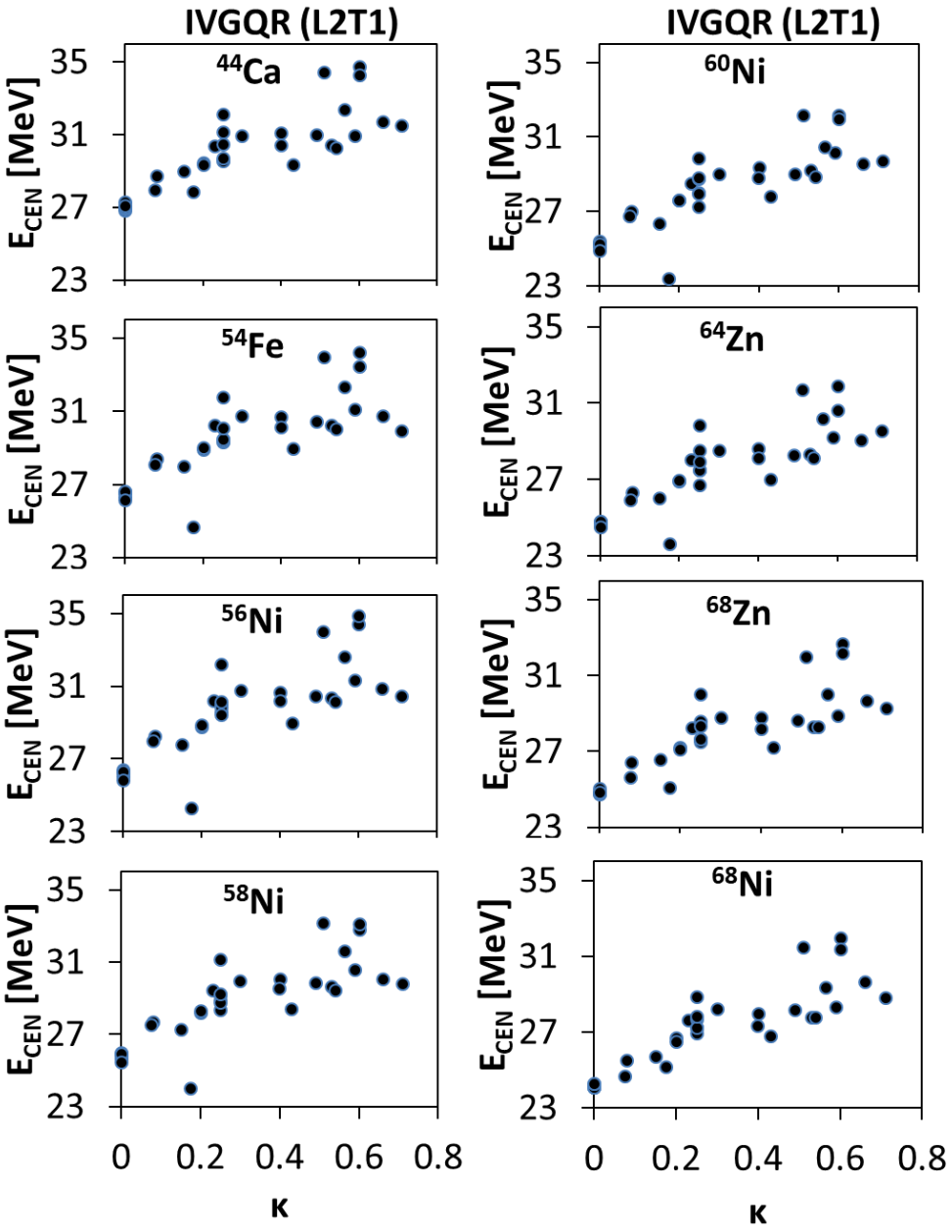

Figure 72 IVGQR E_{CEN} with κ in ^{44}Ca, ^{54}Fe, ^{64,68}Zn and ^{56,58,60,68}Ni. Similar to Figure 51 but for the IVGQR centroid energy as a function of the enhancement coefficient of the EWSR for the IVGDR. A strong correlation is obtained between the calculated values of E_{CEN} and κ, with a Pearson linear correlation coefficient C ~ 0.81.

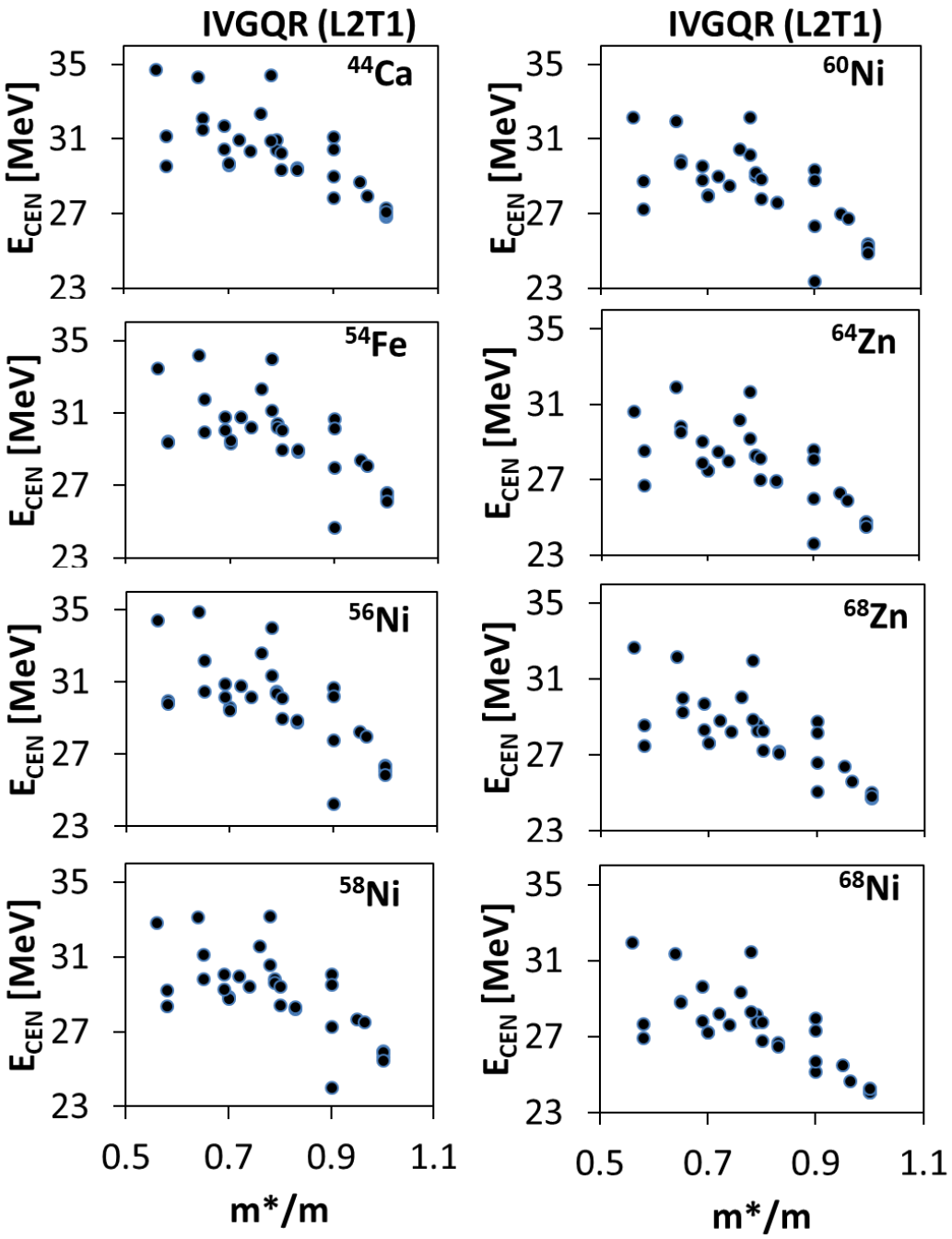

Figure 73 IVGQR E_{CEN} with m*/m in ^{44}Ca, ^{54}Fe, ^{64,68}Zn and ^{56,58,60,68}Ni. Similar to Figure 51 but for the IVGQR centroid energy as a function of the effective mass. A medium correlation is obtained between the calculated values of E_{CEN} and m*/m, with a Pearson linear correlation coefficient C ~ -0.73.

Isovector Giant Octupole Resonance

The centroid energy, E_{CEN}, of the IVGOR is plotted as a function of the symmetry energy coefficient, J, in Figure 74. No experimental data is available in this case. The calculations fall between 34 - 43 MeV. We do not find any correlation between the calculated values of E_{CEN} and J with a Pearson linear correlation coefficient C ~ -0.29. Similarly, we do not find any correlation between the centroid energies and the first or the second derivative of J (C ~ -0.18 and C ~ 0.01, respectively). We plot the centroid energy as a function of the enhancement coefficient, κ, of the EWSR for the IVGDR in Figure 75. A medium correlation was obtained between the calculated values of E_{CEN} and κ (C ~ 0.79). In Figure 76 we demonstrate the strong correlation (C ~ -0.82) between the centroid energy and the effective mass. No other correlations are found between the centroid energy and other NM properties, see Table 13. For completeness we show in Table 37 of the Appendix the calculated centroid energies for this giant resonance.

In Figure 67e the centroid energies of ^{44}Ca, ^{54}Fe and ^{64,68}Zn are plotted as a function of their mass for the IVGOR while the Ni isotopes are shown in Figure 67h. In both figures we find that the value of the centroid energy decreases slowly as the mass increases. However, we note that for the Ni isotopes some interactions predicted the centroid energy of ^{58}Ni above that of ^{56}Ni.

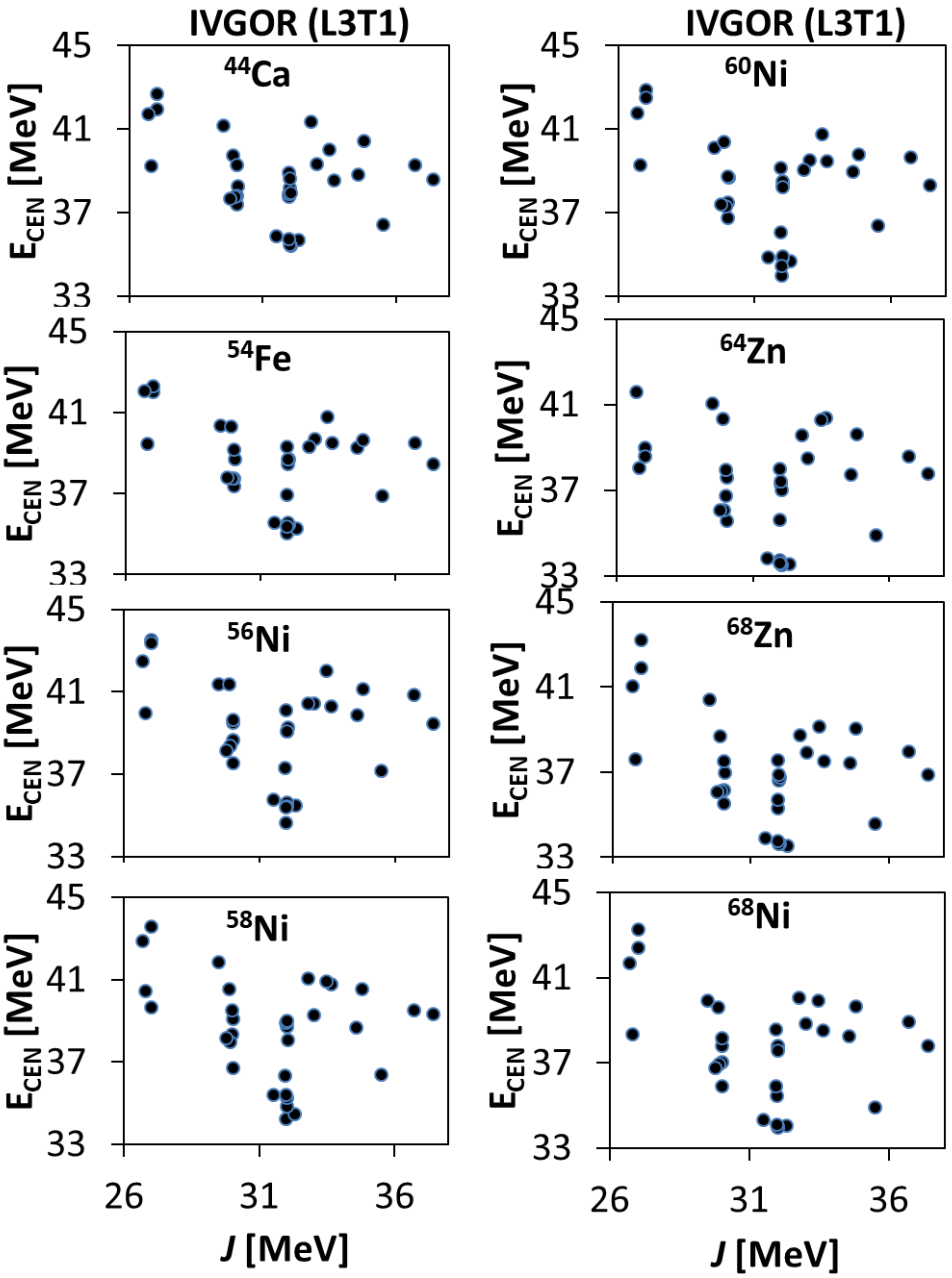

Figure 74 IVGOR E_{CEN} with J in ^{44}Ca, ^{54}Fe, ^{64,68}Zn and ^{56,58,60,68}Ni. Similar to Figure 51 but for the IVGOR centroid energy as a function of the symmetry energy at saturation density. Weak correlation is obtained between the calculated values of E_{CEN} and J, with a Pearson linear correlation coefficient C ~ -0.29.

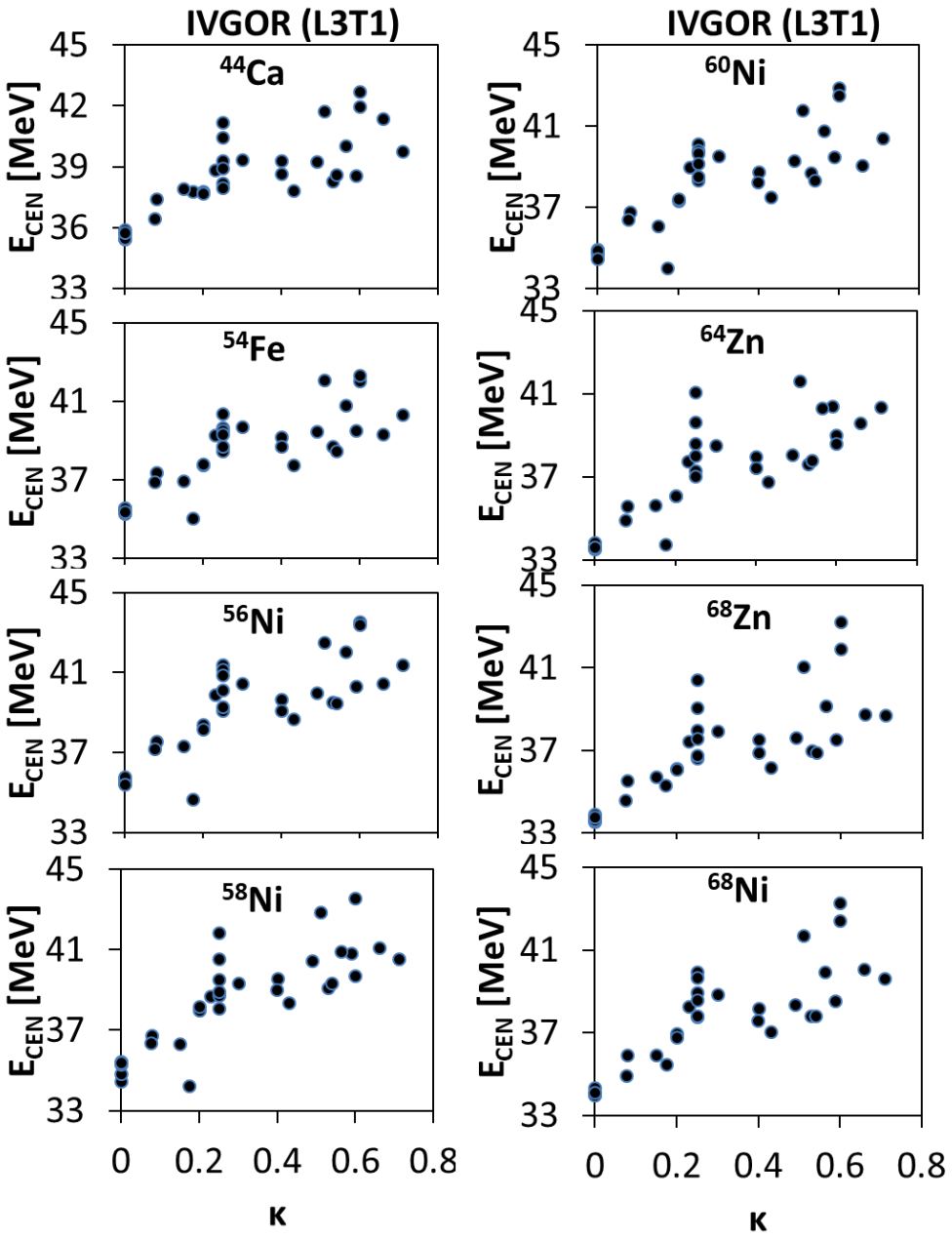

Figure 75 IVGOR E_{CEN} with κ in ^{44}Ca, ^{54}Fe, ^{64,68}Zn and ^{56,58,60,68}Ni. Similar to Figure 51 but for the IVGOR centroid energy as a function of the enhancement coefficient of the EWSR for the IVGDR. A strong correlation is obtained between the calculated values of E_{CEN} and κ, with a Pearson linear correlation coefficient C ~ 0.79.

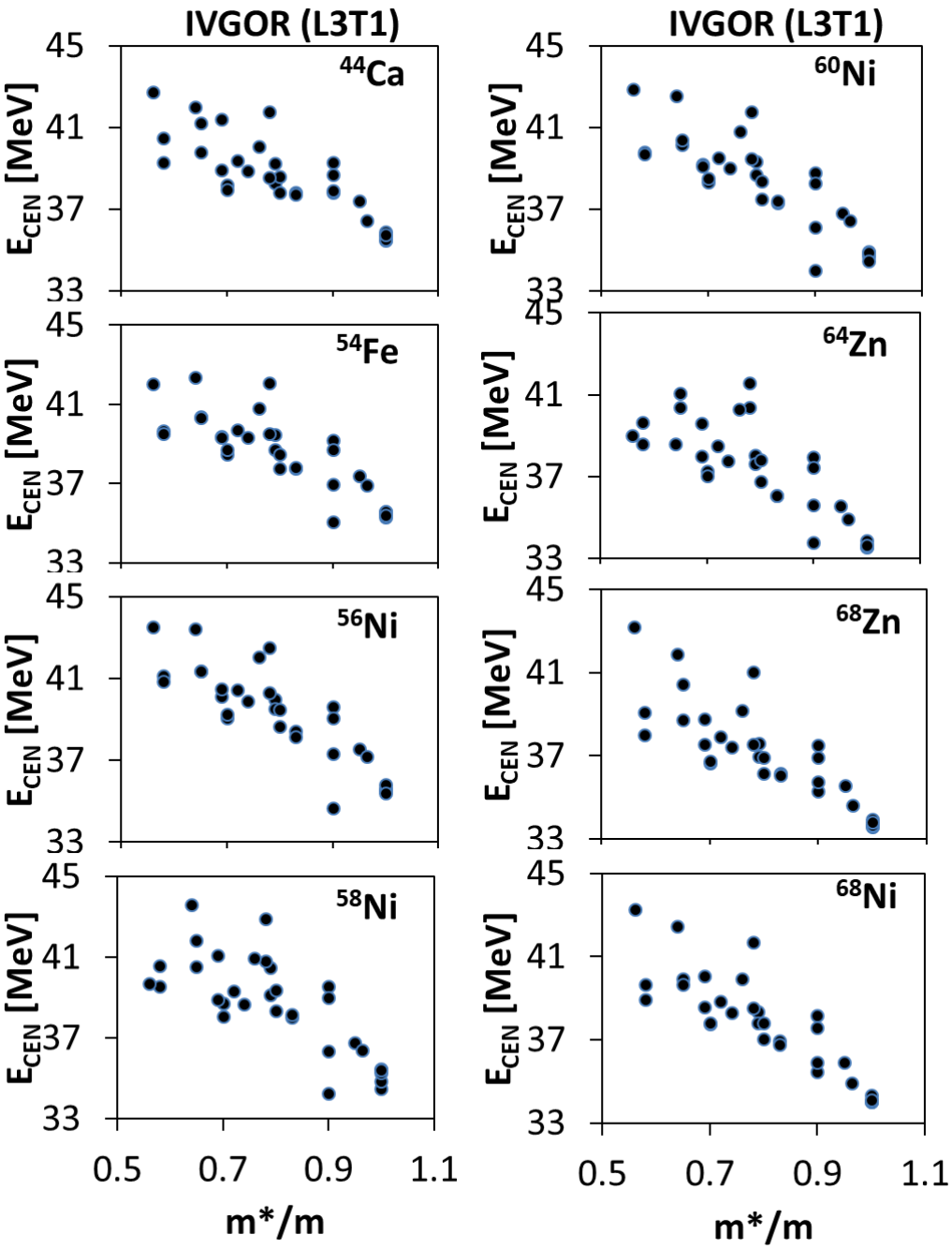

Figure 76 IVGOR E_{CEN} with m*/m in ^{44}Ca, ^{54}Fe, ^{64,68}Zn and ^{56,58,60,68}Ni. Similar to Figure 51 but for the IVGOR centroid energy as a function of the effective mass. A strong correlation is obtained between the calculated values of E_{CEN} and m*/m, with a Pearson linear correlation coefficient C ~ -0.82.

Conclusions

We have presented results of spherical Hartree-Fock based Random Phase Approximation (HF-RPA) calculations for centroid energies of isoscalar and isovector giant resonances of multipolarity L = 0 - 3. We adopted 33 different Skyrme-type effective nucleon-nucleon interactions covering a wide range of values of properties of nuclear matter, see Table 1 and Table 3 for details. In this chapter we focused our attention on the isotopes of ^{44}Ca, ^{54}Fe, ^{64,68}Zn and ^{56,58,60,68}Ni and compared with the recent experimental data to further investigate the disagreement with theoretical results obtained using only the KDE0v1 interaction [24,25]. We obtained good agreement between the calculated results and the experimental data for the ISGMR, ISGQR and IVGDR for some of the Skyrme interactions considered but not for the ISGDR and ISGOR. In agreement with Chapter III we found from the IVGDR that interactions associated with $\kappa = 0.25 - 0.70$ reproduce the data.

We also studied the sensitivity of the calculated values of the centroid energy of each giant resonance to each nuclear matter property, see Table 13. We found that the magnitude of the correlations obtained in this chapter were slightly lower than those of Chapter III and IV.

We note that in some cases, where the single-particle energies are very close to each other, we couldn't obtain a unique orbital configuration valid across all interactions. Therefore, when carrying out the calculations we chose to use the configuration that worked for the majority of the interactions considered for all cases.

CHAPTER VI

SUMMARY AND CONCLUSIONS

We have presented results of spherical Hartree-Fock based Random Phase Approximation calculations for isoscalar and isovector resonances of multipolarity L = 0 - 3 in the isotopes of ^{40,44,48}Ca, ^{54}Fe, ^{64,68}Zn ^{56,58,60,68}Ni, ^{90,92,94}Zr, ^{92,94,96,98,100}Mo,^{116}Sn, ^{144}Sm and ^{208}Pb. In our calculations we adopted 33 different Skyrme-type effective nucleon-nucleon interactions which cover a wide range of values of the properties of nuclear matter, see Table 1 and Table 3 for details, and compared our results with the experimental data shown in Table 6, Table 9 and Table 12. The goal of Chapter III was to determine constraints on nuclear matter properties using a wide range of nuclear masses while in Chapter IV and V we were mostly interested in studying the differences between the calculated and experimental centroid energies. In all cases we investigated the sensitivity of the centroid energy to nuclear matter properties by calculating the Pearson linear correlation coefficient. We also investigated the dependence of the centroid energy on the nuclear mass and the isospin asymmetry coefficient.

We summarize our findings of Chapter III, obtained from studying the spherical closed-shell nuclei ^{40,48}Ca, ^{68}Ni, ^{90}Zr, ^{116}Sn, ^{144}Sm and ^{208}Pb, below:

- We obtained strong, weak, and no correlations between the calculated values of E_{CEN} and the nuclear matter incompressibility coefficient, K_{NM}, for the

compression modes of the ISGMR (C ~ 0.87), ISGDR (C ~ 0.52) and the IVGMR (C ~ 0.23), respectively.

- We obtained strong correlations for the isoscalar dipole (C ~ -0.88), quadruple (C ~ -0.93), octupole (C ~ -0.96) and isovector octupole (C ~ -0.83) giant resonances and medium correlations for the isovector monopole (C ~ -0.70), dipole (C ~ -0.60) and quadrupole (C ~ -0.74) giant resonances between the calculated values of E_{CEN} and the effective mass m*/m.
- We obtained strong correlations between the calculated values of the centroid energy and the enhancement coefficient, κ, for the energy weighted sum rule of the isovector giant dipole resonance for all the isovector giant resonances considered here (C = 0.80 - 0.86).
- We didn't obtain any correlation between the calculated values of E_{CEN} and the symmetry energy coefficient, J, or its first derivative, L, for any of the isoscalar giant resonances considered.
- We obtained weak correlations between the calculated values of E_{CEN} and K_{sym}, the second derivative of the symmetry energy, for all the isoscalar giant resonances considered here for both the symmetric nucleus ^{40}Ca as well as for the asymmetric nuclei ^{48}Ca, ^{68}Ni, ^{90}Zr, ^{116}Sn, ^{144}Sm and ^{208}Pb.
- We found weak to no correlations between the calculated values of E_{CEN} and the symmetry energy coefficients for all the isovector resonances considered, see Table 7 for details.

- Considering the results of the centroid energy of the ISGMR, ISGQR, and IVGDR of ^{40,48}Ca, ^{68}Ni, ^{90}Zr, ^{116}Sn, ^{144}Sm and ^{208}Pb we find that the interactions associated with NM properties in the following range best reproduce the data: K_{NM} = 210 – 240 MeV, m*/m = 0.7 - 0.9 and κ = 0.25 - 0.70.

The constraints on NM properties that we obtained can be used to develop the next generation of energy density functionals by imposing them in the fits used to determine the values of the parameters of the Skyrme interaction. We note that although these constraints may depend on the specific form of the interaction adopted, it is known that the centroid energy of the ISGMR is sensitive to K_{NM} [18]. Similarly, the ISGQR is sensitive to the value of m*/m because the effective mass influences the spacing between major nuclear shells and therefore the distribution of the response function. We also point out that when determining the best range for the effective mass we emphasized the results of the heavier nuclei more. Lastly, the dependence of the centroid energy of the IVGDR on κ is expected from Eq. (2.58) for the isovector energy weighted sum rule which is given by a constant times (1+κ).

Next, we summarize our findings for Chapter IV, where we studied the isotopes of ^{92,94,96,98,100}Mo and ^{90,92,94}Zr:

- The disagreement between theoretical and experimental results of centroid energies, investigated in references [19–21], is also present for the 32 additional interactions we considered here.
- For the ISGMR the centroid energy measured at Texas A&M University (TAMU) of ^{92}Zr and ^{92}Mo are 0.35 MeV and 1.74 MeV above the centroid

energy of ^{90}Zr, in disagreement with the theory.

- For the ISGMR the centroid energy measured at Osaka University (Japan) of ^{92}Mo and ^{92}Zr is lower than that of ^{90}Zr [23], in agreement with the theoretical calculations using interactions with K_{NM} = 210 - 240MeV. However, more recently the same group published new results [91] which are best reproduced by interactions with $K_{NM} \sim 250$ MeV.
- For the ISGMR centroid energies of ^{94}Zr and ^{98,100}Mo we found the calculated values to be 1 – 3 MeV above the experimental result from TAMU for all 33 interactions adopted in this work. We note that to reproduce the experimental values an interaction with $K_{NM} < 200$ MeV would be required.
- We obtained a strong correlation between the calculated values of E_{CEN} and K_{NM} for the ISGMR, in agreement with our results from Chapter III. However, due to the disagreement with the experimental data we cannot extract constraints on K_{NM}.
- For the ISGDR centroid energies of ^{96,100}Mo and ^{92}Zr we found the theoretical values to be below the experimental result by up to 4 MeV, while for the centroid energies of ^{92,94,98}Mo and ^{90,94}Zr the results of the calculations were above the experimental values by almost 4 MeV in some cases.
- For the ISGQR centroid energies we found good agreement between the theoretical results and the experimental data, while for the ISGOR we found the theoretical result to be up to 8 MeV larger than the experimental data.
- For the IVGDR centroid energy, the only isovector resonance with available

experimental data, we obtained good agreement with the data for many of the interactions considered.

- We obtained strong correlation between the calculated values of E_{CEN} and κ for the IVGDR. Interactions with κ = 0.25 - 0.70 reproduce the data, in agreement with Chapter III findings.

Lastly, we summarize our findings from Chapter V for the isotopes of ^{44}Ca, ^{54}Fe, ^{64,68}Zn and ^{56,58,60,68}Ni:

- For the centroid energies of the ISGMR we obtained good agreement between the calculated and experimental values for interactions associated with a value of K_{NM} = 200 – 240 MeV, in agreement with chapter III. However, for the isotopes of ^{68}Zn and ^{68}Ni, our calculated values were 1 – 2 MeV from the experimental values.
- For the ISGDR we found that the calculations result in a lower value for the centroid energy than the data for ^{44}Ca, ^{58,60}Ni, while the opposite is seen for ^{64,68}Zn and the other nuclei studied in chapters III and IV.
- The experimental centroid energies of the ISGQR in ^{44}Ca and ^{54}Fe were obtained in good agreement with results of interactions associated with m*/m = 0.6 – 0.8. However, for the remaining isotopes, interactions associated with a higher value of m*/m reproduced the data. In particular the experimental centroid energy of ^{56,58,60}Ni and ^{64}Zn were reproduced by interactions with m*/m ~ 1.

- The calculated centroid energy of the ISGOR was obtained 2 – 7 MeV above the experimental data, available for ^{58,68}Ni, similar to the nuclei of Chapters III and IV.
- The calculated centroid energy of the IVGDR was below the experimental data of ^{44}Ca ^{56,60}Ni and ^{64}Zn for most of the interactions adopted here. However, for ^{54}Fe and ^{68}Zn the experimental centroid energy was reproduced by interactions with a value of κ as low as 0.1, while for ^{58,68}Ni interactions with κ = 0.25 – 0.7 gave the closest results to the experimental value.
- For the correlations between the calculated values of the centroid energy and the incompressibility coefficients of nuclear matter for the ISGMR, ISGDR and IVGMR we found medium, weak and no correlations, respectively, slightly lower than the correlations obtained for the other sets of nuclei considered in chapter III and IV.
- We obtained strong correlations between the calculated values of the centroid energy and the effective mass for the ISGDR, ISGQR, ISGOR, IVGOR while medium correlations were found for the IVGMR, IVGDR, IVGQR.
- We obtained strong correlations between the calculated values of the centroid energy and the enhancement coefficient, κ, of the EWSR for the IVGDR for the IVGMR, IVGDR and IVGQR while medium correlations were found for the IVGOR, all slightly less than chapter III and IV.
- For the centroid energy of the IVGDR we found that interactions with κ = 0.25 - 0.70 reproduced the data, in agreement with Chapter III findings.

- For the correlations between the calculated values of the centroid energy and the symmetry energy coefficients J, L and K_{sym} we found at most weak correlations.

We note that the magnitude of the Pearson linear correlations coefficients obtained for this set of nuclei was slightly lower than those of Chapter III and IV.

We could not reproduce the experimental centroid energy of the ISGMR for ^{68}Zn, ^{68}Ni, ^{94}Zr and ^{92,98,100}Mo with any of the interactions considered in this work. Further investigation is required into the issue. In particular, we recommend repeating the analysis of the experimental cross-section data [38,82] by replacing the semi-classical transition densities in the folding-model distorted wave Born approximation with the calculated HF-RPA microscopic transition densities. Another possibility is to go beyond the mean-field approximation by including nuclear structure effects [83–86].

REFERENCES

[1] A. Bohr and B. M. Mottelson, *Nuclear Structure II* (Benjamin, New York, 1975).

[2] P. Ring and P. Schuck, *The Nuclear Many-Body Problem* (Springer-Verlag, 1980).

[3] M. N. Harakeh and A. van der (Adriaan) Woude, *Giant Resonances : Fundamental High-Frequency Modes of Nuclear Excitation* (Oxford University Press, 2001).

[4] N. K. Glendenning, Phys. Rev. C **37**, 2733 (1988).

[5] J. M. Lattimer and M. Prakash, Phys. Rep. **442**, 109 (2007).

[6] G. C. Baldwin and G. S. Klaiber, Phys. Rev. **71**, 3 (1947).

[7] M. B. Lewis and F. E. Bertrand, Nucl. Phys. A **196**, 337 (1972).

[8] R. Pitthan and T. Walcher, Phys. Lett. B **36**, 563 (1971).

[9] D. H. Youngblood, C. M. Rozsa, J. M. Moss, D. R. Brown, and J. D. Bronson, Phys. Rev. Lett. **39**, 1188 (1977).

[10] T. H. R. Skyrme, Philos. Mag. **1**, 1043 (1956).

[11] D. Gogny, J. de. Boer, and H. J. Mang, *Proceedings of the International Conference on Nuclear Physics : Munich, August 27 - September 1, 1973* (North-Holland, 1973).

[12] J. . Walecka, Ann. Phys. (N. Y). **83**, 491 (1974).

[13] D. Vautherin and D. M. Brink, Phys. Rev. C **5**, 626 (1972).

[14] M. Dutra, O. Lourenço, J. S. Sá Martins, A. Delfino, J. R. Stone, and P. D. Stevenson, Phys. Rev. C **85**, 035201 (2012).

[15] W. D. Myers and W. J. Świątecki, Phys. Rev. C **57**, 3020 (1998).

[16] L. Satpathy, V. S. U. Maheswari, and R. C. Nayak, Phys. Rep. **319**, 85 (1999).

[17] S. Shlomo, V. M. Kolomietz, and G. Colò, Eur. Phys. J. A **30**, 23 (2006).

[18] B. K. Agrawal, S. Shlomo, and V. Kim Au, Phys. Rev. C **68**, 031304 (2003).

[19] D. H. Youngblood, Y.-W. Lui, Krishichayan, J. Button, G. Bonasera, and S. Shlomo, Phys. Rev. C **92**, 014318 (2015).

[20] J. Button, Y.-W. Lui, D. H. Youngblood, X. Chen, G. Bonasera, and S. Shlomo, Phys. Rev. C **94**, 034315 (2016).

[21] Krishichayan, Y.-W. W. Lui, J. Button, D. H. H. Youngblood, G. Bonasera, and S. Shlomo, Phys. Rev. C **92**, 044323 (2015).

[22] B. K. Agrawal, S. Shlomo, and V. K. Au, Phys. Rev. C **72**, 014310 (2005).

[23] Y. K. Gupta, U. Garg, K. B. Howard, J. T. Matta, M. Şenyiğit, M. Itoh, S. Ando, T. Aoki, A. Uchiyama, S. Adachi, M. Fujiwara, C. Iwamoto, A. Tamii, H. Akimune, C. Kadono, Y. Matsuda, T. Nakahara, T. Furuno, T. Kawabata, M. Tsumura, M. N. Harakeh, and N. Kalantar-Nayestanaki, Phys. Lett. B **760**, 482 (2016).

[24] J. Button, Y.-W. Lui, D. H. Youngblood, X. Chen, G. Bonasera, and S. Shlomo, Phys. Rev. C **96**, 054330 (2017).

[25] J. Button, Y.-W. Lui, D. H. Youngblood, X. Chen, G. Bonasera, and S. Shlomo, Phys. Rev. C (n.d.).

[26] P.-G. Reinhard, Ann. Phys. **504**, 632 (1992).

[27] T. Sil, S. Shlomo, B. K. Agrawal, and P.-G. Reinhard, Phys. Rev. C **73**, 034316 (2006).

[28] V. O. Nesterenko, J. Kvasil, and P.-G. Reinhard, Phys. Rev. C **66**, 044307 (2002).

[29] D. R. Hartree, Math. Proc. Cambridge Philos. Soc. **24**, 89 (1928).

[30] J. C. Slater, Phys. Rev. **32**, 339 (1928).

[31] J. C. Slater, Phys. Rev. **35**, 210 (1930).

[32] V. Fock, Zeitschrift For Phys. **61**, 126 (1930).

[33] E. Chabanat, P. Bonche, P. Haensel, J. Meyer, and R. Schaeffer, Nucl. Phys. A **627**, 710 (1997).

[34] W. Kohn, Rev. Mod. Phys. **71**, 1253 (1999).

[35] S. Shlomo, Reports Prog. Phys. **41**, 957 (1978).

[36] J. Suhonen, *From Nucleons to Nucleus* (Springer Berlin Heidelberg, Berlin, Heidelberg, 2007).

[37] G. Colò, L. Cao, N. Van Giai, and L. Capelli, Comput. Phys. Commun. **184**, 142 (2013).

[38] S. Shlomo and A. I. Sanzhur, Phys. Rev. C **65**, 044310 (2002).

[39] B. K. Agrawal, S. Shlomo, and A. I. Sanzhur, Phys. Rev. C **67**, 034314 (2003).

[40] E. Lipparini and S. Stringari, Phys. Rep. **175**, 103 (1989).

[41] N. Van Giai and H. Sagawa, Phys. Lett. B **106**, 379 (1981).

[42] J. Bartel, P. Quentin, M. Brack, C. Guet, and H.-B. Håkansson, Nucl. Phys. A **386**, 79 (1982).

[43] P.-G. Reinhard and H. Flocard, Nucl. Phys. A **584**, 467 (1995).

[44] P. Klupfel, P.-G. Reinhard, T. J. Burvenich, and J. A. Maruhn, Phys. Rev. C **79**, 034310 (2009).

[45] N. Lyutorovich, V. I. Tselyaev, J. Speth, S. Krewald, F. Grümmer, and P.-G. Reinhard, Phys. Rev. Lett. **109**, 092502 (2012).

[46] E. Chabanat, P. Bonche, P. Haensel, J. Meyer, and R. Schaeffer, Nucl. Phys. A **635**, 231 (1998).

[47] L. Bennour, P.-H. Heenen, P. Bonche, J. Dobaczewski, and H. Flocard, Phys. Rev. C **40**, 2834 (1989).

[48] P.-G. Reinhard, D. J. Dean, W. Nazarewicz, J. Dobaczewski, J. A. Maruhn, and M. R. Strayer, Phys. Rev. C **60**, 014316 (1999).

[49] L. G. Cao, U. Lombardo, C. W. Shen, and N. Van Giai, Phys. Rev. C **73**, 014313 (2006).

[50] L.-W. Chen, C. M. Ko, B.-A. Li, and J. Xu, Phys. Rev. C **82**, 024321 (2010).

[51] A. W. Steiner, M. Prakash, J. M. Lattimer, and P. J. Ellis, Phys. Rep. **411**, 325 (2005).

[52] P. A. M. Guichon, H. H. Matevosyan, N. Sandulescu, and A. W. Thomas, Nucl. Phys. A **772**, 1 (2006).

[53] F. Tondeur, M. Brack, M. Farine, and J. M. Pearson, Nucl. Phys. A **420**, 297 (1984).

[54] B. A. Brown, G. Shen, G. C. Hillhouse, J. Meng, and A. Trzci, Phys. Rev. C **76**, 034305 (2007).

[55] J. Friedrich and P.-G. Reinhard, Phys. Rev. C **33**, 335 (1986).

[56] G. Bonasera, M. R. Anders, and S. Shlomo, Phys. Rev. C **98**, 054316 (2018).

[57] M. Vandebrouck, J. Gibelin, E. Khan, N. L. Achouri, H. Baba, D. Beaumel, Y. Blumenfeld, M. Caamaño, L. Càceres, G. Colò, F. Delaunay, B. Fernandez-Dominguez, U. Garg, G. F. Grinyer, M. N. Harakeh, N. Kalantar-Nayestanaki, N. Keeley, W. Mittig, J. Pancin, R. Raabe, T. Roger, P. Roussel-Chomaz, H. Savajols, O. Sorlin, C. Stodel, D. Suzuki, and J. C. Thomas, Phys. Rev. Lett. **113**, 032504 (2014).

[58] D. H. Youngblood, Y.-W. Lui, and H. L. Clark, Phys. Rev. C **63**, 067301 (2001).

[59] Y.-W. Lui, D. H. Youngblood, S. Shlomo, X. Chen, Y. Tokimoto, Krishichayan, M. Anders, and J. Button, Phys. Rev. C **83**, 044327 (2011).

[60] Krishichayan, Y.-W. Lui, J. Button, D. H. Youngblood, G. Bonasera, and S. Shlomo, Phys. Rev. C **92**, 044323 (2015).

[61] D. H. Youngblood, Y.-W. Lui, H. L. Clark, B. John, Y. Tokimoto, and X. Chen, Phys. Rev. C **69**, 034315 (2004).

[62] D. H. Youngblood, Y.-W. Lui, and H. L. Clark, Phys. Rev. C **65**, 034302 (2002).

[63] Y.-W. Lui, H. L. Clark, and D. H. Youngblood, Phys. Rev. C **61**, 067307 (2000).

[64] D. H. Youngblood, Y.-W. Lui, and H. L. Clark, Phys. Rev. C **60**, 014304 (1999).

[65] A. Veyssière, H. Beil, R. Bergère, P. Carlos, A. Leprêtre, and A. De Miniac, Nucl. Phys. A **227**, 513 (1974).

[66] D. A. Sims, G. J. O'Keefe, R. P. Rassool, A. Kuzin, M. N. Thompson, J.-O. Adler, B.-E. Andersson, K. G. Fissum, K. Hansen, L. Isaksson, B. Nilsson, H.

Ruijter, A. Sandell, B. Schröder, J. R. M. Annand, G. I. Crawford, P. D. Harty, J. C. McGeorge, and G. J. Miller, Phys. Rev. C **55**, 1288 (1997).

[67] G. J. O'Keefe, M. N. Thompson, Y. I. Assafiri, R. E. Pywell, and K. Shoda, Nucl. Phys. A **469**, 239 252 (1987).

[68] N. D. M. Rossi, P. Adrich, F. Aksouh, H. Alvarez-Pol, T. Aumann, J. Benlliure, M. Böhmer, K. Boretzky, E. Casarejos, M. Chartier, A. Chatillon, D. Cortina-Gil, U. Datta Pramanik, H. Emling, O. Ershova, B. Fernandez-Dominguez, H. Geissel, M. Gorska, M. Heil, H. T. Johansson, A. Junghans, A. Kelic-Heil, O. Kiselev, A. Klimkiewicz, J. V Kratz, R. Krücken, N. Kurz, Y. A. Litvinov, K. Mahata, P. Maierbeck, A. Movsesyan, T. Nilsson, C. Nociforo, R. Palit, S. Paschalis, R. Plag, R. Reifarth, H. Scheit, H. Simon, K. Sümmerer, A. Wagner, W. Walu, H. Weick, and M. Winkler, (n.d.).

[69] B. L. Berman, J. T. Caldwell, R. R. Harvey, M. A. Kelly, R. L. Bramblett, and S. C. Fultz, Phys. Rev. **162**, 1098 (1967).

[70] S. C. Fultz, B. L. Berman, J. T. Caldwell, R. L. Bramblett, and M. A. Kelly, Phys. Rev. **186**, 1255 (1969).

[71] P. Carlos, H. Beil, R. Bergère, A. Leprêtre, A. De Miniac, and A. Veyssière, Nucl. Phys. A **225**, 171 (1974).

[72] X. Roca-Maza, M. Brenna, B. K. Agrawal, P. F. Bortignon, G. Colò, L.-G. Cao, N. Paar, and D. Vretenar, Phys. Rev. C **87**, 034301 (2013).

[73] A. Tamii, I. Poltoratska, P. von Neumann-Cosel, Y. Fujita, T. Adachi, C. A. Bertulani, J. Carter, M. Dozono, H. Fujita, K. Fujita, K. Hatanaka, D. Ishikawa,

M. Itoh, T. Kawabata, Y. Kalmykov, A. M. Krumbholz, E. Litvinova, H. Matsubara, K. Nakanishi, R. Neveling, H. Okamura, H. J. Ong, B. Özel-Tashenov, V. Y. Ponomarev, A. Richter, B. Rubio, H. Sakaguchi, Y. Sakemi, Y. Sasamoto, Y. Shimbara, Y. Shimizu, F. D. Smit, T. Suzuki, Y. Tameshige, J. Wambach, R. Yamada, M. Yosoi, and J. Zenihiro, Phys. Rev. Lett. **107**, 062502 (2011).

[74] Y.-W. Lui, D. H. Youngblood, S. Shlomo, X. Chen, Y. Tokimoto, Krishichayan, M. Anders, and J. Button, Phys. Rev. C **83**, 044327 (2011).

[75] J. P. Blaizot, Phys. Rep. **64**, 171 (1980).

[76] U. Garg and G. Colò, Prog. Part. Nucl. Phys. **101**, 55 (2018).

[77] Y.-W. Lui, D. H. Youngblood, S. Shlomo, X. Chen, Y. Tokimoto, Krishichayan, M. Anders, and J. Button, Phys. Rev. C **83**, 044327 (2011).

[78] M. R. Anders, S. Shlomo, T. Sil, D. H. Youngblood, Y.-W. Lui, and Krishichayan, Phys. Rev. C **87**, 024303 (2013).

[79] H. Krivine, J. Treiner, and O. Bohigas, Nucl. Phys. A **336**, 155 (1980).

[80] G. Bonasera, S. Shlomo, D. H. Youngblood, Y.-W. Lui, Krishichayan, and J. Button, Nucl. Phys. A (n.d.).

[81] H. Beil, R. Bergère, P. Carlos, A. Leprêtre, A. De Miniac, and A. Veyssière, Nucl. Phys. A **227**, 427 (1974).

[82] A. Kolomiets, O. Pochivalov, and S. Shlomo, Phys. Rev. C **61**, 034312 (2000).

[83] S. Kamerdzhiev, J. Speth, and G. Tertychny, Phys. Rep. **393**, 1 (2004).

[84] V. M. Kolomietz and S. Shlomo, Phys. Rev. C **61**, 064302 (2000).

[85] D. C. Fuls, V. M. Kolomietz, S. V. Lukyanov, and S. Shlomo, EPL (Europhysics Lett. **90**, 20006 (2010).

[86] V. M. Kolomietz and S. Shlomo, Phys. Rep. **390**, 133 (2004).

[87] Y.-W. Lui, D. H. Youngblood, H. L. Clark, Y. Tokimoto, and B. John, Phys. Rev. C **73**, 014314 (2006).

[88] C. Monrozeau, E. Khan, Y. Blumenfeld, C. E. Demonchy, W. Mittig, P. Roussel-Chomaz, D. Beaumel, M. Caamaño, D. Cortina-Gil, J. P. Ebran, N. Frascaria, U. Garg, M. Gelin, A. Gillibert, D. Gupta, N. Keeley, F. Maréchal, A. Obertelli, J.-A. Scarpaci, M. Gelin, J. P. Ebran, W. Mittig, Y. Blumenfeld, J.-A. Scarpaci, F. Maréchal, C. Monrozeau, E. Khan, D. Beaumel, A. Obertelli, D. Cortina-Gil, P. Roussel-Chomaz, D. Gupta, N. Keeley, N. Frascaria, C. E. Demonchy, M. Caamaño, and U. Garg, Phys. Rev. Lett. **100**, 042501 (2008).

[89] M. Vandebrouck, J. Gibelin, E. Khan et al., Phys. Rev. C **92**, 024316 (2015).

[90] CDFE - Cent. Photonuclear Exp. Data - http://cdfe.sinp.msu.ru/ (2019).

[91] Y. K. Gupta, K. B. Howard, U. Garg, J. T. Matta, M. Şenyiğit, M. Itoh, S. Ando, T. Aoki, A. Uchiyama, S. Adachi, M. Fujiwara, C. Iwamoto, A. Tamii, H. Akimune, C. Kadono, Y. Matsuda, T. Nakahara, T. Furuno, T. Kawabata, M. Tsumura, M. N. Harakeh, and N. Kalantar-Nayestanaki, Phys. Rev. C **97**, 064323 (2018).

APPENDIX

Table 14 ISGMR E_{CEN} (in MeV) for $^{40,48}Ca$, ^{68}Ni, ^{90}Zr, ^{116}Sn, ^{144}Sm and ^{208}Pb.

ISGMR	^{40}Ca	^{48}Ca	^{68}Ni	^{90}Zr	^{116}Sn	^{144}Sm	^{208}Pb
SGII	21.48	20.76	18.71	17.93	16.39	15.19	13.59
KDE0	21.31	20.31	18.62	17.99	16.54	15.46	13.78
KDE0v1	21.25	20.22	18.56	18.01	16.51	15.42	13.78
SKM*	20.72	20.25	18.27	17.64	16.15	15.08	13.40
Sk255	22.25	20.99	19.33	18.78	17.23	16.09	14.24
SkI3	22.67	22.68	20.08	19.65	17.82	16.73	14.93
SkI4	22.36	21.34	19.67	18.98	17.43	16.21	14.49
SkI5	22.75	21.90	19.82	19.22	17.52	16.43	14.50
SV-bas	21.57	20.82	18.89	18.35	16.84	15.67	14.02
SV-min	21.05	20.28	18.46	17.86	16.40	15.29	13.63
SV-sym32	21.53	20.77	18.86	18.30	16.78	15.65	13.89
SV-m56-O	22.81	21.78	19.77	19.26	17.61	16.51	14.71
SV-m64-O	22.16	21.24	19.29	18.73	17.15	16.03	14.33
SLy4	20.87	19.83	18.34	17.72	16.32	15.28	13.67
SLy5	21.29	20.22	18.65	17.96	16.53	15.43	13.79
SLy6	21.34	20.63	18.77	18.16	16.64	15.57	13.91
SkMP	21.36	21.18	18.89	18.31	16.72	15.58	13.92
SKO	21.29	19.78	18.98	17.61	16.42	15.17	13.44
SKO`	21.19	20.10	18.55	17.82	16.33	15.15	13.32
LNS	21.55	21.09	18.94	18.23	16.59	15.45	13.65
MSL0	21.02	20.24	18.60	17.91	16.46	15.34	13.67
NRAPR	21.67	19.60	18.44	17.72	16.26	15.21	13.41
SQMC650	20.30	20.03	17.97	17.63	16.14	15.09	13.43
SQMC700	21.39	20.99	18.71	18.24	16.60	15.47	13.76
SkT1	21.63	20.58	18.90	18.23	16.81	15.65	13.92
SkT2	21.56	20.64	18.89	18.24	16.79	15.68	13.93
SkT3	21.57	20.57	18.90	18.24	16.77	15.63	13.85
SkT8	21.78	20.57	18.98	18.29	16.81	15.69	13.95
SkT9	21.58	20.62	18.89	18.23	16.81	15.64	13.92
SkT1*	21.37	20.18	18.71	18.06	16.66	15.57	13.83
SkT3*	21.65	20.28	18.98	18.12	16.70	15.55	13.74
Skxs20	19.85	19.42	17.46	16.99	15.53	14.42	12.90
Z-sigma	21.77	20.79	18.92	18.49	16.89	15.83	14.10
Exp.	19.18	19.88	21.90	17.88	15.85	15.40	13.96
Error	0.37	0.16	1.90	0.13	0.20	0.30	0.20

Table 15 ISGDR E_{CEN} (in MeV) for $^{40,48}Ca$, ^{68}Ni, ^{90}Zr, ^{116}Sn, ^{144}Sm and ^{208}Pb.

ISGDR	^{40}Ca	^{48}Ca	^{68}Ni	^{90}Zr	^{116}Sn	^{144}Sm	^{208}Pb
SGII	29.77	30.57	31.31	29.29	27.21	26.01	24.14
KDE0	29.43	30.32	31.05	29.93	27.50	26.45	24.92
KDE0v1	29.26	30.13	30.86	29.77	27.40	26.48	24.76
SKM*	29.03	29.93	30.14	28.83	26.65	25.50	23.93
Sk255	29.69	30.35	30.94	29.80	27.78	26.56	24.58
SkI3	30.00	30.95	32.89	31.91	29.28	27.97	25.58
SkI4	29.84	30.62	32.43	30.94	28.40	27.31	25.44
SkI5	30.32	31.01	32.53	31.56	28.76	27.84	25.75
SV-bas	28.89	30.07	30.37	29.02	27.02	25.82	24.02
SV-min	28.56	29.45	29.49	28.34	26.42	25.27	23.42
SV-sym32	28.85	30.05	30.29	28.95	26.99	25.73	23.91
SV-m56-O	30.69	30.38	33.43	31.87	29.01	28.16	26.26
SV-m64-O	29.90	31.14	32.73	31.01	28.18	27.23	25.56
SLy4	29.18	29.83	30.56	29.51	27.22	26.33	24.55
SLy5	29.50	30.20	30.79	29.65	27.44	26.56	24.72
SLy6	29.51	30.26	31.26	29.98	27.51	26.66	25.01
SkMP	29.43	30.66	31.41	30.05	27.58	26.18	24.56
SKO	28.93	29.39	29.81	28.40	26.69	25.38	23.14
SKO`	29.27	29.64	29.98	28.73	26.84	25.54	23.46
LNS	29.92	30.57	31.39	29.90	27.80	26.26	24.68
MSL0	29.17	29.74	30.21	28.90	27.05	25.88	23.96
NRAPR	29.91	31.07	30.76	29.67	27.62	26.35	24.41
SQMC650	29.37	29.49	30.39	29.03	26.74	25.66	24.32
SQMC700	29.74	30.23	31.54	29.94	27.18	26.13	24.98
SkT1	28.92	28.96	29.37	28.49	26.41	25.34	23.40
SkT2	29.09	29.06	29.41	28.53	26.40	25.37	23.43
SkT3	29.30	28.97	29.45	28.52	26.42	25.30	23.36
SkT8	29.35	29.77	30.34	29.27	27.26	26.13	24.33
SkT9	29.28	29.82	30.29	29.26	27.20	25.99	24.37
SkT1*	28.53	29.20	29.21	28.29	26.26	25.19	23.23
SkT3*	28.57	29.43	29.26	28.19	26.30	25.13	23.11
Skxs20	28.68	28.86	29.06	27.80	25.57	24.45	22.88
Z-sigma	29.51	30.05	31.69	30.11	27.73	26.67	25.26
Exp.	23.36	27.30		27.40	25.50	24.51	22.20
Error	0.70	0.15		0.50	0.60	0.40	0.30

Table 16 ISGQR E_{CEN} (in MeV) for ^{40,48}Ca, ^{68}Ni, ^{90}Zr, ^{116}Sn, ^{144}Sm and ^{208}Pb.

ISGQR	^{40}Ca	^{48}Ca	^{68}Ni	^{90}Zr	^{116}Sn	^{144}Sm	^{208}Pb
SGII	17.33	17.73	15.76	14.85	13.76	12.88	11.90
KDE0	17.85	18.11	16.28	15.37	14.23	13.37	12.35
KDE0v1	17.81	17.94	16.09	15.25	14.09	13.27	12.15
SKM*	16.90	17.43	15.52	14.69	13.56	12.83	11.89
Sk255	17.36	16.95	15.27	14.45	13.34	12.54	11.29
SkI3	19.74	20.09	18.03	17.29	16.20	15.42	14.19
SkI4	18.98	18.85	17.26	16.14	15.20	14.26	13.43
SkI5	19.58	19.72	17.66	16.84	15.70	14.79	13.42
SV-bas	16.58	16.78	14.93	14.06	12.96	12.16	11.12
SV-min	16.22	15.86	14.57	13.75	12.67	11.98	10.91
SV-sym32	16.67	16.65	14.88	14.05	13.04	12.16	11.14
SV-m56-O	19.98	20.03	18.07	17.17	16.15	15.29	13.99
SV-m64-O	19.02	19.11	17.18	16.22	15.16	14.56	13.17
SLy4	17.72	17.79	16.15	15.19	14.11	13.33	12.51
SLy5	17.78	17.86	16.23	15.26	14.16	13.37	12.33
SLy6	18.08	18.48	16.52	15.65	14.48	13.65	12.54
SkMP	18.22	17.42	16.81	15.80	14.92	13.94	12.94
SKO	16.62	15.99	14.97	13.62	12.98	12.01	10.92
SKO`	16.62	16.53	14.93	14.01	12.93	12.09	10.96
LNS	15.77	15.84	16.44	15.44	14.30	13.55	12.43
MSL0	17.03	15.47	15.42	14.57	13.55	12.79	11.57
NRAPR	18.34	16.85	16.09	15.09	14.20	13.34	12.01
SQMC650	17.09	16.57	15.84	14.93	14.02	13.04	12.00
SQMC700	18.00	17.02	16.49	15.56	14.56	13.61	12.50
SkT1	15.72	15.81	14.14	13.24	12.34	11.55	10.55
SkT2	15.86	15.86	14.17	13.36	12.27	11.56	10.62
SkT3	15.83	15.84	14.13	13.26	12.37	11.46	10.54
SkT8	16.97	16.85	15.23	14.27	13.29	12.46	11.49
SkT9	16.93	16.94	15.19	14.37	13.35	12.48	11.57
SkT1*	15.96	15.77	14.13	13.26	12.22	11.43	10.48
SkT3*	15.81	15.47	13.93	13.14	12.14	11.33	10.33
Skxs20	15.81	16.40	14.46	13.73	12.58	11.84	10.90
Z-sigma	17.89	18.15	16.27	15.23	14.19	13.31	12.64
Exp.	17.84	18.61	15.90	14.56	13.50	12.78	10.84
Error	0.43	0.24	1.30	0.20	0.35	0.30	0.25

Table 17 ISGOR E_{CEN} (in MeV) for $^{40,48}Ca$, ^{68}Ni, ^{90}Zr, ^{116}Sn, ^{144}Sm and ^{208}Pb.

ISGOR	^{40}Ca	^{48}Ca	^{68}Ni	^{90}Zr	^{116}Sn	^{144}Sm	^{208}Pb
SGII	31.41	31.39	28.94	27.42	25.69	23.65	21.36
KDE0	32.11	31.94	29.93	28.49	26.86	24.28	22.53
KDE0v1	31.87	31.62	29.60	28.21	26.57	24.42	22.29
SKM*	30.35	30.64	28.35	27.00	25.33	23.14	21.10
Sk255	31.13	30.32	28.17	26.82	25.18	23.24	20.91
SkI3	34.17	34.84	32.70	31.06	29.65	27.03	24.80
SkI4	33.74	33.08	31.57	29.92	28.59	25.60	23.45
SkI5	34.87	34.24	32.41	31.17	29.76	26.40	24.08
SV-bas	29.89	29.78	27.36	25.89	24.34	22.47	20.31
SV-min	29.16	29.10	26.71	25.22	23.78	21.93	19.80
SV-sym32	29.94	29.62	27.18	25.78	24.19	22.40	20.12
SV-m56-O	35.28	34.55	33.10	31.68	33.64	27.13	24.89
SV-m64-O	33.88	33.57	31.44	30.10	30.90	25.74	23.54
SLy4	31.76	31.46	29.72	28.26	26.76	24.56	22.63
SLy5	31.90	31.57	29.79	28.36	26.84	24.53	22.65
SLy6	32.44	32.60	30.42	28.88	27.25	24.59	22.63
SkMP	32.22	32.61	30.58	29.19	27.56	24.78	22.68
SKO	30.04	29.25	27.82	25.76	24.33	22.71	20.41
SKO`	30.04	29.78	27.60	26.04	24.53	22.71	20.26
LNS	32.44	32.45	29.95	28.36	28.12	23.98	21.92
MSL0	30.59	30.74	28.43	26.96	26.00	23.34	21.17
NRAPR	33.18	31.22	29.79	28.21	27.84	24.66	22.33
SQMC650	30.41	30.95	28.59	27.40	26.06	23.71	21.72
SQMC700	32.02	32.24	29.89	28.20	27.10	24.20	22.26
SkT1	28.57	28.30	26.09	24.57	23.12	21.46	19.34
SkT2	28.57	28.42	26.13	24.65	23.21	21.54	19.40
SkT3	28.65	28.44	26.16	24.68	23.14	21.57	19.40
SkT8	30.59	30.17	28.14	26.53	24.99	23.22	21.11
SkT9	30.35	30.35	28.14	26.61	25.06	23.13	21.09
SkT1*	28.62	28.21	26.05	24.48	22.96	21.38	19.26
SkT3*	28.49	27.91	25.85	24.33	22.88	21.38	19.16
Skxs20	28.45	29.02	26.49	25.23	23.79	21.70	19.66
Z-sigma	31.81	32.01	29.86	28.13	26.63	24.24	22.46
Exp.				23.10	23.30	19.80	19.60
Error				0.30	0.80	0.50	0.50

Table 18 IVGMR E_{CEN} (in MeV) for $^{40,48}Ca$, ^{68}Ni, ^{90}Zr, ^{116}Sn, ^{144}Sm and ^{208}Pb.

IVGMR	^{40}Ca	^{48}Ca	^{68}Ni	^{90}Zr	^{116}Sn	^{144}Sm	^{208}Pb
SGII	32.38	33.64	31.37	31.62	30.19	29.96	27.73
KDE0	31.93	32.83	30.84	31.63	30.14	30.21	27.98
KDE0v1	31.70	32.43	30.48	31.27	29.76	29.83	27.58
SKM*	31.74	33.34	31.00	31.74	30.32	30.24	28.01
Sk255	33.63	34.13	32.38	33.48	31.92	31.90	29.19
SkI3	32.10	34.50	30.75	32.30	30.04	30.26	27.51
SkI4	33.62	34.55	32.37	33.68	31.66	31.64	28.41
SkI5	32.91	33.42	30.90	31.79	29.72	29.59	26.68
SV-bas	32.57	33.92	31.60	32.54	30.93	30.92	28.44
SV-min	30.84	31.74	29.24	29.99	28.30	28.22	25.82
SV-sym32	32.61	33.92	31.51	32.66	30.94	30.93	28.22
SV-m56-O	35.61	36.37	34.27	36.47	34.10	34.27	31.55
SV-m64-O	35.29	35.96	33.74	35.69	33.67	34.02	31.18
SLy4	30.51	31.01	29.51	29.92	28.68	28.64	26.66
SLy5	30.81	31.27	29.63	30.03	28.77	28.70	26.71
SLy6	31.35	32.46	30.30	30.86	29.35	29.35	27.16
SkMP	32.90	34.71	32.06	33.08	31.46	31.47	29.07
SKO	29.19	29.89	28.99	27.82	26.66	25.82	23.53
SKO`	30.95	32.20	30.15	30.76	29.05	28.88	25.96
LNS	33.01	33.99	31.86	32.28	30.88	30.73	28.41
MSL0	31.16	32.39	30.35	30.93	29.55	29.37	27.05
NRAPR	34.56	33.54	32.89	33.49	32.11	32.03	29.49
SQMC650	31.73	33.70	31.14	32.63	31.10	31.35	29.13
SQMC700	33.26	35.28	32.40	33.79	32.10	32.31	29.78
SkT1	29.38	29.76	27.83	28.22	26.85	26.73	24.66
SkT2	29.24	29.85	27.76	28.22	26.83	26.73	24.66
SkT3	29.71	30.25	28.18	28.64	27.11	27.00	24.75
SkT8	31.16	31.47	29.79	30.10	28.71	28.61	26.40
SkT9	30.70	31.49	29.52	29.98	28.54	28.50	26.33
SkT1*	29.32	29.35	27.77	28.08	26.74	26.62	24.55
SkT3*	30.01	29.81	28.24	28.47	27.04	26.85	24.55
Skxs20	29.32	31.15	28.02	29.52	27.80	27.99	25.84
Z-sigma	33.49	34.75	32.80	33.63	32.21	32.41	30.31
Exp.	31.00						26.00
Error	2.00						2.00

Table 19 IVGDR E_{CEN} (in MeV) for $^{40,48}Ca$, ^{68}Ni, ^{90}Zr, ^{116}Sn, ^{144}Sm and ^{208}Pb.

IVGDR	^{40}Ca	^{48}Ca	^{68}Ni	^{90}Zr	^{116}Sn	^{144}Sm	^{208}Pb
SGII	19.12	19.16	17.39	16.78	15.76	15.15	13.71
KDE0	19.36	19.23	17.69	17.11	16.10	15.59	14.08
KDE0v1	18.93	18.80	17.27	16.81	15.79	15.29	13.80
SKM*	18.93	19.26	17.48	17.05	15.98	15.45	14.04
Sk255	19.48	19.17	17.61	17.29	16.23	15.75	14.05
SkI3	18.16	18.69	16.42	16.32	15.10	14.69	13.04
SkI4	19.96	19.92	17.81	17.43	16.08	15.44	13.59
SkI5	17.62	17.44	15.62	15.48	14.33	13.94	12.25
SV-bas	19.72	19.78	17.87	17.45	16.30	15.62	14.17
SV-min	17.80	17.73	15.99	15.67	14.60	14.11	12.60
SV-sym32	19.27	19.31	17.40	17.12	15.94	15.49	13.84
SV-m56-O	22.68	22.25	19.59	19.37	17.68	17.09	15.00
SV-m64-O	22.34	22.11	19.63	19.29	17.72	17.11	15.20
SLy4	18.29	18.10	16.84	16.23	15.35	14.81	13.49
SLy5	18.22	18.07	16.82	16.21	15.31	14.78	13.45
SLy6	18.72	18.68	17.15	16.56	15.58	15.04	13.58
SkMP	19.18	19.77	17.60	17.35	16.18	15.66	14.06
SKO	16.30	16.04	15.01	13.98	13.14	12.45	11.00
SKO`	17.70	17.77	16.08	15.80	14.74	14.22	12.50
LNS	20.23	19.40	17.98	17.21	16.28	15.69	14.16
MSL0	18.08	18.15	16.55	16.15	15.18	14.68	13.21
NRAPR	20.89	19.80	18.59	17.99	16.92	16.33	14.64
SQMC650	19.47	20.02	18.11	17.89	16.74	16.22	14.78
SQMC700	20.25	20.74	18.56	18.28	17.02	16.44	14.86
SkT1	16.53	16.37	15.05	14.66	13.78	13.36	11.98
SkT2	16.50	16.41	15.02	14.67	13.79	13.37	12.00
SkT3	16.70	16.59	15.15	14.78	13.86	13.44	11.99
SkT8	18.32	18.03	16.64	16.10	15.15	14.65	13.22
SkT9	18.12	18.06	16.53	16.06	15.08	14.60	13.16
SkT1*	16.59	16.28	15.04	14.61	13.79	13.31	11.94
SkT3*	16.79	16.37	15.12	14.70	13.80	13.38	11.91
Skxs20	17.10	17.47	15.62	15.52	14.48	13.90	12.62
Z-sigma	22.01	22.09	20.15	19.29	18.13	17.43	15.89
Exp.	19.80	19.50	17.10	16.83	15.67	15.30	13.40
Error	0.50	0.50	0.20	0.04	0.04	0.10	0.50

Table 20 IVGQR E_{CEN} (in MeV) for $^{40,48}Ca$, ^{68}Ni, ^{90}Zr, ^{116}Sn, ^{144}Sm and ^{208}Pb.

IVGQR	^{40}Ca	^{48}Ca	^{68}Ni	^{90}Zr	^{116}Sn	^{144}Sm	^{208}Pb
SGII	30.38	30.82	28.18	27.40	25.80	24.89	22.64
KDE0	30.40	30.68	28.24	27.74	26.10	25.31	22.92
KDE0v1	29.80	29.99	27.62	27.22	25.58	24.84	22.45
SKM*	29.50	30.23	27.77	27.33	25.82	25.03	22.79
Sk255	30.29	29.95	27.77	27.45	25.95	25.27	22.65
SkI3	30.05	31.28	27.70	27.60	25.79	24.89	21.91
SkI4	31.47	31.54	28.86	28.59	26.44	25.76	23.15
SkI5	29.79	29.76	26.94	26.64	24.83	23.95	21.37
SV-bas	30.13	30.65	27.98	27.62	25.95	25.19	22.71
SV-min	27.87	26.26	25.52	25.20	23.57	23.01	20.60
SV-sym32	29.80	30.01	27.34	27.11	25.52	24.75	22.25
SV-m56-O	34.95	35.06	31.98	32.05	30.01	29.10	25.58
SV-m64-O	34.22	34.48	31.38	31.36	29.41	28.58	25.41
SLy4	29.22	29.25	27.23	26.60	25.13	24.32	22.28
SLy5	29.29	29.35	27.26	26.63	25.13	24.34	22.13
SLy6	29.95	30.34	27.82	27.23	25.59	24.77	22.35
SkMP	30.70	31.23	28.82	28.40	26.96	25.99	23.61
SKO	27.11	26.70	25.15	23.78	22.38	21.39	19.09
SKO`	27.84	28.15	25.71	25.37	23.69	23.01	20.49
LNS	26.55	26.50	28.60	27.88	26.29	25.52	23.04
MSL0	28.62	26.17	26.78	26.27	24.84	24.08	21.77
NRAPR	32.56	28.84	29.66	28.92	27.45	26.65	23.98
SQMC650	29.72	30.69	28.31	28.24	26.77	26.08	23.70
SQMC700	31.26	32.01	29.36	29.14	27.52	26.70	24.06
SkT1	26.19	26.21	24.12	23.65	22.36	21.71	19.55
SkT2	26.10	26.26	24.08	23.66	22.23	21.63	19.56
SkT3	26.38	26.50	24.30	23.87	22.52	21.77	19.60
SkT8	29.01	28.84	26.71	26.08	24.54	23.81	21.65
SkT9	28.64	28.84	26.50	26.00	24.55	23.72	21.59
SkT1*	26.29	26.07	24.11	23.59	22.23	21.57	19.49
SkT3*	26.57	26.17	24.28	23.74	22.32	21.67	19.49
Skxs20	26.45	27.48	24.68	24.64	23.07	22.52	20.22
Z-sigma	33.59	34.03	31.50	30.62	28.99	28.01	25.93
Exp.	31.00						22.80
Error	1.50						0.50

Table 21 IVGOR E_{CEN} (in MeV) for $^{40,48}Ca$, ^{68}Ni, ^{90}Zr, ^{116}Sn, ^{144}Sm and ^{208}Pb.

IVGOR	^{40}Ca	^{48}Ca	^{68}Ni	^{90}Zr	^{116}Sn	^{144}Sm	^{208}Pb
SGII	39.63	39.78	38.36	36.56	35.49	34.16	31.43
KDE0	39.68	40.19	38.85	36.99	36.06	34.62	32.08
KDE0v1	39.19	39.58	38.29	36.50	35.40	34.04	31.53
SKM*	38.49	38.94	37.83	36.17	35.20	33.96	31.55
Sk255	39.16	39.21	37.83	36.28	35.50	34.29	31.76
SkI3	39.68	39.92	39.68	37.93	37.39	35.77	32.75
SkI4	40.88	41.03	39.95	38.07	38.43	35.02	33.38
SkI5	40.28	40.12	38.95	37.02	36.31	34.60	31.57
SV-bas	39.13	39.62	38.17	36.38	35.49	34.12	31.80
SV-min	37.36	37.63	35.92	34.19	33.08	31.55	29.65
SV-sym32	38.90	39.58	37.61	35.83	34.93	33.64	31.39
SV-m56-O	43.16	42.86	43.29	41.69	42.56	38.14	37.22
SV-m64-O	42.50	42.62	42.44	40.80	40.99	39.29	36.12
SLy4	38.75	38.93	37.78	35.94	34.92	33.56	31.16
SLy5	38.80	38.99	37.80	35.92	34.92	33.50	31.12
SLy6	39.53	39.64	38.58	36.56	35.64	34.07	31.52
SkMP	40.03	40.60	39.64	37.72	37.26	36.03	33.29
SKO	37.26	36.97	35.48	33.69	32.28	31.06	27.91
SKO`	37.28	37.69	35.91	34.42	33.14	31.96	29.66
LNS	40.51	40.25	39.09	37.07	36.27	34.67	31.95
MSL0	38.04	38.26	37.06	35.31	34.40	33.05	30.46
NRAPR	41.28	40.80	40.07	37.85	37.22	36.29	33.39
SQMC650	38.51	39.44	38.54	37.65	36.26	35.20	32.88
SQMC700	40.22	41.09	39.94	39.11	37.50	36.26	33.66
SkT1	35.92	35.70	34.02	32.47	31.26	29.97	28.09
SkT2	35.81	35.77	34.00	32.51	31.28	30.00	28.14
SkT3	36.22	36.09	34.35	32.79	31.27	30.20	28.21
SkT8	38.75	38.36	36.94	35.18	33.90	32.60	30.40
SkT9	38.52	38.27	36.79	35.09	33.81	32.49	30.30
SkT1*	35.79	35.64	34.05	32.43	30.99	29.91	27.95
SkT3*	36.29	35.81	34.09	32.54	31.20	30.02	27.99
Skxs20	35.81	36.40	34.92	33.68	32.16	30.98	29.47
Z-sigma	42.51	43.66	41.71	39.48	39.19	37.57	35.08
Exp. Error							

Table 22 ISGMR E_{CEN} (in MeV) for ^{92,94,96,98,100}Mo and ^{90,92,94}Zr.

ISGMR	^{92}Mo	^{94}Mo	^{96}Mo	^{98}Mo	^{100}Mo	^{90}Zr	^{92}Zr	^{94}Zr
SGII	18.03	18.11	17.27	17.35	17.21	17.89	17.96	17.06
KDE0	18.20	18.28	17.50	17.53	17.31	17.96	18.03	17.23
KDE0v1	18.19	18.24	17.45	17.51	17.26	17.97	18.04	17.21
SKM*	17.77	17.91	17.05	17.09	16.94	17.61	17.73	16.83
Sk255	18.86	18.93	18.00	18.17	17.90	18.73	18.79	17.97
SkI3	19.89	19.87	18.80	18.80	18.69	19.57	19.56	18.64
SkI4	19.17	19.19	18.42	18.36	18.04	18.93	18.93	18.12
SkI5	19.35	19.37	18.56	18.34	18.27	19.14	19.11	18.28
SV-bas	18.43	18.58	17.67	17.68	17.54	18.32	18.45	17.66
SV-min	17.96	18.09	17.25	17.27	17.15	17.83	17.95	17.12
SV-sym32	18.42	18.55	17.69	17.66	17.51	18.27	18.41	17.62
SV-m56-O	19.46	19.45	18.65	18.58	18.33	19.18	19.17	18.34
SV-m64-O	18.92	18.94	17.98	17.96	17.91	18.68	18.75	17.94
SLy4	17.90	17.92	17.21	17.24	17.04	17.69	17.72	16.96
SLy5	18.14	18.16	17.24	17.22	17.23	17.93	17.95	17.16
SLy6	18.31	18.36	17.44	17.47	17.38	18.13	18.20	17.40
SkMP	18.49	18.56	17.68	17.73	17.56	18.26	18.32	17.37
SKO	17.52	17.60	16.85	16.84	17.03	17.58	17.70	16.87
SKO`	17.90	18.00	17.26	17.28	17.18	17.79	17.87	17.13
LNS	18.35	18.43	17.48	17.54	17.42	18.20	18.25	17.42
MSL0	18.02	18.13	17.27	17.27	17.19	17.88	17.98	17.08
NRAPR	17.77	17.77	17.09	17.10	17.17	17.67	17.65	16.89
SQMC650	17.76	17.93	17.04	17.07	16.91	17.60	17.71	16.75
SQMC700	18.38	18.49	17.56	17.62	17.42	18.20	18.31	17.47
SkT1	18.32	18.43	17.59	17.56	17.47	18.19	18.31	17.56
SkT2	18.34	18.45	17.61	17.59	17.47	18.21	18.30	17.57
SkT3	18.28	18.40	17.55	17.51	17.43	18.21	18.29	17.54
SkT8	18.39	18.46	17.54	17.59	17.48	18.25	18.33	17.50
SkT9	18.32	18.49	17.56	17.51	17.47	18.19	18.31	17.51
SkT1*	18.13	18.24	17.37	17.58	17.29	18.03	18.15	17.38
SkT3*	18.14	18.24	17.38	17.53	17.29	18.09	18.18	17.43
Skxs20	17.17	17.30	16.49	16.50	16.29	16.96	17.04	16.36
Z-sigma	18.61	18.69	17.64	17.71	17.60	18.44	18.52	17.61
Exp.	19.62	17.99	16.95	16.01	16.13	17.88	18.23	16.16
Error	0.28	0.72	0.12	0.19	0.11	0.12	0.14	0.115

Table 23 ISGDR E_{CEN} (in MeV) for ^{92,94,96,98,100}Mo and ^{90,92,94}Zr.

ISGDR	^{92}Mo	^{94}Mo	^{96}Mo	^{98}Mo	^{100}Mo	^{90}Zr	^{92}Zr	^{94}Zr
SGII	28.54	28.53	27.86	27.76	27.69	28.35	28.34	27.94
KDE0	28.95	28.81	28.53	28.50	28.46	28.84	28.72	28.39
KDE0v1	28.81	28.70	28.37	28.36	28.37	28.69	28.56	28.27
SKM*	28.10	28.13	27.43	27.37	27.22	27.86	27.73	27.47
Sk255	28.71	28.62	28.29	28.17	28.22	28.66	28.51	28.27
SkI3	29.72	29.84	29.69	29.32	29.26	29.41	29.30	29.31
SkI4	29.49	29.58	29.37	29.31	29.35	29.09	29.15	29.00
SkI5	29.71	29.65	29.56	29.50	29.27	29.40	29.24	29.25
SV-bas	28.14	28.20	27.74	27.65	27.59	28.07	27.98	27.63
SV-min	27.61	27.67	27.33	27.26	27.07	27.49	27.52	27.15
SV-sym32	28.11	28.15	27.74	27.62	27.50	28.01	27.92	27.57
SV-m56-O	29.67	29.81	29.67	29.51	29.45	29.56	29.56	29.56
SV-m64-O	29.58	29.49	29.15	29.03	29.09	29.29	29.19	29.02
SLy4	28.60	28.48	28.16	28.19	28.21	28.53	28.42	28.12
SLy5	28.81	28.67	28.41	28.42	28.40	28.63	28.62	28.33
SLy6	29.09	28.97	28.66	28.46	28.24	28.85	28.66	28.32
SkMP	29.03	29.14	28.26	28.27	28.32	28.77	28.73	28.42
SKO	27.50	27.47	27.09	27.00	27.07	27.60	27.52	27.38
SKO`	27.92	27.97	27.69	27.49	27.22	27.85	27.84	27.45
LNS	28.96	28.95	28.56	28.51	28.40	28.83	28.79	28.30
MSL0	28.12	28.18	27.70	27.79	27.45	27.91	27.91	27.55
NRAPR	29.00	28.81	28.45	28.34	28.48	28.83	28.63	28.20
SQMC650	28.16	28.11	27.58	27.55	27.29	27.92	27.83	27.52
SQMC700	28.84	28.99	28.56	28.56	28.39	28.70	28.64	28.33
SkT1	27.50	27.54	27.27	27.15	27.08	27.58	27.60	27.39
SkT2	27.53	27.55	27.30	27.18	27.09	27.56	27.60	27.37
SkT3	27.47	27.49	27.35	27.26	27.10	27.55	27.65	27.35
SkT8	28.23	28.18	27.83	27.77	27.84	28.35	28.20	27.83
SkT9	28.19	28.20	27.82	27.81	27.84	28.17	28.04	27.75
SkT1*	27.53	27.55	27.29	27.22	27.15	27.46	27.53	27.19
SkT3*	27.45	27.46	27.22	27.14	27.11	27.39	27.51	27.19
Skxs20	27.28	27.23	26.85	26.71	26.59	26.95	26.91	26.52
Z-sigma	28.91	28.82	28.50	28.58	28.49	28.87	28.77	28.27
Exp.	27.60	26.50	30.00	27.40	30.10	27.40	30.00	27.00
Error	0.50	0.43	0.70	0.70	0.70	0.50	0.70	0.50

Table 24 ISGQR E_{CEN} (in MeV) for ^{92,94,96,98,100}Mo and ^{90,92,94}Zr.

ISGQR	^{92}Mo	^{94}Mo	^{96}Mo	^{98}Mo	^{100}Mo	^{90}Zr	^{92}Zr	^{94}Zr
SGII	15.04	15.02	14.35	14.34	14.31	14.86	14.83	14.18
KDE0	15.56	15.55	14.90	14.88	14.87	15.38	15.41	14.67
KDE0v1	15.44	15.44	14.78	14.77	14.76	15.27	15.28	14.56
SKM*	14.86	14.93	14.32	14.32	14.21	14.70	14.76	14.13
Sk255	14.63	14.65	13.93	13.89	13.92	14.46	14.45	13.75
SkI3	17.66	17.59	16.38	16.41	16.27	17.37	17.34	16.09
SkI4	16.45	16.41	15.63	15.60	15.52	16.15	16.22	15.39
SkI5	17.11	17.05	16.17	16.13	16.08	16.88	16.86	15.89
SV-bas	14.29	14.29	13.67	13.68	13.66	14.06	14.15	13.49
SV-min	13.92	13.98	13.44	13.35	13.34	13.76	13.75	13.20
SV-sym32	14.19	14.20	13.65	13.59	13.55	14.06	14.05	13.45
SV-m56-O	17.50	17.52	16.62	16.57	16.53	17.21	17.28	16.36
SV-m64-O	16.50	16.58	15.75	15.77	15.69	16.24	16.32	15.51
SLy4	15.41	15.43	14.77	14.77	14.76	15.20	15.22	14.56
SLy5	15.46	15.52	14.79	14.85	14.84	15.27	15.29	14.56
SLy6	15.84	15.83	15.13	15.13	15.10	15.66	15.67	14.93
SkMP	16.07	16.06	15.13	15.12	15.00	15.82	15.89	14.87
SKO	13.75	13.79	13.24	13.13	13.14	13.64	13.68	13.11
SKO`	14.11	14.13	13.56	13.45	13.46	14.02	14.02	13.32
LNS	15.63	15.62	14.96	14.93	14.85	15.46	15.44	14.74
MSL0	14.70	14.78	14.08	14.02	14.04	14.58	14.57	13.90
NRAPR	15.25	15.22	14.57	14.51	14.59	15.10	15.08	14.38
SQMC650	15.10	15.20	14.46	14.45	14.33	14.94	14.96	14.18
SQMC700	15.74	15.76	14.89	14.92	14.77	15.57	15.56	14.69
SkT1	13.49	13.52	12.93	12.86	12.92	13.25	13.36	12.72
SkT2	13.50	13.60	13.03	12.96	12.94	13.37	13.38	12.77
SkT3	13.45	13.56	12.97	12.90	12.95	13.27	13.38	12.76
SkT8	14.45	14.47	13.86	13.84	13.86	14.28	14.38	13.69
SkT9	14.49	14.59	13.93	13.89	13.90	14.38	14.40	13.76
SkT1*	13.44	13.45	12.88	12.87	12.87	13.26	13.25	12.66
SkT3*	13.26	13.27	12.73	12.74	12.74	13.14	13.16	12.56
Skxs20	13.97	14.02	13.43	13.36	13.28	13.74	13.77	13.25
Z-sigma	15.42	15.42	14.77	14.77	14.83	15.24	15.26	14.61
Exp.	14.51	14.55	13.85	13.85	13.60	14.56	14.35	14.49
Error	0.25	0.13	0.20	0.20	0.15	0.20	0.15	0.15

Table 25 ISGOR E_{CEN} (in MeV) for ^{92,94,96,98,100}Mo and ^{90,92,94}Zr.

ISGOR	^{92}Mo	^{94}Mo	^{96}Mo	^{98}Mo	^{100}Mo	^{90}Zr	^{92}Zr	^{94}Zr
SGII	26.16	26.15	25.74	25.69	25.56	26.07	26.04	25.53
KDE0	27.16	27.15	26.44	26.40	26.31	27.21	27.17	26.59
KDE0v1	26.99	27.01	26.35	26.27	26.11	26.98	26.96	26.18
SKM*	25.92	25.93	25.41	25.35	25.17	25.80	25.79	25.20
Sk255	26.29	26.18	25.45	25.33	25.25	26.08	26.12	25.31
SkI3	29.43	29.30	27.94	27.98	27.90	29.26	29.23	27.78
SkI4	28.33	28.36	27.28	27.20	27.18	28.23	28.28	27.43
SkI5	28.92	28.91	27.87	27.95	27.86	28.88	28.90	27.91
SV-bas	25.38	25.27	24.67	24.53	24.45	25.29	25.23	24.58
SV-min	24.83	24.76	24.23	24.09	23.91	24.73	24.60	24.03
SV-sym32	25.33	25.20	24.58	24.46	24.31	25.19	25.10	24.43
SV-m56-O	29.61	29.70	28.28	28.31	28.34	29.41	29.55	28.17
SV-m64-O	28.47	28.43	27.65	27.60	27.51	28.28	28.38	27.43
SLy4	27.18	27.18	26.48	26.47	26.30	27.08	27.05	26.46
SLy5	27.15	27.17	26.50	26.47	26.36	27.14	27.12	26.32
SLy6	27.33	27.33	26.75	26.77	26.65	27.27	27.27	26.49
SkMP	27.60	27.59	26.93	26.91	26.83	27.52	27.55	26.81
SKO	25.14	25.08	24.45	24.26	24.50	25.24	25.17	24.55
SKO`	25.62	25.57	24.88	24.68	24.56	25.52	25.45	24.70
LNS	26.93	26.90	26.34	26.30	26.13	26.88	26.84	26.13
MSL0	26.30	26.27	25.63	25.54	25.39	26.08	26.10	25.47
NRAPR	27.47	27.45	26.42	26.32	26.30	27.36	27.35	26.81
SQMC650	26.45	26.46	25.89	25.90	25.74	26.48	26.44	25.77
SQMC700	27.22	27.24	26.65	26.64	26.43	27.26	27.20	26.46
SkT1	24.48	24.19	23.72	23.53	23.40	24.16	24.05	23.52
SkT2	24.29	24.22	23.80	23.62	23.45	24.15	24.08	23.58
SkT3	24.40	24.29	23.84	23.63	23.51	24.28	24.16	23.66
SkT8	26.09	26.02	25.43	25.29	25.20	25.94	25.95	25.23
SkT9	25.97	25.92	25.34	25.22	25.13	25.77	25.85	25.17
SkT1*	24.23	24.17	23.65	23.45	23.34	24.12	24.01	23.47
SkT3*	24.14	24.04	23.50	23.28	23.20	24.12	24.02	23.41
Skxs20	24.38	24.34	23.89	23.75	23.48	24.39	24.32	23.74
Z-sigma	26.81	26.82	26.28	26.25	26.17	26.89	26.89	26.24
Exp.	21.80	24.60	21.40	21.50	21.51	23.10	23.90	23.6
Error	0.30	0.46	0.30	0.30	0.30	0.30	0.30	0.30

Table 26 IVGMR E_{CEN} (in MeV) for ^{92,94,96,98,100}Mo and ^{90,92,94}Zr.

IVGMR	^{92}Mo	^{94}Mo	^{96}Mo	^{98}Mo	^{100}Mo	^{90}Zr	^{92}Zr	^{94}Zr
SGII	31.71	31.56	30.86	30.73	30.71	31.71	31.54	30.83
KDE0	31.77	31.57	30.83	30.67	30.77	31.72	31.55	30.76
KDE0v1	31.41	31.27	30.52	30.35	30.44	31.36	31.22	30.44
SKM*	31.84	31.70	31.08	30.93	30.91	31.82	31.68	31.05
Sk255	33.70	33.57	32.67	32.50	32.51	33.60	33.48	32.57
SkI3	32.62	32.50	31.44	31.37	31.38	32.36	32.23	31.18
SkI4	33.97	33.93	32.64	32.54	32.65	33.75	33.69	32.37
SkI5	32.07	31.98	30.85	30.75	30.79	31.84	31.73	30.57
SV-bas	32.59	32.45	31.77	31.59	31.59	32.64	32.48	31.76
SV-min	30.06	29.89	29.29	29.11	29.06	30.11	29.94	29.32
SV-sym32	32.76	32.63	31.89	31.74	31.66	32.79	32.63	31.88
SV-m56-O	36.75	36.70	34.92	34.92	35.11	36.53	36.65	34.94
SV-m64-O	35.94	35.93	34.62	34.60	34.77	35.77	35.78	34.43
SLy4	30.07	29.89	29.31	29.15	29.26	30.01	29.87	29.22
SLy5	30.16	30.00	29.41	29.25	29.36	30.12	29.97	29.32
SLy6	30.97	30.79	30.11	29.97	30.02	30.90	30.73	30.00
SkMP	33.37	33.23	32.32	32.29	32.24	33.18	33.03	32.15
SKO	27.82	27.68	27.03	26.85	27.03	27.97	27.83	27.18
SKO`	30.93	30.78	30.02	29.84	29.84	30.89	30.74	29.97
LNS	32.38	32.23	31.54	31.43	31.40	32.36	32.18	31.49
MSL0	31.06	30.97	30.29	30.16	30.15	31.06	30.95	30.25
NRAPR	33.71	33.52	32.43	32.27	32.44	33.62	33.46	32.26
SQMC650	32.79	32.67	32.00	31.92	31.84	32.69	32.60	31.90
SQMC700	33.95	33.82	32.93	32.81	32.78	33.87	33.76	32.85
SkT1	28.27	28.14	27.70	27.50	27.48	28.33	28.19	27.69
SkT2	28.28	28.13	27.68	27.51	27.48	28.33	28.20	27.72
SkT3	28.70	28.55	28.06	27.87	27.80	28.76	28.61	28.05
SkT8	30.21	30.05	29.43	29.26	29.30	30.19	30.07	29.40
SkT9	30.05	29.89	29.31	29.13	29.19	30.06	29.94	29.32
SkT1*	28.17	28.03	27.56	27.39	27.39	28.21	28.06	27.55
SkT3*	28.54	28.38	27.85	27.68	27.68	28.59	28.45	27.87
Skxs20	29.75	29.49	28.96	28.78	28.68	29.67	29.49	28.96
Z-sigma	33.71	33.49	32.56	32.39	32.61	33.73	33.56	32.63
Exp. Error								

Table 27 IVGDR E_{CEN} (in MeV) for ^{92,94,96,98,100}Mo and ^{90,92,94}Zr.

IVGDR	^{92}Mo	^{94}Mo	^{96}Mo	^{98}Mo	^{100}Mo	^{90}Zr	^{92}Zr	^{94}Zr
SGII	16.69	16.58	16.06	16.02	15.88	16.78	16.65	16.09
KDE0	17.05	16.96	16.31	16.24	16.14	17.11	16.99	16.24
KDE0v1	16.75	16.63	16.04	15.95	15.87	16.81	16.68	15.91
SKM*	16.97	16.89	16.39	16.33	16.18	17.05	16.93	16.35
Sk255	17.28	17.20	16.45	16.39	16.32	17.29	17.19	16.26
SkI3	16.37	16.29	15.43	15.42	15.28	16.32	16.22	15.35
SkI4	17.44	17.33	16.24	16.19	16.11	17.43	17.32	16.17
SkI5	15.53	15.45	14.49	14.46	14.42	15.48	15.35	14.41
SV-bas	17.32	17.24	16.67	16.60	16.45	17.45	17.29	16.67
SV-min	15.56	15.48	14.95	14.85	14.73	15.67	15.54	14.90
SV-sym32	17.05	16.94	16.34	16.24	16.11	17.12	16.97	16.28
SV-m56-O	19.37	19.26	17.94	17.87	17.80	19.37	19.21	17.87
SV-m64-O	19.21	19.09	18.10	18.02	17.89	19.29	19.11	18.09
SLy4	16.15	16.08	15.52	15.44	15.39	16.23	16.09	15.21
SLy5	16.14	16.06	15.48	15.45	15.32	16.21	16.06	15.32
SLy6	16.49	16.37	15.82	15.76	15.65	16.56	16.42	15.83
SkMP	17.36	17.28	16.59	16.57	16.42	17.35	17.22	16.52
SKO	13.82	13.74	13.07	13.04	13.10	13.98	13.84	13.29
SKO`	15.74	15.67	14.93	14.84	14.76	15.80	15.67	14.84
LNS	17.15	17.04	16.50	16.49	16.36	17.21	17.07	16.30
MSL0	16.11	16.02	15.42	15.39	15.30	16.15	16.04	15.34
NRAPR	17.89	17.78	16.93	16.85	16.82	17.99	17.82	16.89
SQMC650	17.84	17.77	17.18	17.14	16.98	17.89	17.78	17.19
SQMC700	18.25	18.16	17.45	17.44	17.27	18.28	18.15	17.42
SkT1	14.54	14.51	14.03	13.94	13.85	14.66	14.52	14.05
SkT2	14.60	14.48	14.04	13.97	13.89	14.67	14.54	14.05
SkT3	14.69	14.60	14.08	13.99	13.96	14.78	14.65	14.12
SkT8	16.00	15.88	15.35	15.28	15.18	16.10	15.96	15.03
SkT9	15.96	15.87	15.31	15.25	15.16	16.06	15.94	15.22
SkT1*	14.52	14.42	13.93	13.89	13.81	14.61	14.49	13.99
SkT3*	14.57	14.50	13.99	13.89	13.82	14.70	14.60	14.02
Skxs20	15.49	15.38	14.87	14.79	14.67	15.52	15.40	14.86
Z-sigma	19.12	19.02	18.41	18.33	18.21	19.29	19.14	18.44
Exp.	16.90	16.40	16.20	15.80	15.70	16.83	16.27	16.2
Error	0.10	0.10	0.10	0.10	0.10	0.04	0.04	0.04

Table 28 IVGQR E_{CEN} (in MeV) for ^{92,94,96,98,100}Mo and ^{90,92,94}Zr.

IVGQR	^{92}Mo	^{94}Mo	^{96}Mo	^{98}Mo	^{100}Mo	^{90}Zr	^{92}Zr	^{94}Zr
SGII	27.39	27.24	26.77	26.52	26.33	27.48	27.30	26.97
KDE0	27.78	27.61	27.18	27.02	26.85	27.78	27.61	27.19
KDE0v1	27.25	27.08	26.70	26.51	26.38	27.28	27.08	26.63
SKM*	27.36	27.22	26.74	26.69	26.35	27.39	27.24	26.96
Sk255	27.50	27.35	26.96	26.78	26.65	27.50	27.34	26.91
SkI3	27.80	27.70	27.04	26.92	26.71	27.63	27.54	26.83
SkI4	28.69	28.54	27.72	27.57	27.41	28.62	28.39	27.56
SkI5	26.81	26.65	25.98	25.86	25.72	26.66	26.48	25.72
SV-bas	27.58	27.41	27.11	26.92	26.71	27.67	27.47	27.14
SV-min	25.18	25.03	24.71	24.55	24.35	25.27	25.10	24.77
SV-sym32	27.12	26.95	26.62	26.43	26.23	27.16	27.00	26.62
SV-m56-O	31.93	31.72	30.69	30.55	30.44	32.08	31.54	30.53
SV-m64-O	31.26	31.07	30.30	30.13	29.97	31.39	30.98	30.24
SLy4	26.65	26.47	26.14	25.98	25.87	26.69	26.52	26.10
SLy5	26.67	26.50	26.16	25.97	25.83	26.69	26.50	26.11
SLy6	27.23	27.05	26.65	26.46	26.26	27.27	27.07	26.67
SkMP	28.57	28.41	27.96	27.82	27.54	28.44	28.28	27.85
SKO	23.69	23.55	23.21	23.01	22.76	23.89	23.74	23.36
SKO`	25.39	25.24	24.81	24.62	24.51	25.43	25.28	24.82
LNS	27.85	27.70	27.30	27.15	26.96	27.92	27.73	27.35
MSL0	26.32	26.19	25.86	25.71	25.56	26.34	26.21	25.85
NRAPR	28.91	28.74	28.21	28.04	28.01	28.99	28.78	28.25
SQMC650	28.32	28.17	27.81	27.68	27.50	28.31	28.16	27.87
SQMC700	29.19	29.02	28.60	28.44	28.17	29.19	29.00	28.58
SkT1	23.64	23.48	23.26	23.08	22.94	23.71	23.56	23.30
SkT2	23.64	23.51	23.29	23.13	22.97	23.72	23.57	23.30
SkT3	23.85	23.71	23.42	23.26	23.13	23.93	23.78	23.47
SkT8	26.06	25.91	25.58	25.39	25.28	26.14	25.98	25.60
SkT9	25.98	25.84	25.53	25.34	25.22	26.06	25.90	25.54
SkT1*	23.57	23.45	23.21	23.02	22.89	23.68	23.54	23.24
SkT3*	23.68	23.54	23.24	23.09	22.96	23.83	23.67	23.36
Skxs20	24.74	24.57	24.32	24.15	23.93	24.75	24.59	24.30
Z-sigma	30.53	30.33	30.03	29.86	29.66	30.68	30.49	30.13
Exp. Error								

Table 29 IVGOR E_{CEN} (in MeV) for ^{92,94,96,98,100}Mo and ^{90,92,94}Zr.

IVGOR	^{92}Mo	^{94}Mo	^{96}Mo	^{98}Mo	^{100}Mo	^{90}Zr	^{92}Zr	^{94}Zr
SGII	36.09	35.90	35.54	35.38	34.89	36.12	35.98	35.64
KDE0	36.61	36.32	36.01	35.72	35.55	36.52	36.24	35.94
KDE0v1	36.03	35.81	35.53	35.20	35.05	36.01	35.70	35.39
SKM*	35.61	35.55	35.20	35.10	34.66	35.68	35.53	35.25
Sk255	35.79	35.63	35.22	35.02	34.90	35.78	35.54	35.19
SkI3	36.49	36.55	36.09	36.06	35.94	37.18	36.98	36.92
SkI4	37.43	37.36	36.78	36.67	36.53	37.46	37.19	36.66
SkI5	36.52	36.36	36.14	36.00	36.01	36.52	36.28	35.88
SV-bas	35.79	35.59	35.27	35.16	34.79	35.89	35.71	35.39
SV-min	33.52	33.40	33.01	32.90	32.53	33.63	33.45	33.10
SV-sym32	35.24	35.12	34.74	34.64	34.32	35.35	35.18	34.84
SV-m56-O	39.88	39.64	39.23	39.00	39.15	40.53	39.50	38.95
SV-m64-O	39.79	39.61	39.04	38.87	38.80	40.40	39.44	38.95
SLy4	35.50	35.23	34.97	35.21	35.03	35.44	35.17	34.89
SLy5	35.59	35.32	35.06	35.28	35.07	35.42	35.25	34.95
SLy6	36.27	35.94	35.65	35.40	35.24	36.27	35.94	35.62
SkMP	37.45	37.39	36.85	36.48	36.11	37.30	37.13	36.75
SKO	32.67	32.48	32.01	31.86	31.68	32.94	32.70	32.33
SKO`	33.78	33.63	33.22	32.97	32.84	33.85	33.69	33.27
LNS	36.54	36.37	36.01	35.89	35.60	36.65	36.44	36.05
MSL0	34.87	34.71	34.44	34.21	34.02	34.87	34.71	34.35
NRAPR	37.40	37.07	36.69	36.59	36.61	37.55	37.26	36.84
SQMC650	36.52	36.37	36.08	35.98	35.72	36.49	36.28	36.09
SQMC700	37.69	37.57	37.18	37.13	36.70	37.71	37.50	37.22
SkT1	32.06	31.58	31.30	31.13	30.93	31.88	31.69	31.38
SkT2	31.81	31.60	31.34	31.16	30.94	31.92	31.73	31.42
SkT3	32.07	31.87	31.56	31.38	31.16	32.21	31.99	31.66
SkT8	34.66	34.46	34.10	33.90	33.70	34.66	34.40	34.13
SkT9	34.52	34.38	34.03	33.86	33.59	34.57	34.31	34.02
SkT1*	31.72	31.53	31.25	31.07	30.85	31.83	31.65	31.34
SkT3*	31.83	31.66	31.41	31.12	30.98	32.03	31.86	31.52
Skxs20	32.86	32.68	32.27	32.15	31.87	32.99	32.65	32.33
Z-sigma	38.87	38.67	38.38	38.14	37.98	38.94	38.72	38.34
Exp. Error								

Table 30 ISGMR E_{CEN} (in MeV) for ^{44}Ca, ^{54}Fe, ^{64,68}Zn and ^{56,58,60,68}Ni.

ISGMR	^{44}Ca	^{54}Fe	^{56}Ni	^{58}Ni	^{60}Ni	^{64}Zn	^{68}Zn	^{68}Ni
SGII	20.08	20.06	20.15	19.30	19.76	18.47	18.31	18.66
KDE0	19.77	20.04	20.27	19.15	19.69	18.43	18.25	18.67
KDE0v1	19.79	20.02	20.16	19.18	19.65	18.44	18.26	18.60
SKM*	19.55	19.79	19.93	19.16	19.52	18.26	18.03	18.29
Sk255	20.78	20.62	20.67	19.99	20.13	19.17	19.09	19.47
SkI3	21.29	22.15	22.62	21.03	21.69	19.62	19.30	20.06
SkI4	20.78	21.13	21.34	20.21	20.59	19.07	19.03	19.74
SkI5	20.90	21.20	21.53	20.12	20.71	18.96	18.86	19.75
SV-bas	20.47	20.58	20.60	20.07	20.14	19.29	18.93	19.05
SV-min	20.01	20.02	20.06	19.62	19.69	18.91	18.54	18.66
SV-sym32	20.44	20.52	20.59	20.07	20.07	19.24	18.88	19.04
SV-m56-O	20.88	21.22	21.60	20.05	20.66	18.90	18.81	19.89
SV-m64-O	20.51	20.73	20.95	19.82	20.30	18.77	18.65	19.38
SLy4	19.28	19.58	19.79	18.73	19.27	18.05	17.90	18.38
SLy5	19.71	20.00	20.15	19.13	19.66	18.39	18.20	18.67
SLy6	19.82	20.17	20.37	19.23	19.88	18.43	18.29	18.78
SkMP	20.10	20.58	20.91	19.71	20.23	18.52	18.31	18.90
SKO	19.91	17.87	18.01	17.22	17.36	17.14	18.17	18.81
SKO`	20.04	19.34	19.30	18.74	18.82	18.27	18.37	18.69
LNS	20.37	20.50	20.61	19.65	NaN	NaN	NaN	19.01
MSL0	19.81	19.61	19.67	18.96	19.24	18.27	18.26	18.61
NRAPR	19.46	19.00	19.04	18.87	18.57	17.61	17.71	18.54
SQMC650	19.21	19.79	19.92	19.15	19.51	18.16	17.84	18.25
SQMC700	20.14	20.51	20.75	19.83	20.23	18.76	18.44	18.99
SkT1	20.57	20.31	20.29	19.91	19.89	19.32	19.07	19.04
SkT2	20.58	20.38	20.37	20.00	19.98	19.37	19.08	19.04
SkT3	20.58	20.05	19.94	19.63	19.56	19.12	19.02	19.04
SkT8	20.40	20.17	20.16	19.48	19.68	18.82	18.80	19.05
SkT9	20.33	20.24	20.25	19.58	19.76	18.88	18.79	18.91
SkT1*	20.19	19.95	19.91	19.51	19.50	19.04	18.84	18.87
SkT3*	20.45	19.75	19.60	19.26	19.24	18.88	18.88	19.08
Skxs20	19.04	19.28	19.38	18.83	19.01	18.19	17.68	18.10
Z-sigma	20.28	20.48	20.56	19.57	19.95	18.89	18.82	19.03
Exp.	19.49	19.66	19.30	19.32	18.10	18.88	16.60	21.10
Error	0.34	0.37	0.50	0.32	0.79	0.79	0.17	1.90

Table 31 ISGDR E_{CEN} (in MeV) for ^{44}Ca, ^{54}Fe, ^{64,68}Zn and ^{56,58,60,68}Ni.

ISGDR	^{44}Ca	^{54}Fe	^{56}Ni	^{58}Ni	^{60}Ni	^{64}Zn	^{68}Zn	^{68}Ni
SGII	29.80	30.66	30.92	30.33	30.24	28.14	29.13	29.52
KDE0	28.80	30.77	31.08	30.48	30.53	28.52	29.30	29.97
KDE0v1	28.97	30.67	31.02	30.33	30.36	28.40	29.14	29.85
SKM*	29.46	30.10	30.33	29.95	29.95	27.90	28.81	29.20
Sk255	29.45	30.08	30.50	29.91	29.92	28.34	29.47	29.92
SkI3	31.50	29.92	30.50	29.13	30.29	28.63	30.15	30.76
SkI4	29.36	31.32	31.66	31.09	30.65	28.97	30.10	30.96
SkI5	29.95	31.36	31.70	30.95	30.98	29.17	30.01	31.06
SV-bas	28.93	29.92	30.36	29.79	29.87	27.90	29.10	29.40
SV-min	28.76	29.50	29.79	29.21	29.29	27.51	28.55	28.68
SV-sym32	29.19	29.87	30.27	29.75	29.82	27.86	29.05	29.36
SV-m56-O	30.41	31.61	31.22	31.21	31.22	28.95	30.53	31.41
SV-m64-O	29.89	31.23	31.62	30.98	30.89	28.88	30.46	31.39
SLy4	28.74	30.31	30.77	30.04	30.09	28.39	28.83	29.59
SLy5	29.05	30.74	31.12	30.54	30.56	28.56	29.19	29.78
SLy6	28.98	30.65	30.80	30.26	30.63	28.64	29.45	30.28
SkMP	30.54	31.11	31.33	30.87	30.45	28.51	29.46	30.20
SKO	28.84	28.60	28.53	28.00	28.10	27.42	28.06	28.91
SKO`	28.85	29.26	29.17	28.78	28.94	27.45	28.59	29.02
LNS	29.49	30.92	31.32	30.83	NaN	NaN	NaN	30.33
MSL0	29.18	29.63	29.92	29.42	29.42	27.78	28.67	29.28
NRAPR	28.51	30.20	30.53	29.16	29.34	28.13	29.01	29.93
SQMC650	28.94	29.64	30.02	29.50	29.55	29.10	28.95	29.40
SQMC700	29.73	30.71	30.86	30.53	30.23	28.23	29.45	30.39
SkT1	28.78	29.20	29.47	28.95	28.94	27.48	28.51	28.67
SkT2	28.82	29.30	29.60	29.05	29.06	27.54	28.55	28.70
SkT3	28.91	29.25	29.10	28.71	28.61	27.33	28.46	28.70
SkT8	28.96	29.88	30.08	29.55	29.47	28.06	28.97	29.37
SkT9	29.13	29.82	30.21	29.74	29.65	27.98	28.91	29.28
SkT1*	28.37	29.16	29.11	28.51	28.57	27.22	28.19	28.53
SkT3*	28.47	28.82	29.31	28.47	28.44	27.11	28.15	28.57
Skxs20	28.33	29.52	29.43	28.80	28.95	28.12	28.14	28.40
Z-sigma	29.37	30.69	31.01	30.40	30.47	28.37	29.65	30.53
Exp.	35.03			34.06	36.12	25.66	27.65	
Error	1.45			0.30	0.28	1.21	0.38	

Table 32ISGQR E_{CEN} (in MeV) for ^{44}Ca, ^{54}Fe, ^{64,68}Zn and ^{56,58,60,68}Ni.

ISGQR	^{44}Ca	^{54}Fe	^{56}Ni	^{58}Ni	^{60}Ni	^{64}Zn	^{68}Zn	^{68}Ni
SGII	15.96	17.57	17.69	17.20	17.08	17.07	15.72	15.79
KDE0	16.84	18.21	18.34	17.98	17.72	17.91	16.41	16.32
KDE0v1	16.72	18.05	18.18	17.77	17.59	17.74	16.26	16.13
SKM*	15.81	17.45	17.61	17.23	17.14	17.07	15.56	15.56
Sk255	15.81	16.84	16.97	16.49	16.35	16.47	15.31	15.31
SkI3	19.57	21.16	21.26	19.49	18.95	20.43	18.95	18.33
SkI4	18.58	19.34	19.51	18.25	18.66	19.00	17.66	17.31
SkI5	18.39	20.01	20.19	19.52	19.19	19.70	18.14	17.70
SV-bas	15.39	16.69	16.77	16.43	16.29	16.22	14.96	14.98
SV-min	15.18	16.32	16.42	16.04	15.95	15.91	14.67	14.60
SV-sym32	15.36	16.67	16.76	16.33	16.27	16.22	14.91	14.92
SV-m56-O	18.81	20.42	20.62	19.98	19.57	20.19	18.55	18.13
SV-m64-O	17.76	19.30	19.44	18.86	18.64	18.98	17.38	17.23
SLy4	16.63	17.87	17.98	17.67	17.51	17.71	16.20	16.18
SLy5	16.59	18.00	18.11	17.76	17.59	17.85	16.30	16.26
SLy6	16.89	18.45	18.57	18.15	18.02	18.19	16.68	16.55
SkMP	17.29	18.85	19.55	16.90	17.41	18.42	16.94	16.86
SKO	15.72	14.87	14.82	14.58	14.32	14.72	14.76	14.97
SKO`	15.76	16.16	16.19	15.94	15.60	15.80	15.05	14.98
LNS	16.72	18.42	18.56	18.09	NaN	NaN	NaN	16.48
MSL0	15.90	16.96	17.05	16.71	16.52	16.59	15.45	15.46
NRAPR	16.71	16.98	17.12	16.69	16.50	16.85	16.00	16.11
SQMC650	16.26	17.49	18.22	17.74	17.23	17.49	16.04	15.91
SQMC700	16.92	18.53	19.13	18.42	18.10	17.98	16.72	16.56
SkT1	14.86	15.54	15.61	15.39	15.24	15.30	14.23	14.18
SkT2	14.87	15.76	15.74	15.52	15.37	15.37	14.32	14.21
SkT3	14.87	15.45	15.50	15.33	15.02	15.17	14.30	14.17
SkT8	15.65	16.63	16.67	16.34	16.16	16.26	15.17	15.26
SkT9	15.74	16.78	16.90	16.57	16.34	16.49	15.27	15.22
SkT1*	14.90	15.44	15.48	15.26	15.09	15.17	14.19	14.17
SkT3*	14.70	15.03	15.10	14.85	14.62	14.80	14.04	13.97
Skxs20	15.34	16.32	16.86	16.63	16.38	16.18	14.80	14.54
Z-sigma	16.63	17.91	17.97	17.58	17.52	17.47	16.17	16.31
Exp.	17.21	18.05	16.20	16.34	15.88	15.85	15.54	15.90
Error	0.48	0.87	0.50	0.13	0.14	0.31	0.32	1.30

Table 33 ISGOR E_{CEN} (in MeV) for ^{44}Ca, ^{54}Fe, ^{64,68}Zn and ^{56,58,60,68}Ni.

ISGOR	^{44}Ca	^{54}Fe	^{56}Ni	^{58}Ni	^{60}Ni	^{64}Zn	^{68}Zn	^{68}Ni
SGII	28.34	29.58	29.39	27.73	29.12	27.37	26.80	27.20
KDE0	28.88	30.67	30.47	28.67	30.10	28.17	27.48	28.06
KDE0v1	28.91	30.61	30.38	28.65	30.02	28.19	27.34	28.04
SKM*	27.70	29.27	29.15	27.76	28.94	27.17	26.60	26.84
Sk255	27.98	29.75	29.65	27.70	28.87	27.36	26.78	27.02
SkI3	28.37	29.88	29.73	28.03	28.49	27.02	29.01	29.67
SkI4	30.09	31.62	31.39	29.55	30.41	28.82	29.40	29.37
SkI5	29.42	31.43	31.59	29.03	30.71	28.60	29.58	30.06
SV-bas	27.59	28.82	28.63	27.31	28.14	26.54	26.23	26.20
SV-min	27.26	28.58	28.43	27.19	27.74	26.29	25.88	25.72
SV-sym32	27.51	28.76	28.68	27.27	28.05	26.49	26.12	26.04
SV-m56-O	29.40	31.88	31.50	29.27	30.55	28.47	29.98	30.35
SV-m64-O	29.69	31.48	31.24	29.19	30.75	28.74	28.86	29.24
SLy4	28.45	30.30	30.11	28.34	29.88	27.94	27.49	28.08
SLy5	28.57	30.46	30.30	28.60	30.03	28.11	27.31	28.02
SLy6	29.00	30.63	30.46	28.74	30.11	28.18	27.91	28.58
SkMP	28.72	31.14	31.05	29.09	30.42	27.91	27.77	28.37
SKO	28.09	26.45	26.23	24.93	25.86	26.45	26.17	27.13
SKO`	28.08	29.11	28.93	27.37	28.06	26.94	26.78	26.69
LNS	29.28	30.64	30.43	28.87	NaN	NaN	NaN	28.17
MSL0	28.05	29.73	29.76	27.80	29.10	27.23	26.75	27.23
NRAPR	28.15	29.84	29.80	27.62	29.36	28.17	28.00	28.83
SQMC650	27.47	29.71	29.75	27.99	29.28	27.08	26.69	27.01
SQMC700	28.46	30.98	30.87	29.04	29.97	27.78	27.65	27.86
SkT1	26.96	27.96	27.88	26.79	27.21	25.93	25.42	25.32
SkT2	26.98	28.04	27.90	26.88	27.34	25.91	25.47	25.28
SkT3	27.04	28.04	27.86	26.70	27.12	25.99	25.57	25.41
SkT8	27.75	29.43	29.36	27.60	28.75	27.39	26.80	27.11
SkT9	27.87	29.51	29.54	27.86	28.94	27.28	26.61	26.95
SkT1*	27.12	27.83	27.74	26.57	27.01	25.80	25.40	25.39
SkT3*	27.04	27.34	27.21	26.10	26.51	25.61	25.30	25.34
Skxs20	27.10	28.45	28.23	27.07	27.73	25.98	25.55	25.28
Z-sigma	28.94	30.53	30.37	28.59	30.10	27.98	27.61	28.24
Exp.				23.20	24.40			
Error				0.30	0.26			

Table 34 IVGMR E_{CEN} (in MeV) for ^{44}Ca, ^{54}Fe, ^{64,68}Zn and ^{56,58,60,68}Ni.

IVGMR	**^{44}Ca**	**^{54}Fe**	**^{56}Ni**	**^{58}Ni**	**^{60}Ni**	**^{64}Zn**	**^{68}Zn**	**^{68}Ni**
SGII	32.62	34.03	34.17	32.72	31.92	30.43	30.73	31.37
KDE0	31.93	33.74	33.90	32.39	31.80	30.18	30.45	30.84
KDE0v1	31.71	33.40	33.57	32.16	31.54	30.07	30.21	30.48
SKM*	32.25	34.08	34.14	32.86	32.14	30.78	30.69	31.00
Sk255	33.37	34.86	35.01	33.52	32.76	31.84	32.15	32.38
SkI3	32.65	35.67	36.15	33.04	32.90	29.64	29.46	30.75
SkI4	33.04	36.60	36.88	33.85	33.53	31.01	31.48	32.37
SkI5	31.90	34.10	34.55	31.95	31.77	29.27	29.69	30.90
SV-bas	32.80	34.78	34.86	33.68	32.64	31.52	31.56	31.60
SV-min	31.11	32.65	32.60	31.60	30.68	29.59	29.49	29.24
SV-sym32	32.81	34.89	35.02	33.81	32.78	31.61	31.55	31.51
SV-m56-O	34.45	37.98	38.51	34.54	34.59	32.12	32.88	34.27
SV-m64-O	34.07	37.26	37.50	34.45	34.37	31.91	32.79	33.74
SLy4	30.40	31.87	32.01	30.79	30.34	28.72	28.98	29.51
SLy5	30.73	32.27	32.33	31.12	30.65	29.07	29.17	29.63
SLy6	31.30	32.91	33.08	31.60	31.13	29.34	29.68	30.30
SkMP	32.96	35.70	36.08	33.87	33.38	30.92	31.23	32.06
SKO	29.57	27.69	27.30	26.55	25.90	25.86	27.77	28.99
SKO`	31.58	32.68	32.42	31.30	30.31	29.52	30.14	30.15
LNS	33.13	34.59	34.66	33.62	NaN	NaN	NaN	31.86
MSL0	31.48	32.67	32.67	31.69	30.66	29.64	30.04	30.35
NRAPR	32.80	33.62	33.88	32.54	31.76	30.81	32.11	32.89
SQMC650	32.42	34.68	34.84	33.33	32.75	31.21	30.96	31.14
SQMC700	33.35	35.93	36.34	34.31	33.84	31.94	32.00	32.40
SkT1	29.76	30.50	30.25	29.75	28.84	28.25	28.24	27.83
SkT2	29.79	30.61	30.38	29.85	28.91	28.28	28.18	27.76
SkT3	30.22	30.62	30.31	29.77	28.82	28.34	28.59	28.18
SkT8	31.09	32.07	31.89	30.98	30.18	29.21	29.70	29.79
SkT9	31.00	32.09	32.02	31.04	30.22	29.14	29.47	29.52
SkT1*	29.39	30.09	29.86	29.38	28.47	27.95	28.10	27.77
SkT3*	29.97	30.04	29.73	29.32	28.40	28.13	28.58	28.24
Skxs20	30.70	32.58	32.53	31.53	30.51	29.36	28.71	28.02
Z-sigma	33.33	35.42	35.45	33.64	32.92	31.45	32.23	32.80
Exp.								
Error								

Table 35 IVGDR E_{CEN} (in MeV) for ^{44}Ca, ^{54}Fe, ^{64,68}Zn and ^{56,58,60,68}Ni.

IVGDR	**^{44}Ca**	**^{54}Fe**	**^{56}Ni**	**^{58}Ni**	**^{60}Ni**	**^{64}Zn**	**^{68}Zn**	**^{68}Ni**
SGII	19.89	19.18	19.11	19.84	18.93	18.23	17.85	17.39
KDE0	20.03	19.52	19.44	20.14	19.31	18.62	18.13	17.69
KDE0v1	19.58	19.16	19.05	19.67	18.87	18.25	17.77	17.27
SKM*	20.01	19.44	19.40	20.31	19.27	18.68	18.12	17.48
Sk255	20.19	19.35	19.27	19.76	18.91	18.41	18.18	17.61
SkI3	18.84	19.16	19.26	20.51	19.35	17.69	16.76	16.42
SkI4	20.92	20.74	20.74	22.65	21.94	18.93	18.27	17.81
SkI5	17.46	17.53	17.81	18.00	17.38	16.06	15.65	15.62
SV-bas	20.90	20.00	19.85	20.62	19.59	19.09	18.63	17.87
SV-min	18.58	18.00	17.83	18.36	17.60	17.03	16.61	15.99
SV-sym32	20.37	19.65	19.52	20.27	19.26	18.69	18.18	17.40
SV-m56-O	22.97	22.64	22.72	23.35	22.26	20.23	19.90	19.59
SV-m64-O	23.00	22.37	22.35	23.00	21.89	20.49	20.11	19.63
SLy4	18.71	18.36	18.28	18.90	18.33	17.59	17.19	16.84
SLy5	18.73	18.36	18.29	18.98	18.36	17.66	17.18	16.82
SLy6	19.21	18.83	18.75	19.33	18.68	17.87	17.46	17.15
SkMP	20.19	19.79	20.12	21.17	20.08	18.80	18.07	17.60
SKO	17.01	15.06	14.79	15.56	15.08	14.58	15.03	15.01
SKO`	18.84	17.84	17.64	18.45	17.71	16.89	16.74	16.08
LNS	20.18	19.51	19.47	20.46	NaN	NaN	NaN	17.98
MSL0	18.87	18.17	18.03	18.67	17.77	17.30	17.06	16.55
NRAPR	20.92	19.69	19.56	19.94	19.22	18.72	18.83	18.59
SQMC650	20.83	20.32	20.33	21.29	20.15	19.65	18.89	18.11
SQMC700	21.50	20.98	20.99	21.89	20.70	19.97	19.26	18.56
SkT1	17.23	16.57	16.39	16.91	16.17	15.87	15.58	15.05
SkT2	17.27	16.65	16.44	17.04	16.23	15.95	15.60	15.02
SkT3	17.47	16.63	16.36	16.96	16.20	15.86	15.72	15.15
SkT8	18.94	18.13	17.94	18.46	17.66	17.30	17.10	16.64
SkT9	18.91	18.18	18.01	18.65	17.80	17.39	17.05	16.53
SkT1*	17.14	16.43	16.25	16.66	16.01	15.74	15.51	15.04
SkT3*	17.34	16.32	16.12	16.54	15.89	15.61	15.60	15.12
Skxs20	18.36	18.04	17.93	18.90	17.79	17.32	16.46	15.62
Z-sigma	23.32	22.07	21.84	22.89	21.70	21.12	20.79	20.15
Exp.	21.63	18.94	20.91	20.41	20.41	18.77	17.18	17.10
Error	0.50	0.50	0.50	0.50	0.50	0.50	0.50	0.20

Table 36 IVGQR E_{CEN} (in MeV) for ^{44}Ca, ^{54}Fe, ^{64,68}Zn and ^{56,58,60,68}Ni.

IVGQR	**^{44}Ca**	**^{54}Fe**	**^{56}Ni**	**^{58}Ni**	**^{60}Ni**	**^{64}Zn**	**^{68}Zn**	**^{68}Ni**
SGII	30.99	30.44	30.48	29.84	29.00	28.29	28.64	28.18
KDE0	30.96	30.78	30.77	29.99	29.01	28.53	28.82	28.24
KDE0v1	30.36	30.23	30.19	29.44	28.54	28.03	28.24	27.62
SKM*	30.41	30.24	30.35	29.64	29.23	28.31	28.30	27.77
Sk255	30.28	30.07	30.14	29.45	28.85	28.15	28.32	27.77
SkI3	31.15	29.47	29.99	29.21	28.78	28.54	28.59	27.70
SkI4	32.14	31.77	32.21	31.13	29.85	29.83	30.02	28.86
SkI5	29.55	29.41	29.82	28.37	27.27	26.73	27.52	26.94
SV-bas	31.12	30.70	30.68	30.08	29.34	28.61	28.80	27.98
SV-min	28.72	28.39	28.25	27.69	27.02	26.33	26.42	25.52
SV-sym32	30.45	30.15	30.20	29.53	28.81	28.11	28.21	27.34
SV-m56-O	34.73	33.46	34.43	32.83	32.20	30.65	32.67	31.98
SV-m64-O	34.30	34.22	34.90	33.14	32.00	31.92	32.19	31.38
SLy4	29.64	29.35	29.59	28.87	27.99	27.51	27.64	27.23
SLy5	29.71	29.48	29.46	28.80	27.95	27.50	27.67	27.26
SLy6	30.48	30.07	30.18	29.27	28.81	27.92	28.33	27.82
SkMP	31.50	29.94	30.46	29.83	29.72	29.53	29.28	28.82
SKO	27.84	24.68	24.29	24.02	23.41	23.65	25.12	25.15
SKO`	28.99	28.01	27.78	27.27	26.38	26.01	26.60	25.71
LNS	31.25	30.85	30.92	30.49	NaN	NaN	NaN	28.60
MSL0	29.35	29.00	28.99	28.43	27.82	27.02	27.24	26.78
NRAPR	31.73	30.77	30.90	30.08	29.54	29.05	29.71	29.66
SQMC650	30.92	31.14	31.36	30.56	30.16	29.20	28.91	28.31
SQMC700	32.36	32.32	32.62	31.61	30.49	30.18	30.05	29.36
SkT1	26.93	26.52	26.26	25.91	25.31	24.74	24.79	24.12
SkT2	26.98	26.63	26.38	26.00	25.38	24.79	24.81	24.08
SkT3	27.29	26.60	26.31	25.92	25.28	24.79	25.03	24.30
SkT8	29.45	28.90	28.75	28.23	27.60	26.93	27.21	26.71
SkT9	29.35	29.00	28.85	28.33	27.59	26.94	27.11	26.50
SkT1*	26.83	26.31	26.06	25.67	25.13	24.58	24.73	24.11
SkT3*	27.09	26.15	25.85	25.47	24.90	24.50	24.87	24.28
Skxs20	27.95	28.13	28.01	27.52	26.74	25.91	25.62	24.68
Z-sigma	34.42	34.00	33.99	33.20	32.19	31.70	31.99	31.50
Exp. Error								

Table 37 IVGOR E_{CEN} (in MeV) for ^{44}Ca, ^{54}Fe, ^{64,68}Zn and ^{56,58,60,68}Ni.

IVGOR	**^{44}Ca**	**^{54}Fe**	**^{56}Ni**	**^{58}Ni**	**^{60}Ni**	**^{64}Zn**	**^{68}Zn**	**^{68}Ni**
SGII	39.25	39.48	40.00	40.47	39.32	38.04	37.61	38.36
KDE0	39.36	39.71	40.45	39.33	39.52	38.52	37.92	38.85
KDE0v1	38.86	39.31	39.91	38.67	39.01	37.74	37.43	38.29
SKM*	38.30	38.71	39.54	39.13	38.70	37.63	36.98	37.83
Sk255	38.61	38.50	39.47	39.36	38.36	37.79	36.91	37.83
SkI3	40.47	39.68	41.14	40.57	39.80	39.63	39.07	39.68
SkI4	41.19	40.36	41.37	41.86	40.15	41.08	40.42	39.95
SkI5	39.28	39.53	40.85	39.54	39.70	38.61	38.00	38.95
SV-bas	39.29	39.20	39.64	39.55	38.78	37.97	37.52	38.17
SV-min	37.41	37.40	37.54	36.75	36.79	35.58	35.56	35.92
SV-sym32	38.68	38.72	39.09	39.00	38.27	37.44	36.91	37.61
SV-m56-O	42.71	42.05	43.52	39.70	42.89	39.02	43.22	43.29
SV-m64-O	41.98	42.34	43.41	43.59	42.55	38.58	41.90	42.44
SLy4	38.19	38.47	39.08	38.73	38.34	37.28	36.65	37.78
SLy5	37.95	38.71	39.27	38.07	38.52	37.01	36.75	37.80
SLy6	38.92	39.35	40.13	38.92	39.18	38.00	37.56	38.58
SkMP	39.77	40.33	41.36	40.55	40.39	40.37	38.73	39.64
SKO	37.79	35.07	34.67	34.26	34.02	33.76	35.31	35.48
SKO`	37.91	36.97	37.34	36.35	36.11	35.62	35.74	35.91
LNS	39.54	39.81	40.66	39.50	NaN	NaN	NaN	39.09
MSL0	37.82	37.76	38.66	38.35	37.50	36.76	36.18	37.06
NRAPR	41.38	39.34	40.47	41.09	39.10	39.61	38.76	40.07
SQMC650	38.56	39.52	40.32	40.81	39.48	40.40	37.55	38.54
SQMC700	40.06	40.81	42.05	40.94	40.80	40.30	39.17	39.94
SkT1	35.46	35.50	35.65	34.84	34.85	33.55	33.64	34.02
SkT2	35.50	35.59	35.48	35.30	34.93	33.60	33.66	34.00
SkT3	35.88	35.60	35.80	35.45	34.90	33.86	33.94	34.35
SkT8	37.80	37.77	38.42	38.02	37.33	36.08	36.14	36.94
SkT9	37.71	37.81	38.15	38.17	37.41	36.09	36.09	36.79
SkT1*	35.69	35.32	35.52	34.47	34.68	33.57	33.57	34.05
SkT3*	35.75	35.41	35.39	35.42	34.48	33.62	33.80	34.09
Skxs20	36.44	36.92	37.20	36.38	36.42	34.90	34.61	34.92
Z-sigma	41.75	42.08	42.50	42.88	41.78	41.60	41.04	41.71
Exp. Error								